VIET NAM NATIONAL UNIVERSITY
HO CHI MINH CITY

BK - OISP

THE 12TH

OISP SCIENCE AND TECHNOLOGY

SYMPOSIUM FOR STUDENTS
EDITED BY AUTHORS

JULY 23RD, 2023

HO CHI MINH CITY, VIETNAM

VNUHCM PRESS

THE 12TH OISP SCIENCE and TECHNOLOGY SYMPOSIUM FOR STUDENTS

JULY 23, 2023

HO CHI MINH CITY, VIETNAM

VNUHCM PRESS

TABLE OF CONTENTS

ACKNOWLEDGEMENT

The Symposium Organizers would like to acknowledge:

Organizing Committee

- Dr. Nguyen Huynh Thong - Vice Director of Office for International Study Programs
- Ms. Le Thi Thao - Manager of Academic Affairs Department
- Ms. Vo Dao Trang Thy - Service Team Leader of Academic Affairs Department
- Ms. Huynh Thi Cam Nhung - Executive of Academic Affairs Department
- Ms. Nguyen Thi Bich Nhung - Executive of R&D and Project Management Office
- Ms. Tran Nguyen Nam Phuong - The Associated Organ of Student's Association

Secretariat

- Ms. Le Thi Hong Nhung - Executive MBA in Management Consulting International Program
- Ms. Phan Thi Thanh An - Executive of Academic Affairs Department
- Ms. Pham Minh Thuan - Executive of Academic Affairs Department
- Ms. Huynh Thi Cam Nhung - Executive of Academic Affairs Department

Consultant Committee

- Dr. Pham Tan Thi - R&D and Project Management Office
- Dr. Nguyen Khanh Son - Vice Dean of Faculty of Materials Technology
- Dr. Huynh Phu Minh Cuong - Vice Dean of Faculty of Electrical – Electronics Engineering
- Dr. Dao Hong Hai - Vice Dean of Faculty of Geology and Petroleum Engineering
- Dr. Truong Minh Chuong - Vice Dean of School of Industrial Management
- Dr. Tran Tan Viet - Vice Dean of Faculty of Chemical Engineering
- Dr. Tran Trung Nghia - Vice Dean of Faculty of Applied Science
- Assoc. Prof. Dr. Luong Van Hai - Vice Dean of Faculty of Civil Engineering
- Assoc. Prof. Dr. Nguyen Nhat Huy - Vice Dean of Faculty of Environment and Natural Resources
- Assoc. Prof. Dr. Tran Anh Son - Vice Dean of Faculty of Mechanical Engineering
- Assoc. Prof. Dr. Tran Ngoc Thinh - Vice Dean of Faculty of Computer Science and Engineering
- Assoc. Prof. Dr. Le Dinh Tuan - Vice Dean of Faculty of Transportation Engineering

SYMPOSIUM PROGRAM

Start	End	Symposium Program
Opening Ceremony (7:00 – 08:00) – B4 Hall		
7:00	7:15	- Guests and Delegates welcoming
7:15	7:30	- Remark by the Director of OISP
7:30	7:45	- Poster's exhibiting
COUNCIL 1 (08:00 – 10:20) - Room 408 - A4 **Faculty of Civil Engineering** **Faculty of Geology and Petroleum Engineering**		
Board of Judges: **Dr. Bui Phuong Trinh** **Dr. Lieu Xuan Qui** **Dr. Tran Trung Dung**		
08:00	08:15	**Damage detection in beams using vibration characteristics** **(Chẩn đoán hư hỏng trong kết cấu dầm sử dụng các đặc trưng dao động)** Chi-Khai Nguyen, Vi-Khang Tran, Tran-De-Nhat Truong, Duc-Duy Ho
08:15	08:30	**Experimental study of reusing waste sludge from water supply plant to manufacture interlocking concrete brick** **(Nghiên cứu tái sử dụng bùn phế thải từ nhà máy cấp nước để chế tạo gạch bê tông tự chèn)** Chi-Khai Nguyen, Anh-Khoa Vu, Tran-Hoang-Khoa Phan, Perez Vergara M. Gianina, Phuong Trinh Bui
08:30	08:45	**Ultimate lateral capacity of pile group on soil slope using finite element method** **(Phân tích sức chịu tải ngang của nhóm cọc trên mái dốc bằng phương pháp phần tử hữu hạn)** Bui Van Nhat Thanh, Tran Hoang Giap, Nguyen Trung Kien
08:45	09:00	**Simulation and design of flat slab by using ETABS software** **(Mô phỏng và thiết kế sàn không dầm sử dụng phần mềm ETABS)** Nguyen Thai Binh, Ha Khanh Duy, Duong Quoc Anh, Nguyen Cong Gia Bao, Truong Dinh Thanh Dat, Le Ngoc Thanh, Nguyen Viet Thang
09:00	09:15	**Investigating the properties of sand-bentonite mixture by determining the shear strength parameters using direct shear test to apply to bore pile construction** **(Nghiên cứu đặc tính của hỗn hợp cát và bentonite thông qua việc xác định thông số sức chống cắt bằng thí nghiệm cắt trực tiếp và áp dụng cho thi công cọc khoan nhồi)** Ha Khanh Duy, Le Ngoc Thanh, Nguyen Cong Gia Bao, Duong Dinh Tri, Mikaelah Perez
09:15	09:30	**QR code and augmented reality (AR) applications for facilities management: State of practices** **(Mã QR và các ứng dụng thực tế tăng cường (AR) để quản lý cơ sở vật chất: Ứng dụng thực tiễn)** Hai Phu Huynh, Trung Quang Khuc, Mikaelah Gianina Vergara Perez, Sy Tien Do, Thu Anh Nguyen
09:30	09:45	**Identifying the role of project's stakeholders in the use of a common data environment in construction management of Autodesk 360 platform applications** **(Xác định vai trò của các bên liên quan tham gia dự án trong việc sử dụng môi trường dữ liệu chung trong quản lý xây dựng ứng dụng nền tảng Autodesk 360)** Mikaelah Gianina Vergara Perez, Trung Quang Khuc, Phat Lien Huynh, Thu Anh Nguyen
09:45	10:00	**Optimization of construction method for underground storage facilites** **(Tối ưu hóa phương pháp thi công cho các công trình ngầm lưu chứa)** Pham Ngoc Phuong Quynh, Le Minh Nhat, Huynh Minh Khoi, Nguyen Van Nhan, Nguyen Huynh Thong
10:00	10:20	Result announcement

Start	End	Symposium Program
Opening Ceremony (7:00 – 08:00) – B4 Hall		
7:00	7:15	- Guests and Delegates welcoming
7:15	7:30	- Remark by the Director of OISP
7:30	7:45	- Poster's exhibiting
COUNCIL 2 (08:00 – 10:35) – Room 409 – A4 **Faculty of Chemical Engineering** **Faculty of Environment and Natural Resources**		
Board of Judges: **Assoc. Prof. Nguyen Dinh Quan** **Dr. Ha Cam Anh** **Dr. Phan Thanh Lam**		
08:00	08:15	**A nano-based perfume: Nanoemulsions formulation and characterization** **(Nước hoa Nano: Sự hình thành hệ nhũ Nano và các tính chất)** Hoang Dang Ngoc Lam, Tran Le Hoai Nhi, Phan Kim Quoc Cuong, Nguyen Dinh Quan
08:15	08:30	**Sensory properties and consumer preferences of snack enriched with spirulina biomass** **(Đánh giá tính chất cảm quan và mức độ ưa thích của người tiêu dùng đối với sản phẩm snack khi bổ sung bột tảo spirulina)** Tran Thi Van Anh, Vo Ngoc Mai Anh, Duong Chau Uyen Nhi, Quan Thi Thanh Nhan, Pham Nguyen Quang Minh, Nguyen Le Hoa, Nguyen Quoc Cuong
08:30	08:45	**Fabrication of CO_2 - activated porous carbon aerogel from durian rind for energy storage** **(Chế tạo vật liệu hoạt hóa CO_2 – carbon aerogel từ vỏ sầu riêng ứng dụng trong lưu trữ năng lượng)** Bui Dang Dang Khoa, Long Hoang Le, Duy Khac Anh Nguyen, Phung K. Le
08:45	09:00	**Preparation of solid lipid nanoencapsulation of extracts from spinach (*Spinacia oleracea L.*) leaves** **(Nghiên cứu tạo hệ nano bao bọc chiết xuất từ lá cải bó xôi (*Spinacia oleracea L.*))** Bao Quyen, Le Thi Hong Nhan
09:00	09:15	**Evaluating vitamin E&C encapsulation with solid lipid (NATEROL) in textile applications by using a DPPH scavenging activity method** **(Đánh giá hệ vi nang vitamin E&C với một số loại béo rắn (NATEROL) ứng dụng trên vải bằng phương pháp quét gốc tự do DPPH)** Huynh Tan An, Le Thi Hong Nhan
09:15	09:30	**Evaluating vitamin E&C encapsulation with solid lipid (SABOWAX) in textile applications by using a DPPH scavenging activity method** **(Đánh giá hệ vi nang vitamin E&C với một số loại béo rắn (SABOWAX) ứng dụng trên vải bằng phương pháp quét gốc tự do DPPH)** Pham Kim Khanh, Le Thi Hong Nhan
09:30	09:45	**Research on natural actives of robusta coffee pulp for applications in personal care products** **(Nghiên cứu hoạt chất tự nhiên từ vỏ cà phê robusta định hướng ứng dụng trong sản phẩm chăm sóc cá nhân)** Le Hoang Tin, Le Thi Hong Nhan
09:45	10:00	**Utilization of green kohlrabi leaf powder for partial substitution of wheat flour in high-fiber pasta production: Effects of substituting percentage on high-fiber pasta quality** **(Tận dụng phụ phẩm lá su hào xanh thay thế một phần bột mì trong sản xuất mì pasta giàu xơ: Ảnh hưởng của tỉ lệ bổ sung lá su hào lên chất lượng của sản phẩm)** Nguyen Thu An
10:00	10:15	**Air pollution control and design for Vietnam Finland International School (VFIS)** **(Kiểm soát môi trường không khí và thiết kế hệ thống xử lý khí thải cho trường quốc tế Việt Nam – Phần Lan (VFIS))** Nguyen Duy Khanh, Le Phuoc Minh Duc, Du My Le
10:15	10:35	Result announcement

Start	End	Symposium Program
Opening Ceremony (7:00 – 08:00) – B4 Hall		
7:00	7:15	- Guests and Delegates welcoming
7:15	7:30	- Remark by the Director of OISP
7:30	7:45	- Poster's exhibiting
COUNCIL 3 (08:00 – 10:05) – Room 507 – A4 **School of Industrial Management** **Faculty of Transportation Engineering** **Faculty of Applied Science**		
Board of Judges: **Dr. Truong Minh Chuong** **Assoc. Prof. Ngo Khanh Hieu** **Dr. Le Quoc Khai**		
08:00	08:15	**Designing an electric vehicle powertrain system as educational apparatus** **(Thiết kế hệ thống động lực xe điện hai bánh phục vụ công tác giảng dạy)** Tran Dang Long, Vuong Thoi Hao, Nguyen Xuan Nam, Nguyen Nhu Phuc, Ngo Minh Tan
08:15	08:30	**Reconstructing the conductivity distribution imaging in biological tissue simulation environment by electrical impedance tomography** **(Tái tạo hình ảnh sự phân bố độ dẫn điện trong môi trường giả lập mô sinh học bằng phương pháp cắt lớp điện trở kháng)** Minh Quan Cao Dinh, Quoc Tuan Nguyen Diep, Anh Tu Tran, Trung Nghia Tran
08:30	08:45	**Designing the general layout of the dynamometer used for small power electric motor** **(Thiết kế bố trí chung băng thử động cơ điện cỡ nhỏ)** Le Do Minh Hoang, Truong Tan Phat, Le Duc Minh, Hong Duc Thong
08:45	09:00	**Designing a real-time vibration monitoring system for CVT push-belt testbench** **(Thiết kế hệ thống giám sát thời gian thực rung động dây đai hộp số CVT)** Pham Gia Khanh, Le Dinh Tuan
09:00	09:15	**The impact of corporate social responsibility on firm risk: The importance of institutional ownership** **(Tác động của trách nhiệm xã hội đến rủi ro doanh nghiệp: Tầm quan trọng của sở hữu tổ chức)** Tran Van Son, Nguyen Thuy Khanh Linh, Huynh To Quan, Pham Hieu Hanh, Nguyen Ngoc Van Anh, Dang Quoc Bao, Pham Tien Minh
09:15	09:30	**Sustainable tourism development based on the social exchange theory and bottom-up spillover theory: A case study in Ho Chi Minh City** **(Phát triển du lịch bền vững dựa trên lý thuyết social exchange và lý thuyết bottom-up Spillover: Nghiên cứu tình huống tại Thành phố Hồ Chí Minh)** Thai Minh Nhat, Lai Bao Ngoc, Nguyen Trinh Hoang Oanh, Pham Quoc Trung
09:30	09:45	**Detection of road surface damage from drone images** **(Nhận diện hư hỏng bề mặt đường giao thông từ ảnh chụp bởi drone)** Nguyen Dang Khoa, Nguyen Thi Khanh Ly, Nguyen Vu Nhat Minh, Nguyen Thanh Toan, Quach Bao Khang, Hoang Duc Trung, Assoc. Prof. Dr. Ngo Khanh Hieu
09:45	10:05	Result announcement

Start	End	Symposium Program
Opening Ceremony (7:00 – 08:00) – B4 Hall		
7:00	7:15	- Guests and Delegates welcoming
7:15	7:30	- Remark by the Director of OISP
7:30	7:45	- Poster's exhibiting
COUNCIL 4 (08:00 – 10:05) – Room 508 – A4 **Faculty of Electrical and Electronics Engineering** **Faculty of Computer Science and Engineering** **Faculty of Civil Engineering**		
Board of Judges: **Dr. Tran Hoang Linh** **Dr. Le Trong Nhan** **Dr. Thai Son**		
08:00	08:15	**Analysis of piles location for stabilizing slope by finite element method** **(Phân tích vị trí tối ưu của cọc dùng cho việc ổn định mái bằng phương pháp phần tử hữu hạn)** Tran Nhat Linh, Nguyen Minh Quan, Huynh Trong Tri, Nguyen Trung Kien
08:15	08:30	**Hand gesture recognition for game-based hand rehabilitation** **(Nhận diện cử chỉ tay cho việc chơi trò chơi hỗ trợ phục hồi chức năng tay)** Ho Tri Khang, Tran Tien Phat, Vo Ngoc Sang, Nguyen Ngoc Thanh Xuan, Le Gia Phat
08:30	08:45	**BACHKHOA ECO-FRIENDLY GUIDE – an AIOT device for raising awareness about trash classification at source** **(BACHKHOA ECO-FRIENDLY GUIDE – Thiết bị AIOT nâng cao nhận thức về phân loại rác tại nguồn)** Vo Ngoc Sang, Pham Hoang Anh, Ho Tri Khang, Tran Tien Phat, Nguyen Ngoc Thanh Xuan, Le Gia Phat, Nguyen Lam Tam Nhu
08:45	09:00	**Application of genetic algorithm to optimize the comparator circuit with respect to speed and power consumption** **(Nghiên cứu và ứng dụng thuật toán di truyền vào tối ưu hóa tốc độ và công suất tiêu thụ của mạch so sánh)** Nguyen Trong Hoang, Hoang Trang
09:00	09:15	**Optimizing the PSRR parameter of the Bandgap Reference circuit by using the Bayesian optimization algorithm** **(Ứng dụng giải thuật tối ưu Bayesian nhằm tối ưu thông số PSRR của mạch Bandgap Reference)** Nguyen Quoc Thang, Hoang Trang
09:15	09:30	**Finite element investigation and prediction of the bearing capacity of circular footings resting on sloping rocks** **(Khảo sát và phân tích khả năng chịu tải của móng tròn trên mái dốc đá áp dụng phương pháp phần tử hữu hạn)** Do Vo Kim Khue, Nguyen Hoang Phuc, Ho Ngoc Hao, Nguyen Tri Dung, Lai Van Qui
09:30	09:45	**Specification for the intermediate bracing system design of steel I girder simple span bridges** **(Nghiên cứu đề xuất quy trình thiết kế hệ giằng trung gian trong cầu thép dầm giản đơn)** Pham Thi Khanh Van, Tran Van Huynh, Tran Lam Ha, Huynh Ngoc Thi
09:45	10:05	Result announcement

COUNCIL 1
Faculty of Civil Engineering
Faculty of Geology and Petroleum Engineering

DAMAGE DETECTION IN BEAMS USING VIBRATION CHARACTERISTICS

(CHẨN ĐOÁN HƯ HỎNG TRONG KẾT CẤU DẦM SỬ DỤNG CÁC ĐẶC TRƯNG DAO ĐỘNG)

Chi-Khai Nguyen[1,2], Vi-Khang Tran[1,2], Tran-De-Nhat Truong[1,2], Duc-Duy Ho[1,2,*]

[1] Ho Chi Minh City University of Technology (HCMUT), 268 Ly Thuong Kiet Street, District 10, Ho Chi Minh City, Vietnam

[2] Vietnam National University Ho Chi Minh City, Linh Trung Ward, Thu Duc City, Ho Chi Minh City, Vietnam

[*] Corresponding author: hoducduy@hcmut.edu.vn

Abstract

In this paper, three methods are presented to detect the damage in beam-like structures using vibration characteristics: natural frequency change-based method, mode shape change-based method, and mode shape curvature change-based method. A steel beam is simulated and analysed vibration with undamaged and damaged cases by SAP2000 software, in which damage is created by reducing the bending stiffness of the beam element. In detecting the damage's occurrence, the mode shape change-based method shows higher accuracy than the natural frequency change-based method. Additionally, the mode shape curvature change-based method, which is used for identifying the damage location, is also proposed in this study. Finally, a damage threshold and a damage index are proposed to evaluate the accuracy of the method.

Keywords: *damage detection, natural frequency, mode shape, mode shape curvature, vibration*

1. INTRODUCTION

Nowadays, beam-like structures are common in civil infrastructures. Due to the beam's important roles, it is necessary to detect and reinforce the damage in beam-like structures early. This effort ensures the structure's safety, reduces unfortunate accidents for humans, and minimizes economic losses. Therefore, Structural Health Monitoring (SHM) has received significant attention and development from researchers. In particular, studies related to the application of vibration characteristics (frequency, mode shape) for the purpose of detecting damage have been researched since the 1970s and are now widely applied in the field of SHM (Adams et al. (1978) [1], Pastor et al. (2012) [2], Wahab et al. (2023) [3]…)

In this paper, the vibration characteristics-based detection method is proposed to identify the damage's occurrence and location in beam-like structures. The methods based on the change of the natural frequency and the mode shape (Modal Assurance Criteria index) are the simplest method for practical applications to warn of the occurrence of damage in the structure. Moreover, the damage location is detected through the mode shape curvature change-based method. The steel beam is simulated and analysed vibrations with undamaged and damaged states via SAP2000 software. When damage occurs in the beam, it results in a change in the bending stiffness. Additionally, the bending stiffness has a proportional relationship with the elastic modulus (E) and the moment of inertia (I). Due to this relationship, the damage case is simulated by reducing the beam element's bending stiffness. This study has four main works. Firstly, vibration characteristics (natural frequency and mode shape) are collected in undamaged and damaged cases by SAP2000 software. Secondly, the occurrence of the damage is evaluated by changes in the natural frequency and the mode shape (MAC). Thirdly, the mode shape curvature change-based method is used for identifying the damage location. Finally, a damage threshold and a damage index are proposed to evaluate the accuracy of the mode shape curvature change-based method.

2. METHODOLOGY

2.1. Natural frequency change-based method

According to Adams et al. (1978) [1], with damaged or undamaged states, the natural frequencies can be obtained variously. The damaged structure has a natural frequency less than the natural frequency of the undamaged structure. Based on that change, the occurrence of the damage is detected. The change in frequency is expressed as shown in Equation (1):

$$\Delta f\% = \frac{|f - f^*|}{f} \times 100\% \quad (1)$$

where $\Delta f\%$ is the percentage change in natural frequency (%). f and f^* are the natural frequency in undamaged and damaged cases of the beam (Hz), respectively.

Based on the percentage change of the natural frequency $\Delta f(\%)$ in mode shape, we can evaluate the damage's occurrence in the steel beam. If damage occurs, the percentage change of the natural frequency $\Delta f\%$ will be different from 0.

2.2. Mode shape change-based method

MAC (Modal Assurance Criteria) index is a formula that indicates the difference of mode shapes in undamaged and damaged cases [2]. If the MAC value is less than "1", it signifies the occurrence of the damage in the beam. MAC

index is expressed as shown in Equation (2):

$$MAC(A,X) = \frac{|\sum_{i=1}^{n}\{\phi_A\}_i\{\phi_X\}_i|^2}{\left(|\sum_{i=1}^{n}\{\phi_A\}_i|^2\right)\left(|\sum_{i=1}^{n}\{\phi_X\}_i|^2\right)} \quad (2)$$

where A and X are structural models in the undamaged case and damaged case, respectively. $MAC(A, X)$ reflects the correlation between two mode shapes, which are obtained from undamaged and damaged states. ϕ_A and ϕ_X are displacement vectors of undamaged and damaged models, respectively.

2.3. Mode shape curvature change-based method

According to Pandey et al. (1991) [4], when damage occurs, resulting in a change in the mode shape curvature. Therefore, the mode shape curvature, which is used for detecting the damage location, is calculated by using a central difference approximation algorithm. The formula is shown below:

$$\phi_i'' = \frac{\phi_{i+1} - 2\phi_i + \phi_{i-1}}{h^2} \quad (3)$$

where:

ϕ_i'' : The second derivative of the displacement vector i^{th};

ϕ_i : The displacement vector i^{th};

ϕ_{i-1} : The displacement vector $(i-1)^{th}$;

ϕ_{i+1} : The displacement vector $(i+1)^{th}$;

h : The length of the beam's element.

2.3.1. Proposed damage threshold

The damage threshold Z_0, which is calculated as a percentage of the largest Z_i index in beams, is proposed to identify the damage zones, as follows:

- $Z_i \geq Z_0$: *element beam* i^{th} *is damaged.*
- $Z_i < Z_0$: *element beam* i^{th} *is undamaged.*

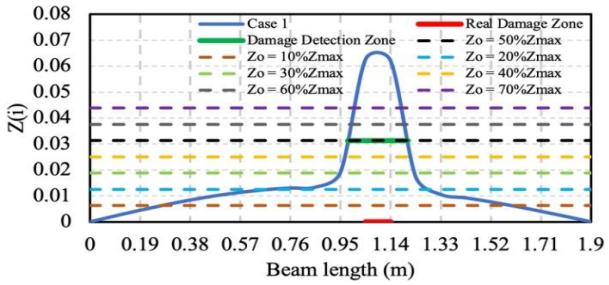

Figure 1. The damage index chart

In this study, the damage threshold is surveyed according to the following levels Z_0 = 10%Z_{max} ; . . . ; 70%Z_{max}. Finally, the damage threshold Z_0 = 50%Z_{max} is used for detecting the damage zone and evaluating the accuracy of the detection method (Fig. 1).

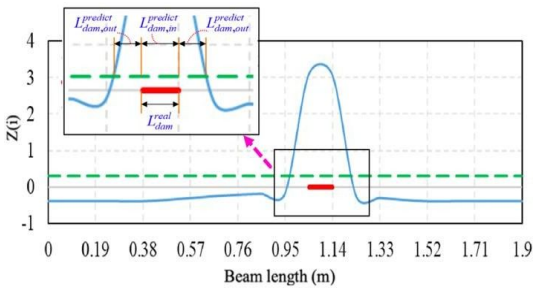

Figure 2. Convention of the damage detection zone and real damage zone

2.3.2. Damage index

Damage index is defined as the ratio of the damage detection zone within the real damage zone to the actual damage zone's length, as shown in Fig. 2. This index is used for evaluating the method's accuracy, the formula is shown below:

$$A = \frac{L_{dam,in}^{predict}}{L_{dam}^{real}} \times 100\% \quad (4)$$

where $L_{dam,in}^{predict}$ is the damage detection zone's length within the length of the actual damage zone. L_{dam}^{real} is the real damage zone's length (Fig. 2).

2.3.3. Influence of boundary condition

For the ends of the beam boundary, the data of nodes *i-1* and *i+1* are not available for the left boundary and right boundary nodes, respectively. According to Ho et al. (2018) [5], for the free and hinged conditions, determining data at two end nodes according to the principle of symmetry as follows:

- The left boundary node : $\phi_{i-1} = -\phi_{i+1}$.
- The right boundary node : $\phi_{i+1} = -\phi_{i-1}$.

3. NUMERICAL VERIFICATION

3.1. Beam model

This study considers a steel beam, span L = 19 m, rectangular cross-section h = 20 mm, b = 150 mm. The beam has the following material properties: elastic modulus$E$ = 2.06 × 10^5 MPa, mass density ρ = 7850 kg/m^3, Poisson's coefficient u = 0.3. In the finite element model, the beam is divided into 20 elements and 21 nodes (Fig. 3).

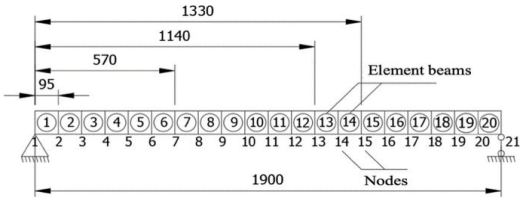

Figure 3. Finite element model of the simply supported beam

The damage cases are investigated by reducing the bending stiffness of the beams at different locations. Assume that the i^{th} element has a 10% decrease (or damage index = 0.1) in bending stiffness, i.e. $(EI)_i th$ = 0.9$(EI)_{undamaged}$. The damage is simulated by reducing the bending stiffness of the

beam element with 6 damage cases as shown in Table 1.

Table 1. Damage scenarios

Damage case	Damage element	Damage index (%)
Case 0	0	0
Case 1	12^{th}	10
Case 2	12^{th}	30
Case 3	12^{th}	50
Case 4	$6^{th}, 12^{th}$	20, 50
Case 5	6^{th}	10
Case 6	$6^{th}, 12^{th}$	50, 50

3.2. Natural frequency

To check the accuracy of the simulation, the natural frequencies of the intact beam are compared with the results calculated from the analytic theory [6]. The comparison results are presented in Table 2. In addition, with each damage case, the natural frequency peaks have deviation and are shown in Fig. 4.

Table 2. Natural frequency (Hz) comparison between this study and analytic theory (Case 0)

Frequency (Hz)	This study	Analytic theory [6]	Difference (%)
Mode 1	12.867	12.869	0.015
Mode 2	51.446	51.477	0.060
Mode 3	115.667	115.823	0.135
Mode 4	205.403	205.907	0.246

In accordance with the results presented in Table 2, natural frequency values obtained from the numerical simulation and the analytic theory are almost identical, indicating that the SAP2000 model is highly reliable. For Mode 1 and Mode 2 of Case 0, there is nearly no difference between thetwo methods when it approaches zero. The number of elements affects the accuracy of the result, the finer the division, the more accurate the result. In engineering problems, the results with less than 5% difference are acceptable. The more severe the damage, the lower the vibration frequency. In all mode shapes, the vibration frequency decreases corresponding to the increasing tendency of the damage index.

Table 3. Natural frequency (Hz) with different damage cases

Mode	Case 1	Case 2	Case 3	Case 4	Case 5	Case 6
1	12.800	12.615	12.299	12.219	12.826	11.987
2	51.388	51.223	50.950	50.319	51.175	48.632
3	115.306	114.317	112.716	112.328	115.492	111.339
4	204.691	202.807	199.938	199.663	205.265	198.895

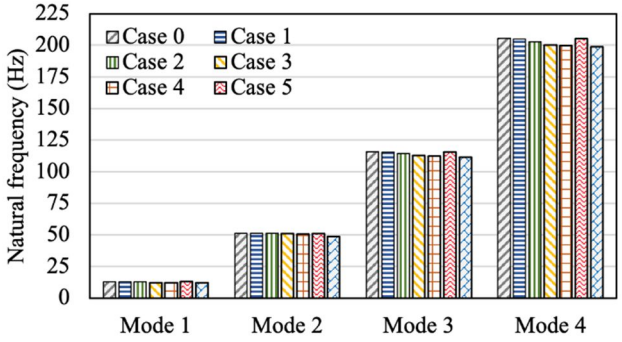

Figure 4. Natural frequencies with damage cases

3.3. Mode shape

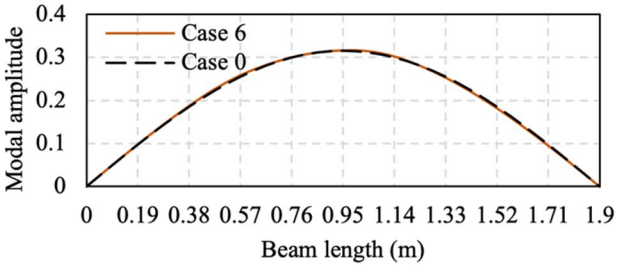

Figure 5. The 1st mode shape

Generally, the half-sine shape in the first mode of the beam in all damage cases is identical, consistent with the simply supported beam vibration theory. The larger the damage is, the larger the deviation in the mode shape between two cases is.

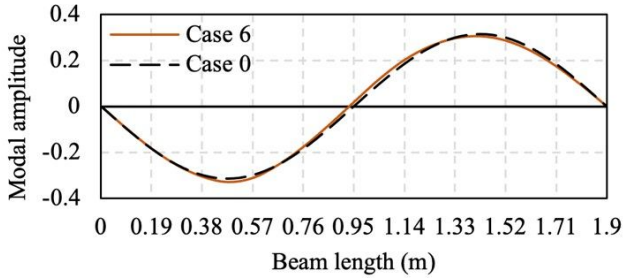

Figure 6. The 2nd mode shape

Similar to the first mode shape, the second mode shape of the beam in the damage cases is nearly unchanged. The stiffness of the beam is greatly reduced in case 6, leading to the local extrema value at the damage position having a larger deviation compared to the remaining damage cases.

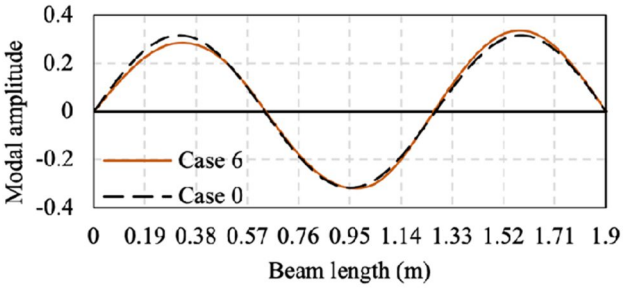

Figure 7. The 3rd mode shape

The deviation of the third mode shape is larger than the first and second modes. Similar to mode 2, with the appearance of an additional damage beam element (from 0.475 m to

0.57 m), at the range from 0.19 m to 0.57 m, the results of case 4 and case 6 have larger deviations than the rest of the cases.

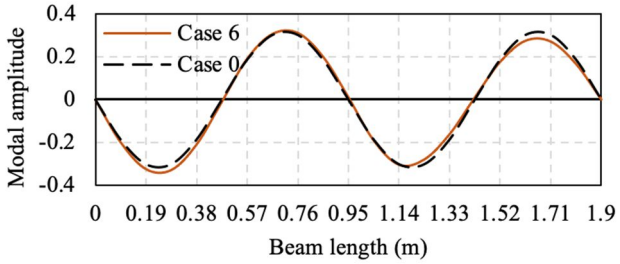

Figure 8. The 4th mode shape

In mode 4, the comparison charts clearly show the significant deviation between the two curves corresponding to the undamaged and damaged beams.

4. DAMAGE OCCURRENCE

4.1. Natural frequency change-based method

The larger the deviation, the more severe the damage. The largest frequency deviation occurs in the first mode shape because in this case, there are no insensitive points that do not represent the change in displacement between damaged and undamaged cases. In addition, observing case 6, there is the most obvious frequency change between the mode shapes (Table 4, Fig. 9). The disadvantage of this method is that small frequency changes are difficult to identify the damage occurrence in beam-like structures accurately. In addition, it is impossible to detect the damage location in the beam.

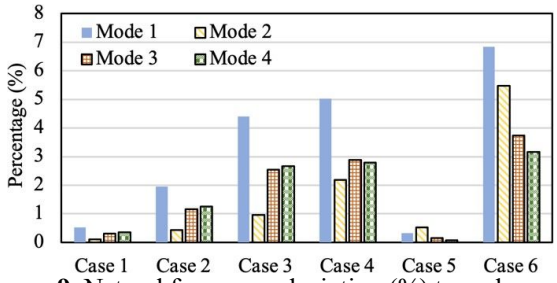

Figure 9. Natural frequency deviation (%) to undamaged case

Table 4. Natural frequency deviation (%) compared to the undamaged case

Mode	Case					
	1	2	3	4	5	6
1	0.52%	1.96%	4.41%	5.03%	0.32%	6.84%
2	0.11%	0.43%	0.96%	2.19%	0.53%	5.47%
3	0.31%	1.17%	2.55%	2.89%	0.15%	3.74%
4	0.35%	1.26%	2.66%	2.79%	0.07%	3.17%

4.2. Mode shape change-based method

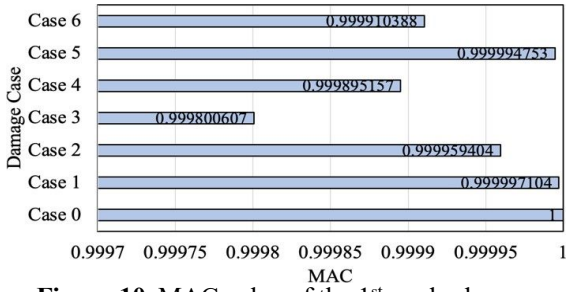

Figure 10. MAC value of the 1st mode shape

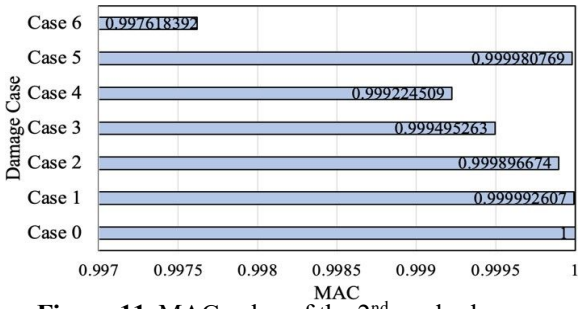

Figure 11. MAC value of the 2nd mode shape

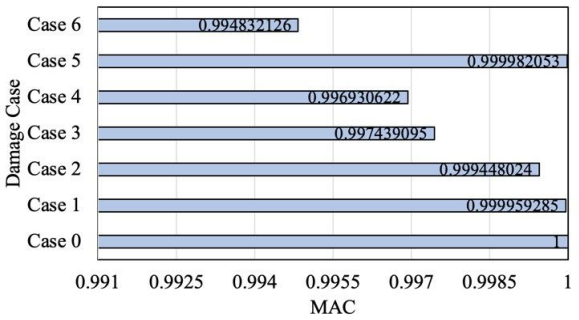

Figure 12. MAC value of the 3rd mode shape

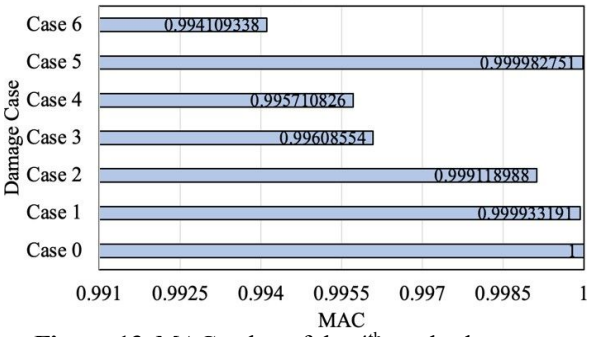

Figure 13. MAC value of the 4th mode shape

As shown in Figures 10-13, in the same mode shape, the more severe the damage case is, the lower the *MAC* value is andfurther away from the value 1. The decline in the *MAC* valueis obvious in case 6 – the most severe damage case. This method gives more accurate results than the natural frequency change-based method. However, the results are still not great because the *MAC* value is comparatively close to 1. The method also cannot determine the damage location in the beam.

5. DAMAGE LOCATION

In this study, the first four mode shapes are used for the mode shape curvature change-based method. Figures 14, 15, and 16, 17 show respectively the change in the mode shape curvature graphs without and using the Spline function in MATLAB, which is a series of polynomials joined at knots. The Splines can be used to smooth data and perform interpolation.

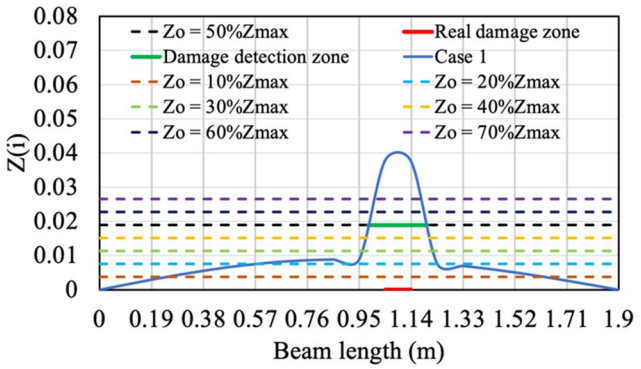

Figure 14. The change in mode shape curvature without using Spline function (1 damage beam element)

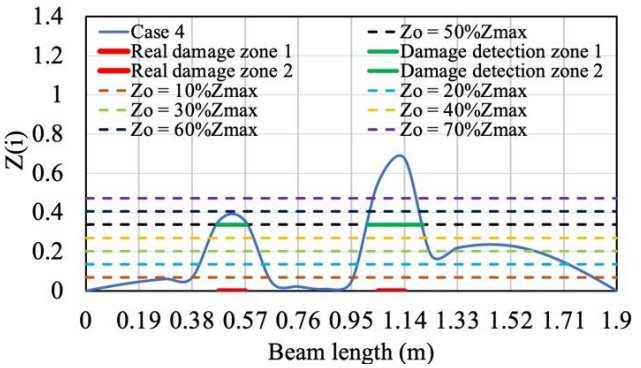

Figure 15. The change in mode shape curvature without using Spline function (2 damage beam elements)

Table 5. Damage zone accuracy-A index (Without using Spline function-1 damage zone)

Mode	Case 1	Case 2	Case 3	Case 5
	Damage zone 2	Damage zone 2	Damage zone 2	Damage zone 1
1	100%	100%	100%	100%
2	100%	100%	100%	100%
3	100%	100%	100%	100%
4	100%	100%	100%	72%
Average	100%	100%	100%	84%

Table 6. Damage zone accuracy-A index (Without using Spline function-2 damage zones)

Mode	Case 4		Case 6	
	Damage zone 1	Damage zone 2	Damage zone 1	Damage zone 2
1	0%	100%	100%	100%
2	100%	100%	100%	100%
3	0%	100%	71%	100%
4	0%	100%	29%	100%
Average	20%	100%	73%	100%

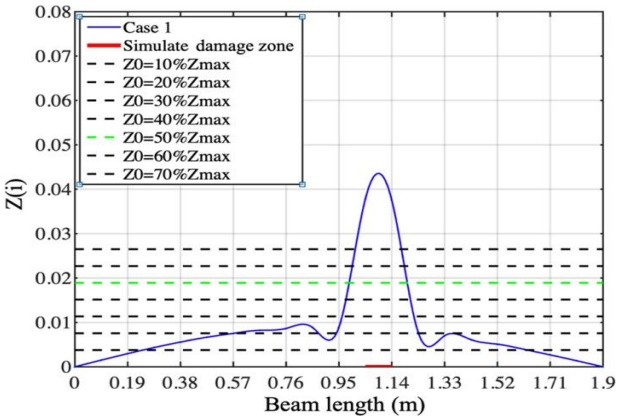

Figure 16. The change in mode shape curvature by using Spline function (1 damage beam element)

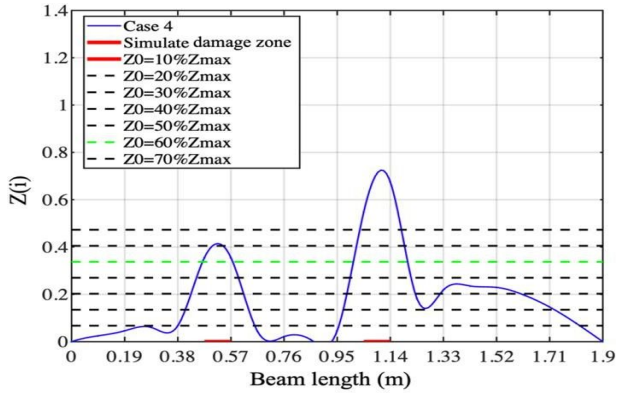

Figure 17. The change in mode shape curvature by using Spline function (2 damage beam elements)

Table 7. Damage zone accuracy-A index (Using Spline function-1 damage zone)

Mode	Case 1	Case 2	Case 3	Case 5
	Damage zone	Damage zone 2	Damage zone 2	Damage zone 1
1	100%	100%	100%	100%
2	100%	100%	100%	100%
3	100%	100%	100%	100%
4	100%	100%	100%	78%
Average	100%	100%	100%	95%

Table 8. Damage zone accuracy-A index (Using Spline function-2 damage zones)

Mode	Case 4		Case 6	
	Damage zone 1	Damage zone 2	Damage zone 1	Damage zone 2
1	0%	100%	100%	100%
2	100%	100%	100%	100%
3	0%	100%	98%	100%
4	0%	100%	39%	100%
Average	20%	100%	84%	100%

According to the results of the accuracy, the proposed method shows high accuracy. The results with 100% accuracy are in the majority, not only for the case of 1 damage zone (Cases 1, 2, 3, and 5) but also for the case of 2 damage zones simultaneously (Case 4 and Case 6). Specifically, Mode 1 and Mode 2 are capable of detecting the damage location well in all cases. In addition, the detection results also depend on the selection of the damage threshold Z_0 and the amount of mode shape data.

The damage zone in which the method can detect properly (A index = 100%) is the 12th beam element (from 1.045 m to 1.14 m). In contrast, the method cannot detect accurately the damage position for cases that have damage at the 6th beam element (from 0.475 m to 0.57 m). With a sufficiently large amount of mode shape data, each mode shape will detect damage at a certain position on the structure; at the same time, there will be some damage position on the structure where the mode shape cannot detect. More specifically, only Mode 2 can detect the damage position fordamage zone 1 of case 4. Therefore, using multiple mode shape data to detect structural damage is necessary.

6. CONCLUSION

Overall, the main findings from this study were summarized as follows:

1. Both the natural frequency change-based method and the Modal Assurance Criteria (MAC) index identify the damage's occurrence.
2. The mode shape curvature change-based method detects the location of the damage with two damage locations occurring simultaneously.
3. This study surveyed various damage thresholds and proposed the optimal damage threshold which is $50\%Zmax$.
4. The A-index is also applied to evaluate the accuracy of the detection method. Therefore, the study shows that the mode shape curvature change-based method, which is combined with the Spline function, gives the best detection results.

Acknowledgment

This research is funded by the Office for International Study Programs (OISP), Ho Chi Minh City University of Technology (HCMUT), VNU-HCM under grant number **SVOISP-2022-KTXD-135**. We acknowledgethe support of time and facilities from HCMUT, VNU-HCM for this study.

References

[1] Adams, R.D., Cawley, P., Pye, C.J., and Stone, B.J., "A vibration technique for nondestructively assessing the integrity of structures", *Journal of Mechanical Engineering Science*, vol. 20, pp. 93–100, 1978.

[2] Pastor, M., Binda, M., and Harcarik, T, "Modal Assurance Criterion", *Procedia Engineering*, vol. 48, pp. 543-548, 2012.

[3] Wahab, M.A., and Nguyen, D.H, "Damage detection in slab structures based on two-dimensional curvature mode shape method and Faster R-CNN," *Advances in Engineering Software*, 2023.

[4] Pandey, A.K., Biswas, M., and Samman, M.M, "Damage detection from changes in curvature mode shapes," *Journal of Sound and Vibration*, vol. 145, No. 2, pp. 321–332, 1991.

[5] Ho, D.D., Le, T.C., Le, Q.H., Nguyen, M.T.A. and Nguyen, T.C, "Development of modal strain energy method for damage detection of beam-like structures with various boundary conditions," *Journal of construction*, vol. 9, pp. 341-347, 2018.

[6] Chopra, A.K, "Dynamics of structures: Theory and applications to earthquake engineering, 5th edition," Prentice-Hall, 2017.

EXPERIMENTAL STUDY OF REUSING WASTE SLUDGE FROM WATER SUPPLY PLANT TO MANUFACTURE INTERLOCKING CONCRETE BRICK

(NGHIÊN CỨU TÁI SỬ DỤNG BÙN PHẾ THẢI TỪ NHÀ MÁY CẤP NƯỚC ĐỂ CHẾ TẠO GẠCH BÊ TÔNG TỰ CHÈN)

Chi-Khai Nguyen[1,2], Anh-Khoa Vu[1,2], Tran-Hoang-Khoa Phan[1,2], Perez Vergara M. Gianina[1,2], Phuong Trinh Bui[1,2,*]

[1] Faculty of Civil Engineering, Ho Chi Minh City University of Technology (HCMUT), 268 Ly Thuong Kiet Street, District 10, Ho Chi Minh City, Vietnam

[2] Vietnam National University Ho Chi Minh City, Linh Trung Ward, Thu Duc City, Ho Chi Minh City, Vietnam

[*] Corresponding author: buiphuongtrinh@hcmut.edu.vn

Abstract

Cement is one of the most widely used construction materials in the world. As a result, the cement industry is often considered as a field consuming too much energy and causing serious environmental pollution. There is extensive research interest in ecological cement produced from waste materials such as municipal solid waste, construction waste, demolition materials, and industrial by-products to minimize their environmental impact. This study focuses on reusing sludge from Thu Duc water supply plant in replacinga part of cement to make interlocking concrete bricks. Three replacements of cement by such sludge were 5%, 10%, and 15%. The experimental results from the comparison of compressive strength at 3, 7, and 28 days of interlocking concrete bricks with and without the use of sludge showed that the compressive strength of brick samples tended to decrease gradually when increasing the replacement of cement by suchwaste sludge. The compressive strengths at 28 days of interlocking concrete bricks with the replacements of cement by 5%, 10%, and 15% sludge were lower by 1%, 18%, and 26%, respectively, as compared with those of the control sample without sludge. Additionally, the water absorption of the samples decreased corresponding to the increase in sludge replacement. In summary, the replacement of cement by such sludge at 5% was optimal in terms of the compressive strength of interlocking concrete brick samples.

Keywords: *compressive strength, ecological cement, interlocking concrete brick, waste sludge, water absorption*

1. INTRODUCTION

The production of cement is accompanied by high energy consumption and high carbon emissions, which adversely impact the environment. Therefore, it is necessary to replace cement with other supplementary cementitious materials (SCMs), particularly industrial by-products and solid wastes, to achieve better economic and environmental benefits. The utilization of industrial by-products, such as fly ash (FA) and granulated blast furnace slag (GGBS) in concrete has been investigated in detailed in previous research and adopted in actual construction to achieve certain economic and environmental benefits [1][2]. However, with the development of cleaner fuels, the availability of industrial by-products has decreased, resulting in increased research interest in other waste materials that can replace cement [3].

Sewage sludge ash (SSA) is the final by-product during the procedure of sewage sludge incineration. The main SSA components include SiO_2, Al_2O_3, Fe_2O_3, and CaO which are consistent with the components of cement and other SCMs such as FA and GGBS [4]. Thus, recycling SSA as a building material has been done for several years. Previous research confirms that SSA had a certain pozzolanic reactivity and it could be used as a SCM to partly replace cement in traditional concrete [5]. However, owing to the low pozzolanic reactivity and high porosity of SSA, the addition of SSA to traditional concrete decreases the compressive strength [6]. The compressive strengths at 28 days of the blended mortar samples with the SSA additions of 10, 20 and 30% by mass were 20%, 40% and 50% lower than that of pure cement mortar without SSA, respectively [7]. However, little research on the practical utilization of waste sludge has still been done in Vietnam. In 2006, Nguyen et al. [8] used hydraulics to separate organic components and get inorganic sludge. Inorganic substances account for 70÷93% used to produce building materials such as wall bricks, pavement bricks, or leveling by the plasticmethod. In 2017, Hoang et al. [9] studied the use of urban sewage sludge from canals to make burnt clay bricks. The results showed that the replacement of sludge can be up to 30% to make bricks by plastic method to meet the technicalrequirements of TCVN 1451:1998 [10].

This paper focuses on researching the reuse of waste sludge from Thu Duc water supply plant to replace the part of cement and make interlocking concrete bricks (ICB). The purpose of this research was to utilize such waste sludge and reduce the amount of cement to protect the environment.

The following studies were carried out to achieve the above goal: (1) selecting a system of raw materials available in the country to make ICB; (2) investigating the reuse and treatment process of waste sludge for cement replacement; (3) evaluating the effect of waste sludge content on compressive strength and water absorption of ICB. Based on the experimental results, the present study proposed an optimal waste sludge content as an appropriate limit to replace cement for producing ICB with similar good workability, compressive strength and water absorption which were satisfied with TCVN 6476:1999 [11].

2. EXPERIMENTS

2.1. Materials

2.1.1. Aggregate and water

The natural coarse and fine aggregates (NA) used in this experiment were crushed stone (CS) and river sand (S), respectively. The density and bulk density of CS tested following TCVN 7572:2006 [12] were 2.65 and 1.46 g/cm^3, respectively. Similarly, the density and bulk density of S were 2.56 and 1.47 g/cm^3. As fine aggregate, sand with a fineness modulus of 1.6 was used from a local source in Vietnam. Crushed stone with particle sizes ranging from 5 to 10 mm was used as coarse aggregate. Additionally, tap water used in the experiment was confirmed as per TCVN 4506:2012 [13].

2.1.2. Cement

Type I Portland cement used in this study with a strength grade of 40 MPa for the preparation of ICB specimens was supplied by Nghi Son company and was compliant with the requirements of TCVN 2682:2020 [14]. The density and bulk density of cement used following TCVN 4030:2003 [14] were 3.1 and 1.1 g/cm^3, respectively.

2.1.3. Waste sludge

The sludge transported from the Thu Duc water supply plant was dried in air until no longer moist. Before drying, the sludge was manually pulverized until the particle size was about 5 mm to reduce drying time. The sludge was heated at 110°C by a dry oven until the mass was unchanged. After that, a ball milling machine was used to finely grind the cement-like sludge. The sludge after being ground was sieved to select a particle size of less than 0.14 mm in diameter. **Figure 1** shows a procedure of sludge preparation and **Figure 2** shows a treating process of waste sludge by using the dry oven and a ball milling machine.

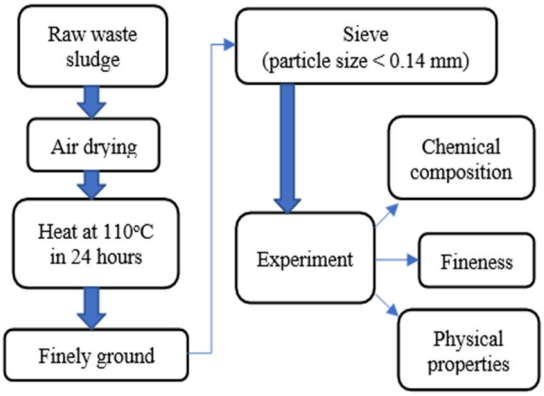

Figure 1. Procedure of preparing for sludge

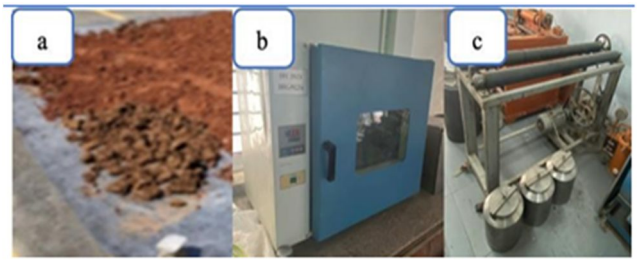

Figure 2. Treating process for waste sludge
(a) air-dried sludge; (b) heated sludge at 110^{0}C in a dry oven; (c) grinding sludge in a ball milling machine

2.2. Mixture proportions

The mixture proportion without sludge replacement was designed following TCVN 6476:1999 [11]. In Vietnam, where traffic jams occur frequently during rush hour, it's not uncommon for motorbike drivers to "climb" onto the sidewalk and cause cracking bricks. Therefore, the design concrete strength grade of the present study was proposed to be M400 in order to make a precaution for the deterioration of the sidewalk. In addition, this mixture proportion was used for I-shaped ICB samples for testing compressive strength and water absorption. A water-to-cement ratio of 0.6 was proposed for all the mixture proportions. The volume ratio of sand-to-aggregates (S/(S+CS)) was 0.41 to ensure the degree of coverage of mortar. Three proposed replacements percentage of cement by sludge were 5%, 10%, and 15% by mass, which were referred to in the previous studies of Rezaee et al. [16]. All the mixture proportions are shown in **Table 1**. The mixture proportion ID designated as B0 was the control concrete without sludge as a reference. Meanwhile, B5, B10, and B15 as alternative samples contained 5%, 10%, and 15% waste sludge replacement, respectively.

2.3. Casting and curing

The experimental procedure for casting the ICB was conducted as follows: (1) all the materials need to be carefully prepared and quantified by a technical balance; (2) after mixing binders and fine aggregate (cement, sludgeand sand) together, a half volume of water content was added to a tilting drum mixer and then the mixer was operated for two minutes before stopping to grind the lumpsinto small pieces; (3) remaining water and coarse aggregate(crushed stone) were added to the mixer and then operating for the additional three minutes to achieve a uniform fresh concrete; (4) the fresh concrete was placed into I-shaped molds and cubic molds; (5) the placing surface of concrete specimens were all then wrapped in polyethylene sheets forcuring in 20±4 hours for preventing evaporation and carbonation. After that, all the specimens were de-molded and then cured in normal atmospheric conditions (air curing) while the cubic concrete samples were cured in water.

2.4. Test procedure

2.4.1. Slump of fresh concrete

After mixing all the materials together, the Abrams cone received three injections of fresh concrete. The cone was compacted 25 times using a steel rod for each layer. After

Table 1. Mixture proportions of ICB samples

Mixture proportion ID	Waste sludge (% by mass ofbinder)	Unit (kg/m^3)					S/(S+CS)
		Cement(C)	Waste sludge (WS)	Crushed stone (CS)	Sand (S)	Water(W)	
B0	0	350	0	1051	718	210	0.41
B5	5%	333	18	1051	715	210	0.41
B10	10%	315	35	1051	711	210	0.41
B15	15%	298	53	1051	708	210	0.41

that, the slump of fresh concrete was tested according to TCVN 3106:1993 [17].

2.4.2. Compressive strength of concrete brick

The compressive strength of the hardened concrete samples was measured according to TCVN 3118:1993 [18]. The cubic concrete samples with dimensions of 100×100×100 mm were prepared for 27 days of water curing (i.e., at the age of 28 days). Meanwhile, for ICB samples, the procedure for determining compressive strength was done as per TCVN 6476:1999 [11]. The I-shaped ICB samples with dimensions of 140×200×60 mm were cured in the air for designated ages (i.e., 3, 7, and 28 days). After that, two steel plates with a length of 120±0.2 mm, width of 60±0.2 mm, and thickness not less than 15 mm were put on the top and bottom surfaces of ICB samples which had been covered with Sona-Cap 40 mortar. The rate of load should be gradual and equal to 0.6±0.2 N/mm^2 per 1 second as per TCVN 6476:1999 [11]. **Figure 3** shows the I-shaped brick mold used for casting ICBs and **Figure 4** shows the position of steel plate at center of ICB samples when testing compression strength. It is noted that the compressive strength of all samples including the cubic concrete and ICB samples were tested by using a compressive machine with a capacity of 2000 kN.

Figure 3. The I-shaped brick mold

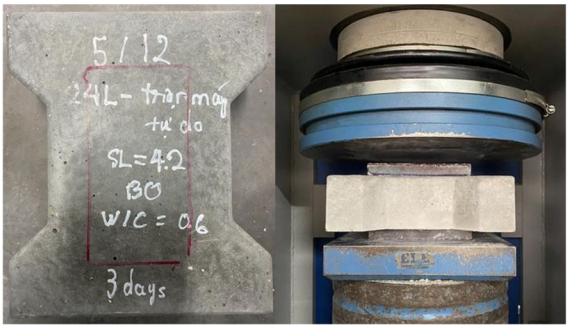

Figure 4. Steel plate position on the sample and that onthe compression testing machine

2.4.3. Water absorption

The water absorption test was conducted according to TCVN 6355-4:2009 [19]. Water absorption is used to determine the amount of water absorbed under specified conditions. A procedure was done as follows: (1) the samples were dried in an oven at 110ºC for 24 hours for the water absorption test and then placed in a desiccator to cool; (2) after cooling, the samples were weighed and then emerged in water at 23°C for 24 hours. After that, the samples were weighed in the air. Water absorption was expressed as an increase in weight percent following Eq. (1).

$$WA = \frac{m_2 - m_1}{m_1} \times 100\% \quad (1)$$

where, m_1 is mass of sample after drying in oven (g); m_2 is mass of sample after emerging in water for 24 hours (g).

3. RESULTS AND DISCUSSION

3.1. Slump of fresh concrete

Workability is defined as the ease of freshly mixed concrete that can be placed, compacted, and finished. In this study, the slump test was chosen as the workability test for fresh concrete. Every different batch of fresh concrete was tested for slump test to ensure the workability of the concrete. **Figure 5** illustrates the slump of fresh concretes of all the mixture proportions where the highest slump of 4.5 cm for the control concrete without slump (B0) and the slump decreased as the replacement percentage of cement by waste sludge increased. The slump of fresh concrete with 5%, 10%, and 15% sludge replacements was 4.0, 2.5 cm, and 2.0 cm, respectively. Ing et al. [20] showed that the higher the waste sludge content, the lower the slump of the fresh concrete. Waste sludge which has the ability to absorb water as compared to cement powder, slightly reduced the slump of the fresh concrete [20]. The decrease in workability can be explained by two factors, which are the irregular morphology of sludge particles and the high-water absorption on sludge particle surfaces [21]. The shape of waste sludge particles were not spherical which caused a negative influence on workability [22]. The sludge could slightly decrease the workability of cement-based concrete due to the high-water demand of sludge [20].

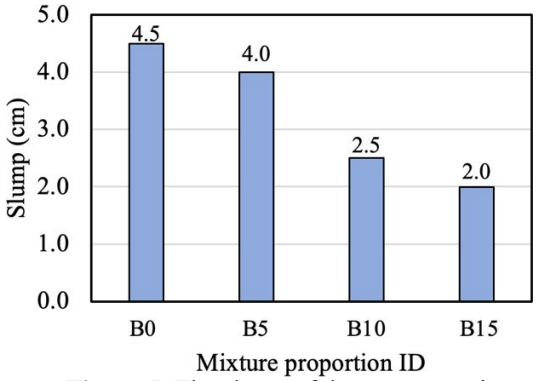

Figure 5. The slump of the concrete mixtures

3.2. Compressive strength of cubic concrete samples

Figure 6 illustrates the compressive strength of cubic concrete samples with and without waste sludge replacements at the age of 28 days. The strength grade of concrete corresponds to compressive strength of a 150×150×150 mm cubic concrete specimen at 28 days as per TCVN 4453:1995 [23]. **Figure 6** illustrated the compressive strengths of cubic concrete samples without waste sludge (B0) reached 63.4 MPa which was satisfied with the designed strength grade of M400. Meanwhile, the compressive strengths of cubic concrete samples with the replacements of cement by 5%, 10%, and 15% waste sludge were 52.0, 39.2, and 35.4 MPa respectively. The compressive strengths of the concrete samples declined as waste sludge replaced more cement in the mixture. With respect to the cubic specimens with sludge, the replacements of cement by 5% waste sludge showed the higher compressive strength which was satisfied with the designed strength grade of M400. According to Ing et al. [20], SSA decreases the compressive strength of cubic concrete samples due to the high water demand of SSA.

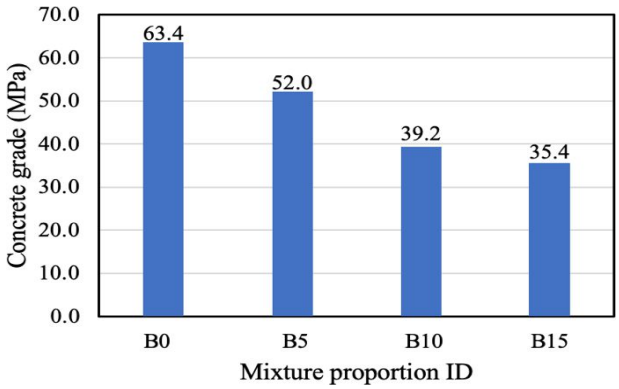

Figure 6. Compressive strength of cubic concrete samples at the age of 28 days

3.3. Compressive strength of ICB samples

The compressive strength results of various ICB samples with and without waste sludge are shown in **Table 2**. Based on the experimental results as shown in **Table 2**, all the concretes with waste sludge showed lower compressive strength at all days of aging as compared with the control concrete without sludge (B0). In terms of the concrete with sludge, the replacement of cement with 5% waste sludge showed the highest compressive strength of 46.7 MPa at 28 days while the lowest compressive strength corresponded to the concrete with 15% sludge replacement (B15), which was 34.9 MPa. Because waste sludge has a high porosity and low pozzolanic reactivity, it reduces the compressive strength of traditional concrete [6].

Table 2. Compressive strength of ICB with and without waste sludge at 3, 7, and 28 days

Mixture proportion ID	Compressive strength (MPa) at		
	3 days	7 days	28 days
B0	27.5	38.0	47.2
B5	25.5	35.5	46.7
B10	24.2	32.4	38.7
B15	20.3	27.0	34.9

Figure 7 shows the compression strength ratio of the alternative ICB sample to the control sample. The compressive strengths at 28 days of ICBs with the replacements of cement by 5%, 10%, and 15% sludge were 99%, 82%, and 74%, respectively, as compared with the control sample without sludge (B0). Standard deviation of compressive strength of ICB with and without waste sludge at 3, 7, and 28 days is shown in **Table 3**. The standard deviation was calculated from a set of three specimens corresponding to the age and mixture proportion of ICBs.

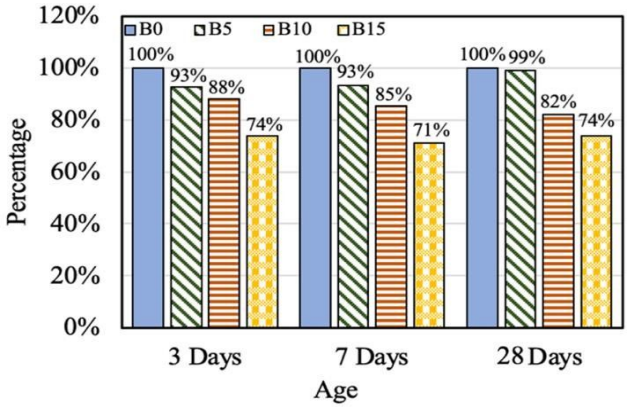

Figure 7. The compression strength ratio of the alternative ICB sample to the control sample

Table 3. Standard deviation of compressive strength of ICB with and without waste sludge at 3, 7, and 28 days

Mixture proportion ID	Standard deviation (MPa) at		
	3 days	7 days	28 days
B0	4.4	4.0	3.9
B5	2.0	2.4	3.0
B10	1.0	1.4	1.6
B15	0.5	2.0	1.4

The compressive strength at 28 days of ICBs with the 5% waste sludge (B5) was nearly the same as that of the control concrete without sludge (B0). Therefore, the replacement of cement by waste sludge was optimal at 5% when the compressive strength of concrete tended to decrease sharply at 10% sludge replacement. The compressive strength decreased as the replacement percentage of cement by waste sludge increased. According to Jamshidi et al. (2012) [24], the sewage sludge ash concrete showed an increase in compressive strength with curing time and the compressive strength loss which is proportional to the percentage increment of sludge content. Furthermore, Yagüe et al. (2005) [25] stated that the mechanical strength of hardened concrete is decreased when sludge is added, and with the addition of 10% sludge in proportion to the amount of concrete, the mechanical strength is dramatically reduced, making it unsuitable for medium to high-strength reinforced concrete.

3.4. Water absorption of ICB samples

The water absorption of ICB samples was tested after 28-day of curing in air. **Figure 8** illustrates the water absorption of the ICB samples with and without waste sludge at 28 days. For the ICB samples with sludge replacement, the ICB sample with the 5% sludge replacement (B5) had the lowestabsorption capacity where the average mass increment ratio was only 3.63%, as compared to that of the control sample (B0) (i.e., 3.54%). The high porosity of the waste sludge results in excellent water absorption ability [26].

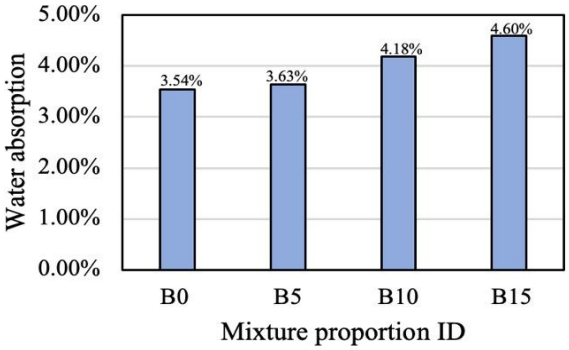

Figure 8. Water absorption of the ICB samples with andwithout waste sludge at 28 days

4. CONCLUSION

From the analysis of the results of this study, the followingconclusion can be established:

1. Waste sludge was a potential cement replacement as the major oxides of such sludge (SiO_2, CaO, and Al_2O_3) were similar to those of Portland cement.
2. In terms of the concrete containing waste sludge, the replacement of cement with 5% waste sludge showed the highest compressive strength of the concrete which was nearly the same as the control sample.
3. In terms of the concrete containing waste sludge, the replacement of waste sludge in the IBC sample of 5% had the lowest water absorption value.

Briefly, the 5% Thu Duc waste sludge replacement was beneficial for compressive strength and water absorption of ICB samples.

Acknowledgment

This research is funded by the Office for International Study Programs (OISP), Ho Chi Minh City University of Technology (HCMUT), VNUHCM under grant number **SVOISP-2022-KTXD-110**. We acknowledge Ho Chi Minh City University of Technology (HCMUT), VNUHCM for supporting this study.

References

[1] Shi, C., Wu, Z., Xiao, J., Wang, D., Huang, Z., Fang, Z., 2015. A review on ultra high performance concrete: Part I. Raw materials and mixture design. *Journal of Construction and Building Materials.*

[2] Yazıcı, H., Yardımcı, M.Y., Aydın, S., Karabulut, A.S., 2009. Mechanical properties of reactive powder concrete containing mineral admixtures under different curing regimes. *Journal of Construction and Building Materials.*

[3] Wang, X., Yu, R., Shui, Z., Song, Q., Zhang, Z., 2018. Development of a novel cleaner construction product: Ultra-high performance concrete incorporating lead-zinc tailings. *Journal of Cleaner Production.*

[4] Chen, Z., Poon, C.H., 2017. Comparative studies on the effects of sewage sludge ash and fly ash on cement hydration and properties of cement mortars. *Journal of Construction and Building Materials.*

[5] Ottosen, L.M., Thornberg, D., Cohen, Y., Stiernström. S., 2022. Utilization of acid-washed sewage sludge ash as sand or cement replacement in concrete. *Journal of Resources, Conservation & Recycling Advances.*

[6] Donatello, S., Tyrer, M., Cheeseman, C.R., 2010. Comparison of test methods to assess pozzolanic activity. *Journal of Cement and Concrete Composites.*

[7] Lynn, C.J., Dhir, R.K., Ghataora, G.S., West, R.P., 2015. Sewage sludge ash characteristics and potential for use in concrete. *Journal of Construction and Building Materials.*

[8] Ministry of Construction (Vietnam). Waste sludge recycling technology as building materials. *Journal of Scientific Activities, issue 4/2005*. Retrieved June 5, 2023.

[9] Hoang, V.L., 2017. Research on using sludge from dredging canals to make baked clay bricks. *Journal of Construction*, 5:38–42.

[10] Ministry of Science & Technology (Vietnam), "TCVN 1451:1998: Solid clay bricks," 2006.

[11] Ministry of Science & Technology (Vietnam), "TCVN 6476:1999: Interlocking concrete brick," 1999.

[12] Ministry of Science & Technology (Vietnam), "TCVN 7572:2006: Aggregates for concrete and mortar-Test methods," 2006.

[13] Ministry of Science & Technology (Vietnam), "TCVN4506:2012: Water for concrete and mortar - Technicalspecification," 2012.

[14] Ministry of Science & Technology (Vietnam), "TCVN2682:2020: Portland cement-Specifications," 2020.

[15] Ministry of Science & Technology (Vietnam), "TCVN 4030:2003: Cement-Test method for determination of fineness," 2003.

[16] Rezaee, F., Danesh, S., Tavakkolizadeh, M., Mohammadi-Khatami, M., 2019. Investigating chemical, physical, and mechanical properties of eco-cement produced using dry sewage sludge and traditional raw materials. *Journal of Cleaner Production*, 214, 749–757.

[17] Ministry of Science & Technology (Vietnam), "TCVN 3106:1993: Fresh heavyweight concrete-Method forslump test," 1993.

[18] Ministry of Science & Technology (Vietnam), "TCVN 3118:1993: Heavyweight concrete-Method for determination of compressive strength," 1993.

[19] Ministry of Science & Technology (Vietnam), "TCVN6355-4:2009: Bricks – Test Methods – Part 4: Determination of water absorption," 2009.

[20] Ing, D.S., Chin, S.C., Guan, T.K., and Suil. A., 2016. The use of sewage sludge ash (SSA) as partial replacement of cement in concrete. *Journal of Engineering and Applied Sciences.*

[21] Paya, J., Borrachero, M. V and Girbe, I. 2003. Reuse ofSewage Sludge Ashes (SSA) in Cement Mixtures: The Effect of SSA on the Workability of Cement Mortars. *Journal of Waste Management*, 23, 373-381.

[22] Monzo, J., Paya, J., Borrachero, M. V. and Corcoles, A. 1996. Use of Sewage Sludge Ash (SSA)-Cement Admixtures in Mortars. *Journal of Cement and Concrete Research*, 26(9), 1389–1398.

[23] Ministry of Science & Technology (Vietnam), "TCVN4453:1995: Monlithic concrete and reinforced concretestructures - Codes for construction, check and acceptance," 1995.

[24] Jamshidi, A., Jamshidi, M., Mehrdadi, N., Shasavandi, A. and Pacheco-Torgal F.2012. Mechanical Performance of Concrete with Partial Replacement of Sand by Sewage Sludge Ash from Incineration. *Masterials Science Forum,* 730-732, 462-467

[25] Yagüe, A., Valls, S., Vázquez, E. and Albareda, F. 2005. Durability of Concrete with Addition of Dry Sludge from Waste Water Treatment Plants. *Journal of Cement and Concrete Research*, 35(6), 1064-1073.

[26] Xia, Y., Liu, M., Zhao, Y., Chi, X., Lu, Z., Tang, K., Guo, J., 2023. Utilization of sewage sludge ash in ultra- high-performance concrete (UHPC): Microstructure and life-cycle assessment. *Journal of Environmental Management.*

ULTIMATE LATERAL CAPACITY OF PILE GROUP ON SOIL SLOPE USING FINITE ELEMENT METHOD

(PHÂN TÍCH SỨC CHỊU TẢI NGANG CỦA NHÓM CỌC TRÊN MÁI DỐC BẰNG PHƯƠNG PHÁP PHẦN TỬ HỮU HẠN)

Bui Van Nhat Thanh[1,2,3], Tran Hoang Giap[1,2,3], Nguyen Trung Kien[1,3,*]

[1] Faculty of Civil Engineering, Ho Chi Minh City University of Technology (HCMUT), 268 Ly Thuong Kiet Street, District 10, Ho Chi Minh City, Vietnam
[2] Office for International Study Programs, Ho Chi Minh City University of Technology (HCMUT), 268 Ly Thuong Kiet Street, District 10, Ho Chi Minh City, Vietnam
[3] Vietnam National University Ho Chi Minh City, Linh Trung Ward, Thu Duc City, Ho Chi Minh City, Vietnam
[*] Corresponding author: nguyentrungkien@hmcut.edu.vn

Abstract

Piles under lateral load are usually applied in the foundation of harbor bridge construction as well as the foundation of power transmission towers. In reality, there are various regions in which laterally loaded piles are located near or even on the slope, such as mountains, river basins and coastal areas. Because of the slope soil condition, the lateral load of soil in front of piles will be weaker than that in the flat soil condition, therefore, the calculation of lateral load on piles becomes much more complicated and needs to be studied carefully. In the current practice, there are many methods to study the laterally loaded piles, however, they are mostly applicable to the flat soil condition. Meanwhile, approaches used to investigate the piles subjected to lateral loading in the slope condition are limited. In this study, we use the finite element method (FEM) implemented in the PLAXIS commercial software to investigate the behavior of laterally loaded pile groups located on sloping ground, considering the variation in slope angle, foundation axis rotation angle, and soil condition. The obtained results show that the behavior of pile groups, illustrated by the P-y (load-displacement) curves, depends on not only the number of piles, the distance between the piles, the slope angle but also the angle between the direction of load and the axial axis of pile groups.

Keywords: *compressive strength, ecological cement, interlocking concrete brick, waste sludge, water absorption*

1. INTRODUCTION

In the current context of economic recovery after the Covid-19 pandemic, there is a strong emphasis on transportation infrastructure and industrial facilities, both globally and specifically in Vietnam. As we can see, hundreds of harbor bridges and power transmission towers have been built annually and most of them are exposed to impacts of lateral load. In reality, there are various regions where laterally loaded piles are located near or even on the slope, such as mountains, river basins and coastal areas. The constructions such as bridges, ports, and high-voltage power pylon foundations have been loaded laterally in slope soil condition, which makes its structure weaker than in flat soil condition. Because of irregular slope geometry, it's challenging to determine the distribution and magnitude of lateral forces. Another reason is soil behavior, which is often different from that in flat conditions. Slopes are subjected to increased stress and strain due to the effects of gravity and lateral loads. The soil's shear strength, displacement characteristics, and drainage properties can vary significantly along the slope, making the analysis of lateral loads more complex. In flat conditions, the soil behavior tends to be more homogeneous and easier to characterize. Therefore, the piles under lateral load on slopes are more complicated and need to be studied carefully.

Scientists have been studying the behavior of laterally loaded piles for the past 40 years, with many methods have been used but the approaches used to investigate the piles subjected to lateral loading in the slope condition are limited. Therefore, it is necessary to enrich the research on the lateral response of the pile group's in sloping ground. In this paper, our team proposes the use of the Finite Element Method (FEM), implemented in the commercial Plaxis software, to analyze the behavior of laterally loaded pile groups under various conditions, including different slope angles, pile axis rotations, and geological conditions.

2. METHODOLOGY AND IMPLEMENTATION

2.1. Finite Element Method – PLAXIS 3D software

The Finite Element Method (FEM) is a numerical technique used to solve complex engineering problems involving differential equations. It is commonly used in structural, geotechnical, and civil engineering applications.

Plaxis 3D is a geotechnical finite element software used for the analysis of soil and rock deformation and stability in three-dimensional (3D) geotechnical engineering applications. It allows engineers to model and simulate complex geotechnical problems by creating a 3D numerical representation of the soil or rock mass and applying appropriate boundary conditions. The software utilizes the FEM to solve the governing equations of soil and rock behavior, including soil mechanics, plasticity, and consolidation.

The geometry and meshes of the FEM model are shown in **Figure 1.** The deformation of each pile in the pile group subjected to lateral loading under different circumstances (soil conditions, slope angles, pile axis rotation…) will be analyzed by Plaxis.

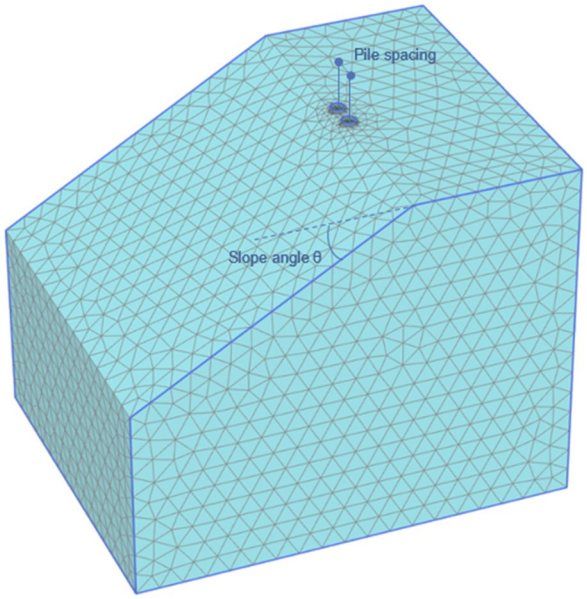

Figure 1. Connectivity plot by using Plaxis 3D

2.2. Case study

2.2.1. General information

According to the laboratory model test conducted by Chen et al. (2022), a soil sample was created in different cases of slope angle and pile spacing. In this case study, solid piles will replace the hollow piles in the laboratory test in order to simplify the test model using Plaxis 3D, however, it is necessary to remain the moment of inertia stable at $2.188 \times 10^5\ mm^4$. All other dimensions as well as the properties of piles and soil samples are still the same as in the laboratory test model by Chen et al. (2022) as shown in **Figure 2**.

The formula of inertia moment of a circle (diameter D) with respect to any axis passing through its center is given as $I_\rho = \frac{\pi}{64} D^4$. Then the moment of inertia of piles in this study is calculated by the following equations:

$$I'_\rho = \frac{\pi}{64} D^4 = I_\rho = 2.188 \times 10^5\ mm^4$$

$$\Rightarrow D = \sqrt[4]{\frac{64 \times 2.188 \times 10^5}{\pi}} \approx 4.6mm$$

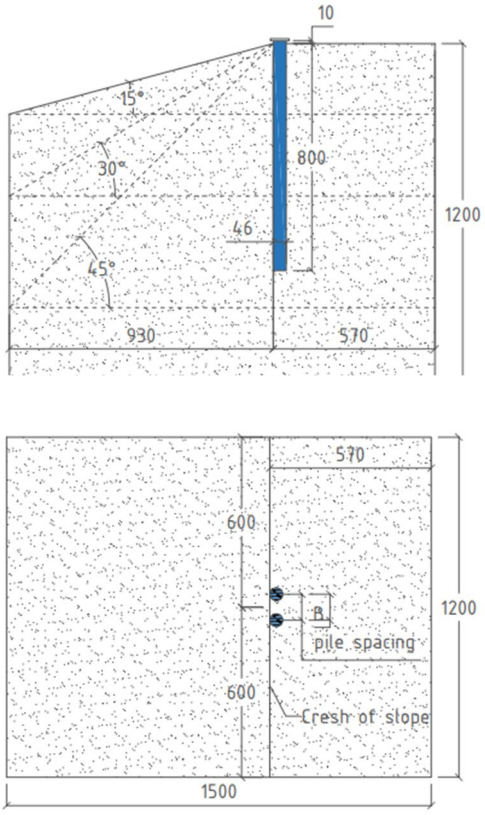

Figure 2. Sketch of lateral load soil sample of the two-pile group [1]

Moreover, interfaces ($R_{inter} = 0.6$) need to be used to create joint elements added to allow for a proper modelling of soil-structure interaction. **Table 1** represents all the cases of slope angle (θ), lateral load, pile spacing and horizontal axis rotation angle (β).

Table 1. Properties of piles group

Slope angles (θ°)	15	30	45	
Pile spacing (d=diameter of pile=0.046m)	2d	3d	4d	5d
Horizontal axis rotation angles (β°)	0	30	60	90
Lateral load (N)	500	1000	1500	2000

3. RESULTS AND DISCUSSION

3.1. Validation

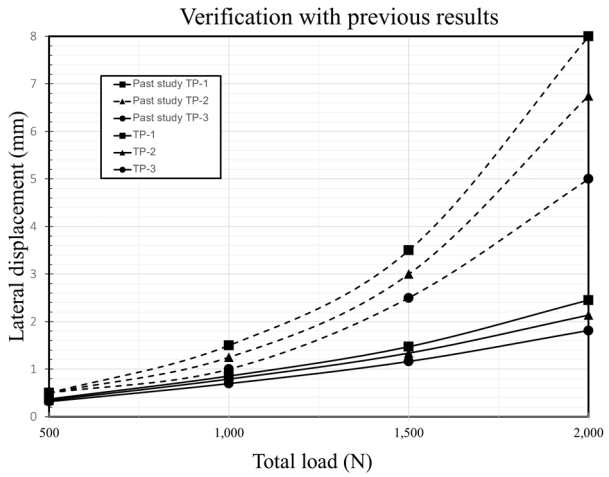

Figure 3. Validation of load-displacement curve

By using Plaxis 3D, a soil model with the same properties as the previous study was built to investigate. The results indicate that FEM by Plaxis 3D gives a similar trend of line with the past study in all three different situations (as shown in **Figure 3**).

3.2. Factors affecting the displacement of the pile group

First and foremost, the soil sample has been created in some specific cases of pile spacing ranging from 2d to 5d. When steadily increasing the value of lateral force, a comparison among the graphs of different slope angles is considered to recognize the effect of the displacement of the piles. As shown in **Figure 4**, in all cases of pile spacing, the higher the slope angles, the larger the displacements of the pile group will be. When comparing three separate slope angles of 15°, 30° and 45°, it is obvious that the soil sample with 45° slope angle will result in the highest displacement of pile groups, while the sample with 15° case of slope angle brings about the lowest values of displacement. All in all, the displacement of pile group is considered to be increases when rising the slope angle.

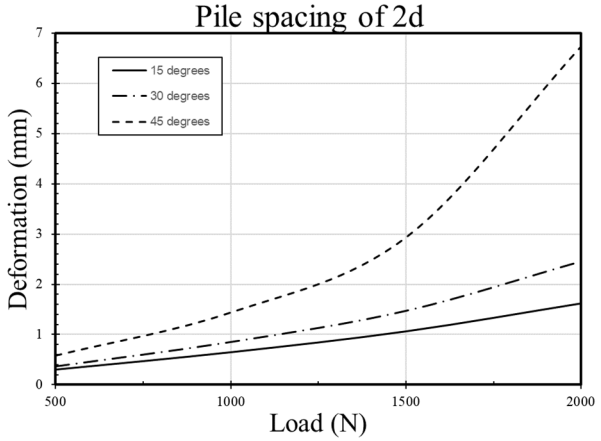

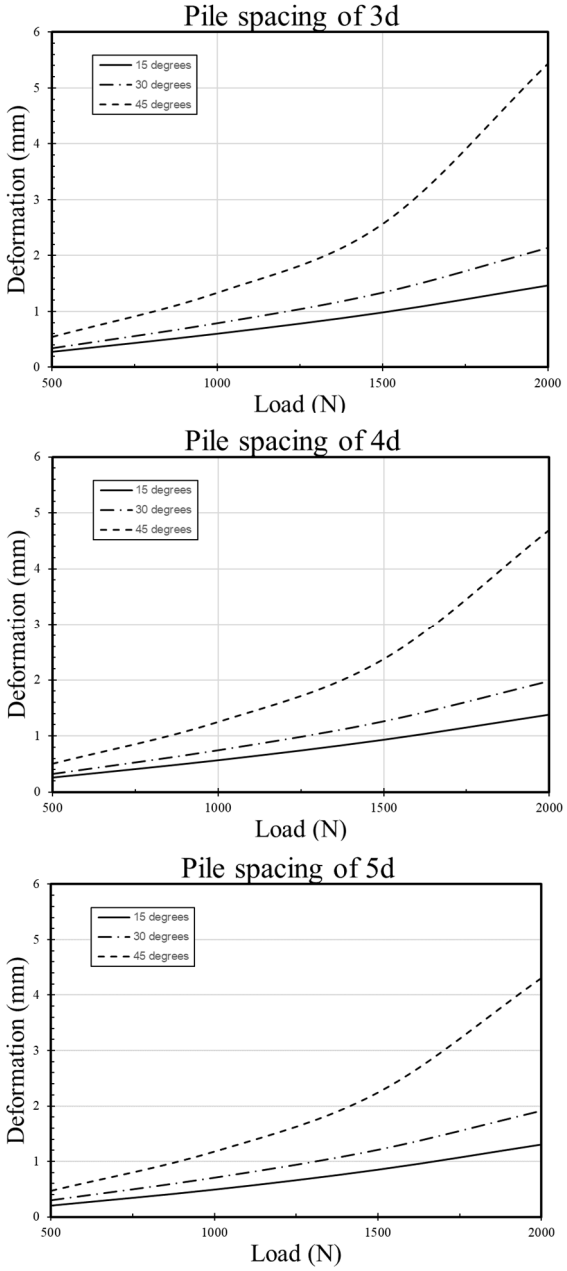

Figure 4. Effect of slope angle to the displacement of piles

In another case, when considering the change of displacement of pile group related to alternative value of pile spacing, the same step has been conducted. Different case of pile spacing has been compared when the horizontal axis rotation still remained unchanged at 90°. **Figure 5** represents the results of this case study.

For the 2d spacing of the pile, the displacement of pile group is always at the highest value because the contact surface is inversely proportional to the stress on the pile group. As can be seen in **Figure 5**, in the slope angle cases of 15° and 30°, the displacement of the pile group seems to increase gradually when accelerating the lateral load from

500 to 2000. Generally, it can be concluded that the displacement of the pile group will be larger in the case that the piles are more adjacent to the others.

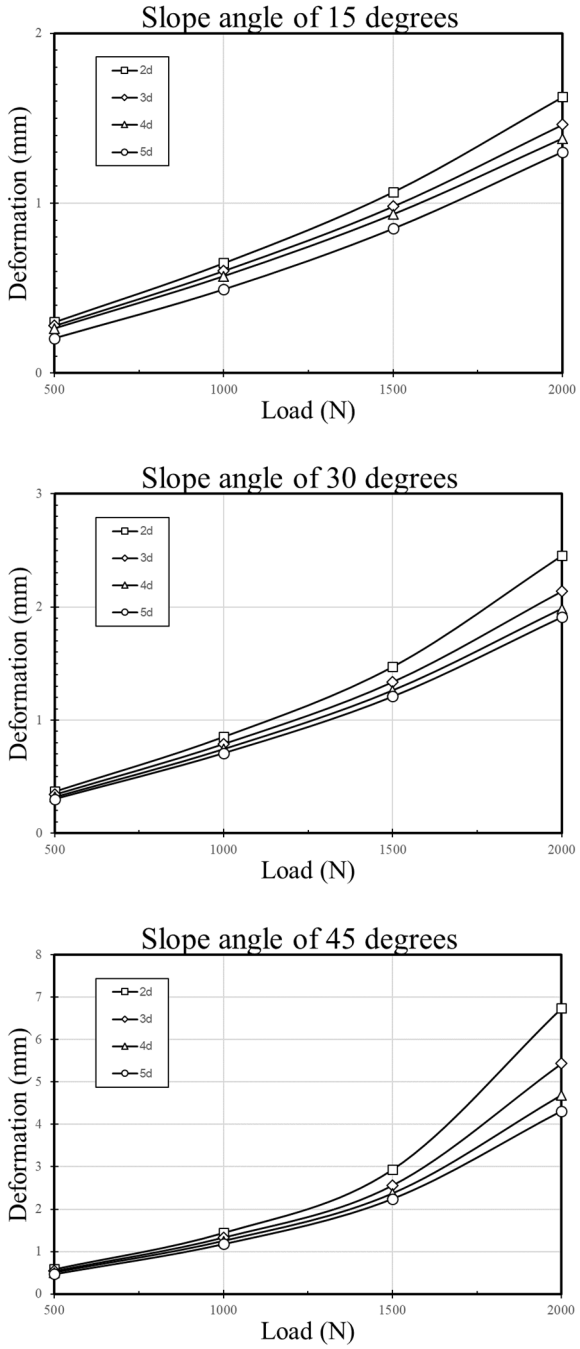

Figure 5. Effect of pile spacing to the displacement of piles

In this paper, to investigate the effect of horizontal axis rotation on displacement by utilizing remaining all the properties of the soil sample as well as pile spacing (2d), we rotated just the horizontal axis of pile groups, we want to compare the displacement between pile in (pile near the slope) and pile out (pile on the slope) under the same slope angle and between slope angles (**Figure 6**). Generally, we chose 3 cases of slope angles (15°, 30°, 45°) under different lateral loads (500 N, 1000 N, 1500 N, 2000 N) and horizontal axis rotation (0°, 30°, 60°, 90°).

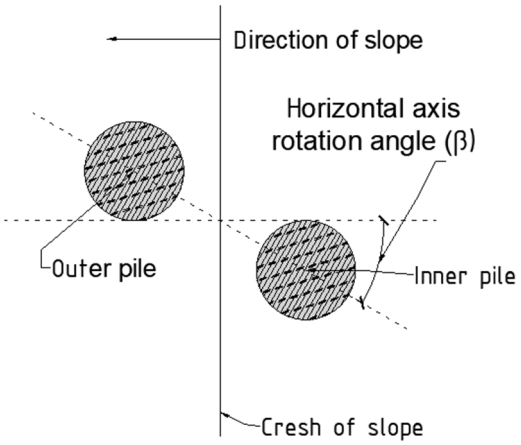

Figure 6. Pile group with horizontal axis rotation of β

Generally, in the case of β=0°, the displacement value is always the highest case in both inner and outer piles, because when the outer pile disfigures it makes the soil around destroyed so that the inner pile gets nothing left to hold when it's lateral loaded. Furthermore, β= 90° is the most stable case because the deformation of each pile does not affect each other. After calculation, we can conclude that when we increase the load to pile group it leads to a growth of the difference between two piles under every condition. The results are shown in **Figure 7** below.

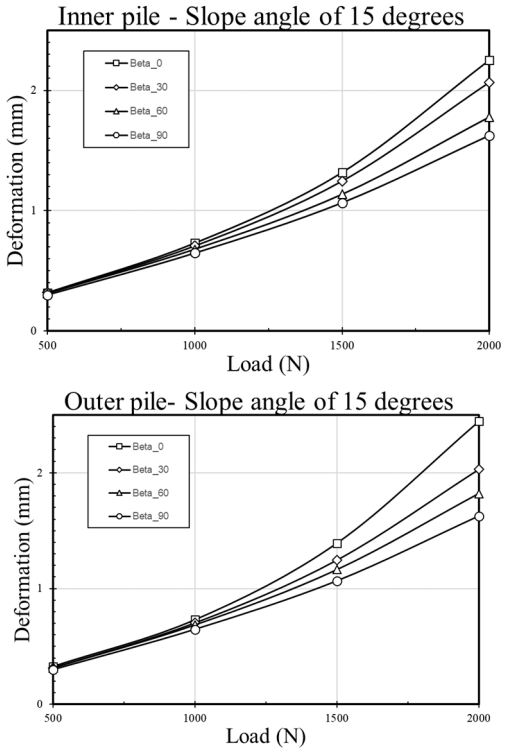

Figure 7a. Effect of horizontal axis rotation to the displacement of piles on slope angle of 15°

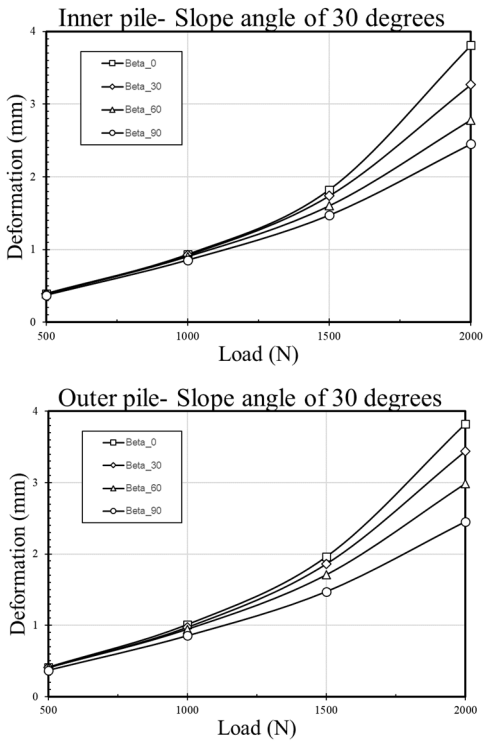

Figure 7b. Effect of horizontal axis rotation to the displacement of piles on slope angle of 30°

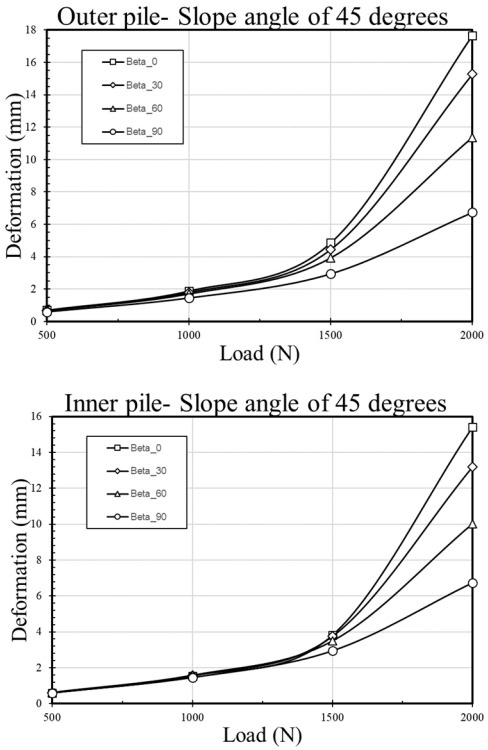

Figure 7c. Effect of horizontal axis rotation to the displacement of piles on slope angle of 45°

4. CONCLUSION

In general the proposed method to investigate the pile's displacement under many conditions of slope angles, pile spacing and horizontal axis rotation is a helpful methodology that gives censorious data to help designing the pile groups on soil slope. In addition, this method is validated with laboratory tests to ensure accuracy. Moreover, based on the results of displacement analyzed by Plaxis 3D by 3 factors: slope angles, pile spacing, horizontal axis rotation angles. Some summaries can be drawn as follows:

In the slope angles condition, the higher the slope angles, the bigger the deformation of the pile group will be. In three cases of slope angles, the biggest deformations always occur at 45°.

Therefore, it is shown to conclude that the piles must be reinforced carefully when it's on a high-degree slope.

When checking out the impact of the pile spacing factor, a conclusion can be figured out if pile spacing is too close, the structure of pile groups can be endangered.

Last but not least is the effect of horizontal axis rotation angles, the 90 ° is the most stable case because the deformation of each pile does not affect each other. Furthermore, after calculation, a conclusion can be made that when increasing the load to the pile group, it leads to a growth of the difference between two piles under every condition.

In conclusion, the most stable way to build a pile group on soi slope condition is with the horizontal axis rotation of 90° with a moderate pile spacing to ensure the sustainability of the structure.

Acknowledgement

This research is funded by the Office for International Study Programs (OISP), Ho Chi Minh City University of Technology (HCMUT), VNUHCM under grant number **SVOISP-2022-KTXD-135**. We acknowledge the support of time and facilities from HCMUT, VNUHCM for this study.

References

[1] Lujie Chen, Jiang Chong, Li Pang, Chaoyang Zhang, 2022. "Lateral capacity of a two-pile group foundation model located near slopes in sand". *Ocean Engineering 266* (2022) 112847.

[2] Chae, K. S., Ugai, K., & Wakai, A. (2004). Lateral resistance of short single piles and pile groups located near slopes. *International Journal of Geomechanics*, *4*(2), 93-103.

[3] Deendayal, R., Muthukkumaran, K., & Sitharam, T. G. (2016). Response of laterally loaded pile in soft clay on sloping ground. *International Journal of Geotechnical Engineering*, *10*(1), 10-22.

[4] Huang, A. B., Hsueh, C. K., O'Neill, M. W., Chern, S., & Chen, C. (2001). Effects of construction on laterally loaded pile groups. *Journal of geotechnical and geoenvironmental engineering*, *127*(5), 385-397.

SIMULATION AND DESIGN OF FLAT SLAB BY USING ETABS SOFTWARE

(MÔ PHỎNG VÀ THIẾT KẾ SÀN KHÔNG DẦM SỬ DỤNG PHẦN MỀM ETABS)

Nguyen Thai Binh[1,2,3], Ha Khanh Duy[1,2,*], Duong Quoc Anh[1,2], Nguyen Cong Gia Bao[1,2], Truong Dinh Thanh Dat[1,2], Le Ngoc Thanh[1,2], Nguyen Viet Thang[1,2]

[1] Faculty of Civil Engineering, Ho Chi Minh City University of Technology (HCMUT), 268 Ly Thuong Kiet Street, District 10, Ho Chi Minh City, Vietnam

[2] Office for International Study Programs, Ho Chi Minh City University of Technology (HCMUT), 268 Ly Thuong Kiet, District 10, Ho Chi Minh City, Vietnam

[3] Vietnam National University Ho Chi Minh City, Linh Trung Ward, Thu Duc City, Ho Chi Minh City, Vietnam

[*] Corresponding author: duy.hadhbk@hcmut.edu.vn

Abstract

Flat slab is considered a new step in the construction industry, with many outstanding advantages compared to the traditional slab, and has attracted the attention of many firms to find out the designing process. Therefore, this paper is a study focusing on the construction of these beamless slabs. First, the paper examines the theory and structural properties of flat slabs used in civil engineering. Second, the study provides the procedures to design the floor using ETABS software and export the model. Based on the results, the comparison of ETABS with other software and a conclusion can be made and presented.

Keywords: *flat slab, ETABS, drop panels, structure, load*

1. INTRODUCTION

Slabs are horizontal plate elements and normally carry vertical actions. Reinforced concrete slabs are used in floors, roofs and walls of buildings and as the deck of bridges. The floor system of a structure can take many forms such as in situ solid slabs, ribbed slabs or precast units. Slabs may span in one direction or two directions and they may be supported on monolithic concrete beams, steel beams, walls or directly by the structure's columns. Continuous slabs should in principle be designed to withstand the most unfavorable arrangements of loads, in the same manner as beams.

A flat slab floor is a reinforced concrete slab supported directly by concrete columns without the use of intermediary beams. The slab may be of constant thickness throughout or in the area of the column it may be thickened as a drop panel. Drop panels help to increase the overall capacity and sturdiness of the flooring system beneath the vertical loads thereby boosting the cost-effectiveness of the construction. The height of drop panels is usually about two times the height of the slab. The column may also be of constant section or it may be flared to form a column head or capital. These various forms of construction are illustrated in Figure 1.

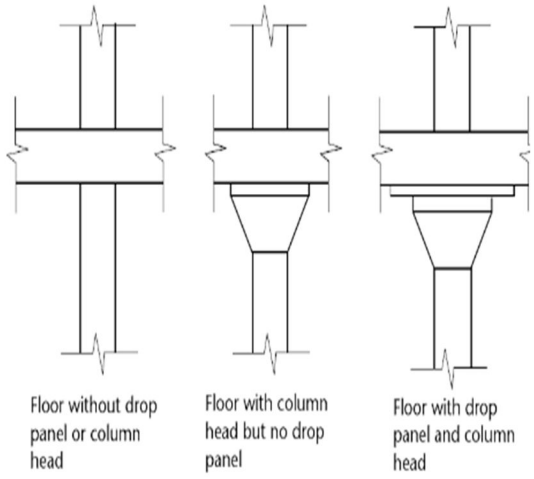

Figure 1. Drop panels and column heads [1]

The drop panels are effective in reducing the shearing stresses where the column is liable to punch through the slab, and they also provide an increased moment of resistance where the negative moments are greatest.

Flat slabs are considered suitable for asymmetrical column layouts such as floors with curved shapes and ramps. The flat slab floor has many advantages over the beam and slab floor. The simplified formwork and the reduced story heights and foundation load, make it more economical. Architects are able to introduce partition walls anywhere required, this allows the owner to change the size of the room layout. Use of flat slab allows a choice of omitting false ceiling and finishing soffit of slab with skim coating. Windows can extend up to the underside of the slab, and there are no beams to obstruct the light and the circulation of air. The absence of sharp corners gives greater fire resistance as there is less danger of the concrete spalling and exposing the reinforcement.

In other words, applying flat slabs can solve the problem of depth and flexibility in design. Although the cost might be expensive, flat slabs provide architects and engineers with immense freedom in design.

2. METHODS AND IMPLEMENTATION

Mostly, the concrete slab is designed to govern deflection criteria and not by shear in general. Because the load on the slab is uniformly distributed and shear stress due to this distributed load is generally small, hence shear reinforcement will not be often required for such load. Even concrete has shear capacity to withstand such small shear stress.

The support shear is maximum for that alternate bent-up provided in slab to withstand diagonal shear and prevent cracking. Also, the use of bent-up bar permitted the development of tensile strength also they acted as shear reinforcement.

2.1. EC2 particular rules for flat slabs

- **Section 6 Ultimate Limit States**

– cl 6.4 Punching (shear) & PD 6687 cl 2.16, 2.17 & 2.1.8

- **Section 9 Detailing of members and particular rules**

– Cl 9.4 Flat slabs

9.4.1 Slab at internal columns

9.4.2 Slab at edge and corner columns

9.4.3 Punching shear reinforcement

- **Annex I (Informative) Analysis of flat slabs and shear walls**

I.1 Flat Slabs

I.1.1 General

I.1.2 Equivalent frame analysis

I.1.3 Irregular column layout

All of these relevant sections are according to "The Concrete Society, Technical Report 64 - Guide to the Design and Construction of Reinforced Concrete Flat Slabs"

The distribution of moments is given according to EC2 as shown in Figure 2 and Table 1.

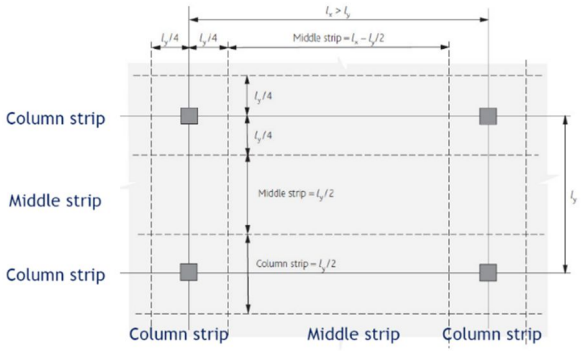

Figure 2. Positioning of the middle strip and column strip [2]

Table 1. EC2 moments design for flat slabs [3]

Location	Negative moments	Positive moments
Column strip	60% – 80%	50% – 70%
Middle strip	40% – 20%	50% – 30%

Notes

The total negative and positive moments to be resisted by the column and middle strips together should always add up to 100%

The distribution of design moments given in BS 8110 (column strip: hogging 75%, sagging 55%; middle strip: hogging 25%, sagging 45%) may be used

• Arrangement of reinforcement should reflect behaviors under working conditions.

• At internal columns 0.5At should be placed in a width = 0.25 × panel width.

• At least two bottom bars should pass through internal columns in each orthogonal direction.

• Design reinforcement at edge and corner reinforcement should be placed within b_e

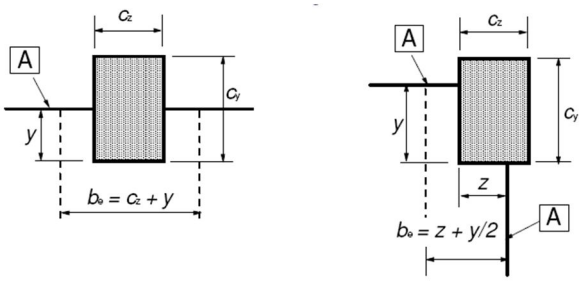

Figure 3. Parameters for edge and corner reinforcement [2]

• The maximum moment that can be transferred from the slab to the column should be limited to $0.17 b_e d^2 f_{ck}$

Note that edge and corner columns have limited capacity to transfer moments from slab. This is why redistribution may be necessary.

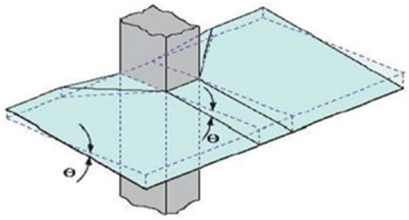

Figure 4. Slabs behavior around column [2]

2.2. Design constraints

a. Fire resistance

Table 2 gives the minimum dimensions and adequate fire resistance cover, referred to as axis distances a, of the reinforcement in the lower layer for flat slabs (taken from Table 5.9 of Eurocode 2, Part 1.2).

Table 2. Minimum slab thickness and axis distances for flat slabs [3]

Fire resistance (minutes)	Minimum dimensions (mm)	
	Slab thickness	Axis distance, *a*
30	150	10*
60	180	15*
90	200	25
120	200	35

b. Punching shear

The punching shear rules of Eurocode 2 are based on the CEB/FIP Model Code 1990(20). The basic control perimeter is set at 2d from the loaded area and has rounded corners as shown in Figure 5.

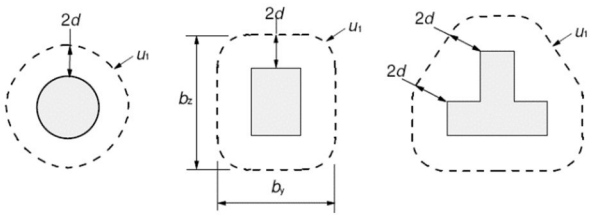

Figure 5. Typical basic control perimeters around a column[2]

Where the punching shear reinforcement is required, the shear resistance is the sum of the concrete and shear reinforcement resistances. Punching shear reinforcement is not necessary if:

$$V_{Ed} \leq V_{Rd,c}$$

**Calculating effective applied shear stress V_{Ed}*

The effect of slab/column moment transfer on punching shear may be considered as a uniform increase of shear stress at the control perimeter considered. The resulting effective applied shear stress is given in the following equation:

$$V_{Ed} = \beta V_{Ed}/u_1 d$$

Where:

V_{Ed} = applied shear force

β = $1 + k(M_{Ed}/V_{Ed})u_1/W_1$

u_i = length of the control perimeter considered

d = mean effective depth $(d_y + d_z)/2$

For structures where:

- Lateral stability does not depend on frame action.
- Adjacent spans do not differ by more than 25%

The approximate value for β shown may be used:

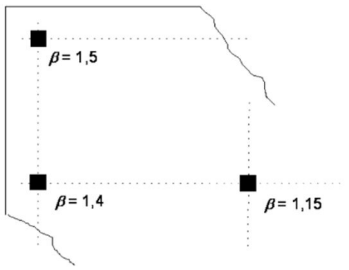

Figure 6. Approximate value of β in simple arrangement [2]

For other situations, there is plenty of guidance on determining β given in Cl 6.4.3 of the Eurocode 2 which will not be discussed here.

As for the basic perimeter u_1, it can be determined from the following figure:

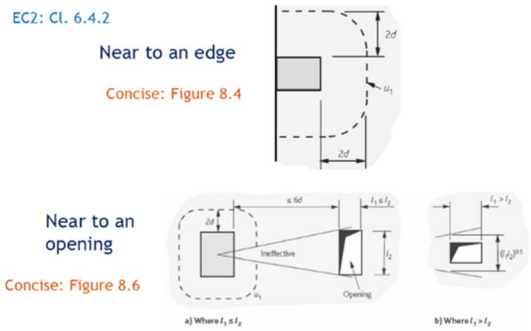

Figure 7. Control perimeter [2]

The outer control perimeter at which shear reinforcement is not required, should be calculated from:

$$u_{out,ef} = \beta V_{Ed}/V_{Rd,c}d$$

The outermost perimeter of shear reinforcement should be placed at a distance not greater than *kd* (k = 1.5) within the outer control perimeter.

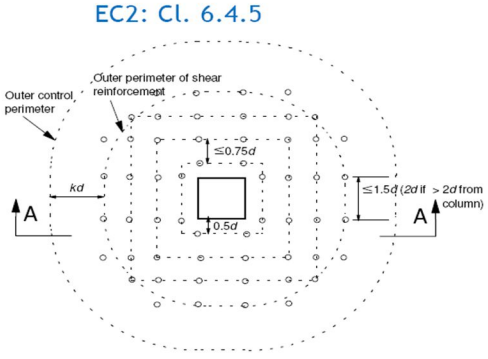

Figure 8. Outer perimeter [2]

**Calculating punching shear stress resistance $V_{Rd,c}$*

Check for punching shear resistance without shear reinforcement using the following expression:

$$V_{Rd,c} = 0.12k(100\rho_1 f_{ck})^{1/3} \geq 0.035k^{3/2} {f_{ck}}^{1/2}$$

Where:

$$k = 1 + \sqrt{(200/d)} \leq 2.0$$

$$\rho_1 = \sqrt{(\rho_{ly} + \rho_{lz})}$$

In which ρ_{ly} and ρ_{lz} are the mean values of the tension steel, A_s/bd, in the y- and z-directions for a width, b, of slab equal to the column width plus 3d on each side.

c. Deflection

For flat slab analysis, the deflection limit in accordance with Eurocode 2 is Span/250 and span over effective depth ratio. Furthermore, it also limits the deflection that occurs due to the construction of finishes and partitions to span/500. However, during construction, the slab will be supported by slab formwork, we will take the deflection limit as the operation condition, which is span/250.

d. Moment transfer from slab to column

Edge and corner columns have limited capacity to transfer moments from slab – redistribution may be necessary (Annex I.1.2 (5), EC2 cl 9.4.2 & TR 64)

$$M_{t,max} = 0.17 b_e d^2 f_{ck}$$

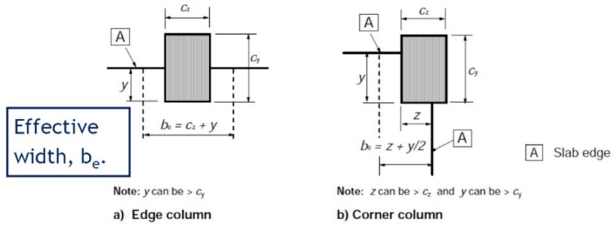

Figure 9. Column at the edge and corner of the slab [2]

2.3. Model of analysis

For the analysis of flat slab, we will establish the following model of a typical low-rise building:

- Number of stories: 3
- Typical story height: 3.5m
- The length from the top level of foundation to base: 1.5m
- Longer direction span: 6.2m
- Shorter direction span: 4.7m
- Characteristic dead load from finishes: 1.2 kN/m^2
- Live load: 2 kN/m^2
- Concrete material C25/30
- Reinforcing steel: CB300-T

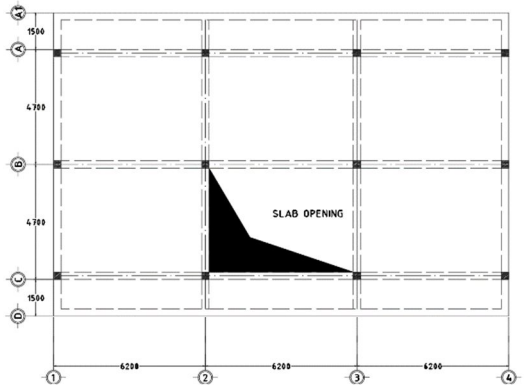

Figure 10. Plan view of low-rise structure

For the design of flat slab in this low-rise building, we will input into ETABS software the thickness of the slabs being 250mm, and the dimension of the columns are 350x350mm.

3. RESULTS AND DISCUSSION

3.1. Punching shear

Using the "Display punching check" function in ETABS, we obtain the following D/C ratio of a typical story:

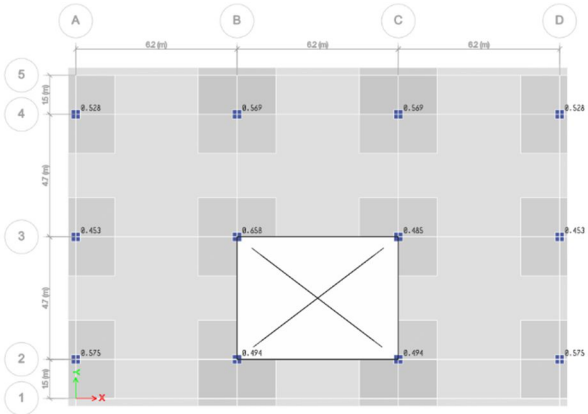

Figure 11. D/C ratio of a typical story in ETABS

The highest D/C ratio being 0.658, which is at the middle column where the opening is positioned. This parameter is less than 1, for ETABS this implies that the punching shear condition is not critical and the design is appropriate.

3.2. Deflection

Using finite element method analysis in ETABS, we have obtained the highest deflection for slab is -3mm, which took place in the slab edges or near the openings. Comparing with span/250 = 6200/250 = 24.8 mm, we can conclude the slab satisfy deflection condition.

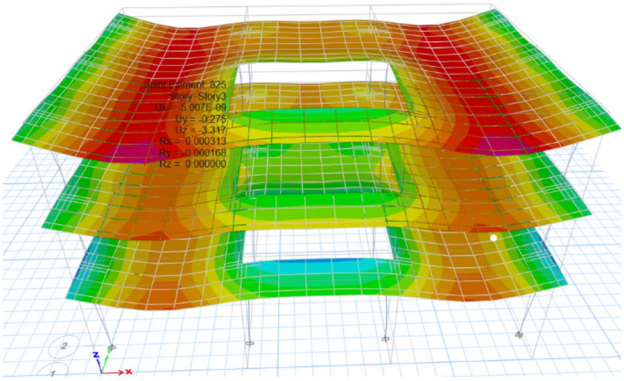

Figure 12. Deflection of slabs in ETABS

3.3. Comparison with conventional design

Through the process of modeling this low-rise structure with conventional slab and flat slab method, we have established two different design of structure components as follows:

Table 3. Dimension of structural components in conventional slab method

Structural component	Dimension/thickness (mm)
Slab	140
Column	300x300
Beam	200x550

Table 4. Dimension of structural components in flat slab method

Structural component	Dimension/thickness (mm)
Slab	140
Column	350x350
Beam	N/A

The difference in the dimension of slab and column of these two designs is due to the beam. In conventional slabs, the load acting onto the slab will be transferred through the beams and then to the column. Whereas for flat slab, the absence of beams acting as the intermediate component for load transfer has required an increase in the dimension of slab and column, in order to satisfy the deflection condition, as well as avoid being overstressed.

4. CONCLUSION

Throughout the paper, we have discussed about how to take into consideration the design constraints in order to put flat slabs into construction. The flexibility of flat slab construction can lead to economic efficiency while also allow the architect great freedom of form. With the help of today's technology, specifically with the use of ETABS software, it has made long computations to be feasible for engineers to work with [4]. One great advantage of ETABS in comparison SAFE, a similar software specifically for slab analysis, is that ETABS can evaluate and analyze the entirety of the structure, which also includes beams and columns, making it more convenient for design application.

The numerical method of finite element method (FEM) is applicable when analyzing the structure within the software. From there we can provide reinforcement for the slab and study the dynamics of the structure as a whole.

By following the procedures mentioned in section 3 of this paper, we hope to popularize the concept of flat slabs, allowing flat slabs to become widespread in many buildings, in which helps shorten the construction time while also spending less on materials.

The abovementioned ETABS procedures are made on a quantitative basis since the authors are at the undergraduate level. The design needs further evaluation based on the deeper theory and analysis and this is our goal in future research.

Acknowledgement

This research is funded by the Office for International Study Programs (OISP), Ho Chi Minh City University of Technology (HCMUT), VNUHCM under grant number SVOISP-2022-KTXD-113. We acknowledge the support of time and facilities from HCMUT, VNUHCM for this study.

References

[1] P. Novak, C. Nalluri, R. Narayanan, "Reinforced Concrete Design To Eurocode 2", 7th ed., 2007, Chapter 8: Design of reinforced concrete slabs.

[2] PHG-N-Rev, " Lecture 5 - Slabs and Flat-Slabs" MPA *The Concrete Centre*, 19th October 2016.

[3] A J Bond, O Brooker, A J Harris, T Harrison, R M Moss, R S Narayanan, R Webster, "How to design concrete structures using Eurocode 2", December 2006.

[4] The Concrete Centre, "Technical Report No.64 Guide to the design and construction of reinforced concrete flat slabs", 2007.

INVESTIGATING THE PROPERTIES OF SAND-BENTONITE MIXTURE BY DETERMINING THE SHEAR STRENGTH PARAMETERS USING DIRECT SHEAR TEST TO APPLY TO BORE PILE CONSTRUCTION

(NGHIÊN CỨU ĐẶC TÍNH CỦA HỖN HỢP CÁT VÀ BENTONITE THÔNG QUA VIỆC XÁC ĐỊNH THÔNG SỐ SỨC CHỐNG CẮT BẰNG THÍ NGHIỆM CẮT TRỰC TIẾP VÀ ÁP DỤNG CHO THI CÔNG CỌC KHOAN NHỒI)

Ha Khanh Duy[1,2,*], Le Ngoc Thanh[1,2], Nguyen Cong Gia Bao[1,2], Duong Dinh Tri[1,2], Mikaelah Perez[1,2]

[1] Faculty of Civil Engineering, Ho Chi Minh City University of Technology (HCMUT), 268 Ly Thuong Kiet Street, District 10, Ho Chi Minh City, Vietnam
[2] Office for International Study Programs, Ho Chi Minh City University of Technology (HCMUT), 268 Ly Thuong Kiet, District 10, Ho Chi Minh City, Vietnam
[*] Corresponding author: duy.hadhbk@hcmut.edu.vn

Abstract

A borehole pile foundation is a type of deep foundation that has been applied to many constructions in recent years. What makes borehole construction special is its convenience, when the workers can easily adjust big piles into the ground. This makes borehole piles popular in many high-rise buildings, or constructions requiring large load-bearing capacity. Hence, the determination of shear strength parameters is crucial for analyzing the properties of sand and bentonite mixtures in the context of borehole construction. This study aimed to investigate the shear strength parameters of sand and bentonite mixtures using the direct shear test. The experimental program involved preparing different mixtures of sand and bentonite at various proportions, with the shear tests conducted on these mixtures. The test results are then analyzed to determine the peak and residual shear strength, cohesion, and angle of internal friction for each mixture. The effects of varying bentonite content on the shear strength parameters are also going to be assessed. The findings will indicate whether the addition of bentonite to the sand significantly influences the shear strength parameters or not. As the bentonite content increase, the cohesion of the mixtures is predicted to increase, while the angle of internal friction decrease. These findings provide valuable insights into the engineering properties of sand and bentonite mixtures and can aid in optimizing the design and construction of boreholes. Future research could focus on exploring the long-term behavior and stability of such mixtures under different environmental conditions.

Keywords: *borehole, pile, bentonite, direct shear test*

Tóm tắt

Cọc khoan nhồi là một loại móng sâu ứng dụng trong xây dựng trong những năm trở lại đây. Điểm nổi bật là cọc được tạo nên bằng phương pháp khoan hiện đại, giúp người thi công dễ dàng điều chỉnh hạ độ sâu rất lớn và đường kính rộng. Phương án dùng cọc này hiện nay khá phổ biến, nhất là trong những công trình cao tầng, những công trình cần độ chịu tải lớn. Do đó, việc xác định các thông số cường độ cắt là rất quan trọng để phân tích các tính chất của hỗn hợp cát và bentonite trong việc xây dựng cọc khoan nhồi. Nghiên cứu này nhằm mục đích khảo sát các thông số về độ bền chống cắt của hỗn hợp cát và bentonite bằng thí nghiệm cắt trực tiếp. Thí nghiệm liên quan đến việc chuẩn bị các hỗn hợp cát và bentonite khác nhau ở các tỷ lệ khác nhau, với các thí nghiệm cắt được tiến hành trên các hỗn hợp này. Các kết quả thí nghiệm sẽ được phân tích để xác định cường độ kháng cắt cực đại và kháng cắt dư, lực dính và góc nội ma sát cho từng hỗn hợp. Các tác động của hàm lượng bentonite khác nhau đối với các thông số độ bền cắt cũng sẽ được đánh giá. Từ các phát hiện, nhóm sẽ chỉ ra rằng việc bổ sung bentonite vào cát có ảnh hưởng đáng kể đến các thông số cường độ cắt hay không. Khi hàm lượng bentonite tăng lên, lực dính của hỗn hợp được dự đoán sẽ tăng lên, trong khi góc ma sát bên trong giảm. Những phát hiện này cung cấp những hiểu biết có giá trị về các đặc tính kỹ thuật của hỗn hợp cát và bentonite và có thể hỗ trợ tối ưu hóa việc thiết kế và xây dựng các lỗ khoan. Nghiên cứu trong tương lai có thể tập trung vào khám phá biểu hiện lâu dài và tính ổn định của các hỗn hợp như vậy trong các điều kiện môi trường khác nhau.

Từ khóa: *lỗ khoan, cọc, bentonite, thí nghiệm cắt trực tiếp*

Acknowledgement: This research is funded by the Office for International Study Programs (OISP), Ho Chi Minh City University of Technology (HCMUT), VNUHCM under grant number **SVOISP-2022-KTXD-135**. We acknowledge the support of time and facilities from HCMUT, VNUHCM for this study.

QR CODE AND AUGMENTED REALITY (AR) APPLICATIONS FOR FACILITIES MANAGEMENT: STATE OF PRACTICES

(MÃ QR VÀ CÁC ỨNG DỤNG THỰC TẾ TĂNG CƯỜNG (AR) ĐỂ QUẢN LÝ CƠ SỞ VẬT CHẤT: ỨNG DỤNG THỰC TIỄN)

Hai Phu Huynh[1,2], Trung Quang Khuc[1,2], Mikaelah Gianina Vergara Perez[1,2], Sy Tien Do[1,2], Thu Anh Nguyen[1,2,*]

[1] Faculty of Civil Engineering, Ho Chi Minh City University of Technology (HCMUT), 268 Ly Thuong Kiet Street, District 10, Ho Chi Minh City, Vietnam
[2] Office for International Study Programs, Ho Chi Minh City University of Technology (HCMUT), 268 Ly Thuong Kiet, District 10, Ho Chi Minh City, Vietnam
[3] Vietnam National University Ho Chi Minh City, Linh Trung Ward, Thu Duc City, Ho Chi Minh City, Vietnam
[*] Corresponding author: nathu@hcmut.edu.vn

Abstract

In this study, the benefits, and advantages of Augmented Reality (AR) and Building Information Modelling (BIM) technologies are used for integrating Facilities Management (FM) with a deflected sample of a steel connector in a structure of a building. The role of AR will be as a visual model for the user guidance on the steel connector to see from their smartphones through an app from Hai's previous paper and interact with its environment. With the advances of BIM, the FM can see and predict the level of deterioration of the steel connector at a certain period. This can help FM further plan their risk as well as provide a more accurate solution to maintain the building's service life. The paper concludes with a potential development in precision, flexibility, and detailed information for the maintenance scheduling of any objects that run buildings smoothly and safely.

Keywords: *Building Information Modeling, Facility Management, QR Code, Augmented Reality, Maintenance Scheduling*

Tóm tắt

Trong nghiên cứu này, ứng dụng thực tế gia tăng (AR) và công nghệ Building Information Modelling (BIM) được sử dụng để tích hợp Quản lý Cơ sở vật chất (FM) với một mẫu mô hình của kết nối thép trong một cấu trúc của một tòa nhà. Vai trò của AR sẽ là một mô hình hình ảnh cho hướng dẫn người dùng về kết nối thép, mà họ có thể xem từ điện thoại thông minh của mình thông qua một ứng dụng từ bài báo trước đó của Hai và tương tác với môi trường xung quanh. Với sự tiến bộ của BIM, FM có thể xem và dự đoán mức độ hư hỏng của kết nối thép trong một khoảng thời gian nhất định. Điều này có thể giúp FM lên kế hoạch quản lý rủi ro cũng như cung cấp giải pháp chính xác hơn để duy trì tuổi thọ dịch vụ của tòa nhà. Bài báo kết luận với tiềm năng phát triển về độ chính xác, linh hoạt và thông tin chi tiết cho lịch trình bảo dưỡng của bất kỳ đối tượng nào giúp tòa nhà hoạt động một cách hiệu quả.

Từ khóa: *Mô hình thông tin công trình, Quản lý thiết bị, Mã QR, Thực tế ảo, Quản lý tiến độ bảo trì*

Acknowledgement: This research is funded by Office for International Study Programs (OISP), Ho Chi Minh City University of Technology (HCMUT), VNUHCM under grant number **SVOISP-2022-KTXD-114**. We acknowledge the support of time and facilities from HCMUT, VNUHCM for this study.

IDENTIFYING THE ROLE OF PROJECT'S STAKEHOLDERS IN THE USE OF A COMMON DATA ENVIRONMENT IN CONSTRUCTION MANAGEMENT OF AUTODESK 360 PLATFORM APPLICATIONS

(XÁC ĐỊNH VAI TRÒ CỦA CÁC BÊN LIÊN QUAN THAM GIA DỰ ÁN TRONG VIỆC SỬ DỤNG MÔI TRƯỜNG DỮ LIỆU CHUNG TRONG QUẢN LÝ XÂY DỰNG ỨNG DỤNG NỀN TẢNG AUTODESK 360)

Mikaelah Gianina Vergara Perez[1,2], Trung Quang Khuc[1,2], Phat Lien Huynh[1,2], Thu Anh Nguyen[1,2,*]

[1] Faculty of Civil Engineering, Ho Chi Minh City University of Technology (HCMUT), 268 Ly Thuong Kiet Street, District 10, Ho Chi Minh City, Vietnam
[2] Office for International Study Programs, Ho Chi Minh City University of Technology (HCMUT), 268 Ly Thuong Kiet, District 10, Ho Chi Minh City, Vietnam
[3] Vietnam National University Ho Chi Minh City, Linh Trung Ward, Thu Duc City, Ho Chi Minh City, Vietnam
[*] Corresponding author: nathu@hcmut.edu.vn

Abstract

Over the last several decades, investments in more sophisticated building projects combining numerous professions and teams have raised the demand for more complex communication methods. The architecture, engineering, and construction (AEC) sector is undergoing upheaval, with enterprises keen to catch up with the rate of digital transformation in other industries. The Common Data Environment (CDE) and BIM 360 platform are viewed as an opportunity to improve collaboration and efficiency during project management, as well as to serve as the foundation for Industry 4.0. BIM 360 improves construction project delivery processes by providing the tools required to evoke informed-decision making as the platform has well-structured data that is continuously kept up to date. This research provides an overview of the principles considerations and challenges when implementing a common data environment for the construction of high-rise building. The aims of the research conclude (1) an overview of the BIM 360 platform with CDE and (2) the application of BIM 360 and CDE in high-rise buildings. As a result, the BIM 360 platform in general, and the CDE, in particular, improves the team performance by exchanging information and enhancing knowledge about other participant skills or their availability. In the future, BIM 360 will be used for collaboration in design, drawing management, statistics, review and evaluation, quality control, feedback and correction, which supports construction management.

Keywords: *CDE, BIM 360, construction management, high-rise building, BIM*

Tóm tắt

Trong những thập kỷ gần đây, các nhà đầu tư vào các dự án xây dựng phức tạp ngày càng có nhu cầu cao về phương pháp giao tiếp chuyên nghiệp, đặc biệt khi kết hợp nhiều ngành nghề và đội ngũ làm việc. Lĩnh vực kiến trúc, kỹ thuật và xây dựng (AEC) đang trải qua sự biến đổi với mục tiêu bắt kịp tốc độ chuyển đổi kỹ thuật số trong các ngành khác. Môi trường dữ liệu chung (CDE) và nền tảng BIM 360 được xem là cơ hội để cải thiện sự hợp tác và hiệu quả trong quá trình quản lý dự án, đồng thời đóng vai trò quan trọng trong Công nghiệp 4.0. Nền tảng BIM 360 cải thiện quy trình trao đổi thông tin trong dự án xây dựng bằng cách cung cấp các công cụ cần thiết để đưa ra quyết định sáng suốt, nhờ vào việc cập nhật dữ liệu liên tục. Nghiên cứu này nhằm tổng quan các thách thức trong việc triển khai môi trường dữ liệu chung cho xây dựng nhà cao tầng. Mục tiêu của nghiên cứu là (1) tổng quan về nền tảng BIM 360 và CDE, và (2) áp dụng BIM 360 và CDE trong xây dựng nhà cao tầng. Kết quả cho thấy rằng nền tảng BIM 360 nói chung và CDE nói riêng tăng cường hiệu suất của nhóm thông qua trao đổi thông tin, cải thiện kiến thức và kỹ năng của các thành viên và khả năng sẵn có. Trong tương lai, BIM 360 sẽ được sử dụng để cộng tác trong thiết kế, quản lý bản vẽ, thống kê, xem xét và đánh giá, kiểm soát chất lượng, phản hồi và hiệu chỉnh, hỗ trợ quản lý xây dựng.

Từ khóa: *môi trường dữ liệu chung (CDE), quản lý xây dựng, nhà cao tầng, mô hình thông tin công trình (BIM)*

Acknowledgment: This research is funded by the Office for International Study Programs (OISP), Ho Chi Minh City University of Technology (HCMUT), VNUHCM under grant number **SVOISP-2022-KTXD-115**. We acknowledge the support of time and facilities from HCMUT, VNUHCM for this study.

OPTIMIZATION OF CONSTRUCTION METHOD FOR UNDERGROUND STORAGE FACILITIES

(TỐI ƯU HÓA PHƯƠNG PHÁP THI CÔNG CHO CÁC CÔNG TRÌNH NGẦM LƯU CHỨA)

Pham Ngoc Phuong Quynh[1,2], Le Minh Nhat[1,3], Huynh Minh Khoi[1,2], Nguyen Van Nhan[1,2], Nguyen Huynh Thong[1,2,*]

[1] Faculty of Petroleum Engineering Ho Chi Minh City University of Technology (HCMUT), 268 Ly Thuong Kiet Street, District 10, Ho Chi Minh City, Vietnam
[2] Office for International Study Programs, Ho Chi Minh City University of Technology (HCMUT), 268 Ly Thuong Kiet Street, District 10, Ho Chi Minh City, Vietnam
[3] Vietnam National University Ho Chi Minh City, Linh Trung Ward, Thu Duc City, Ho Chi Minh City, Vietnam
[*] Corresponding author: nhthong@hcmut.edu.vn

Abstract

Underground construction methods have been deployed in developed countries to support for utilizing underground space, socio-economic purposes, subsurface space savings, and accessibility in the supply chain. Nevertheless, depending on each type of underground facility, there will have appropriated construction methods to satisfy the project's purpose, types of construction, conditions, and geological properties about rock mass rating, stress, and elevation of X location, hence, selecting the appropriate position and construction method. The research paper aims to focus on optimizing typical subsurface construction approaches for underground storage facilities as a result of rock mass rating evaluation and geological cross-section model analysis from Rockworks software from good data and properties from lithology, location, direction, and stress at X area. We use qualitative and quantitative methods through Rock Mass Rating (RMR) calculation, and 3D cross-section model analysis, thereby determining construction methods based on analysis. In summary, this research presents a proposal for electing optimal underground construction approaches at X area to obtain economical, time savings, safe applied construction solutions, and high efficiency.

Keywords: *underground construction, RMR, geological structure model, underground storage*

Tóm tắt

Các phương pháp xây dựng ngầm đã được triển khai ở các nước phát triển nhằm hỗ trợ tận dụng không gian ngầm, mục đích kinh tế xã hội, tiết kiệm không gian dưới lòng đất và khả năng tiếp cận trong chuỗi cung ứng. Tuy nhiên, tùy từng loại công trình ngầm sẽ có biện pháp thi công phù hợp với mục đích của dự án, loại hình công trình, điều kiện và tính chất địa chất về phân loại đất đá, ứng suất và cao độ của vị trí X, từ đó lựa chọn vị trí và biện pháp thi công phù hợp. Mục đích của bài báo nghiên cứu là tập trung vào việc tối ưu hóa các phương pháp thi công ngầm điển hình cho các công trình lưu trữ ngầm dựa trên đánh giá phân loại chất lượng đất đá và phân tích mô hình mặt cắt địa chất từ phần mềm Rockworks từ dữ liệu giếng khoan và các thuộc tính từ thạch học, vị trí, hướng và ứng suất tại khu vực X. Sử dụng hương pháp định tính kết hợp định lượng thông qua tính toán chất lượng đá (RMR), đánh giá mô hình mặt cắt 3D, từ đó xác định phương pháp thi công dựa trên các phân tích. Tóm lại, nghiên cứu này trình bày đề xuất lựa chọn phương án thi công tối ưu cho công trình ngầm tại khu vực X nhằm đạt được giải pháp thi công tiết kiệm thời gian, kinh tế, an toàn và hiệu quả cao.

Từ khóa: *phương pháp thi công, đánh giá chất lượng đá, mô hình cấu trúc địa chất, lưu chứa ngầm*

Acknowledgement: This research is funded by the Office for International Study Programs (OISP), Ho Chi Minh City University of Technology (HCMUT), VNUHCM under grant number **SVOISP-2022- KTĐC&DK - 117**. We acknowledge the support of time and facilities from HCMUT, VNUHCM for this study.

COUNCIL 2
Faculty of Chemical Engineering
Faculty of Environment and Natural Resources

A NANO-BASED PERFUME: NANOEMULSIONS FORMULATION AND CHARACTERIZATION

(NƯỚC HOA NANO: SỰ HÌNH THÀNH HỆ NHŨ NANO VÀ CÁC TÍNH CHẤT)

Hoang Dang Ngoc Lam[1,2], Tran Le Hoai Nhi[1,2], Pham Kim Quoc Cuong[1,2], Nguyen Dinh Quan[1,2,*]

[1] Laboratory of Biofuel and Biomass Research, Faculty of Chemical Engineering, Ho Chi Minh City University of Technology (HCMUT), 268 Ly Thuong Kiet Street, District 10, Ho Chi Minh City, Vietnam
[2] Vietnam National University Ho Chi Minh City, Linh Trung Ward, Thu Duc City, Ho Chi Minh City, Vietnam
[*] Corresponding author: ndquan@hcmut.edu.vn

Abstract

Nanoemulsions with oil-in-water dispersions offered advantages over conventional emulsions due to their optical clarity and availability of encapsulated substances. In this study, nanoemulsions of essential oil and perfume were formulated by inspecting the composition of essential oil, water, and surfactant with two methods: mechanical homogenization and sonication. The mixture was characterized to clarify the nature of the nanoemulsion for perfume production. The dynamic light scattering (DLS) resulted in the most transparent and durable oil/tween 80 mixture with a ratio of 1:1.4, which had a minimum diameter of 24.2 nm. Meanwhile, the zeta potential measurements indicated a negative charge ranging from -0.22mV to -0.664mV. Furthermore, various temperature and pH tests were conducted to assess the stability of the solvent when applied to human skin. The positive properties demonstrated by the essential oil nanoemulsion highlight its significant potential for commercial applications and successful integration into everyday life.

Keywords: *nanoemulsion, emulsion, nanotechnology, perfume, essential oil*

1. INTRODUCTION

Nanoemulsions [1] [2], also known as submicron emulsions, ultrafine emulsions, or mini emulsions, are colloidal systems characterized by the stable dispersion of two immiscible liquids, such as water and oil, with the aid of a surfactant and co-surfactant. These dispersions possess submicron-sized particles and exhibit both thermodynamic and kinetic stability, resulting in a homogeneous and isotropic single-phase dispersion. [3] Perfume, a blend of alcohol and fragrances, is employed for its aromatic qualities, but it necessitates perceptible stability. Consequently, nanoemulsion represents a promising strategy to enhance the longevity and stability of the fragrance in perfumes..

Fragrances are classified into various categories depending on the content of their fragrance composition. Eau de parfum typically comprises 10-15% fragrance composition, eau de toilette contains 5-10%, and eau de cologne contains 3-5%. However, individuals with allergies or sensitive skin may experience skin irritation and inflammation when using ethanol-based perfumes, as ethanol has been identified as a potential irritant.

In the realm of non-alcohol-based perfumes, solid-state options like solid emulsions, gels, and pomades, as well as perfumed oils, offer an alternative to traditional alcohol-based fragrances. The scientific literature has proposed various alternatives, including emulsions, microemulsions, liposomes, and micelles, which serve as non-alcohol-based perfumed products [4]. These alternatives rely on water as a safe solvent for fragrance encapsulation. Nevertheless, the integration of lipophilic systems into water in the absence of a cosurfactant presents technological hurdles in terms of achieving thermodynamic stability. To overcome this issue, solubilizers such as polyols (including glycols and glycerin) or surfactants are employed to enhance the solubility of essential oils [5].

Several nanoemulsion cosmetic products are currently available on the market, such as the anti-UV hair spray manufactured by Korres, Nanocream developed by Sinerga, Nanogel produced by Kemira, Vital Nanoemulsion A-VC serum offered by Marie Louise, Bepanthol Ultra face cream provided by Bayer, and NanoVital face cleanser created by Vitacos Cosmetics. Furthermore, the esteemed cosmetics company L'Oreal holds patents for numerous nanoemulsion cosmetic formulations. Nanoemulsions play a dual role in perfume products by serving as a medium for fragrance compositions and simultaneously improving the chemical stability of the compounds, thus offering protection against oxidation [5] [6].

In order to optimize the utilization of nanoemulsions in perfume and cosmetic formulations, meticulous consideration is dedicated to the choice of preparation methods and the composition of both the oil and aqueous phases. The oil phase commonly encompasses essential oils and lipophilic surfactants, whereas the aqueous phase is composed of ethanol and water [5]. The exploration of the optimal ratio between essential oil and surfactant is of

utmost importance as it directly affects the distribution of droplet sizes, a critical factor that greatly influences the stability of the nanoemulsion. The utilization of ultrasonic technology is frequently considered a suitable method for enhancing the efficiency of nanoemulsion generation processes. [7]

This study utilized a range of analytical techniques, such as dynamic light scattering (DLS), zeta potential measurement, and viscosity measurement, to comprehensively assess the stability and physical properties of the nanoemulsions under investigation. Moreover, temperature and pH tests were performed to mimic conditions similar to those of human skin and to evaluate the robustness of the solvent when applied topically. The objective of these tests was to gain valuable insights into the formulation and characterization aspects of nanoemulsions, with a specific focus on their potential applications in perfumes and cosmetics.

2. METHODS AND IMPLEMENTATION

2.1. Materials

Lavender essential oil from a Vietnamese source was purchased from an organic international joint stock company in Vietnam. The non-ionic surfactant, polyethylene glycol sorbitan mono-oleate, also commonly known as Tween 80, which was utilized as a surfactant in the study, was acquired from Sheaghana Cosmetic Ingredient Company, Vietnam. Ethanol was procured from the Oil Perfume Company in Vietnam. And all procedures involved the utilization of distilled water.

2.2. Preparation of nanoemulsions

Lavender nanoemulsion was formulated using the following four components: lavender essential oil, Tween 80, water, and ethanol. The methodology for generating emulsions through spontaneous emulsification involved three steps.

Preparation of the homogeneous solution (S1) composed of lavender essential oil and hydrophilic surfactant (Tween® 80) [8] [9]. The homogeneous aqueous phase (S2) was formed by water and ethanol at specific concentrations using a magnetic stirrer at a speed of 500 rpm for 10 min (Table 1). In this formulation, different oil-to-surfactant ratios (in v/v%) were implemented, including 1:1 (Lavender-A), 1:1.2 (Lavender-B), 1:1.4 (Lavender-C), 1:1.6 (Lavender-D), 1:1.8 (Lavender-E), and 1:2 (Lavender-F).

Diffusion of the organic solvent in the aqueous phase under magnetic stirring instantly formed the o/w emulsion, causing the formation of nanodroplets. The magnetic stirring was kept up for 45 minutes to allow the system to come into equilibrium.

These emulsions were then prepared by utilizing an ultrasonicator with a 240 W input power processor (JP-040S 10L, 40 kHz) to generate the corresponding nanoemulsions. Each concentration experienced specific sonication time periods of 15 min.

Table 1. Optimization of Lavender Oil-Based Nanoemulsion Formulations

Formulation Code	Essential Oil: Surfactant Ratio (v/v)	Essential Oil: Surfactant: Alcohol: Water (v/v)	Sonication Time
Lavender-A	1:1	10:10:30:50	15 min
Lavender-B	1:1.2	10:12:30:48	15 min
Lavender-C	1:1.4	10:14:30:46	15 min
Lavender-D	1:1.6	10:16:30:44	15 min
Lavender-E	1:1.8	10:18:30:42	15 min
Lavender-F	1:2	10:20:30:40	15 min

2.3. Optimisation of the oil, surfactant and water-miscible solvents

All tests involving the optimization of emulsion formation were carried out at 25°C with solvents that had a low hazardous potential, such as distilled water and ethanol, for safety reasons.

2.4. Characterization of nanoemulsion

The following nanoemulsion characteristics were investigated: droplet size, polydispersity index, viscosity, pH, and stability. All measurements were conducted in triplicate, and the mean ± standard deviation (± S.D) was reported.

The droplet size distribution [3] [6] was measured by the particle size analyzer Zetasizer Nano ZS90 (Malvern Panalytical, United Kingdom). The ZS90 assessed the size distribution using dynamic light scattering (DLS), which generated a relationship between the extent of nanoparticle dispersion and the intensity of scattered light.

The degree of homogeneity was described by the polydispersity index, which was determined by DLS and increased with higher surfactant content.

The viscosity of the samples was measured utilizing the NDJ-1 at 60 rpm, a range of 10–100,000 mPa.s., ± 5% S.D., and the original in China. The rheological characteristics of the nanoemulsion were provided by viscosity, which also aids in comprehending the inversion between phases during formulation.

The pH was measured quantitatively using a digital pH meter [SK-620pH, SATO Japan] at 20-30 ± 0.5°C.

The physical stability of different formulations was measured by analyzing the degree of phase separation post-ultrasonication, and formulation stability was also observed over long periods of time under varied pH and

temperature conditions. The assessment of physicochemical stability for various formulations that incorporate other optimal parameters, such as lower surfactant concentration utilization, optimal droplet size distribution and PDI, low viscosity, as well as a proper pH, aids in the identification of the high-efficiency formulation.

3. RESULTS AND DISCUSSION

3.1. Identification of lavender essential oil constituents by GC-MS

The lavender essential oil was depicted using Gas Chromatography-Mass Spectroscopy. The total ion chromatogram (TIC) and the retention time of active components were shown in Fig. 1. According to ISO Standard 3515, the different components of lavender essential oil identified by GC-MS include 1,8-cineole, 0–15%; limonene, 0–0.5%; trans-β-ocimene, 2–6%; cis-β-ocimene, 4–10%; 3-octane, 0–2%; camphor, 0–0.5%; linalool, 25–38%; linalyl acetate, 25–45%; α-terpinene-4-ol, 2–6%; lavandulol minimum, 0.3%; Lavandula acetate minimum, 2.0%; a-terpineol, 0–1%. These results provide valuable insights into the chemical composition of lavender essential oil as presented in Fig. 2. The presence and relative abundance of these identified components contribute to the characteristic aroma and potential therapeutic properties associated with lavender oil. The quantification of each component allows for a more comprehensive understanding of the oil's composition, aiding in quality control and standardization efforts. This information can be useful for industries involved in the production of lavender-based products, such as cosmetics, perfumes, and aromatherapy. These findings provide a comprehensive understanding of the chemical composition of lavender essential oil and serve as a basis for further investigation into its nanoemulsion formation with surfactants.

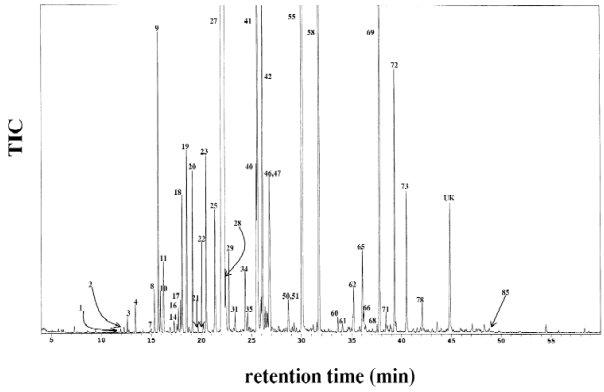

Figure 1. Typical GC–MS TIC chromatogram for lavender essential oil

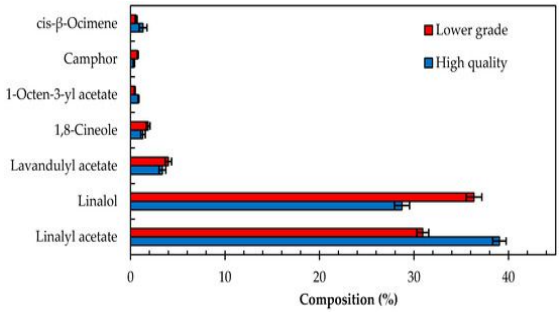

Figure 2. Main scent and aromatic components in lavender essential oil.

3.2. Nanoemulsion characterization

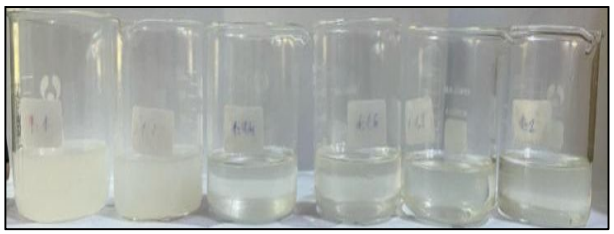

Figure 3. Visual transparency of a. Lavender-A, b. Lavender-B, c. Lavender-C, d. Lavender-D, e. Lavender-E, f. Lavender-F.

The samples were subjected to sonication for a duration of 15 minutes, then selected for further characterization. The visual appearances of the formulations, which were prepared using different oil-to-surfactant ratios, were depicted in Fig. 3. The finding reveals an interesting relationship between surfactant concentration and the visual appearance of nanoemulsions. Specifically, as the surfactant concentration increased, a distinct transparency change in the emulsions was observed, transforming them from a milky white appearance to a transparent state. This change in color indicates that higher concentrations of surfactant played a crucial role in enhancing the transparency of the nanoemulsions. However, it must be reminded that high concentration of surfactants leads to high viscosity and the uncomfort on skin of users of perfumes. Therefore, an appropriate ratio of compositions will be discussed later.

The improved transparency observed with higher surfactant concentrations can be attributed to the enhanced stability of the nanoemulsion system. The smaller and more uniformly dispersed oil droplets contribute to a more homogeneous refractive index throughout the emulsion, resulting in reduced light scattering. This reduction in light scattering leads to the observed transition from a milky white appearance to a transparent one.The visual appearances of the formulations with varied oil-to-surfactant ratios were illustrated in Fig. 3. When there was an increase in both surfactant concentrations, the transparency of the emulsions showed a noticeable change from milky white to transparent.

A rapid decrease in droplet size was observed as the concentration of surfactant increased (Fig. 6). The non-ionic surfactant was preferred due to its outstanding oil-in-water (O/W) properties. The O/W emulsion system was more stable overall due to the efficient solubility of Tween 80 with essential oils as well as its capacity to minimize droplet diameter by sticking to the surface of the droplet. According to the Characterization of Nanoemulsion [2], droplet size showed nanoemulsion stability, and their polydispersity index influenced the extent of homogeneity in nanoemulsion stability. This was a method preferred in industrial operations because it allowed for flexible emulsion droplet size distribution control and the efficient production of fine emulsions from a wide range of materials with minimum energy consumption. The high-energy shockwaves can break the droplets by forming turbulence.

The concentration of surfactants had an obvious and direct relationship with viscosity. As shown in Fig. 4, the increase in surfactant concentration was directly proportional to the increase in viscosity.

The pH values increased with increasing surfactant concentration, as demonstrated in Fig. 5. Chemical degradation reactions were caused by changes in pH value, which indicated the stability of the nanoemulsion.

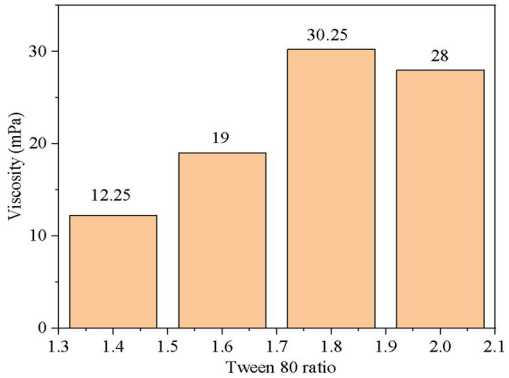

Figure 4. The viscosity of four samples with clear color

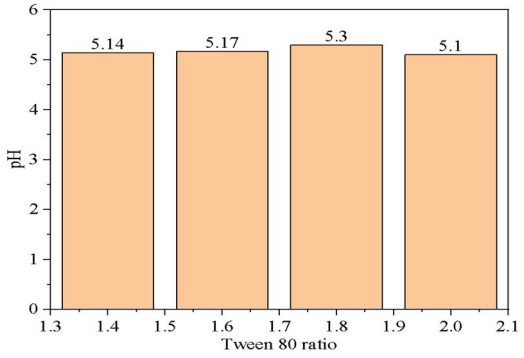

Figure 5. The pH of four samples with clear color

3.3. Lavender nano-emulsions stability

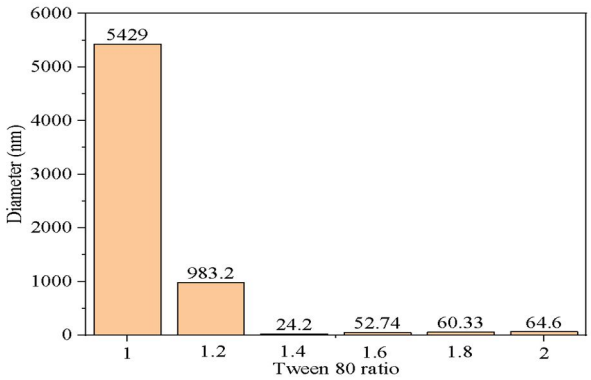

Figure 6. The average droplet diameter of Lavender oil Nano-emulsion

The oil/tween 80 ratio was a significant element influencing nano-emulsion stability and even emulsion type. Droplet size had a direct impact on the interfacial area that the nano-emulsion can use, which in turn affected the permeability of the active compounds through the membranes in tissues and blood tissues, determining their bioavailability. Both the ratio 1:1 and 1:1.2 ratio exhibited relatively little stability because of their milky colors, indicating a lack of nanoscale. Besides, monitoring droplet size aided in determining uniformity and stability. A smaller droplet size helped to prevent droplet coalescence, which reduced the breakdown of the nano-emulsion by well-known phenomena, including sedimentation and creaming through Ostwald ripening [10]. The average droplet sizes of nano-emulsion were 5.4 and 0.983 m, respectively, when the oil/tween 80 ratio was 1:1 and 1:1.2. This huge diameter was caused by a low concentration of tween 80 surfactants, which prevented the nanoparticle from forming. Four remaining ratios effectively generated nano-suspension, resulting in diameters of 24.2, 52.74, 60.33, and 64.6 nm, respectively. The results showed that the ratio 1:1.4 produced the smallest nanoparticle size, with the diameter increasing as the number of surfactants linked to the particles increased. Thus, this nanosystem presented a stable state with a small (24.2-64.6 nm) and uniform particle size (PDI $\leq$ 0.30), which was an ideal encapsulation state with the results obtained from the DLS experiments (Fig. 6). A high surfactant concentration indicated that there was enough of the substance present to encapsulate each oil droplet and produced a flexible film that prevented the oil droplets from adhesion or cohesion, thereby ensuring homogeneity throughout the entire oil droplet in the nanoemulsion

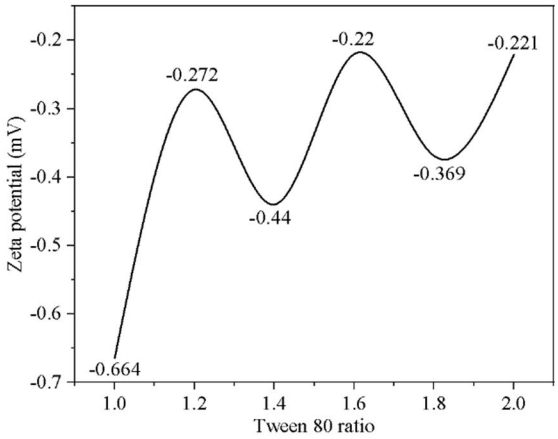

Figure 7. Effect of pH on zeta potential of the LEO Nanoemulsions

According to the data presented in Fig. 7, the zeta potential grew negatively, which could be attributable to an increase in the viscosity of the solution as the amount of surfactants increased, as well as nanoparticle adherence. The pH variation between the samples was only 5.1 to 5.3. The statistics revealed a fluctuation in potential ranging from -0.22 to -0.664 mV. The zeta potentials of the emulsions remained negative at all pH values, which was possible because of the negatively charged –O- group from the –OH- group. The results also showed that it was sterically protected, such as by polyethylene glycol ligands like Tween 80.

4. CONCLUSION

Nanoemulsions offer significant advantages over conventional emulsions due to their exceptional optical clarity and improved availability for encapsulated substances. The application of ultrasonic technology in the production process further enhanced the formulation of nanoemulsions. The experimental findings revealed that the optimal oil/tween 80 ratio, yielding a minimum diameter of 24.2 nm of the encapsulation particle after the emulsion, was determined to be 1:1.4. Zeta potential measurements indicated a negative charge ranging from -0.22mV to -0.664mV, indicating the stability of the suspension. Additionally, viscosity and pH tests, simulating conditions similar to human skin, were conducted to evaluate the solvent's durability upon topical application. The results demonstrated a pH range of approximately 5.1 to 5.3, along with an optimum viscosity of 12.25 mPa for the 1:1.4 ratio, ensuring the safety of the solvent for human skin. Consequently, the remarkable stability and physical properties observed in nanoemulsions formulated for nano-based perfumes indicate their strong potential for application in the perfume and cosmetics industry.

References

[1] M. N. Y. a. A. P. Odile Sonneville-Aubrun, "Application of Nanoemulsions in Cosmetics".

[2] J. C. R. H. M. Oca-Avalos, "Nanoemulsions: stability and physical properties," *COFS,* 2017.

[3] Małgorzata M., Elwira L., Elżbieta S., Katarzyna W.-K., "Preparation and Characterization of Water-Based Nano-Perfumes," nanomaterials, 2018.

[4] K. G. A. S. K. SINGH, "Review of Nanoemulsion Formulation and Characterization Techniques," The Indian Journal of Pharmacy, pp. 781-789, 2018.

[5] R. Shick, C. Piechocki, C. Tucker and L. Gatz, "Ethanol-free aqueous perfume composition," U.S. Patent US8343521B2, 1 January 2013.

[6] L. M., P. M., G. D. Robert Shellie, "Characterisation of lavender essential oils by using gas chromatography–mass spectrometry with correlation of linear retention indices and comparison with comprehensive two-dimensional gas chromatography," Journal of Chromatography A, pp. 225–234, 2002.

[7] L. D. K. A. R. &. R. N. M Joyce Nirmala, "Ultrasonic Nanoemulsification of Cuminum cyminum Essential Oil and Its Applications in Medicine," International Journal of Nanomedicine, pp. 795-807, 2020.

[8] L. D. V. G. &. R. N. : M Joyce Nirmala, "Preparation of Celery Essential Oil-Based Nanoemulsion by Ultrasonication and Evaluation of Its Potential Anticancer and Antibacterial Activity," International Journal of Nanomedicine, pp. 7651-7666, 202.

[9] S. S. W. B. M. R. Z. Q. Y. H. L. Yan Zhou, "Preparation and antimicrobial activity of oregano essential oil Pickering emulsion stabilized by cellulose nanocrystals," International Journal of Biological Macromolecules, 2018.

[10] G. R. M. R. Masoumeh Marhamati, "Effects of emulsifiers on the physicochemical stability of Oil-in-water Nanoemulsions: A critical review," Journal of Molecular Liquids, 2021.

[11] S. Saffarionpour, "Nanocellulose for Stabilization of Pickering Emulsions and Delivery of Nutraceuticals and Its Interfacial Adsorption Mechanism," Food and Bioprocess Technology, 2020.

[12] Y. Z. J. C. W. J. Wanli Zhang, "Improving the performance of edible food packaging films by using nanocellulose as an additive," International Journal of Biological Macromolecules, 2018.

[13] J. Marcus, M. Klossek, D. Touraud and W. Kunz, "Nano-droplet formation in fragrance tinctures," Flavour Fragr. J, Vols. 294-299, p. 28, 2013.

[14] S. Ophaswongse and H. Maibach, "Alcohol dermatitis: Allergic contact dermatitis and contact urticaria syndrome. A review," Contact Derm, Vols. 1-6, p. 30, 1994.

[15] N. Usón, M. Garcia and C. Solans, "Formation of water-in-oil (W/O) nano-emulsions in a water/mixed non-ionic surfactant/oil systems prepared by a low-energy emulsification method," Colloids Surf, Vols. 415-421, p. 250, 2004.

[16] B. Mishra, B. Patel and S. Tiwari, "Colloidal nanocarriers: A review on formulation technology, types and applications toward targeted drug delivery," Nanomedicine, Vols. 9-24, p. 6, 2010.

[17] M. G. a. P. S. Tim J. Wooster, "Impact of Oil Type on Nanoemulsion Formation and Ostwald Ripening Stability," Food Science Australia (CSIRO), Werribee, Victoria 3030, Australia, July 14, 2008.

SENSORY PROPERTIES AND CONSUMER PREFERENCES OF SNACK ENRICHED WITH SPIRULINA BIOMASS

(ĐÁNH GIÁ TÍNH CHẤT CẢM QUAN VÀ MỨC ĐỘ ƯA THÍCH CỦA NGƯỜI TIÊU DÙNG ĐỐI VỚI SẢN PHẨM SNACK KHI BỔ SUNG BỘT TẢO SPIRULINA)

Tran Thi Van Anh[1,2,3], Vo Ngoc Mai Anh[1,2,3], Duong Chau Uyen Nhi[1,2,3], Quan Thi Thanh Nhan[1,2,3], Pham Nguyen Quang Minh[1,2,3], Nguyen Le Hoa[1,2,3], Nguyen Quoc Cuong[1,3,*]

[1] Faculty of Chemical Engineering, Ho Chi Minh City University of Technology (HCMUT), 268 Ly Thuong Kiet Street, District 10, Ho Chi Minh City, Vietnam
[2] Office for International Study Programs, Ho Chi Minh City University of Technology (HCMUT), 268 Ly Thuong Kiet Street, District 10, Ho Chi Minh City, Vietnam
[3] Vietnam National University Ho Chi Minh City, Linh Trung Ward, Thu Duc City, Ho Chi Minh City, Vietnam
[*]Corresponding author: nqcuong@hcmut.edu.vn

Abstract

Snack foods have been increasingly popular, especially among busy young individuals who sometimes substitute these products for meals. Unfortunately, these snack foods are typically lacking in essential nutrients and may result in malnutrition for consumers. One potential strategy to address this issue is to enrich snack foods with nutritious ingredients. Spirulina, with its high nutrient content, is one of the most promising ingredients. However, incorporating spirulina into snack products can be challenging due to its unpleasant sensory properties. This study aims to explore the sensory properties and consumer preferences of snack products enriched with spirulina at different ratios. A panel of 107 naive consumers evaluated snack samples with different ratios of spirulina using a descriptive test called Check-all-that-apply (CATA) and a hedonic test on a 7-point Likert scale. The results showed that the snack products with 2% spirulina incorporation were the most preferred among consumers. The sensory profile of the spirulina snack products was described as fishy and vegetable in flavor, and soft, cohesive, hard, and salty in texture. Additionally, the study found that sweet taste increased consumer liking, while fishy, dry, and astringent aftertastes lowered consumer preference. Overall, the results suggest that spirulina has good potential as a nutritious ingredient for creating healthy and acceptable snack products.

Keywords: *spirulina biomass, snack, consumer preferences, descriptive test CATA, hedonic test*

1. INTRODUCTION

The term “snack” refers to foods that are consumed between meals. Snacks can be considered as a light meal and can include a variety of food items such as potato chips, puffs, popcorn, cookies, and crackers [1]. These foods are typically high in carbohydrates, fat, and calories but often lack protein, dietary fibers, and micronutrients [2]. In addition, snacks are popular among all age groups, especially children and young adults. Market research done by Orion also found that the savory snack consumption of Vietnamese people is increasing and is forecasted to reach over 1000 million U.S. dollars in 2026 [3].

Many studies have found that chronic malnutrition is more dangerous and widespread than acute malnutrition [4]. To address this issue, providing proper, balanced nutrition is essential. Fortifying food products with necessary nutrients has become a prominent aspect of the food industry. Given the increasing consumption of snack products, fortifying snacks with essential nutrients is highly recommended to provide a balanced diet.

Spirulina refers to cyanobacterium, commonly known as blue-green algae. It is considered a cholesterol-free, low-fat and low-calorie source of protein, containing all essential amino acids [5]. Moreover, it is also rich in vitamins (especially vitamin B12), minerals, polyunsaturated fatty acids including Omega 3 and other bioactive compounds like pigment compounds (carotenoids, chlorophylls and especially C-phycocyanins which gives spirulina its signature blue color), phenolic compounds, antioxidants, etc. [6], [7], [8]. In a study about extruded snacks enriched by bioactive peptides from spirulina [9], the result shows that the addition of spirulina significantly increases the protein and lipid content of the snack compared to the control sample.

Results from studies have shown that the dark green color, fishy smell, and unpleasant taste of the algae have a negative impact on the acceptability of products with added spirulina [10]. Moreover, food products enriched with spirulina powder have been shown to have changes in their sensory properties [11][12]. And since consumers tend to focus more on the texture and flavor of snacks

when eating, these qualities should be considered when spirulina is added to the product.

In this study, we aimed to describe the sensory properties of one control snack product and four snack products with the addition of spirulina biomass at different ratios and evaluate the influences of sensory attributes on consumer preference with different liking patterns.

The two main methods of collecting data include the Check-All-That-Apply (CATA) method and Hedonic liking test. CATA is used in sensory evaluation to describe sensory properties by using naive consumers. In Hedonic liking test, consumers are asked to taste each snack sample and rate their liking of each sample on a 7-point categorial scale.

Defining homogeneous groups of consumers is a critical stage to include in the process of product optimization, regardless of the methodology employed. If customer clusters are not considered, it can lead to nonsense and the creation of products that are rejected (or not fully liked) by all consumers. In that instance, the optimized product will not meet its primary aim since it will underperform. Because ideal information includes a liking component, it is also possible to group consumers based on their ideals rather than their liking. However, because consumers with similar liking patterns can have rather diverse ideals (while remaining consistent), it is suggested to categorize consumers into homogeneous groups based on liking. Visual segmentation based on Principle Component Analysis (PCA) plot used in this study is based on a PCA of the consumer likings, followed by a review of the consumer loadings plot [13]. The data matrix, usually using the standard matrix setup with assessors as columns and products as rows, gives scores for the products and loadings for the assessors. The loadings plot can then be used for identifying clusters of assessors which have a special and interesting relation to the products in the score plot [14].

After clustering consumers, the Multiple-response Correspondence Analysis (MR-CA) approach is applied to describe the sensory properties of products. It illustrates the relationship between attributes and products. The better an attribute is distinguished, the further it is

positioned from the origin. Additionally, there will be a strong association between the attribute(s) and products that are oriented in the direction of the attribute(s) on the axis. To determine whether a product is well discriminated, confidence ellipses on the product coordinates are utilized. The two results diverge more from one another the less closely the two ellipses coincide [15]. After describing the products, the attributes that significantly impact consumer's preference are determined. The Penalty-Lift Analysis (PLA) is a useful tool to identify so-called drivers of product liking or other hedonic measures from CATA or similar datasets that include some hedonic measures along with them [16].

2. METHODS AND IMPLEMENTATION

2.1. Materials

The formula of snack production included 44g shortening, 40g water, 12g sugar, 12g cooking oil, 6g baking powder and 2g salt (calculated on g/100g of wheat flour). Moreover, spirulina powder was provided by Asia Chemical Corporation, Vietnam. Other materials were bought from local markets, including wheat flour no.8 (Interflour Company, Vietnam), shortening (CALOFIC Corporation, Vietnam), sugar (Bien Hoa, Vietnam), cooking oil (Tuong An Vegetable Oil Joint Stock Company, Vietnam), baking powder (Tuan Phuong, Vietnam), salt (VIFON, Vietnam).

2.2. Samples

Different snack samples were made by changing the concentration of spirulina added to the snack formulation. The amount of spirulina powder used was calculated based on 100g of wheat flour. The differences between the samples are shown in Table 1.

Table 1. Spirulina concentration in each sample

Sample	Spirulina concentration
P1 (R0)	0%
P2 (R2)	2%
P3 (R4)	4%
P4 (R6)	6%
P5 (R8)	8%

2.3. Participants

A total of 107 consumers, aged between 18 and 25 years, mostly students at the Ho Chi Minh City University of Technology (HCMUT) were enrolled in the study. The sample size fulfilled the requirements to perform a sensory characterization of products using the CATA approach and gather hedonic data [17].

2.4. Sample preparation

The snack products were manufactured at Innovation Center - Asia Chemical Corporation. The snack production was included in Figure 1.

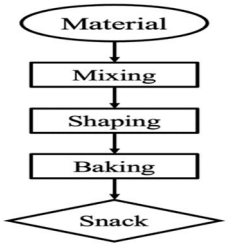

Figure 1. Production of snacks added with spirulina powder

The procedure of making snacks was briefly described by the following stages:

- Mixing: the ingredients were mixed simultaneously in the mixer at 120 rpm for 4 minutes, forming a dough.

- Shaping: the dough was divided manually into small balls, with each ball weighing 3-5g.

- Baking: the snack samples were baked at 150°C for 25 minutes.

2.5. Experimental design

The sensory test was conducted at the Sensory Laboratory of the Ho Chi Minh City University of Technology.

The study consisted of two separate tasks performed on the same day: first panelists assessed the overall liking of snacks added with spirulina powder, and then they described sensory properties of these products by CATA questions.

Evaluations were conducted using Compusense software. The panelists must eat at least 2/3 of the sample. Panelists rated their likings on 7-point Likert scale anchored with 1 (Strongly Dislike) and 7 (Strongly Like), followed by the CATA test for the same sample. A list of descriptive terms of textural properties is presented in Table 2.

Table 2. List of descriptive terms of textural properties

Taste	Aftertaste	Flavor	Texture
Sweet, Salty.	Salty, Astringent	Doughy, Buttermilk, Fishy, Nutty, Vegetable.	Hard, Soft, Dense, Spongy, Brittle, Adhesive, Cohesive, Dry.

The list of sensory attributes was developed previously from the pre-test of snack samples. The sensory attributes along with the definition/description of the attribute were selected by consensus of all assessors.

3. RESULTS AND DISCUSSION

3.1. Clustering consumer on liking data

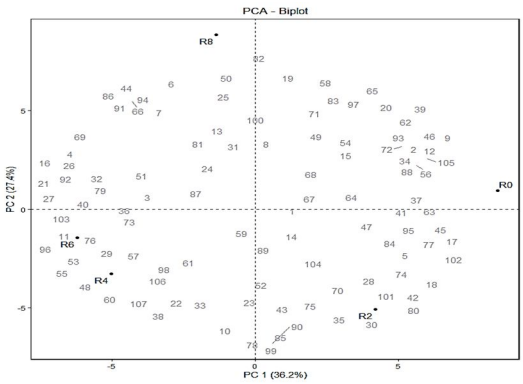

Figure 2. PCA bi-plot

By combining individual (products) plot and variables (consumers) plots, a PCA bi–plot was obtained that showed both the position of consumers and products within the same graph. Figure 2 displays the graph of principle components 1 and 2, which accounted for 36.20% and 27.44% of the variability of liking. Consumers and products were segmented into 3 different clusters based on their coordinates: Cluster 1 (PC1 > 0); Cluster 2 (PC1 < 0, PC2 > 0); Cluster 3 (PC1 < 0, PC2 < 0). Cluster 1 consisted of 55 consumers who had a preference for both the R0 and R2 samples. Within cluster 2, there were 28 consumers who prefered the R8 sample. In cluster 3, 24 consumers showed a preference for both the R4 and R6 samples.

3.2. Liking patterns

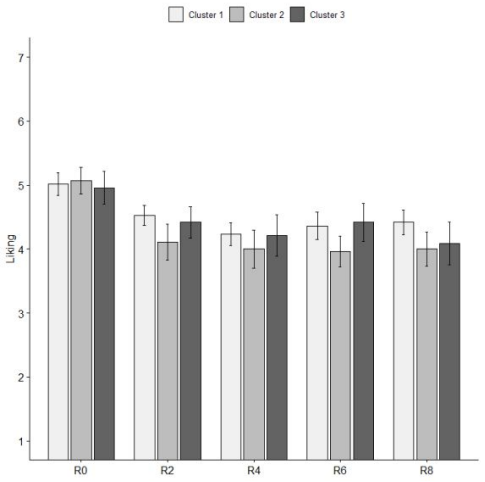

Figure 3. Liking values of snack samples for 3 clusters. Error bars represent standard error of the mean (SEM)

Figure 3 illustrates the hedonic ratings of different products categorized into three clusters. The overall liking scores for sample R0 were highest, ranging from 4.95 to 5.1 across all clusters. The ratings for other samples were considerably lower, with the highest score being for sample R2 in cluster 1 at around 4.5, and the lowest score for sample R6 in cluster 2 at around 3.95.

In cluster 1, the highest liking score was 5.0 for R0, followed by R2 at around 4.5. R8 and R6 received ratings of around 4.3 to 4.5, while R4 was the least liked with a score of approximately 4.2. In cluster 2, R0 has the highest liking rating with 5.1, followed by R2 with 4.1. R4 and R8 had similar liking ratings at around 4.0, while R6 scored the lowest value at 3.95. In cluster 3, both products R2 and R6 had the second-highest scores within the cluster at around 4.4, following R0 with a rating of 4.95. Next was R4 with a liking score of 4.25, and the least preferred sample was R8 with a score of 4.1.

3.3. Sensory profile

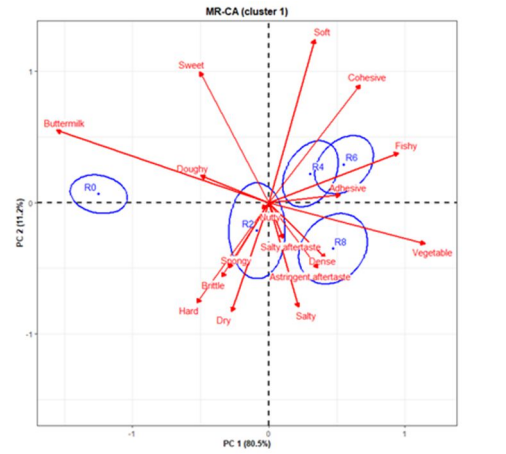

a) Cluster 1

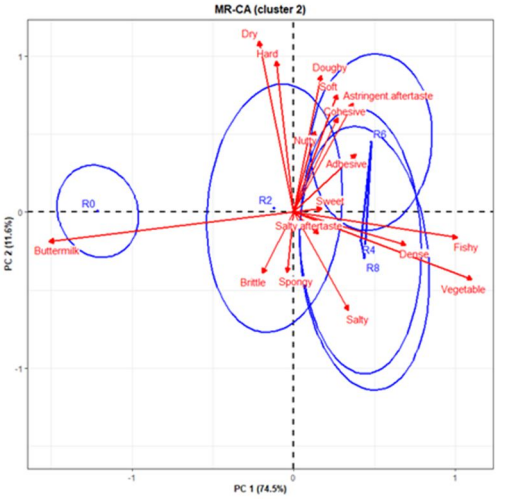

b) Cluster 2

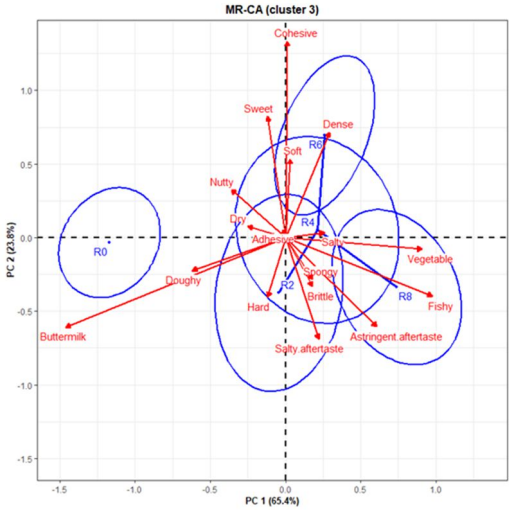

c) Cluster 3

Figure 4. MR-CA plot for three clusters

According to the MR-CA plot of descriptive analysis, Dimension 1 of the plot explained over 65% (80.5% for cluster 1, 80.5% for cluster 2 and 65.4% for cluster 3) of the total variability of sensory data based on the flavor of snack samples such as Fishy, Vegetable and Buttermilk. Dimension 2 could explain more than 10% (11.2% for cluster 1, 11.2% for cluster 2 and 23.8% for cluster 3) of total variability based on taste, texture and aftertaste such as Soft, Sweet, Cohesive, Hard, Salty and Dry.

For cluster 1: In Dimension 1, R0 was associated with Buttermilk on the far left, while R4, R6, and R8 were linked to Fishy and Vegetable on the right side. In Dimension 2, R4 and R6 were associated with Cohesive and Soft on the positive side, while R8 was related to Hard and Salty on the negative side.

For cluster 2: In Dimension 1, the blank sample R0 was associated with Buttermilk, while samples R4, R6, and R8 were characterized by Fishy and Vegetable. In Dimension 2, R6 was linked to Cohesive and Soft, while R4 and R8 were associated with Salty. However, sample R2's interpretation was difficult due to its proximity to the origin, suggesting the need for another dimension to describe it accurately.

For cluster 3: In Dimension 1, R0 was associated with Buttermilk on the far left, while R4, R6, and R8 were linked to Fishy and Vegetable on the right side. In Dimension 2, R6 was characterized by Cohesive and Dense, while R2 and R8 were associated with Hard and Salty aftertaste on the negative side.

In general, three clusters of consumers had the ability to distinguish the blank sample R0 based on the attributes Fishy and Vegetable. Cluster 1 specifically could differentiate between fortified samples with varying concentrations of spirulina. On the other hand, Cluster 2 and Cluster 3 showed a correlation in sensory properties for the fortified samples.

3.4. Drivers of liking

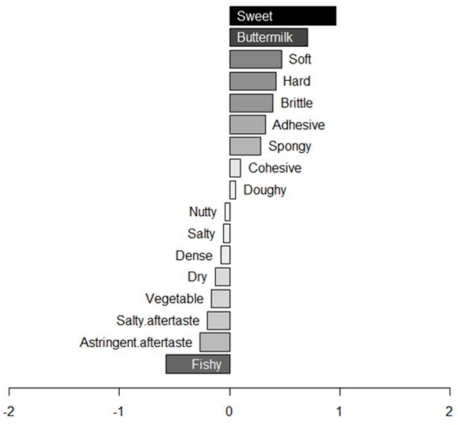

a) Cluster 1

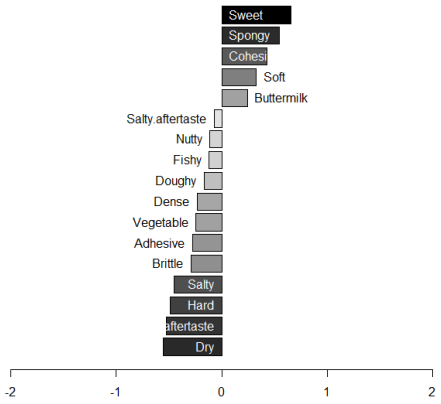

b) Cluster 2

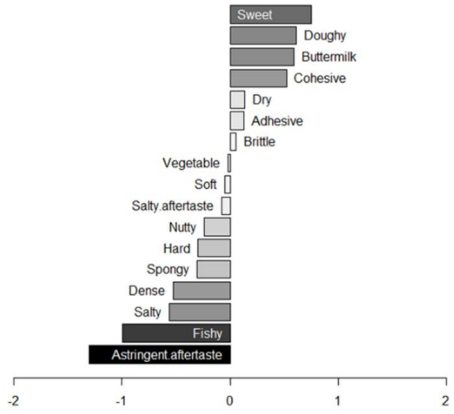

c) Cluster 3

Figure 5. PLA plot on the liking for 3 clusters

For cluster 1: the attribute Sweet had the greatest positive impact on the liking score, increasing it by around 1.0 point. Buttermilk also contributed positively, raising the liking score by 0.7 points. However, Fishy had a negative impact, reducing the liking score by 0.6 point. The remaining attributes did not have a significant effect on the liking rating for products.

For cluster 2: Dry was the attribute that had the strongest negative impact on the liking score, reducing it by 0.6 points. The astringent aftertaste, Hard, and Salty also decreased the liking score by 0.4 to 0.5 points. Conversely, Sweet and Spongy had the most positive influence, increasing the liking score by 0.7 and 0.55, respectively. The remaining attributes did not have a significant effect on the liking rating for products.

For cluster 3: Sweet was the attribute that had the strongest positive impact on the liking score, increasing it by 0.65 points. Conversely, Astringent aftertaste and Fishy had a significant negative influence, reducing the liking score by 1.0 to 1.3 points. The remaining attributes did not have a significant effect on the liking rating for products.

4. CONCLUSION

The findings suggested that spirulina have potential as an ingredient in snack products. Although the addition of spirulina led to a decrease in preference ratings, consumers did not dislike spirulina-enriched snacks. Among the four samples tested, product R2 with 2% spirulina generally received the highest liking. Different clusters of consumers had varying preferences for the other products.

In terms of flavor, the control sample R0 had a Buttermilk flavor, while spirulina snacks were perceived to have fishy and vegetable flavors, except for R2, which had an indistinct flavor. Regarding taste and texture, R6 was described as soft and cohesive, while R8 was characterized as hard and salty. R2 and R4 had different attributes assigned to them by different clusters.

The study also explored the drivers of liking different preference patterns. Sweetness positively influenced liking ratings for all three clusters of consumers, while attributes such as Fishy flavor, Dryness, and Astringent aftertaste had negative impacts. However, the degree of influence varied among the clusters.

The results from this study were collected from a small group of Gen Z students at HCMUT, Ho Chi Minh City, Vietnam. Other research was suggested to conduct sensory testing with different groups of consumers for more accuracy in sensory profiles of spirulina snacks. Moreover, further research should investigate the effects of different concentrations of spirulina on sensory properties and consumer preferences. Additionally, exploring the influence of spices and seasonings on the sensory attributes of spirulina snacks could be considered.

Acknowledgment

This research is funded by the Office for International Study Programs (OISP), Ho Chi Minh City University of Technology (HCMUT), VNUHCM under grant number **SVOISP – 2022 – KTHH – 123**. We acknowledge the support of time and facilities from HCMUT, VNUHCM for this study.

References

[1] Chaplin, K., Smith, A. (2006). *Definitions and perceptions of snacking. Appetite*, 47(2), 260. https://doi.org/10.1016/j.appet.2006.07.014

[2] Udayasree V, U. V., Dr. Manjula K, D. M., & Sowjanya M, S. M. (2012). Effect of spirulina as a nutritional supplement in malnourished children. *International Journal of Scientific Research*, 2(5), 311–312. https://doi.org/10.15373/22778179/may2013/104

[3] Nguyen, M.-N. (2022, April 29). Vietnam: Savory snacks market size 2026. Statista. Retrieved May 14, 2022, from https://www.statista.com/statistics/1199285/vietnamsavory-snacks-market-size/

[4] Bhan, M. K., Bhandari, N., and Bahl, R. (2003). Management of the Severely malnourished child: perspective from developing countries. *BMJ*

(Clinical research ed.), 326 (7381), 146–151. https://doi.org/10.1136/bmj.326.7381.1 46

[5] Srilakshmi, B. 2001. *Food Scienc*e. 2nd Edition. Delhi: New Age International Limited Publishers

[6] Colla, L. M., Oliveira Reinehr, C., Reichert, C., & Costa, J. A. (2007). Production of biomass and nutraceutical compounds by spirulina platensis under different temperature and nitrogen regimes. *Bioresource Technology*, 98(7), 1489–1493. https://doi.org/10.1016/j.biortech.2005.09.030

[7] Mazokopakis, E. E., Karefilakis, C. M., Tsartsalis, A. N., Milkas, A. N., & Ganotakis, E. S. (2008). Acute rhabdomyolysis caused by spirulina (arthrospira platensis). *Phytomedicine*, 15(6-7),

525–527. https://doi.org/10.1016/j.phymed.2008.03.003

[8] Oliveira, E. G., Duarte, J. H., Moraes, K., Crexi, V. T., & Pinto, L. A. (2010). Optimisation of spirulina platensis convective drying: Evaluation of phycocyanin loss and lipid oxidation. *International Journal of Food Science & Technology*, 45(8), 1572–1578. https://doi.org/10.1111/j.1365-2621.2010.02299.x

[9] Silva, P. C., Toledo, T., Brião, V., Bertolin, T. E., & Costa, J. A. (2021). Development of extruded snacks enriched by bioactive peptides from microalga spirulina sp.. LEB 18. *Food Bioscience*, 42, 101031. https://doi.org/10.1016/j.fbio.2021.101031

[10] Thomas, C., Symoneaux, R., Pantin-Sohier, G., Picouet, P., Maître. I. (2020). Perceptions of spirulina from French consumers of organic products.

[11] Devi, S., Varkey, A., Sheshshayee, M. S., Preston, T., & Kurpad, A. V. (2018). Measurement of protein digestibility in humans by a dual-tracer method. *The American Journal of Clinical Nutrition*, 107(6), 984–991. https://doi.org/10.1093/ajcn/nqy062

[12] Şahin, O. I. (2020). Functional and sensorial properties of cookies enriched with spirulina and Dunaliella biomass. *Journal of Food Science and Technology*, 57(10), 3639–3646. https://doi.org/10.1007/s13197-020-04396-4

[13] Næs, T., Brockhoff, P. B., & Tomić Oliver. (2010). Statistics for sensory and consumer science. Wiley.

[14] Washburn, D. A., Smith, J. D., Taglialatela, L. A. (2005). Individual differences in metacognitive responsiveness: cognitive and personality correlates. *J. Gen. Psychol*. 132(4), 446–461.

[15] Mahieu, B., Schlich, P., Visalli, M., & Cardot, H. (2021). A multiple-response chi-square framework for the analysis of Free-Comment and Check-All-That-Apply data. Food Quality and Preference, 93. https://doi.org/10.1016/j.foodqual.2021.104256

[16] Meyners, M. (2016). Testing for differences between impact of attributes in penalty-lift analysis. Food Quality and Preference, 47, 29–33. https://doi.org/10.1016/j.foodqual.2014.11.001

[17] Novel techniques. (2008). *Journal of Neurochemistry*, 88, 72–72. https://doi.org/10.1046/j.1474-1644.2003.2314p28_01.x

FABRICATION OF CO_2 – ACTIVATED POROUS CARBON AEROGEL FROM DURIAN RIND FOR ENERGY STORAGE

(CHẾ TẠO VẬT LIỆU HOẠT HÓA CO_2 – CARBON AEROGEL TỪ VỎ SẦU RIÊNG ỨNG DỤNG TRONG LƯU TRỮ NĂNG LƯỢNG)

Bui Dang Dang Khoa[1,2,3], Long Hoang Le[1,2,3], Duy Khac Anh Nguyen[1,2,3], Phung K. Le[1,2,3,*]

[1] Faculty of Chemical Engineering, Ho Chi Minh City University of Technology (HCMUT), 268 Ly Thuong Kiet Street, District 10, Ho Chi Minh City, Vietnam
[2] Office for International Study Programs, Ho Chi Minh City University of Technology (HCMUT), 268 Ly Thuong Kiet Street, District 10, Ho Chi Minh City, Vietnam
[3] Vietnam National University Ho Chi Minh City, Linh Trung Ward, Thu Duc City, Ho Chi Minh City, Vietnam
[*] Corresponding author: phungle@hcmut.edu.vn

Abstract

Significant interest in green manufacturing of biomass-based carbon aerogel for energy storage has been generated in the context of sustainable development. A previous investigation involved the synthesis of durian rind carbon aerogel (DCA) at a temperature of 800 degrees Celsius, without activation. This process yielded a notably high specific capacitance of 591 F/g in a two-electrode system. Further exploration into the pyrolysis and activation parameters of this material is warranted. In this study, activated durian rind-derived carbon aerogel (ACA) materials with improved surface structures were generated using a straightforward manufacturing process. This method consisted of hydrothermal, freeze-drying, and pyrolysis at 900°C, followed by CO_2 activation. The results of X-ray diffraction (XRD), Fourier-transform infrared spectroscopy (FTIR), and Thermogravimetric analysis (TGA) indicate how the conditions of the synthesis affect the properties of the materials that are formed. Consequently, the ACA material demonstrates certain fascinating qualities, including a low density (0.006 g/cm^3), a high porosity (more than 98%), and an abundance of micro-meso porous structures. In addition, the electrochemical characteristics of the as-prepared ACA materials were evaluated by employing the methodologies of cyclic voltammetry (CV), galvanostatic charge-discharge curve (GCD), and electrochemical impedance spectroscopy (EIS). The electrochemical properties of the produced materials were examined in a three-electrode setup using Ag/AgCl as a reference. The results showed a remarkable electrochemical performance at a current density of 0.5 and 1 A/g within a potential window of 1.0 to 0 V in a 0.5 M KOH solution. This was achieved in a 0.5 M solution of potassium hydroxide. The findings indicated a potential and sustainable pathway for using a vast source of biowaste to fabricate a multifunctional material for energy storage via a green production strategy without harmful chemicals.

Keywords: *supercapacitors, energy storage, carbon aerogel, biomass-derived carbon aerogel*

1. INTRODUCTION

Driven by such need for power storage, rectification, transport, and supply on various scales, sustained and extensive research and exploration have been conducted, and a number of electrical energy storage (EES) technologies have been developed so far; some are in use in our daily lives, such as batteries and fuel cells, and others are more for industrial applications, including pumped hydro, flywheel, compressed air, superconducting magnetic, and supercapacitors.

Of these EES technologies, batteries have been widely used on various scales and have been continuously studied due to their outstanding performance. Based on the specific battery chemistry, they can be rechargeable or non-rechargeable. However, there are certain areas where batteries revealed shortcomings or failed to meet the needs, including: 1) Low power density: This issue has severely hindered applications where high-power discharge and/or recharge rates are required. 2) Heat generation: The redox reactions in batteries may lead to Joule heating and thermochemical heating during their operation. Such heat, if not dissipated, will effectively result in overheating, thermal runaway, and even fire. 3) Limited cycle life: The cycle lives of batteries are normally limited due to the lack of fully reversible redox reactions during the discharge and recharge process. Because of the issues listed above, batteries alone are unable to provide the full solution for electricity storage [1]. A durable and safe electricity storage device, with high power and/or energy performance, will undoubtedly transform the landscape of electric energy generation, distribution, and utility.

Supercapacitors often referred to as ultracapacitors or electrochemical capacitors, demonstrate outstanding power performance, excellent reversibility, very long cycle life, simple mode of operation, and ease of integration into electronics. In addition, they generate less thermochemical heat because of the simpler charge storage mechanisms associated [2]. Therefore, they have been widely used in consumer electronics, memory backup systems, and industrial power and energy management and will be found in more niche markets in the near future. The supercapacitor, also known as an electrochemical capacitor, stores energy primarily through ion adsorption (electrical double-layer capacitance, EDLC) or reversible Faradic reactions (pseudocapacitors) on the electrode surfaces. While supercapacitors with a dominating pseudocapacitance made of electroactive materials such as conducting polymers or metal oxides can achieve higher faradaic capacitive performance than the EDLC, they frequently exhibit poor long-term cycling stability [3].

Carbon aerogel (CA) has a three-dimensional (3D) structure with ideal properties, including low density, high porosity, a large specific surface area, and hydrophobicity on the surface [4]. In addition, the preparation of CA is mainly based on chemical methods, using expensive inorganic/organic precursors like resorcinol-formaldehyde, cresol formaldehyde, melamine-formaldehyde, and graphene/graphene oxides. These procedures, however, involve the use of toxic chemicals and sophisticated processes. Fortunately, recent research indicates a very efficient approach for the green synthesis of CA by using hydrothermal carbonization (HTC), which encompasses both hydrothermal and post-pyrolysis processes [5]. HTC can be defined as the combined dehydration and decarboxylation of fuel to raise its carbon content with the aim of achieving a higher calorific value. It is realized by applying elevated temperatures (180–220°C) to biomass in a suspension with water under saturated pressure for several hours. With this conversion process, a lignite-like, easy-to-handle fuel with well-defined properties can be created from biomass residues, even with high moisture content. Thus it may contribute to a wider application of biomass for energetic purposes [6]. Although hydrothermal carbonization has been known for nearly a century, it has received little attention in current biomass conversion research.

Durian is a fruit which is famous all over the world, especially in Southeast Asia as its name is “King of the fruits”. Durian is popular for its special flavor and high-quality nutrients which could afford health benefits for the human body [7]. However, less than half part of the entire durian is edible, while the other parts (rind and seeds) are treated as food waste in the durian industry. Durian residues (rind and seeds) are usually used in landfills or burned, which poses a serious problem to the environment, and in the meanwhile is also a waste of a natural resource. Durian rind is comprised of 31.6% cellulose, 15.5% hemicellulose, and 10.9% lignin in dried durian rind [8].

In this work, a green synthesis route was approached for the first time the direct conversion of Durian rind to activated durian rind-derived carbon aerogel (ACA) for fabrication of supercapacitor’s electrodes via hydrothermal treatment, freeze-drying, and carbonization under CO_2 atmosphere. The characteristics of the obtained materials were studied by X-ray diffraction (XRD), Fourier-transform infrared spectroscopy (FTIR), and thermogravimetric analysis (TGA). The electrochemical properties of the as-prepared ACA and CA materials were measured in three-electrode system via cyclic voltammetry (CV), galvanostatic charge-discharge curve (GCD), and electrochemical impedance spectroscopy (EIS).

2. EXPERIMENTAL METHODS

2.1. Materials and Chemicals

Waste durian rind was collected in a single instance for all subsequent experiments from the local market, Ho Chi Minh City, Vietnam. Absolute ethanol (C_2H_5OH), Acetylene black (AB), and Nafion were purchased from Xilong Scientific (China),

2.2. Preparation of CA and ACA

The durian rind was peeled off the exocarp and mesocarp [9]. Then they were soaked in ethanol for 24 hours and washed with distilled water to eliminate the impurities. The pre-treated durian rind endocarp was then sealed inside a Teflon-lined stainless-steel autoclave and placed into an oven for hydrothermal treatment at 180°C for 10 hours without the addition of any chemicals. The obtained hydrochar was immersed in distilled water for one day to remove the impurities and oils remaining. After that, the aerogel was obtained by freezing the hydrochar at -50°C and freeze-drying by Toption TPV-50F. To prepare ACA, the aerogel was carbonized under a nitrogen (N_2) atmosphere in a tube furnace, heated from 30°C to 900°C at a heating rate of 10°C.min^{-1}, maintained at 900°C for 1 h. The N_2 input was then turned off and the system was flushed with CO_2. The furnace was maintained at 900°C under a CO_2 atmosphere for 2 h. The CA was obtained with the same procedure as ACA without using CO_2 atmosphere.

2.3. Characterization

The presence of crystal structures was characterized by X-ray diffraction (XRD) from 2θ = 5–80° (Rigaku, D/max 2200). Functional groups of the durian rind, hydrochar, CA, and ACA were verified by Fourier-transform infrared (FTIR) spectroscopy (Bruker TENSOR-27, Germany). The thermal behavior of hydrochar was evaluated on thermogravimetric analysis and differential scanning calorimetry (TGA/DSC) instrument METTLER TOLEDO.

2.4. Electrochemical measurement

Electrochemical measurements were performed on an electrochemical workstation (CHI660C, Chen Hua, Shanghai) in a three-electrode system in 0.5M KOH electrolyte. To prepare the working electrode, ACA material, and AB were mixed in ethanol with a mass ratio of 9:1, then 5 µL of the prepared mixture with the concentration of 10 mg/mL was drop-casted onto a glassy carbon electrode (GCE) (diameter of 3 mm) and dried in an oven at 100 ºC. Platinum foil and a Ag/AgCl served as the counter and reference electrodes, respectively. The active material was 0.7 mg/cm^2 on the working electrode. Cyclic voltammetry (CV). Galvanostatic charge/discharge (GCD), and Electrochemical impedance spectroscopy (EIS) analysis occurred to characterize the electrochemical properties of the samples. All the experiments were observed at the voltage range of −1.0 to 0 V. The CV curves were tested by varying the scan rate from 10 to 200 mV/s. GCD measurements were obtained under 0.5 and 1.0 A/g. EIS analysis was conducted at the open-circuit voltage in the frequency range of 0.01 Hz–10 kHz. In the three-electrode system, the specific capacitances (Csp, F/g) calculated from the experimental data of CV and GCD analysis were presented in Equations (1) and (2), respectively:

$C_{sp} = \frac{Q}{m\Delta V}$	(1)
$C_{sp} = \frac{I}{m}\frac{\Delta t}{\Delta V}$	(2)

where I (A) is the current during discharge, m (g) is the mass of active material, Δt (s) is the time during discharge, ΔV (V) is the voltage window, and Q is stored charge in coulombs (equals half the integrated area of the corresponding CV curve).

3. RESULTS AND DISCUSSION

3.1. Characteristics

To investigate the chemical functional groups of durian rind endocarp, hydrochar, CA-900, and ACA-900 the FTIR spectroscopy was carried out, as presented in Fig. 1. For hydrochar, a broad band from 3300 to 3400 cm^{-1} is related to −O−H stretching vibration [10]. Other peaks at 1065, 1240, and 1750 cm^{-1} indicate oxygen-functional group vibrational peak of C−O, epoxy group, and C=O stretching from carbonyl or acetyl groups in hemicellulose, respectively. Meanwhile, peaks at 1570 and 1620 cm^{-1} are attributed to the C=C stretching. Hydrochar also had the vibration of −C−H alkane stretching at around 2920 cm^{-1} [11]. These aforementioned peaks indicate the presence of the remaining cellulose and hemicellulose in the raw cucumber after hydrothermal treatment. The FTIR spectra from ACA-900 show that some of these oxygen-containing functional groups (−O−H, C=O, and C−O) were reduced or disappeared due to the pyrolysis process and CO_2 activation treatment [12]. In addition, it can be easily noticed that at the same pyrolysis temperature, the ACA-900 exhibits more appearance of oxygen functional groups such as hydroxyl, carboxyl, and carbonyl functional groups, indicating the interference of the CO_2 during the pyrolysis process [13].

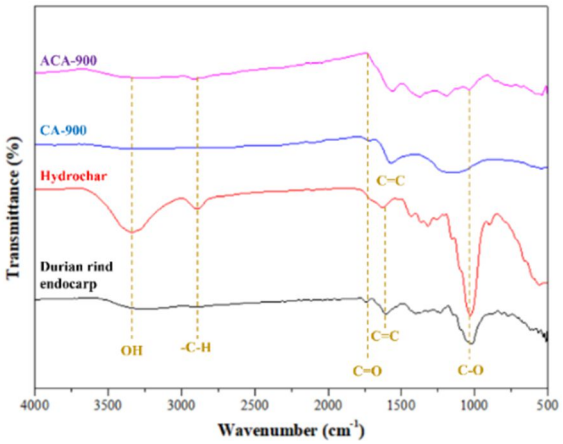

Figure 1. FTIR spectra of durian rind endocarp, hydrochar, CA-900, and ACA-900

The structure of the synthesized materials was investigated by XRD patterns, as presented in Fig. 2. XRD pattern of durian rind endocarp illustrates two low-intensity broad peaks at 22º and 55º, indicating the high amorphous structure of the durian rind's endocarp. After the hydrothermal process, the hydrochar demonstrates cellulose characteristic peaks at 16, 22, and 35º assigned to the overlapping of ($\bar{1}$10)/(110), (200), and (004) planes, respectively. These diffraction peaks imply the orderly crystal structure of cellulose [14, 15]. However, after the carbonization and activation process, ACA shows the structure of graphite carbon by presenting two diffraction peaks at 23º (002) and 44º (100) [1, 16, 17]. Notably, the peak located at 2θ = 11º (001) introduces the graphene oxide-like structures [18].

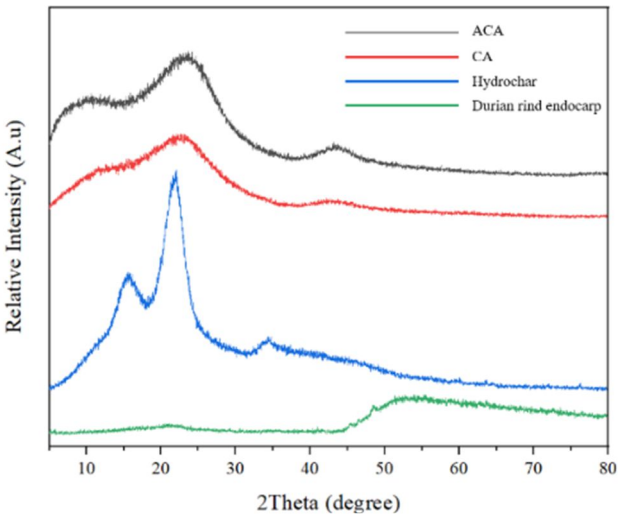

Figure 2. XRD patterns of the materials

There are three stages in the pyrolysis process in nitrogen. It is obvious in Fig. 3. that at a range between 40 – 80°C the mass of hydrochar has been slowly decreased, corresponding to the first stage. The weight loss in this stage can be attributed to the evaporation of water. Stage II –volatile matter release, during this stage the structural changes start to depolymerize hemicellulose and cellulose. As seen on the graph, about 50% of weight has been removed between the range of temperature 250 - 350°C. Stage III corresponds with char oxidation, this stage occurred lignin degradation and carbonization of aerogel between 350 - 600°C. DSC was used to measure the heat flow behavior during the combustion process (with a constant temperature increase). Observations revealed that the temperature of hydrothermal carbonization changed the heat flow dynamics of hydrochar during the combustion process. Hydrochar generated greater heat flow (HF) combustion than precursor biomass [19]. The increase in heat released during the combustion of hydrochar is related to its carbonization temperature.

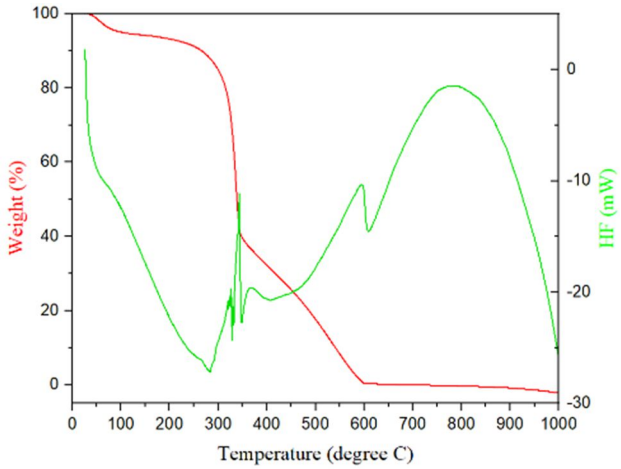

Figure 3. TG and DSC curves of hydrochar at a heating rate of 10°C/min under 10 ml/min N2 atmosphere

3.2. Electrochemical performance

The CV profiles of ACA and CA at 900ºC at a scan rate of 200 mV/s are displayed in Fig. 4(a) and the CV curves of ACA-900 at different scan rates are exhibited in Fig. 4(b). It can be observed unambiguously that the CV curves of the two samples all present quasi-rectangular shape, which indicates that materials have the characteristics of ideal electrochemical double-layer capacitance instead of pseudo-capacitance owing to the redox reaction of oxygen heteroatoms [20]. The CV curves' closed area can reflect the samples' specific capacitance. Contrary to the activation process, the CA-900 exhibited the smallest area of the CV curve, which corresponded to the material's poor capacitance without activation. The ACA-900 sample with the largest encircled CV area was the one that was activated, indicating that it possessed the most significant capacitance. Moreover, with the increase of scanning rate, the CV curves of ACA-900 expand, but even at a high scanning rate of 200 mV/s, a good symmetric rectangle of CV curve maintains, which proves the fast transfer of ions in the carbon electrode along with small diffusion resistance. In addition, the specific capacitances of ACA-900 at the scan rates of 10, 50, 100, and 200 were determined as 195.25, 165.28, 155.33, and 137.93 F/g, respectively (Fig. 4(c)). Per the inflation in scan rate from 10 to 200 mV/s, the specific capacitance tended to drop down from 195.25 to 137.93 F/g, which was caused by the inadequate time for the electrolyte to diffuse into the porous structure of the material under the rapid scan rate [21]. Interestingly, only a small loss of capacitance was recorded according to the capacitance retention of 70.46 % (at 200 mV/s), indicating the stability of the electrode during the electrochemical performance [22].

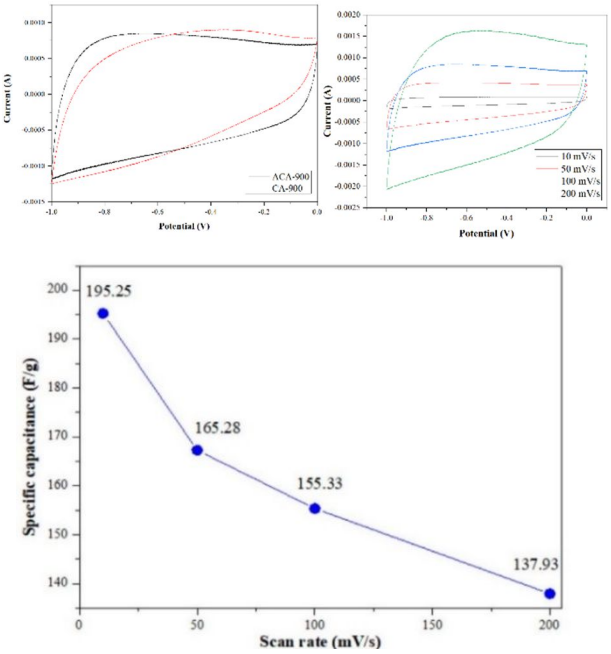

Figure 4. (a) CV curves of ACA-900 and CA-900 at 200 mV/s, (b) CV curves of ACA-900 at different scan rates, and (c) Specific capacitance of ACA-900 at different scan rates

To evaluate the charge/discharge performance and specific capacitance of the materials, a GCD test was conducted for both CA-900 and ACA-900 at 1 A/g under a potential voltage from -1.0 to 0.0 V, as presented in Fig. 5(a). Generally, the shape of the GCD curve presents that all the tested materials exhibited a nearly symmetric triangle even at the high current density, indicating high reversibility between the charge/discharge process [23]. Consequently, the charge-discharge time of ACA-900 (Fig. 5. (a)) was longer than that of CA-900. It indicates that ACA-900 can be charged with more electrolyte ions than others, which means it has higher specific capacitance. The gravimetric specific capacitance of ACA-900 at different current densities calculated from the GCD curves are given in Fig. 5. (b). The ACA-900 delivers high specific capacitances of 213 and 175 F/g at 0.5 and 1.0 A/g, respectively. The specific capacitance of ACA-900 decreased with the increase of current density (from 0.5 to 1.0 A/g), which was concerned with the limited transportation of the electrolyte ions on the electrode surface during fast charging [24].

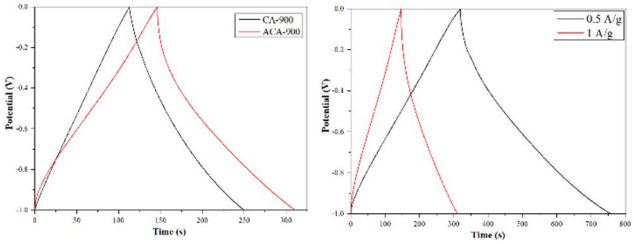

Figure 5. (a) GCD curves of CA-900 and ACA-900 at current density of 1 A/g, (d) GCD curves of ACA-900 at different current densities

On a complex plane, a Nyquist plot displays the imaginary and actual cell impedance components. It has been reported that a Nyquist plot obtained from an EIS analysis typically consists of two major parts: a semicircle in the high-frequency region and a straight line in the low-frequency region, with the former revealing the charge-transfer resistance and the latter indicating the diffusion-limited process [25]. According to Fig. 6, the semicircles of all prepared materials were barely discernible, indicating a low charge transfer resistance and non-faradaic charge transfer process [26]. Among the two materials, the ACA-900 exhibited the most vertical line in the low-frequency region, indicating the most pronounced capacitive pattern with the lowest resistance to the electron transport process.

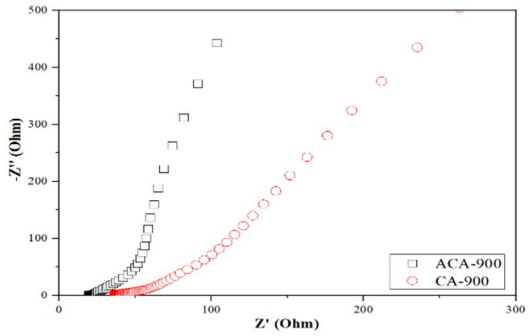

Figure 6. The Nyquist plots of ACA-900 and CA-900

4. CONCLUSION

In conclusion, the activated durian rind endocarp-derived carbon aerogel (ACA) materials were successfully fabricated for the first time by a facile and green synthesis route, including hydrothermal, freeze-drying, and pyrolysis in CO_2 condition for energy storage application. Consequently, the ACA material demonstrates certain fascinating qualities, including a low density (0.006 g/cm^3), a high porosity (more than 98 %), and an abundance of micro-meso porous structures. The ACA-900 compound exhibits remarkable electrochemical characteristics, notably demonstrating excellent behaviour as an electric double-layer capacitor (EDLC) with stable semi-rectangular CV curves at varying scan rates. Additionally, it highlights a specific capacitance of 213 F/g at a current density of 0.5 A/g, and low charge/transfer resistance. These properties surpass those of the reference sample, CA-900, which was pyrolyzed at the same temperature but in a N_2 atmosphere. The ACA-900 electrode exhibited a minimal decrease in capacitance retention ratio, measuring at 70.46%, upon increasing the scan rate to 200 mV/s. The discoveries of this research demonstrate a promising and enduring approach for utilising a significant amount of biowaste to synthesise an adaptable material for energy storage, employing an environmentally friendly production methodology that avoids the use of hazardous chemicals.

Acknowledgement

This research is funded by the Office for International Study Programs (OISP), Ho Chi Minh City University of Technology (HCMUT), VNUHCM under grant number **SVOISP-2022-KTHH-121**. We acknowledge the support of time and facilities from HCMUT, VNUHCM for this study.

References

[1] A. R. Dehghani-Sanij, E. Tharumalingam, M. B. Dusseault, and R. Fraser, "Study of energy storage systems and environmental challenges of batteries," *Renewable and Sustainable Energy Reviews*, vol. 104, pp. 192–208, Apr. 2019, doi: 10.1016/j.rser.2019.01.023.

[2] B. C. Kim, J.-Y. Hong, G. G. Wallace, and H. S. Park, "Recent Progress in Flexible Electrochemical Capacitors: Electrode Materials, Device Configuration, and Functions," *Adv Energy Mater*, vol. 5, no. 22, p. 1500959, Nov. 2015, doi: 10.1002/aenm.201500959.

[3] D. Qu and H. Shi, "Studies of activated carbons used in double-layer capacitors," *J Power Sources*, vol. 74, no. 1, pp. 99–107, Jul. 1998, doi: 10.1016/S0378-7753(98)00038-X.

[4] H. Liu, B. Geng, Y. Chen, and H. Wang, "Review on the Aerogel-Type Oil Sorbents Derived from Nanocellulose," *ACS Sustain Chem Eng*, vol. 5, no. 1, pp. 49–66, Jan. 2017, doi: 10.1021/acssuschemeng.6b02301.

[5] R. B. Marichi *et al.*, "Direct hydrothermal treatment of sugarcane juice for 3D oxygen-rich carbon Aerogel/NiCo2O4 based supercapacitor," *Mater Chem Phys*, vol. 239, p. 121957, Jan. 2020, doi: 10.1016/j.matchemphys.2019.121957.

[6] A. Funke and F. Ziegler, "Hydrothermal carbonization of biomass: A summary and discussion of chemical mechanisms for process engineering," *Biofuels, Bioproducts and Biorefining*, vol. 4, no. 2, pp. 160–177, Mar. 2010, doi: 10.1002/bbb.198.

[7] N. A. Husin, S. Rahman, R. Karunakaran, and S. J. Bhore, "A review on the nutritional, medicinal, molecular and genome attributes of Durian (Durio zibethinus L.), the King of fruits in Malaysia," *Bioinformation*, vol. 14, no. 06, pp. 265–270, Jun. 2018, doi: 10.6026/97320630014265.

[8]X. Cui, J. Lee, K. R. Ng, and W. N. Chen, "Food Waste Durian Rind-Derived Cellulose Organohydrogels: Toward Anti-Freezing and Antimicrobial Wound Dressing," *ACS Sustain Chem Eng*, vol. 9, no. 3, pp. 1304–1312, Jan. 2021, doi: 10.1021/acssuschemeng.0c07705.

[9] N. S. Ha, G. Lu, D. Shu, and T. X. Yu, "Mechanical properties and energy absorption characteristics of tropical fruit durian (Durio zibethinus)," *J Mech Behav Biomed Mater*, vol. 104, p. 103603, Apr. 2020, doi: 10.1016/j.jmbbm.2019.103603.

[10] D. Li, J. Huang, L. Huang, S. Tan, and T. Liu, "High-Performance Three-Dimensional Aerogel Based on Hydrothermal Pomelo Peel and Reduced Graphene Oxide as an Efficient Adsorbent for Water/Oil Separation," *Langmuir*, vol. 37, no. 4, pp. 1521–1530, Feb. 2021, doi: 10.1021/acs.langmuir.0c03062.

[11] Y. Ding *et al.*, "Influence of process water recirculation on hydrothermal carbonization of rice husk at different temperatures," *J Environ Chem Eng*, vol. 11, no. 2, p. 109364, Apr. 2023, doi: 10.1016/j.jece.2023.109364.

[12] R. Hoseinzadeh Hesas, W. M. A. Wan Daud, J. N. Sahu, and A. Arami-Niya, "The effects of a microwave heating method on the production of activated carbon from agricultural waste: A review," *J Anal Appl Pyrolysis*, vol. 100, pp. 1–11, Mar. 2013, doi: 10.1016/j.jaap.2012.12.019.

[13] K. Phothong, C. Tangsathitkulchai, and P. Lawtae, "The Analysis of Pore Development and Formation of Surface Functional Groups in Bamboo-Based Activated Carbon during CO2 Activation," *Molecules*, vol. 26, no. 18, p. 5641, Sep. 2021, doi: 10.3390/molecules26185641.

[14] B. Zhang, J. Azuma, and H. Uyama, "Preparation and characterization of a transparent amorphous cellulose film," *RSC Adv*, vol. 5, no. 4, pp. 2900–2907, 2015, doi: 10.1039/C4RA14090G.

[15] F. Liu, R. Yu, and M. Guo, "Hydrothermal carbonization of forestry residues: influence of reaction temperature on holocellulose-derived hydrochar properties," *J Mater Sci*, vol. 52, no. 3, pp. 1736–1746, Feb. 2017, doi: 10.1007/s10853-016-0465-8.

[16] K. Lee, L. Shabnam, S. N. Faisal, V. C. Hoang, and V. G. Gomes, "Aerogel from fruit biowaste produces ultracapacitors with high energy density and stability," *J Energy Storage*, vol. 27, p. 101152, Feb. 2020, doi: 10.1016/j.est.2019.101152.

[17] L. E, W. Li, C. Ma, Z. Xu, and S. Liu, "CO2-activated porous self-templated N-doped carbon aerogel derived from banana for high-performance supercapacitors," *Appl Surf Sci*, vol. 457, pp. 477–486, Nov. 2018, doi: 10.1016/j.apsusc.2018.07.001.

[18] A. Gopalakrishnan and S. Badhulika, "Ultrathin graphene-like 2D porous carbon nanosheets and its excellent capacitance retention for supercapacitor," *Journal of Industrial and Engineering Chemistry*, vol. 68, pp. 257–266, Dec. 2018, doi: 10.1016/j.jiec.2018.07.052.

[19] M. Santos Santana, R. Pereira Alves, W. M. da Silva Borges, E. Francisquini, and M. C. Guerreiro, "Hydrochar production from defective coffee beans by hydrothermal carbonization," *Bioresour Technol*, vol. 300, p. 122653, Mar. 2020, doi: 10.1016/j.biortech.2019.122653.

[20] C. Costentin, T. R. Porter, and J.-M. Savéant, "How Do Pseudocapacitors Store Energy? Theoretical Analysis and Experimental Illustration," *ACS Appl Mater Interfaces*, vol. 9, no. 10, pp. 8649–8658, Mar. 2017, doi: 10.1021/acsami.6b14100.

[21] W. Gu, M. Sevilla, A. Magasinski, A. B. Fuertes, and G. Yushin, "Sulfur-containing activated carbons with greatly reduced content of bottle neck pores for double-layer capacitors: a case study for pseudocapacitance detection," *Energy & Environmental Science*, vol. 6, no. 8, pp. 2465–2476, 2013.

[22] X. Wu, B. Huang, R. Lv, Q. Wang, and Y. Wang, "Highly flexible and low capacitance loss supercapacitor electrode based on hybridizing decentralized conjugated polymer chains with MXene," *Chemical Engineering Journal*, vol. 378, p. 122246, Dec. 2019, doi: 10.1016/j.cej.2019.122246.

[23] X. Xu, J. Yang, X. Zhou, S. Jiang, W. Chen, and Z. Liu, "Highly crumpled graphene-like material as compression-resistant electrode material for high energy-power density supercapacitor," *Chemical Engineering Journal*, vol. 397, p. 125525, Oct. 2020, doi: 10.1016/j.cej.2020.125525.

[24] A. K. Mondal *et al.*, "Nitrogen-Doped Porous Carbon Nanosheets from Eco-Friendly Eucalyptus Leaves as High Performance Electrode Materials for Supercapacitors and Lithium Ion Batteries," *Chemistry – A European Journal*, vol. 23, no. 15, pp. 3683–3690, Mar. 2017, doi: 10.1002/chem.201605019.

[25] S. Xian-Zhong, H. Bo, Z. Xiong, Z. Da-Cheng, Z. Hai-Tao, and M. Yan-Wei, "Experimental Investigation of Electrochemical Impedance Spectroscopy of Electrical Double Layer Capacitor," *Acta Physico-Chimica Sinica*, vol. 30, no. 11, pp. 2071–2076, 2014, doi: 10.3866/PKU.WHXB201408292.

[26] Z. Zou, W. Zhou, Y. Zhang, H. Yu, C. Hu, and W. Xiao, "High-performance flexible all-solid-state supercapacitor constructed by free-standing cellulose/reduced graphene oxide/silver nanoparticles composite film," *Chemical Engineering Journal*, vol. 357, pp. 45–55, Feb. 2019, doi: 10.1016/j.cej.2018.09.143.

PREPARATION OF SOLID LIPID NANOENCAPSULATION OF EXTRACTS FROM SPINACH (*Spinacia oleracea L.*) LEAVES

(NGHIÊN CỨU TẠO HỆ NANO BAO BỌC CHIẾT XUẤT TỪ LÁ CẢI BÓ XÔI (*Spinacia oleracea L.*))

Bao Quyen[1,2], Le Thi Hong Nhan[1,3,*]

[1] Faculty of Environment and Natural Resources, Ho Chi Minh City University of Technology (HCMUT), 268 Ly Thuong Kiet Street, District 10, Ho Chi Minh City, Vietnam
[2] Office for International Study Programs, Ho Chi Minh City University of Technology (HCMUT), 268 Ly Thuong Kiet Street, District 10, Ho Chi Minh City, Vietnam
[3] Vietnam National University Ho Chi Minh City, Linh Trung Ward, Thu Duc City, Ho Chi Minh City, Vietnam
[*] Corresponding author: lthnhan@hcmut.edu.vn

Abstract

Spinach (*Spinacia oleracea* L.) was developed and demonstrated to be rich in polyphenols which have been recognized and proven to have decent antioxidant capacity, contributing its role to many products and applications. The goal of this study was to evaluate the extraction conditions of Spinach leaves (originated from Da Lat, Viet Nam) and enhance the chemical stability of the Spinach leaf extract. The advisable extraction conditions were using Ethanol 98° as a solvent with an extraction temperature of 60-70°C. The condensed extracts obtained through rotary evaporation possessed the total phenolic content of 39.88 mg GAE/g absolute dry weight and high antioxidant capacity with an IC50 value of 308.9 mg/L (compared with the liquid extract that of 215.2 mg/L). After that, the solid extracts of Spinacia oleracea L. were encapsulated with the support of a solid lipid (Emulgade SE-PF from BASF Company) together with Polysorbate 80 (Tween 80) to form a solid lipid nanoparticle (SLN) dispersion in water through high-speed homogenization. The dispersion had a median size of 126 nm (by Laser Diffraction Analysis) and the shape of these particles appeared to be spherical (by Scanning electron microscopy). The stability studies of the SLN dispersion showed significantly increased protecting ability compared to the non-encapsulated extract, regarding the stability in polyphenols and antioxidant capacity content. Furthermore, the lower temperature, the better protecting performance of the system. Ultra-violet radiation from light also had no effect on the encapsulated extracts. In conclusion, this study's outcomes proved that *Spinacia oleracea* L. can be utilized as a novel source of natural polyphenols which provides applications as an antioxidant, and with regard to keeping natural extracts effective and stable, solid lipid nanoencapsulation is one of the promising approaches.

Keywords: *spinach, natural active compound, polyphenols, antioxidant, solid lipid nanoencapsulation*

1. INTRODUCTION

The annual plant species known as spinach (*Spinacia oleracea* L.) is a member of the Chenopodiaceae family. The genus was first found in South-West Asia, and S. oleracea was likely transported to Spain by Arabs in the 14th century, where it spread to other nations by the 16th [1]. Spinach is a rich source of flavonoids especially patuletin, spinacetin, jaceidin, and flavones [2, 3]. There have also been reports of the existence of luteolin, isorhamnetin, kampherol, quercetin [4]. β-carotene, vitamins of the B group, and ascorbic acid are also abundant in spinach leaves [1]. Additionally, spinach is a great source of carotenoids like lutein, zeaxanthin, and chlorophyll [5, 6]. Among mentioned compounds, polyphenols derivatives have been discovered to possess lots of benefits: antioxidant activity [7], anti – aging [8], oral health [9, 10], anticancer capacity [7] and others.

Natural active ingredients possess outstanding advantages such as diversity of biological activity, low toxicity, few side effects and good therapeutic potential, especially when used in the form of active ingredient clusters from plant extracts for their synergistic effects. However, some typical characteristics such as poor aqueous solubility, low permeability as well as poor chemical stability, high temperature, light and oxidant sensitivities are considered the biggest obstacles in the development of natural active ingredients in clinical or pharmaceutical treatment or self – care products.

Therefore, the challenge when using natural products in the treatment of diseases is to increase the solubility, permeability and minimize the degradation of biologically active substances. Nanoencapsulation is one of the state-of-the-art technologies to ensure and improve the quality and efficiency of bioactive ingredients.

Spinach leaves were found to have various beneficial and potential actives, not only have been used as a source of nutrients, this kind of plant has been getting attention for other further applications related to cosmetics or drug ingredients. However, research about Spinach in Vietnam has been still insignificant, products that utilized active ingredients deprived of Spinach were not popular and widely used. In order not to waste the potential of probably abundant good substances, this research was initiated to conduct a survey, evaluation and availability of extraction process as well as the amounts of actives in Spinach leaves (originated from Da Lat, Viet Nam) for further applications, then prepare the solid lipid nanoencapsulation of extracts and further assessments. The solid lipid selected was Emulage SE-PF, a self-emulsifier suitable for the creation of oil-in-water creams and lotions for the cosmetic and pharmaceutical industries. High-speed homogenization technique was the chosen preparation method for nanoencapsulation system.

2. METHODS AND IMPLEMENTATION

2.1. Materials

Spinach plants were the main material of this research, which were planted and harvested at VietGAP garden located in Da Lat province, Viet Nam. This place is well-known for its cool weather, which is extremely suitable to grow Spinach plants because Spinach is very fond of cool climates. After purchase, Spinach leaves were pretreated and preserved for later use. Emulgade SE-PF™ was provided by BASF company, Viet Nam. All the organic solvents used in this study were of analytical grade.

2.2. Methods

2.2.1. Raw material pretreatment

Fresh Spinach plants were purchased, rotten and decayed leaves were eliminated, and then repeatedly washed under RO water until dirtless, left drying at room temperature to measure the moisture content of fresh leaves. After being washed carefully, fresh leaves were dried in a simple dry chamber at temperature of approximately 40 – 50°C until the moisture content left was under 10%. The ground powder of dried leaves was stored in sealed plastic bags with 2 – 3 silica gel desiccant packs to prevent the power from absorbing moisture and in darkness to avoid light, at room temperature.

2.2.2. Extraction conditions evaluation

For the dried Spinach leaf powder, the ratio of material mass and solvent volume was 1:100 (g/mL), extraction duration was 1 hour. The residue powder was kept to continue the second extraction, the procedure for the second and third extraction was the same as the first one.

A total of 3 systems of conditions were conducted, which were: EtOH – 40-50 – 1st/2nd/3rd; EtOH – 60-70 – 1st/2nd/3rd; H_2O – 60-70 – 1st/2nd/3rd.

The first part showed the solvent used:

EtOH: Ethanol 98° – H_2O: Distilled water

The second part was the range of temperature at which the extraction process was conducted:

40-50: 40 to 50 °C – 60-70: 60 to 70°C

The final part represented the time of extraction:

1st: 1st extraction – 2nd: 2nd extraction – 3rd: 3rd extraction

2.2.3. Total phenolic compound measurement

The total phenolic compound (TPC) of liquid extract and in the initial material was determined based on method ISO 14502 – 1:2005 by using Folin – Ciocâlteu reagent (FCR) with some modifications. 1 mL of sample was added with 2.5 mL of FCR solution, followed by 2 mL of 7.5% sodium carbonate solution. The chemicals were combined and incubated at room temperature for 30 min in the dark. Then, a triplicate 760 or 765 nm absorbance measurement was made. The total phenolic content was reported as mg Gallic Acid Equivalents (GAE)/g of dry weight (DW) after the average data was interpolated in a gallic acid calibration curve.

2.2.4. Antioxidant capacity assay

In this research, the chosen method to determine the antioxidant capacity of Spinach leaves was using 2,2-diphenyl-1-picrylhydrazyl (DPPH) free radical scavenging [11]. Briefly, 2800 µL methanol and 100 µL of DPPH 6 mM or 1.5 mM (used for different situations) solution were prepared and added to 100 µL of dimethyl sulfoxide. 100 µL of samples of different concentrations was then mixed into the previously formed solution and allowed to react in the dark, at room temperature. After 1 hour of incubating, the measurement of absorbance at 517 nm of reacting samples (A_{sample}) was conducted against the DPPH blank sample (A_{DPPH} – prepared by replacing the measured sample with methanol at the beginning). The percent of inhibition (or remaining free radical DPPH) was computed by applying Equation (1):

$$Q_{inhibition}(\%) = \frac{A_{DPPH} - A_{sample}}{A_{DPPH}} \times 100\% \quad (1)$$

2.2.5. Vacuum rotary evaporation process

Liquid extract would undergo rotary evaporation (about 45-50°C under vacuum conditions) to get rid of solvent to obtain the condensed extract.

2.2.6. Preparation of solid lipid nanoencapsulation (SLN) system

Solid lipid encapsulation of active compounds was formulated using Emulgade as solid lipid and Polysorbate 80 as an emulsifier. The process to establish Spinach extract solid lipid nanoencapsulation comprised of 2 procedures: hot and cold homogenization. Hot homogenization: Solid lipids were heated until melting and combined with a proficient amount of Spinach condensed extract to a make lipid phase. The water phase comprising Polysorbate 80 (Tween 80) and distilled water was heated to the same temperature as the oil phase to keep solid lipids melted when mixing the oil phase and water

phase. Then the mixture of all ingredients was ready to be homogenized at high speed and hot temperature (80°C). Cold homogenization: The dispersion after 30 minutes of homogenization at high temperature was then cooled to 10°C in an ice bath and proceeded to be homogenized at that low temperature. The homogenization speed and duration were set similarly at 13000 rpm and 30 min for each cycle of homogenization because increasing homogenization would cause an increase in particle size due to particle coalescence [12].

2.3. Solid lipid nanoencapsulation system characterization and stability study

2.3.1. Particle size distribution by Laser diffraction spectroscopy (LDS)

The nanoencapsulation system was evaluated through the mean/median size and the particle size distribution was determined using a LDS instrument of Horiba, model LA950V2 at the Laboratory of Organic Chemical Engineering, Ho Chi Minh City University of Technology – Viet Nam National Univeristy HCMC.

2.3.2. Particle morphology by Scanning electron microscopy (SEM)

The particle morphology was performed via SEM instrument by Environmental Protection Centre (VITTEP), Phu Nhuan District, Ho Chi Minh City.

2.3.3. Utilization efficiency

Utilization efficiency is the ratio of the amount of material (polyphenols in this case) present in the system after preparation (C_1) to the total amount of material present in the original preparation mixture (C_0).

It is evaluated through the number of polyphenols before and after forming the nanoencapsulation system using Folin – Ciocalteu method as described in Section 2.2.3.

$$Utilization\ efficiency\ (\%) = \frac{C_0}{C_1} \times 100\% \qquad (2)$$

2.3.4. Stability study

The SLN system was evaluated for its protecting performance by conducting stability tests over a period. To do so, firstly, the SLN system was separated into 4 smaller batches with the same volume; three of them were wholly covered with aluminum foil paper to avoid Ultra – Violet radiation while the last one was left to be exposed to light. The SLN batch without aluminum foil paper covering was stored at room temp, each of the remaining batches was stored at 10°C, room temperature (about 30°C), and 45°C, respectively. Moreover, the non – encapsulation system (consisting of all the same ingredients as the SLN system but without any homogenization) was also constructed and left exposed to UV radiation at room temperature. The stability study in this project focused on the total phenolic content and antioxidant capacity after each week for a total period of 2 months.

Each of the SLN systems stored at different conditions and non – the encapsulation system was denoted as below for easier further indication:

Table 1. Denotations in stability study

System	Storing conditions	Denotation
SLN	10°C, without UV radiation exposure	SLN-10
	45°C, without UV radiation exposure	SLN-45
	Room temp., without UV radiation exposure	SLN-30
	Room temp., with UV radiation exposure	SLN-30UV
Non - encapsulation		Non

- Total phenolic content

The total content of polyphenols was the first subject in the stability study. The method of evaluating the amount of polyphenols was the same as in Section 2.2.3. However, before adding Follin – Ciocalteu solution to the sample, the SLN system was heated at 80°C for a short time for Emulgade molecules to melt and let active compounds unencapsulated for full reaction with the reagent.

- Antioxidant capacity

Besides total phenolic content, the antioxidant ability of subjective systems was also determined weekly. The procedure to inspect antioxidant capacity was similar to the procedure in Section 2.2.5 (using DPPH 1.5 mM solution).

The results of concentration and antioxidant capacity were converted to percentages compared with the initial concentration and antioxidant capacity of the week when the systems were formed to see the durability of the systems throughout periods:

$$\%\ remaining = \frac{X_i}{X_o} \times 100\% \qquad (3)$$

With X_i was phenolic content or antioxidant capacity at ***i*** week and X_o was phenolic content or antioxidant capacity at week **0** (right after preparation).

3. RESULTS AND DISCUSSION

3.1. Preparing and evaluating raw materials

The Spinach plants were fresh with green color; there were very few decayed and rotten leaves.

Figure 1. Appearances of Spinach plants and leaves
1) Spinach plants at VietGAP garden, 2) Fresh Spinach leaves, 3) Dried Spinach leaves

The moisture content of fresh leaves was also measured to be 97.36%, which means the dry matter (or dry weight) in fresh leaves was 2.64%.

The leaves after drying had the color of a fairly deep and darker green. The moisture content of dried leaves was 6.57%.

3.2. Investigating extraction conditions from Spinach leaves

3.2.1. General characteristics

Appearances of liquid extracts were different depending on the system of conditions.

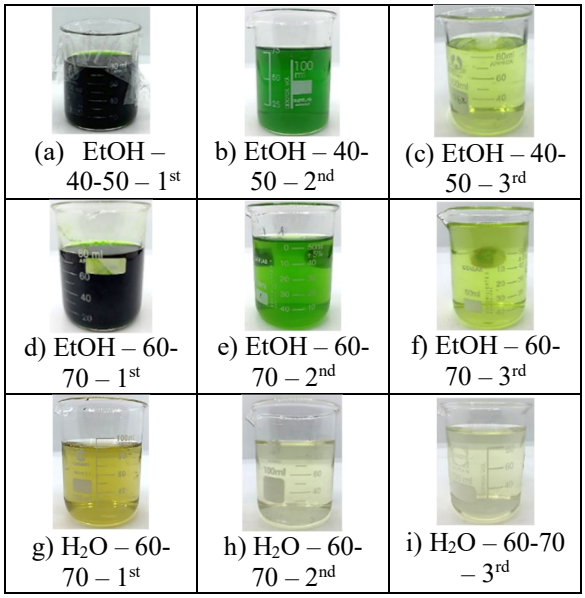

Figure 2. Appearances of liquid extracts according to each system of conditions

3.2.2. Total phenolic compound

Phenolic compounds content and extraction ratio are described in **Figure 3**, in this section, device UV-Vis Helios Epsilon was used.

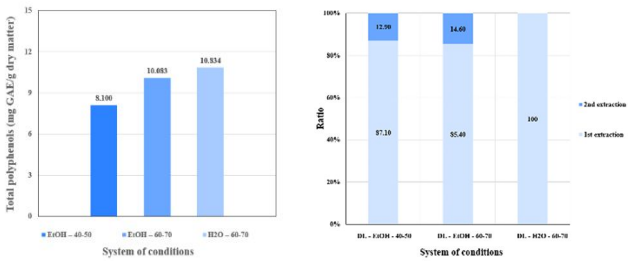

Figure 3. Total phenolic compounds (left) and phenolic compounds ratio of each system of conditions

3.2.5. Conclusion

Among several extraction conditions conducted to obtain polyphenols from Spinach leaves, these seemed to be the most suitable ones: dried leaf powder as initial materials; ethanol 98° or distilled water as a solvent, both performed great extraction; higher temperature, better extraction outcome, therefore 60 – 70°C was proper extraction temperature; only one extraction time was necessary.

3.3. Preparing and evaluating liquid and condensed extracts

Polyphenols were chosen to be the main research subject and focused in this section; additionally, its antioxidant capacity in different extracts was also determined. Therefore, ethanol 98° as extraction solvent was preferable to distilled water because ethanol with high purity can undergo much easier rotary evaporation and certain products could be collected for further procedure and assessments. To prepare a big batch, the ratio of dried leaf powder and ethanol was 1:10 g/mL, extraction duration was adjusted to 2 hours.

From this section, the UV-Vis Jenway Spectrophotometer device was used instead of UV-Vis Helios Epsilon one as in the previous section, therefore, about phenolic content evaluated by Folin – Ciocalteu method, the Gallic acid calibration curve established on this device was also applied.

3.3.1. General characteristics

The general characteristics of liquid and condensed extracts are shown in **Table 2**.

Table 2. General characteristics of liquid and condensed extracts

	Liquid extract	Condensed extract
Appearance		
Total phenolic content	1111.72 ± 27.07 mg GAE/L	37.79 ± 0.95 mg GAE/g sample
	38.68 ± 1.07 mg GAE/g DW	39.88 ± 1.00 mg GAE/g DW

The moisture content or volatile content of the extracts was 94.46% in the liquid reducing to 5.23% after the rotary evaporation process, indicating the efficiency of this step was high. Additionally, polyphenols concentration in condensed extract was satisfactorily high. The condense had almost adequate phenolics of 39.88 ± 1.00 mg/g absolute dry matter. The result was favorable for the study to show that Spinach is one positive choice for the source of polyphenols in nature.

3.3.2. Antioxidant capacity

Using DPPH assay (with 6mM DPPH solution), the antioxidant ability of positive control vitamin C, the liquid and condensed extracts was also figured out and illustrated in **Figure 4** and **Table 3.**

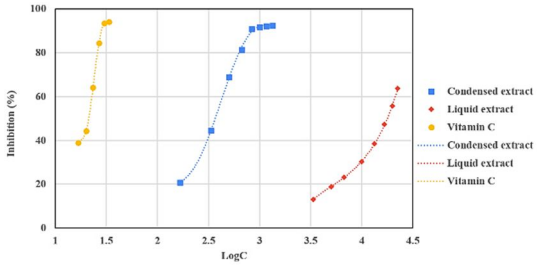

Figure 4. Antioxidant capacity of positive control Vitamin C, liquid, and condensed extracts (based on normal samples)

Table 3. IC_{50} value of liquid and condensed extracts

		Liquid extract	Condensed extract
IC_{50} value	**Based on sample**	16430.6 mg/L	325.9 mg/L
	Based on absolute dry matter	215.2 mg/L	308.9 mg/L

For objective comparison, firstly, the oxidant inhibition ability of positive control Vitamin C was assessed. The half-maximal inhibitory concentration (IC_{50}) value of vitamin C was 21.1 mg/L.

When the data was calculated based on absolute dry matter, IC_{50} values of the liquid and condensed extracts were 215.2 and 308.9 mg/L (**Table 3**). Both extracts' IC_{50} values were 10-15 times higher than positive control Vitamin C, which indicated they still had a great capacity for oxidation prevention and expected feasibility in applications as antioxidants as well.

3.4. Solid lipid nanoencapsulation system

The formulation of the solid lipid nanoencapsulation (SLN) system was as follows:

Table 4. Formulation conditions of the SLN system

Condensed extract	Emulgade	Tween 80	Water
0.5 g	2 g	1 g	96.5 g

3.4.1. General characteristics

The SLN system had milky dark green color. Compared to the non-encapsulation system, whose color was translucent dark green, the SLN dispersion's milky coloring might be originated from the solid lipid Emulgade.

Figure 5. The appearances of the SLN system (left) and non – encapsulation system (right)

3.4.2. Utilization efficiency

The utilization efficiency of the SLN system was **99.38%**, which proved that after the encapsulation process with mentioned conditions, the actives in the dispersion remained almost completely. This result showed the excellent usability of Spinach leaf extracts as the main ingredient in the solid lipid encapsulation along with the formulated conditions.

3.4.3. Particle size and morphology

The analytic result from LDS and SEM are shown in **Figure 6.**

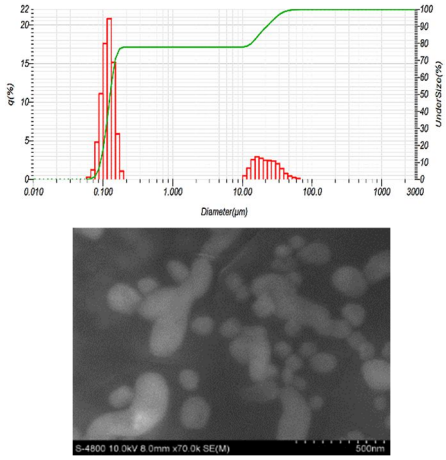

Figure 6. LDS result (a) and SEM image (b) of the SLN system

Table 5. Particle size and morphology of the SLN system

Morphology	Spherical (SEM)
Size	126 nm (median – LDS) 5.3 µm (mean – LDS) 60-200 nm (SEM)

Additionally, based on the figures and data provided by the LDS device, **77.78%** of particles were smaller than **197 nm**. The bell curve shape of the size distribution graph exhibited by the LDS program implied the uniformity in the size of the particles, although several unexpected microsized clusters appeared. With these sizes of nanoparticles, the SLN system is promising in many applications and products that require certain dimensional characteristics.

Most of the particles appeared to be spherical while there were some bigger clusters, which might occur due to the probability of flocculation and led to coalescence of these particles.

3.4.4. Stability study

3.4.4.1. General characteristics

Appearances of the SLN system at different storing conditions over 8 weeks were shown in **Figure 7.**

Figure 7. Appearances of the SLN system right after preparing (left) and storing at different conditions (right) after 8 weeks

As can be seen, after 2 months, most of the SLN system appearances were the same as in the initial week.

Nevertheless, the SLN system stored at 45°C had a slight color difference, lighter and milkier dark green was observed. This dissimilarity could be explained due to degradation of natural substances at high temperatures.

3.4.4.2. Total phenolic compound

Ultra – Violet radiation

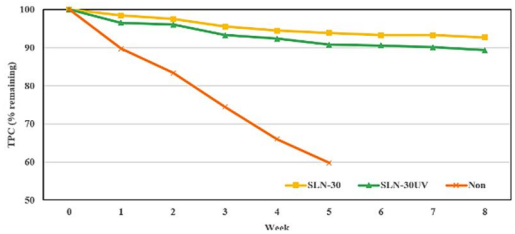

Figure 8. Effect of UV – radiation on phenolic content of SLN system and non – encapsulation systems

A non – encapsulation system (Non) was also prepared and quantitively evaluated to be compared with the encapsulation one. The polyphenols loss rate of the non – encapsulation was a lot higher, with about **8% per week** and only approximately **60%** of polyphenols remained after 5 weeks. While the encapsulation samples (SLN-30 and SLN-30UV) had TPC stability of about **90-93%** at the end of 8 weeks. The performance of Emulgade in protecting active compounds was undeniably effective.

Take the SLN system stored at room temperature with prolonged exposure to ultra–violet radiation from light into account, after 8 weeks, polyphenols remained at **89.34%**. Compared with the SLN sample without the light affecting, the stability was **92.66%**. UV radiation seemed to have very little effect on the encapsulated active compounds, which was a positive note for this study and further applications.

- *Temperature*

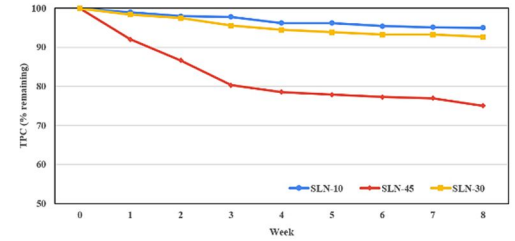

Figure 9. Effect of storing temperature on phenolic content of SLN system

Concerning temperature, the phenolic content of the SLN system at 10°C showed its best capacity to cover active compounds from environmental factors. Only **5%** of phenolic **substances were lost, and that percentage of the SLN system at** 30°C temperature was just a bit higher by **3%** after 8 weeks. At 45°C within a 2 – month period, the proportion of polyphenols lasting was **three–fourths**.

To draw a conclusion, the lower temperature, the better-protecting performance of the SLN system.

3.4.4.3. Antioxidant capacity

- *Ultra – Violet radiation*

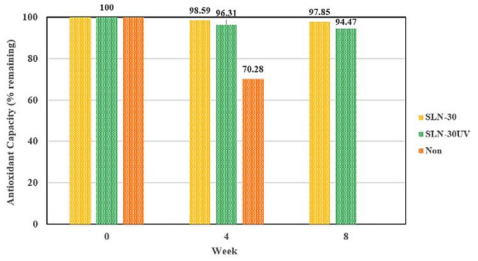

Figure 10. Effect of UV – radiation on antioxidant capacity of SLN and non – encapsulation systems

Looking at the decrease of antioxidant ability within 4 weeks of non – encapsulated system, the degradation rate was extremely fast, only **70%** was available compared to the capacity at initial.

The SLN system at room temperature exposed to light appeared to be quite influenced by UV radiation in terms of bioactivity; howbeit, SLN dispersion at this condition still had an acceptably good ability to keep the antioxidant nature of active components. The antioxidant inhibition only decreased by around **5%** after 8 weeks.

- *Temperature*

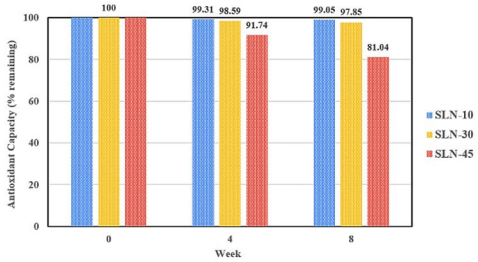

Figure 11. Effect of storing temperature on antioxidant capacity of SLN systems

The antioxidant performance of the SLN system stored at 10 and 30 °C was practically unaffected throughout 2 – month period. Furthermore, the antioxidant capacity loss rate of the SLN system at 45 °C was expectedly higher than two other samples, at approximately **9.5%** per month. To summarize, variable acceleration of total phenolic contents was proportional to that of antioxidant capacity.

4. CONCLUSION

To achieve a good amount of polyphenols in extracts, dried leaf powder should be used as initial material, ethanol 98° and distilled water were favorable choices as solvents, extraction temperature of 60 – 70 °C, and only one extraction time was required. The total phenolic compound calculated in liquid extract was determined to be 38.68 ± 1.07 mg GAE/g DW and that of condensed one was 39.88 3 ± 1.00 mg GAE/g. The result showed that the liquid extract possessed an IC50 value of 215.2 mg/L and

the condensed extract had a value of 308.9 mg/L. The particle size distribution of the SLN system formed had a median size of 126 nm and a mean size of 5.3 µm (LDS). Furthermore, spherical was the shape of these particles according to the SEM result, and the size range of particles from 60 – 200 nm was observed as well. The encapsulation dispersion by Emulgade prevented expectedly well active compounds in an extract from denaturing by environmental factors, particularly, temperature and UV radiation. The lower temperature, the better protecting performance of the SLN system. These results would broaden more and more orientations for other research and applications of using the encapsulation method, in general, and solid lipid, in particular, to protect active compounds from natural plants.

Acknowledgment

This research is funded by Office for International Study Programs (OISP), Ho Chi Minh City University of Technology (HCMUT), VNUHCM under grant number **SVOISPLV-2022-KTHH-36**. We acknowledge the support of time and facilities from HCMUT, VNUHCM for this study.

References

[1] M. Nešković and L. Ćulafić, "Spinach (Spinacia oleracea L.)," in *Crops II*, Y. P. S. Bajaj, Ed. Berlin, Heidelberg: Springer Berlin Heidelberg, 1988, pp. 370-385.

[2] M. Watanabe and J. Ayugase, "Effect of low temperature on flavonoids, oxygen radical absorbance capacity values and major components of winter sweet spinach (Spinacia oleracea L.)," (in eng), *J Sci Food Agric,* vol. 95, no. 10, pp. 2095-104, Aug 15 2015.

[3] M. J. Cho, L. R. Howard, R. L. Prior, and T. Morelock, "Flavonoid content and antioxidant capacity of spinach genotypes determined by high-performance liquid chromatography/mass spectrometry," *Journal of the Science of Food and Agriculture,* https://doi.org/10.1002/jsfa.3206 vol. 88, no. 6, pp. 1099-1106, 2008/04/30 2008.

[4] M. Alarcón-Flores, R. Romero-González, J. Vidal, and A. Frenich, "Determination of Phenolic Compounds in Artichoke, Garlic and Spinach by Ultra-High-Performance Liquid Chromatography Coupled to Tandem Mass Spectrometry," *Food Analytical Methods,* vol. 7, 11/01 2014.

[5] M. Kamoshita *et al.*, "Lutein acts via multiple antioxidant pathways in the photo-stressed retina," *Scientific Reports,* vol. 6, no. 1, p. 30226, 2016/07/22 2016.

[6] R. L. Roberts, J. Green, and B. Lewis, "Lutein and zeaxanthin in eye and skin health," (in eng), *Clin Dermatol,* vol. 27, no. 2, pp. 195-201, Mar-Apr 2009.

[7] D. Vauzour, A. Rodriguez-Mateos, G. Corona, M. J. Oruna-Concha, and J. P. Spencer, "Polyphenols and human health: prevention of disease and mechanisms of action," (in eng), *Nutrients,* vol. 2, no. 11, pp. 1106-31, Nov 2010.

[8] M. E. Obrenovich, N. G. Nair, A. Beyaz, G. Aliev, and V. P. Reddy, "The role of polyphenolic antioxidants in health, disease, and aging," (in eng), *Rejuvenation Res,* vol. 13, no. 6, pp. 631-43, Dec 2010.

[9] N. Lolayekar and C. Shanbhag, "Polyphenols and oral health," (in Inglés), *RSBO Revista Sul-Brasileira de Odontologia,* vol. 9, no. 1, pp. 74-84, 2012.

[10] S. Petti and C. Scully, "Polyphenols, oral health and disease: A review," (in eng), *J Dent,* vol. 37, no. 6, pp. 413-23, Jun 2009.

[11] M. S. Blois, "Antioxidant Determinations by the Use of a Stable Free Radical," *Nature,* vol. 181, no. 4617, pp. 1199-1200, 1958/04/01 1958.

[12] S. Mukherjee, S. Ray, and R. S. Thakur, "Solid lipid nanoparticles: a modern formulation approach in drug delivery system," (in eng), *Indian J Pharm Sci,* vol. 71, no. 4, pp. 349-58, Jul 2009

EVALUATING VITAMIN E&C ENCAPSULATION WITH SOLID LIPID (NATEROL) IN TEXTILE APPLICATIONS BY USING A DPPH SCAVENGING ACTIVITY METHOD

(ĐÁNH GIÁ HỆ VI NANG VITAMIN E&C VỚI MỘT SỐ LOẠI BÉO RẮN (NATEROL) ỨNG DỤNG TRÊN VẢI BẰNG PHƯƠNG PHÁP QUÉT GỐC TỰ DO DPPH)

Huynh Tan An[1,2,3], Le Thi Hong Nhan[1,3,*]

[1] Faculty of Chemical Engineering, Ho Chi Minh City University of Technology (HCMUT), 268 Ly Thuong Kiet Street, District 10, Ho Chi Minh City, Vietnam
[2] Office for International Study Programs, Ho Chi Minh City University of Technology (HCMUT), 268 Ly Thuong Kiet Street, District 10, Ho Chi Minh City, Vietnam
[3] Vietnam National University Ho Chi Minh City, Linh Trung Ward, Thu Duc City, Ho Chi Minh City, Vietnam
[*] Corresponding author: lthnhan@hcmut.edu.vn

Abstract

The remarkable developments in science and technology have accelerated the development of cosmetotextiles and opened the door to important research on the use of the microencapsulation system on fabric, particularly for encapsulating vitamins and active ingredients. In this research, a mixture of vitamin C, E, and olive oil with a mass ratio of 6:3:1 was encapsulated with Naterol solid lipid (an emulsifying wax was provided by CISME Italy company) and evaluated for applicability on cotton fabrics. The microencapsulated particles were effectively coated with Naterol with a median size of 0.67 µm (according to LDS). Additionally, the utilization and encapsulation efficiency of the solid lipid nanoparticles system accounted respectively for 96.64% and 77.74% through DPPH free radical scavenging methods. Besides, in order to enhance the antioxidation ability of fabrics, the suspension was applied to cotton fabrics by two methods and effects of the two methods on the fabric were also investigated and evaluated. The total amount of active ingredients in the fabric sample after impregnating or soaking was 59.49% and 57.14%, respectively. Whereas the release efficiency was 45.3% for the impregnating method and 42.76% for soaking method by measuring after 30 minutes. With outstanding properties, Naterol solid lipid encapsulating vitamin E&C was considered a promising candidate for textile application, especially in the current trend of functional fabrics.

Keywords: *Vitamin mixture, encapsulation, DPPH radical scavenging, Naterol, cotton fabric*

Tóm tắt

Với những bước tiến nổi bật của khoa học và công nghệ đã dẫn tới sự phát triển nhanh chóng của lĩnh vực vải mỹ phẩm, mở đường cho những nghiên cứu quan trọng về khả năng ứng dụng của hệ bao bọc vi nang trên vải, đặc biệt là bao bọc các vitamin và hoạt chất. Trong nghiên cứu này, hỗn hợp vitamin C, vitamin E và dầu olive với tỉ lệ khối lượng 6:3:1 được bao bọc bởi chất béo rắn Naterol (chất nhũ hóa được cung cấp bởi công ty CISME Italy) và sau đó được đánh giá khả năng ứng dụng trên vải cotton. Các hạt vi nang được bao bọc bởi béo rắn Naterol một cách hiệu quả với kích thước trung bình 0.67 µm (theo đánh giá LDS). Ngoài ra, hiệu quả sử dụng và hiệu quả bao bọc của hệ cao, lên đến 96.64% and 77.74% thông qua phương pháp bắt gốc tự do DPPH. Bên cạnh đó, nhằm nâng cao khả năng kháng oxy hóa của vải, hệ béo rắn Naterol được ứng dụng lên vải cotton thông qua phương pháp tẩm và ngâm. Ảnh hưởng của hai phương pháp này lên hoạt tính trên vải cũng được nghiên cứu và đánh giá. Hoạt tính tổng đo được của hệ béo rắn Naterol trên mẫu vải tẩm và ngâm lần lượt là 59.49% and 57.14%. Trong đó, hiệu quả giải phóng đo được sau khi chiết 30 phút là 45.3% đối với phương pháp tẩm và 42.76% đối với phương pháp ngâm. Kết quả chứng minh rằng hoạt tính giải phóng của mẫu vải tẩm cao hơn so với mẫu vải ngâm. Với đặc tính nổi bật, hệ béo rắn Naterol bao bọc vitamin E&C được coi là một triển vọng cho các ứng dụng may mặc, đặc biệt là các loại vải chức năng xu hướng hiện nay.

Từ khóa: *Hỗn hợp vitamin, bao bọc, bắt gốc tự do DPPH, Naterol, vải cotton*

Acknowledgement: This research is funded by the Office for International Study Programs (OISP), Ho Chi Minh City University of Technology (HCMUT), VNUHCM under grant number **SVOISPLV-2022-KTHH-48.** We acknowledge the support of time and facilities from HCMUT, VNUHCM for this study.

EVALUATING VITAMIN E&C ENCAPSULATION WITH SOLID LIPID (SABOWAX) IN TEXTILE APPLICATIONS BY USING A DPPH SCAVENGING ACTIVITY METHOD

(ĐÁNH GIÁ HỆ VI NANG VITAMIN E&C VỚI MỘT SỐ LOẠI BÉO RẮN (SABOWAX) ỨNG DỤNG TRÊN VẢI BẰNG PHƯƠNG PHÁP QUÉT GỐC TỰ DO DPPH)

Pham Kim Khanh[1,2,3], Le Thi Hong Nhan[1,3]

[1] Faculty of Chemical Engineering, Ho Chi Minh City University of Technology (HCMUT), 268 Ly Thuong Kiet Street, District 10, Ho Chi Minh City, Vietnam
[2] Office for International Study Programs, Ho Chi Minh City University of Technology (HCMUT), 268 Ly Thuong Kiet Street, District 10, Ho Chi Minh City, Vietnam
[3] Vietnam National University Ho Chi Minh City, Linh Trung Ward, Thu Duc City, Ho Chi Minh City, Vietnam
[*] Corresponding author: lthnhan@hcmut.edu.vn

Abstract

The outstanding advances in science and technology led to the rapid development of the cosmetotextile, paving the way for significant studies on the applicability of the microencapsulation system on fabric, especially encapsulating vitamins and active ingredients. In this research, a mixture of vitamin C, E, and olive oils with a mass ratio of 6:3:1 g:g:g was encapsulated with Sabowax solid lipid (an emulsifying wax from SABO S.p.A) and evaluated for applicability on cotton fabrics. The microencapsulated particles were effectively coated with Sabowax with a median size of 0.342 µm (according to LDS). Additionally, the utilization and encapsulation efficiency of the solid lipid nanoparticles system accounted respectively for 98.02% and 83.78% through DPPH free radical scavenging methods. The SLN system was applied to the cotton fabric by impregnating and soaking methods, and the effects of the two methods on the fabric were also investigated and evaluated. The total amount of active ingredients in the fabric samples after impregnating or soaking was 57.28% and 55.15%, respectively. The release efficiency of the impregnating and soaking samples was 40.73% and 31.06% by measuring after 30 minutes on a methanol medium. With outstanding properties, Sabowax solid lipid encapsulating vitamin E&C was considered a promising candidate for textile application, especially in the current trend of functional fabrics.

Keywords: *Vitamin mixture, encapsulation, DPPH radical scavenging, Sabowax, cotton fabric*

Tóm tắt

Những bước tiến nổi bật của khoa học và công nghệ đã dẫn tới sự phát triển nhanh chóng của lĩnh vực vải mỹ phẩm, mở đường cho những nghiên cứu quan trọng về khả năng ứng dụng của hệ bao bọc vi nang trên vải, đặc biệt là bao bọc các vitamin và hoạt chất. Trong nghiên cứu này, hỗn hợp vitamin C, E và dầu olive với tỉ lệ khối lượng 6:3:1 g:g:g được bao bọc bởi chất béo rắn Sabowax (một chất béo nhũ hóa từ SABO S.p.A) và đánh giá khả năng ứng dụng trên vải cotton. Các hạt vi nang được bao bọc bởi béo rắn Sabowax một cách hiệu quả với kích thước trung bình 0.342 µm (theo đánh giá LDS). Ngoài ra, hiệu quả sử dụng và hiệu quả bao bọc của hệ lần lượt là 98.02% và 83.78% thông qua phương pháp bắt gốc tự do DPPH. Hệ béo rắn được ứng dụng lên vải cotton bằng phương pháp ngâm và tẩm và ảnh hưởng của hai phương pháp này lên vải cũng được nghiên cứu và đánh giá. Tổng lượng hoạt chất trong các mẫu vải ngâm và tẩm lần lượt là 57.28% và 55.15%. Hiệu quả giải phóng của mẫu tẩm và ngâm đo được là 40.73% và 31.06% sau 30 phút trong môi trường methanol. Với đặc tính nổi bật, béo rắn Sabowax bao bọc vitamin E&C được coi là một ứng cử viên triển vọng cho các ứng dụng may mặc, đặc biệt là các loại vải chức năng xu hướng hiện nay.

Từ khóa: *Hỗn hợp vitamin, bao bọc, bắt gốc tự do DPPH, Sabowax, vải cotton*

Acknowledgement: This research is funded by Office for International Study Programs (OISP), Ho Chi Minh City University of Technology (HCMUT), VNUHCM under grant number **SVOISPLV-2022-KTHH-85**. We acknowledge the support of time and facilities from HCMUT, VNUHCM for this study.

RESEARCH ON NATURAL ACTIVES OF ROBUSTA COFFEE PULP FOR APPLICATIONS IN PERSONAL CARE PRODUCTS

(NGHIÊN CỨU HOẠT CHẤT TỰ NHIÊN TỪ VỎ CÀ PHÊ ROBUSTA ĐỊNH HƯỚNG ỨNG DỤNG TRONG SẢN PHẨM CHĂM SÓC CÁ NHÂN)

Le Hoang Tin[1,2,3,*], Le Thi Hong Nhan[1,2,3]

[1] Faculty of Chemical Engineering, Ho Chi Minh City University of Technology (HCMUT), 268 Ly Thuong Kiet, District 10, Ho Chi Minh City, Vietnam
[2] Office for International Study Programs, Ho Chi Minh City University of Technology (HCMUT), 268 Ly Thuong Kiet Street, District 10, Ho Chi Minh City, Vietnam
[3] Vietnam National University Ho Chi Minh City, Linh Trung Ward, Thu Duc City, Ho Chi Minh City, Vietnam
[*] Corresponding author: lthnhan@hcmut.edu.vn

Abstract

This study focused on evaluating the Robusta coffee pulp, which was harvested from Cư M'gar, Dak Lak province of Vietnam, activity and its application capacity in personal-care products. Firstly, the coffee cherries were classified following their ripeness such as green (G), medium ripped (M) and ripped (R) types, and evaluated for mass ratio, pH, and water content. The coffee cherries were depulped and extracted with ethanol 98º at ratio of 1:7 g:mL at 50ºC for an hour. The liquid extracts were analyzed for concentration of chlorophylls, carotenoids, total polyphenol compounds (TPC) (by Folin – Ciocalteu method), and antioxidant activity by DPPH assay. As a result, the R extracts exhibited as the highest active compounds which had chlorophyll, carotenoid and total polyphenol contents of 0.0364 µg/g, 0.117 µg/g and 533.39 mgGAE/g, respectively. The TPC of the M and G extracts was also quite high which was 479.06 and 436.46 mgGAE/g. The extract from the pulp mixture was condensed and the concentrated one had the chlorophyll, carotenoid and total polyphenol contents of 0.0392 µg/g, 0.109 µg/g and 460.75 mgGAE/g, respectively and high antioxidant capacity with IC_{50} value of 64.34 ppm. The gel cream was mixed with the concentrated extract at ratio of 0.5%, 1%, and 1.5%, the best ratio was selected by investigating changes in appearance, chemical content, antioxidant activity and stability. In conclusion, the extract from Robusta coffee pulp exhibited as a promising candidate for the cosmetic industry.

Keywords: *robusta coffee pulp, total polyphenol compounds, antioxidant, personal-care products*

Tóm tắt

Nghiên cứu này tập trung đánh giá hoạt tính vỏ cà phê Robusta, được thu hoạch ở huyện Cư M'gar, tỉnh Đắk Lắk của Việt Nam, và ứng dụng vào sản phẩm chăm sóc cá nhân. Đầu tiên, những trái cà phê được phân loại theo độ chín của chúng, cụ thể là trái xanh (G), chín vừa (M), chín (R) và chúng được đánh giá về tỷ lệ khối lượng, pH và độ ẩm. Vỏ cà phê sau khi tách mang đi chiết xuất với cồn 98º ở tỉ lệ 1:7 g:mL ở 50 ºC trong 1 tiếng. Dịch chiết được đánh giá hàm lượng chlorophyll, carotenoid, tổng hàm lượng polyphenol (TPC) (bằng phương pháp Folin–Ciocalteu) và hoạt tính kháng oxi hóa bằng DPPH. Kết quả thu được là dịch chiết R có hàm lượng hoạt chất cao nhất, với nồng độ chlorophylls, carotenoids, và tổng hàm lượng polyphenol lần lượt là 0.0364 µg/g, 0.117 µg/g và 533.39 mgGAE/g. Bên cạnh đó, dịch chiết M và G có lượng TPC khá cao, cụ thể là 479.06 và 436.46 mgGAE/g. Dịch chiết từ hỗn hợp giữa ba loại cà phê được cô đặc và dịch đặc cho kết quả với nồng độ chlorophylls, carotenoids, và tổng hàm lượng polyphenol lần lượt là 0.0392 µg/g, 0.109 µg/g and 460.75 mgGAE/g, và khả năng kháng oxi hóa khá tốt với chỉ số IC_{50} của hỗn hợp là 64.34 ppm. Kem gel phối với chiết xuất cô đặc theo tỷ lệ 0.5%, 1% và 1.5%, và được đánh giá theo sự thay đổi về ngoại quan, hợp chất hóa học, hoạt tính chống oxy hóa, và độ bền để chọn ra sản phẩm với tỉ lệ tối ưu. Tổng kết lại, chiết xuất từ vỏ cà phê Robusta thể hiện như một ứng cử viên đầy triển vọng cho ngành công nghiệp mỹ phẩm.

Từ khóa: *vỏ cà phê Robusta, tổng hàm lượng polyphenol, kháng oxi hóa, sản phẩm chăm sóc cá nhân*

Acknowledgement: This research is funded by Office for International Study Programs (OISP), Ho Chi Minh City University of Technology (HCMUT), VNUHCM under grant number **SVOISPLV-2022-KTHH-51**. We acknowledge the support of time and facilities from HCMUT, VNUHCM for this study.

UTILIZATION OF GREEN KOHLRABI LEAF POWDER FOR PARTIAL SUBSTITUTION OF WHEAT FLOUR IN HIGH-FIBER PASTA PRODUCTION: EFFECTS OF SUBSTITUTING PERCENTAGE ON HIGH-FIBER PASTA QUALITY

(TẬN DỤNG PHỤ PHẨM LÁ SU HÀO XANH THAY THẾ MỘT PHẦN BỘT MÌ TRONG SẢN XUẤT MÌ PASTA GIÀU XƠ: ẢNH HƯỞNG CỦA TỈ LỆ BỔ SUNG LÁ SU HÀO LÊN CHẤT LƯỢNG CỦA SẢN PHẨM)

Nguyen Thu An[1,2,3,*]

[1] Faculty of Chemical Engineering, Ho Chi Minh City University of Technology (HCMUT), 268 Ly Thuong Kiet Street, District 10, Ho Chi Minh City, Vietnam
[2] Office for International Study Programs, Ho Chi Minh City University of Technology (HCMUT), 268 Ly Thuong Kiet Street, District 10, Ho Chi Minh City, Vietnam
[3] Vietnam National University Ho Chi Minh City, Linh Trung Ward, Thu Duc City, Ho Chi Minh City, Vietnam
[*] Corresponding author: an.nguyen0830@hcmut.edu.vn

Abstract

Green kohlrabi *(Brassica oleracea Gongylodes)* is widely consumed in regions with cool weather, especially the tuber. On the other hand, green kohlrabi leaf is disposed of as an agricultural by-product or is fed to animal farming. In recent, many studies have shown that green kohlrabi leaf has such high amounts of dietary fiber, antioxidant compounds as well as mineral content. In this research, substituting percentage of green kohlrabi leaf from 0%, 5%, 10%, 15%, 20% for wheat flour (*semolina*) was investigated. As a result, significantly high dietary fiber, mineral content and antioxidant activity were observed in pasta fortified with green kohlrabi leaf powder. However, addition of fiber content, which is believed to disrupt the gluten network (the main component that contributes to the distinctive texture of pasta) has placed a negative impact on textural profile and the overall acceptability. The percentage of 5% was chosen to be optimal since pasta supplemented with 5% of green kohlrabi leaf powder significantly increased the dietary fiber and mineral content as well as antioxidant capacity, but it was not different from control pasta, in terms of textural profile andoverall acceptability.

Keywords: *green kohlrabi, green kohlrabi leaf, agricultural by-product, supplemented ratio, pasta*

Tóm tắt

Củ su hào xanh *(Brassica oleracea Gongylodes)* được sử dụng thường xuyên trong các món ăn ở các vùng có khí hậu lạnh. Trong khi đó, lá su hào xanh hầu hết đều bị bỏ đi như một phụ phẩm nông nghiệp, hoặc dùng làm thức ăn cho gia súc. Mặc dù vậy, trong các nghiên cứu gần đây, lá su hào xanh đã được chứng minh có hàm lượng xơ, khoáng cũng như hoạt tính oxi hóa rất cao. Trong bài nghiên cứu này, tỉ lệ thay thế bột mì (*semolina*) bằng bột lá su hào trong việc sản xuất mì pasta giàu xơ từ 0%, 5%, 10%, 15%, 20% được khảo sát. Kết quả cho thấy rằng, hàm lượng xơ và hoạt tính kháng oxi hóa tăng đáng kể khi tăng dần tỉ lệ thay thế. Hiện tượng đó cũng được ghi nhận ở hàm lượng khoáng. Tuy nhiên, việc bổ sung một lượng chất xơ đã làm đứt gãy các liên kết mạng gluten (liên kết tạo nên cấu trúc đặc trưng của mì pasta), làm giảm điểm cảm quan của mì được bổ sung bột lá su hào xanh. Tỉ lệ bổ sung 5% được xem là phù hợp vì mẫu mì được bổ sung 5% bột lá su hào có hàm lượng xơ, khoáng và khả năng kháng oxi hóa tăng đáng kể so với mì trắng nhưng lại được ghi nhận không có sự khác biệt, so với mì trắng, về cấu trúc và độ chấp nhận chung.

Từ khóa: *su hào xanh, lá su hào xanh, phụ phẩm nông nghiệp, tỷ lệ bổ sung, mỳ ống*

Acknowledgement: This research is funded by the Office for International Study Programs (OISP), Ho Chi Minh City University of Technology (HCMUT), VNUHCM under grant number **SVOISP-2021-KTHH-50**. We acknowledge the support of time and facilities from HCMUT, VNUHCM for this study.

AIR POLLUTION CONTROL AND DESIGN FOR VIETNAM FINLAND INTERNATIONAL SCHOOL (VFIS)

(KIỂM SOÁT MÔI TRƯỜNG KHÔNG KHÍ VÀ THIẾT KẾ HỆ THỐNG XỬ LÝ KHÍ THẢI CHO TRƯỜNG QUỐC TẾ VIỆT NAM - PHẦN LAN (VFIS))

Nguyen Duy Khanh[1,2,3,*], Le Phuoc Minh Duc[1,2,3], Du My Le[1,3]

[1] Faculty of Environment and Natural Resources, Ho Chi Minh City University of Technology (HCMUT), 268 Ly Thuong Kiet Street, District 10, Ho Chi Minh City, Vietnam
[2] Office for International Study Programs, Ho Chi Minh City University of Technology (HCMUT), 268 Ly Thuong Kiet Street, District 10, Ho Chi Minh City, Vietnam
[3] Vietnam National University Ho Chi Minh City, Linh Trung Ward, Thu Duc City, Ho Chi Minh City, Vietnam
[*] Corresponding author: khanh.nguyenkbg@hcmut.edu.vn

Abstract

VFIS is a Vietnam-Finland International School located inside the campus of Ton Duc Thang University in District 7, HCMC. The school is designed with a Finnish-standard curriculum with a focus on practice. Therefore, all 40 classrooms in the school are mostly functional classrooms, such as the music room, laboratory, computer room, STEM classroom, art room, mechanical room, wood workshop, painting room, and oriented room. The topic focuses on controlling air pollution and treating internal environmental emissions inside the VFIS campus, to ensure that the air quality is in line with the standards set by an international standard school for children who are elementary and middle school students.

The project carries out two primary tasks: (1) suggesting appropriate pollution control measures (collection and treatment) for centralized and non-centralized waste sources for units on all three floors of the VFIS building, as well as (2) calculating the detailed design of the suggested units (6 units).

Most of the harmful emissions are generated from many sources and different practices, such as painting, welding, metalworking, woodworking, ceramics, cooking, chemistry experiments, etc. Small-sized dust and volatile gases (VOCs), which are present in the exhaust stream from particular specific sources such spray booths, welding chambers, etc., are the principal pollutants from these processes. Additionally, due to the fact that all VFIS classrooms have an air conditioning-based ventilation system, solutions to control and treat emissions in this enclosed space must also maintain the proper air temperature in order to give students and teachers a sense of thermal comfort. This is in addition to ensuring a quality volume of air.

The study team has categorized the different types of emission sources from each function space of the three-story building to gather and map the collection path. To provide a range of solutions for collecting emissions from local intake hoods to the gas treatment system and select the best one based on the layout characteristics of the emission sources, architectural plan, and classroom space to maintain the aesthetics of each classroom while ensuring energy efficiency.

The design calculation outcomes demonstrate that the proposed exhaust gas treatment system in the study has achieved the necessary goals, including satisfying QCVN 05:2013/BTNMT, Standard 3733/2002/QD-BYT, and particularly striving to reach TCVN 13521:2022 on indoor air quality.

Keywords: *indoor air quality, air pollution control, improve indoor air quality*

Tóm tắt

VFIS là Trường Quốc tế Việt Nam - Phần Lan có vị trí bên trong khuôn viên của trường Đại học Tôn Đức Thắng tại Quận 7, TP.HCM. Trường được thiết kế theo chương trình học tập đạt tiêu chuẩn của Phần Lan với xu hướng giáo dục chú trọng vào thực hành. Vì vậy, toàn bộ 40 phòng học của trường hầu hết là các phòng học chức năng như phòng nhạc, phòng thí nghiệm, phòng vi tính, phòng học STEM, phòng mỹ thuật, phòng cơ khí, xưởng gỗ, phòng sơn, phòng định hướng,…

Đề tài tập trung kiểm soát ô nhiễm không khí và xử lý khí thải môi trường nội vi bên trong khuôn viên VFIS, nhằm đảm bảo chất lượng không khí phù hợp với tiêu chuẩn quy định của một trường học đạt chuẩn quốc tế dành cho trẻ em lứa tuổi nhỏ là học sinh cấp 1 và cấp 2.

Đề tài thực hiện hai nhiệm vụ chính là (1) đề xuất giải pháp kiểm soát ô nhiễm (thu gom và xử lý) phù hợp cho nguồn thải không tập trung và nguồn thải tập trung cho các đơn vị trong toàn bộ 03 tầng của VFIS; và (2) tính toán thiết kế chi tiết các công trình đơn vị đã đề xuất (6 đơn vị).

Các dòng khí thải độc hại hầu hết là dòng khí thải phát sinh từ nhiều nguồn và từ các quá trình thực hành khác nhau như phun sơn, hàn, gia công kim loại, chế tác đồ gỗ, làm gốm sứ, thực hành nấu ăn, thí nghiệm hoá học... Thành phần ô nhiễm chính từ các quá trình này là bụi có kích thước nhỏ và khí dễ bay hơi (VOCs), ở một số nguồn cụ thể như buồng phun sơn, buồng hàn… còn có sự hiện diện của khí độc hại (HAPs) trong dòng khí thải. Ngoài ra, với đặc thù là toàn bộ hệ các phòng học của VFIS đều được trang bị hệ thống thông gió sử dụng điều hòa không khí, giải pháp kiểm soát và xử lý khí thải trong không gian kín này ngoài việc cần đảm bảo chất lượng không khí, còn phải giữ được nhiệt độ phù hợp cho không khí trong phòng, đáp ứng cảm giác thoải mái nhiệt cho học sinh và giáo viên.

Với mục tiêu thu gom và vạch tuyến thu gom, nhóm nghiên cứu đã tiến hành phân loại các loại nguồn phát thải từ từng phòng chức năng của khối nhà 3 tầng. Dựa vào đặc điểm bố trí của các nguồn phát thải, mặt bằng kiến trúc và không gian của các phòng học để đưa ra nhiều phương án thu gom khí thải từ các chụp hút cục bộ đến hệ thống xử lý khí và chọn phương án vừa đảm bảo hiệu quả về năng lượng vừa giữ được tính thẩm mỹ cho từng phòng học.

Kết quả tính toán thiết kế cho thấy, hệ thống xử lý khí thải đề xuất trong nghiên cứu đã đảm bảo mục tiêu yêu cầu, đáp ứng QCVN 05:2013/BTNMT, Tiêu chuẩn 3733/2002/QĐ – BYT, và đặc biệt là hướng đến đạt TCVN 13521:2022 về chất lượng không khí trong nhà.

Từ khóa: *chất lượng không khí trong nhà, kiểm soát ô nhiễm không khí, cải thiện chất lượng không khí trong nhà*

Acknowledgement: This research is funded by Office for International Study Programs (OISP), Ho Chi Minh City University of Technology (HCMUT), VNUHCM under grant number **SVOISPLV-2022-MT&TN-17**. We acknowledge the support of time and facilities from HCMUT, VNUHCM for this study.

COUNCIL 3
School of Industrial Management
Faculty of Transportation Engineering
Faculty of Applied Science

DESIGNING AN ELECTRIC VEHICLE POWERTRAIN SYSTEM AS EDUCATIONAL APPARATUS

(THIẾT KẾ HỆ THỐNG ĐỘNG LỰC XE ĐIỆN HAI BÁNH PHỤC VỤ CÔNG TÁC GIẢNG DẠY)

Tran Dang Long[1,3*], Vuong Thoi Hao[1,2,3], Nguyen Xuan Nam[1,2,3], Nguyen Nhu Phuc[1,2,3], Ngo Minh Tan[1,2,3]

[1] Office for International Study Programs, Ho Chi Minh City University of Technology (HCMUT), 268 Ly Thuong Kiet Street, District 10, Ho Chi Minh City, Vietnam
[2] Vietnam National University Ho Chi Minh City, Linh Trung Ward, Thu Duc City, Ho Chi Minh City, Vietnam.
[3] Faculty of Transportation Engineering, Ho Chi Minh City University of Technology (HCMUT), 268 Ly Thuong Kiet Street, District 10, Ho Chi Minh City, Vietnam
[*] Corresponding author: trandanglong@hmcut.edu.vn

Abstract

To address the need to fully understand electric vehicles, a model that simulates an EV powertrain system's characteristics, structure, and operation is crucial for students and lecturers. The purpose of this project is to design an educational apparatus for an electric powertrain system that can simulate the characteristics, structure, and operation of an electric vehicle. The project will involve researching and analyzing existing electric powertrain systems of the OLA S1 electric scooter, designing an educational apparatus, and testing the apparatus's performance under various operating conditions. The apparatus will provide a simplified representation of an electric powertrain system, helping students to better understand the dynamic characteristics that underlie electric vehicle technology.

Keywords: *Electric powertrain, dynamic characteristics, educational model, electric vehicles*

1. INTRODUCTION

Electric powertrains are becoming more sustainable and recently many automakers have introduce new electric vehicles. Therefore, automotive engineering students should have a clear understanding of electric powertrains. However, electric powertrain systems can be very complicated, so it is critical to have a low-cost, precise, and reliable educational apparatus.

An electric powertrain educational apparatus is based on the working principle of a dynamometer. It is specifically designed for illustrating an electric motorcycle powertrain operating on variable road conditions. The powertrain can accurately simulate different driving and road conditions, while also providing reliable powertrain parameters to the students. In this paper, we will discuss the electric powertrain apparatus' technical design and its various components, such as BLDC motor, rolling mass, load generator, and measurement devices. We will also discuss the control systems' characteristics, such as accuracy, precision, and quick responses.

As the motorcycle is operating on a road, the total resultant force acting upon the motorcycle's tire consists of driving force, aerodynamics force, rolling resistant force, gradient force, and inertial force. These forces' direction and magnitude combined with the motorcycle's mass will determine the acceleration of the vehicle and can be calculated as follows:

$$F_D - F_{RL} = m_v \dot{v}_v \qquad (1.1)$$

Where:

$$F_{RL} = F_{f1} + F_{f2} + F_\omega + F_j = F_f + F_\omega + F_j$$

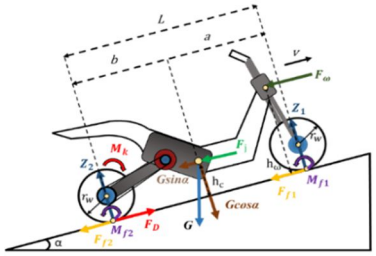

Figure 1. Forces acting upon a motorcycle on road condition

2. GENERAL LAYOUT DESIGN

2.1. Specifications of the used vehicle for designing the model

Table 1. OLA S1 Specification

No.	Parameter	Value
1	Weight with 2 people	250 (kg)
2	Max speed	95 (km/h)
3	From $0-60\ km/h$	5,9 (s)
4	Driving wheel	$110/70-R12$
5	Front brake – Disc brake	220 mm
6	Rear brake – Disc brake	180 mm
8	Rated/Max Power	5,5 (kW)/ 8,5 (kW)
9	Transmission ratio	3
10	Battery capacity	3 (kWh)

2.2. Determination of dynamic parameters for the chosen vehicle while moving on the road

- Full – load weight: $m_{vehicle} = 250$ (kg) (2 people seated).
- Climbing angle: $\alpha = 0$, Due to the limitation of the subject, only simulate when the vehicle moves on a level road.
- The rolling resistance coefficient of the good condition road: $f = 0{,}018$.
- Air density at normal conditions (temperature 20°C and 1 atm atmosphere): $\rho = 1{,}204\ kg/m^3$
- Vehicle max speed: 95 km/h.
- Area of frontal wind resistance of the vehicle: $A = B \times H = 0.85 \times 0.9 = 0.765\ (m^2)$
- Aerodynamics coefficient: $C_d = 0.5$

2.3. Selecting the electric motor

Based on the specifications of the simulated vehicle engine (rated/maximum power: 5.5 kW/ 8.5 kW), we choose **Golden Motor's 5 kW BLDC Motor Liquid Cooled** motor as the driving force for the model.

Table 2. Technical specification of 5 kW BLDC Motor Liquid Cooled motor

No.	Parameter	Value
1	Rated voltage	72 (V)
2	Rated/Maximum power	5 / 9 (kW)
3	Rated/Maximum speed	$3500\ /\ 5000\ (rpm)$
4	Maximum torque	28 (N. m)
5	Efficiency	91%
6	Weight	11 (kg)

Figure 2. 5 kW BLDC Motor Liquid Cooled Motor

2.4. Calculating and choosing generator

Total forces acting on the vehicle when traveling on the road.

- Gradient resistant force:

$$F_l = m.g.\sin(\alpha) = 250 \times 9.81 \times 0 = 0\ (N)$$

- Rolling resistant force:

$$F_f = f \times m \times g \times \cos(\alpha) = 0.018 \times 250 \times 9.81 \times 1 = 44.145\ (N)$$

- Aerodynamic resistant force:

$$F_\omega = \frac{1}{2} \times \rho \times C_d \times A \times v^2 = \frac{1}{2} \times 1.204 \times 0.5 \times 0.765 \times (\frac{80}{3.6})^2 = 113.7172\ (N)$$

- The total resistant force equation:

$$F_{res} = F_l + F_f + F_\omega = 0 + 44.145 + 113.7172 = 157.8622\ (N)$$

- The power of the generator needed:

$$P_{needed} = F_{res} \times v = 157.8622 \times \frac{80}{3.6} = 3508.049\ (W)$$

$$P_{generator} = P_{needed} \times \frac{1}{\eta.DOD} = 3508.049 \times \frac{1}{0.9 \times 0.85} = 4585.685\ (W)$$

⇨ We choose **3-phase AC asynchronous 7.5 kW** motor for ease of controlling and maintenance.

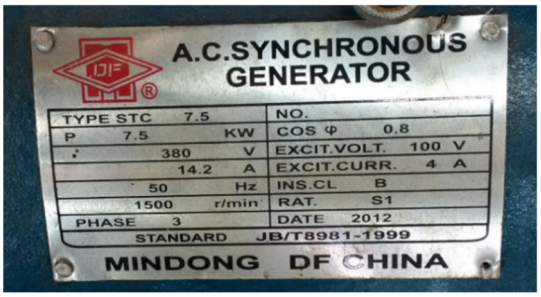

Figure 3. 7.5 kW AC Synchronous generator

2.5. Rolling mass design

From the equation of moment of inertia of the resistance force generator:

$$I_{sys} = m_{vehicle}.r_{rulo}^2 = 250.r_{rulo}^2$$

Where: $m_{vehicle} = 250$ (kg).

Choose steel as material with specific weight: $D = 7800(\ kg/m^3)$.

While we are calculating, divide the rolling mass into 2 separate parts: Hollow cylinder and solid cylinder.

Moment of inertia:

$$I = \frac{1}{2}.D.\pi.2.w_2\left(\frac{d_2}{2}\right)^4 + \frac{1}{2}.D.\pi.w_1\left(\left(\frac{d_1}{2}\right)^4 - \left(\frac{d_2}{2}\right)^4\right) = 250.\left(\frac{d_1}{2}\right)^2 \quad (2.1)$$

Rolling will have the shape and the parameter shown in Fig. 4.

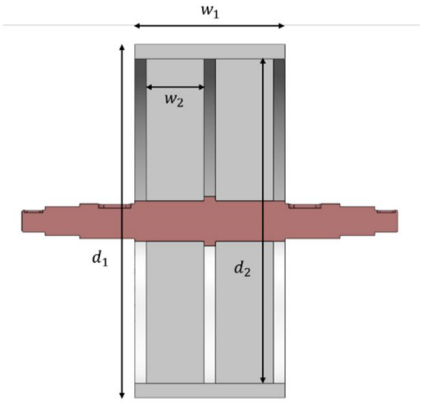

Figure 4. Parameter and Shape of rolling mass

From the standard material and calculated parameter, choose the size of the rolling mass:

$$d_1 = 610\ (mm) = 0{,}61\ (m).$$

$$d_2 = 560\ (mm) = 0{,}56\ (m).$$

$$w_2 = 100\ (mm) = 0{,}1\ (m).$$

Add in the (2.1), we have:

$$w_1 = 260\ (mm) = 0{,}26\ (m)$$

Rolling mass weight: $m = 477$ (kg).

2.6. General layout

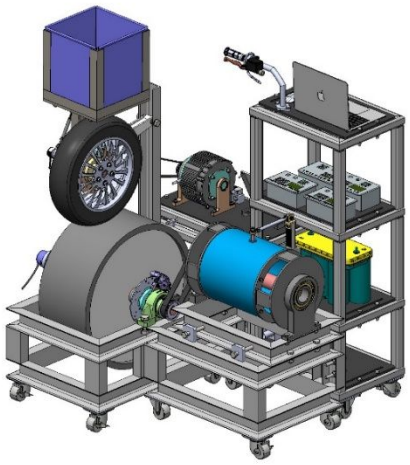

Figure 5. The 3D general layout of the Electric powertrain system

3. METHODS AND IMPLEMENTATION

The vehicle must have the applied force of this resistance and the inertia to function on the road. During the vehicle's operation on the road, the vehicle must experience these resistant forces including rolling resistance, gradient resistance, aerodynamics drags, and inertia force only when accelerating or decelerating. The dynamics of vehicle motion expressed in drive cycles and the vehicle systems must be developed and then implemented in Simulink as subsystems, blocks, and signals in order to use equation-based modeling. The equations that control vehicle motion and the vehicle systems required for modeling are outlined in the following sections. When a vehicle is accelerating, the vehicle is subject to the forces described in Equation below.

$$F_T - F_{RL} = m_v v_v \quad (3.1)$$

Where:

F_T: the tractive force which the electric machine delivers.

F_{DL}: road load forces.

M: vehicle mass.

v_v: the velocity in the tangential direction of the roadway.

3.1. Establishing simulation model of driving force

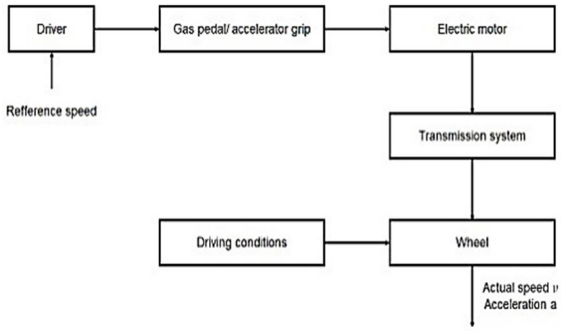

Figure 6. General layout diagram of vehicle's powertrain system

To the desired speed, the user controls through changing the position of the scooter, resulting in the engine changing operating mode, different states, the transmission system may have changes (transmission index, etc.), ultimately making the speed of the wheel rotation and the wheels angular velocity [4].

The rotational speed and the angular velocity of the wheel is also the cause of changing the barriers of the environment affecting the vehicle, which also leads to a change in the rotational speed and the accelerating angle of the vehicle.

Based on practical system, establishing physical model of speed controller is shown in Figure 7.

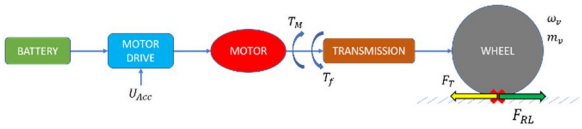

Figure 7. Physical model of speed controller for electric motorcycle driven by BLDC motor.

The simulation platform's driver model was utilized to recreate the driver's operational response to the brake and accelerator. The driver model took the required throttle opening and brake torque as inputs and converted them into outputs via the PI controller for modulating the vehicle dynamics at the next instant. The simulation platform also calculated the difference between the actual and desired vehicle speeds and their respective averages.

The wheel driving force is mostly the total of the different forms of resistance experienced when driving, including air resistance, rolling resistance, slope resistance, braking force, and inertia resistance. The rotational speed of the wheel and the vehicle speed at each instant might be determined using this mathematical model of dynamics, acting as feedback to the transmission system and driver model for adjusting the motorcycle's instantaneous motion.

In order to simulate the performance and energy consumption of the test motorcycle when actual driving on roads, the world motorcycle test cycle (WMTC – part 1) [7], which was shown in Fig. 8.

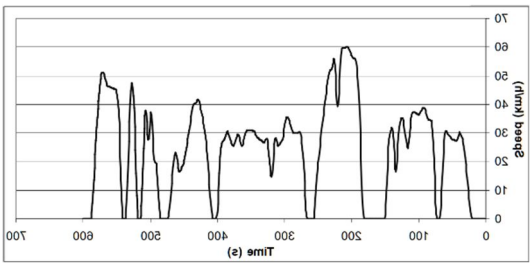

Figure 8. World Motorcycle Test cycle (WMTC): part 1

This research focused on vehicle and maximal speed ≤ 60 km/h, referring to urban driving. The total driving time and maximum driving speed for WMTC were 600 s and 60 km/h, respectively.

From Fig. 8, we set the WMTC as the reference speed and build up a numerical model to evaluate the efficiency of this controlling algorithm. The specifications of BLDC motor that we use in this work are shown in the table below:

Table 3. Specifications of used motor

No.	Parameters	Value
1	Rated Voltage	72 (V)
2	Rated/ Max Power	5 / 9 (kW)
3	Rated/ Max angular velocity	3500 / 5000 (rpm)
4	Maximum torque	28 (N. m)
5	Maximum efficiency	91%

3.2. Algorithm of road load simulation

This project utilizes a three-phase AC synchronous machine as the absorber unit capable to work in simulating vehicle road load. Road load simulation is to control the electromagnetic resistive force Fe of the electric machine which makes the rotational motion of the wheel on the apparatus as the rotational motion of wheel on the road. It means with the differences of working conditions ($F_{RL} \neq F_{DL}$), the tractive force and acceleration of the vehicle apparatus are the same as that of the vehicle on the road ($F_D = F_T$, and $\dot{v}_D = \dot{v}_T$, respectively) as shown in Fig. 9 and Fig. 10.

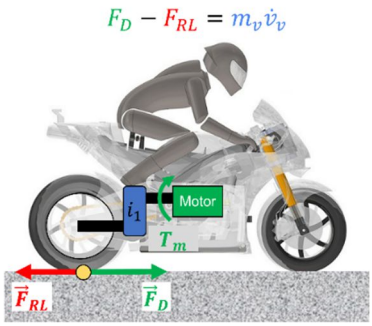

Figure 9. Longitudinal forces of vehicle on the road

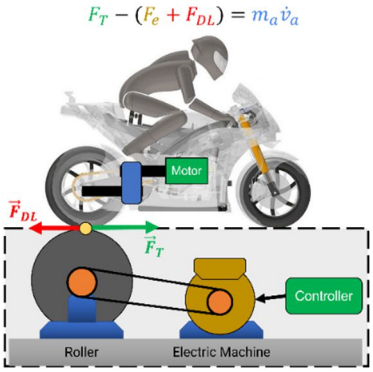

Figure 10. Longitudinal forces of vehicle on dynamometer

As shown in Fig. 9 and Fig. 10, if the resistive forces of the two model are not the same ($F_{RL} \neq F_{DL}$), then F_D is not equal to F_T, so it leads to the wrong simulation results of vehicle characteristics. Therefore, the electric machine of apparatus must add more electromagnetic resistive force F_e to simulate road load ($F_{RL} = F_{DL} + F_e$), than the F_D will be equal to F_T. These explainations are summarized by the equations:

$$\begin{cases} F_D = m_v\dot{v}_v + F_{RL} \\ F_T = m_a\dot{v}_a + F_{DL} + F_e \end{cases} \quad (3.2)$$

The value of $\dot{v}_a$ and $\dot{v}_v$ is define by:

$$\dot{v}_v = \frac{F_T - F_{RL}}{m_v} \quad (3.3)$$

The value of $\dot{v}_a$ is equal to the value of $\dot{v}_v$ because at the same time, with the affect of electromagnetic force F_e, the working conditions of vehicle apparatus and vehicle on the road is the same, so the acceleration and longitudinal tractive forces of these two model are the same.

The resistive electromagnetic force F_e is calculated by $F_D - F_T$:

$$F_e = F_{RL} - F_{DL} + (m_v - m_a)\dot{v}_v \quad (3.4)$$

The algorithm of vehicle road load simulation is designed base on this equation. The control diagram will become:

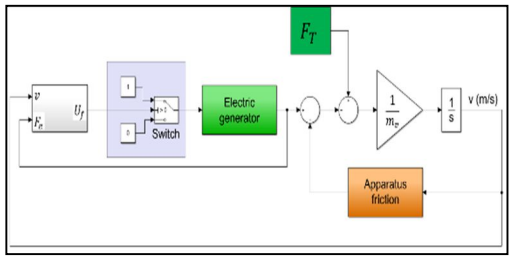

Figure 11. Control diagram for vehicle road load simulation

As shown in Fig. 11, the inputs of the controller is linear speed of apparatus wheel and electromagnetic force from electric machine. The controller will calculate the current tractive force of the apparatus F_T, resistive friction force on the apparatus F_{DL}, desired road load F_{RL}, current and desired acceleration $\dot{v}_a$ and $\dot{v}_v$, then define the desired electromagnetic force F_e.

If the value of F_e is greater than zero ($F_e > 0$), the switcher will turn on the generator by letting the voltage from battery flows to the excitation part of the electric machine to generate electromagnetic force.

If the value of F_e is less than or equal to zero ($F_e \leq 0$), it means the electromagnetic resistive force from the electric machine exceeds the desired value, so the switcher will turn of the generator by cutting off the excitation voltage from battery.

4. RESULTS AND DISCUSSION

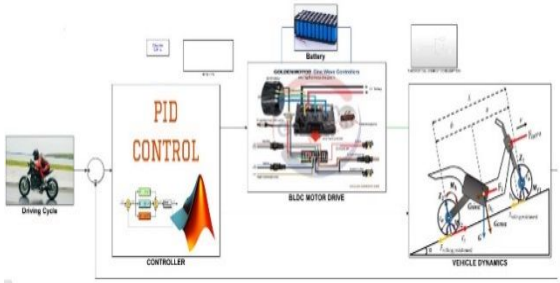

Figure 12. Numerical model of powertrain system in Simulink

In this project, we will examine the speed control algorithm built above when the electric motor runs according to a drive cycle but there is a change in the weight of the vehicle and also the coefficient of resistances on vehicles (this means changing the total road load force affecting the car when the vehicle moves on the road) as below:

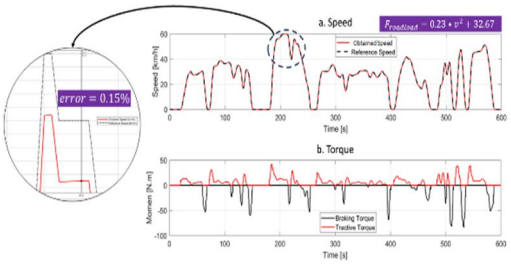

Figure 13. The Tractive torque and Brake torque response to speed upon the WMTC part 1 driving cycle

As you can see from the figure above, we could generate accurate, precise speed with small speed error (nearly 0.15%). Besides that, the braking torque and tractive torque also fluctuate sequently to make the powertrain system create actual speed change critically with the reference speed. Whenever we increase the coefficient of resistance – we could realize the tractive torque would go up (while braking torque has downward change due to higher inertia of whole system)

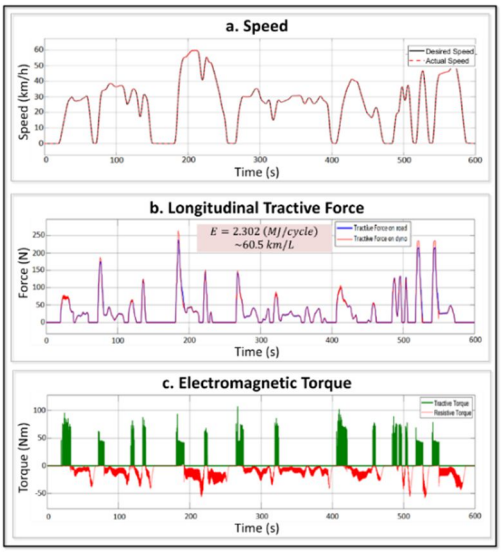

Figure 14. Calculated dynamometer response to a total motorcycle weight of 160 kg upon the WMTC part 1 driving cycle

As shown in Fig. 14, the inertial mass of simulating model is a quite less than the inertial mass of roller (m_v = 160kg compare to m_a = 250 kg). Therefore, in the accelerating parts, the electric machine will provide the tractive torque (green line) to simulate the vehicle inertia, and vice versa, when the motorcycle decelerates, the electric machine will also increase the resistive torque (red line), to make sure that the vehicle operating on the dynamometer is the same characteristics as that vehicle operating on the road.

When all the working conditions on the apparatus are the same as the working conditions on the road, the simulating vehicle will have the same longitudinal dynamics characteristics, and the tractive torque of vehicle on the road is the same as the tractive torque of vehicle on the apparatus. It leads to the tractive torque of vehicle operating on the road (blue line) is the same as the tractive torque of vehicle operating on the apparatus (red line).

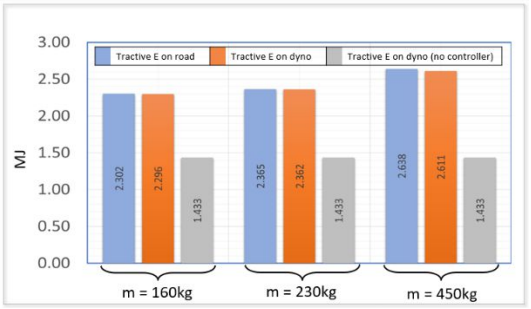

Figure 15. Comparison of calculated tractive energies on apparatus and road under WMTC part 1 driving cycle

The results of Fig. 15 show the comparison of calculated tractive energies on apparatus and road under WMTC part 1 driving cycle with the mass of 160kg, 230kg and 450kg. The tractive energies on apparatus (orange columns) and on road (blue columns) will increase with the increase of vehicle mass.

The tractive energy on apparatus will not be changed if the controller is not working (grey columns), so the simulating results in this case is wrong.

With one set of control parameters, the error of the apparatus will be more deviation if the mass is larger (2% for the mass of 160kg, 3% for the mass of 250kg, and 6% for the mass of 450kg). It can be concluded that the control parameters should be adjusted up to the vehicle mass before simulating to get the better results.

5. CONCLUSION

In conclusion, an electric powertrain system apparatus for teaching purposes is critical in automotive engineering education. With the growing need for green transportation, electric powertrains have become a more viable solution for sustainable development. Therefore, students must learn about electric powertrain design, working principles, and operation. In this paper, the educational apparatus provides an effective and low-cost way to teach students the operating principles of electric powertrains, including BLDC motor control, battery performance and efficiency, and energy management. Flexibility in experimentation and operation can be achieved by the fully modular design of the apparatus. In addition, the user interface lets students

interact with and understand the apparatus's control system easily.

Overall, the electric powertrain system apparatus presented in this paper is an efficient tool for educating engineering students in the electric automotive field.

Acknowledgement

This research is funded by Office for International Study Programs (OISP), Ho Chi Minh City University of Technology (HCMUT), VNUHCM under grant number **SVOISP-2022-KTGT-102**. We acknowledge the support of time and facilities from HCMUT, VNUHCM for this study.

References

[1] Assoc. Prof. Dr. Pham Xuan Mai, "Automotive Theory", National University Publishing House Ho Chi Minh City, 2004.

[2] Chang-liang Xia, "Permanent Magnet Brushless DC Motor Drives and Controls", Wiley, 2012.

[3] Fachkunde Faraftfahrzeugtechnik, "Specialization in Modern Automotive and Motorcycle Engineering", Youth Publishing House, 2016.

[4] Juha Pyrhönen, Tapani Jokinen, Valéria Hrabovcová, "Design of Rotating Electrical Machines", Wiley, 2014.

[5] Le Phan Hong Nguyen, "Thiết kế bộ điều khiển mô phỏng quán tính xe và lực cản đường cho bệ thử dây đai vô cấp" - Luận văn tốt nghiệp 2023.

[6] Nguyen Huu Can, "Theory of Automobiles and Tractors", Hanoi Science and Technology Publishing House, 2005.

[7] Nguyen Huu Loc, "Fundamentals of Machine Design Textbook", Vietnam National University Ho Chi Minh City Publishing House, 2016.

[8] T. J. Barlow, S. Latham, I. S. McCrae and P. G. Boulter. Res in June 2009, Version 3, page 59.

RECONSTRUCTING THE CONDUCTIVITY DISTRIBUTION IMAGING IN BIOLOGICAL TISSUE SIMULATION ENVIRONMENT BY ELECTRICAL IMPEDANCE TOMOGRAPHY

(TÁI TẠO HÌNH ẢNH SỰ PHÂN BỐ ĐỘ DẪN ĐIỆN TRONG MÔI TRƯỜNG GIẢ LẬP MÔ SINH HỌC BẰNG PHƯƠNG PHÁP CẮT LỚP ĐIỆN TRỞ KHÁNG)

Minh Quan Cao Dinh[1,2], Quoc Tuan Nguyen Diep[3], Anh Tu Tran[1,2], Trung Nghia Tran[1,2,*]

[1] Faculty of Applied Science, Ho Chi Minh City University of Technology (HCMUT), 268 Ly Thuong Kiet Street, District 10, Ho Chi Minh City, Vietnam
[2] Vietnam National University Ho Chi Minh City, Linh Trung Ward, Thu Duc City, Ho Chi Minh City, Vietnam
[3] Doctor Quoc Ltd., D20A/42 Doan Nguyen Tuan, Hung Long Ward, Binh Chanh District, Ho Chi Minh City, Vietnam
[*] Corresponding author: ttnghia@hcmut.edu.vn

Abstract

Electrical Impedance Tomography (EIT) is a technique that reconstructs the electrical conductivity distribution in a turbid medium and displays the structures and irregularities within using recorded voltage data. Comparing this imaging technology to existing methods such as Magnetic Resonance Imaging (MRI), Computed Tomography Scan (CT-Scan), and Ultrasonic, the benefits include non-ionization, non-invasive, impact and continuous monitoring, optimal design, and cheaper manufacturing costs. The application of EIT has been demonstrated in several medical fields, including the diagnosis of pneumothorax, the evaluation of pulmonary edema, and the assessment of ventilation distribution across various breathing modes. The EIT is also being investigated for use in imaging reconstruction utilized to obtain pictures for geological exploration, environmental sciences, industrial applications, and medical imaging. In this study, a system of 16 electrodes is created to replicate biological tissue by simulating the inside milieu of the human body with ground pork. The studies that have been proven are done with a phantom while varying the frequencies between 10 kHz and 100 kHz. The measured data is gathered and processed using an Arduino and a PC. The cross-sectional picture is recreated using Electrical Impedance Tomography and Diffusion-based Optical Tomography (EIDORS) software. The reconstructed images achieved a high level of precision in accurately representing the position and size of the subject under examination, particularly when the frequency used for imaging was set at 100 kHz. This suggests that the study successfully demonstrated the capability of Electrical Impedance Tomography (EIT) to provide detailed and accurate imaging results. This study introduced several novel aspects. It utilized a system of 16 electrodes to mimic biological tissue, using ground pork as a medium to simulate the electrical conductivity variations present in living organisms. The study investigated a range of frequencies (10 kHz to 100 kHz) for imaging, allowing the researchers to evaluate the effects of different electrical signals on the quality of reconstructed images. Notably, the study placed particular emphasis on imaging at 100 kHz to explore the optimal frequency for achieving precise image reconstruction.

Keywords: *electrical impedance tomography, EIDORS, electrodes, frequency, ARDUINO*

1. INTRODUCTION

Electrical Impedance Tomography (EIT) is a technique that has shown promise in reconstructing the electrical conductivity distribution within biological tissue. To simulate conductivity distribution in biological tissue, several studies have utilized ground pork as a suitable medium. By replicating the electrical properties of living organisms, these investigations aimed to create controlled experimental conditions for assessing the capabilities of EIT.

In a study by Xie et al. (2018), ground pork was employed to simulate biological tissue for EIT measurements. The researchers demonstrated the feasibility of using EIT to reconstruct conductivity images in this medium, highlighting its potential for medical imaging applications. However, the study primarily focused on a limited frequency range and did not explore the effects of varying frequencies on image reconstruction accuracy [1].

Another study by Zhang et al. (2019) investigated the use of EIT with ground pork as a phantom for assessing electrical impedance variations. The researchers explored the impact of different frequencies (ranging from 10 kHz to 100 kHz) on the reconstructed images. While this study provided valuable insights into the frequency-dependent behavior of EIT in pork-based phantoms, it had a limited number of electrodes and did not examine the positioning or size accuracy of the reconstructed images [2].

To address some of the limitations of previous studies, several investigations have employed a system with 16 electrodes to improve imaging precision. For example, Liu et al. (2020) [3] utilized a 16-electrode system with ground pork to simulate biological tissue and performed EIT measurements at various frequencies. The study focused on investigating the impact of electrode placement on image reconstruction accuracy. The findings demonstrated the importance of optimal electrode positioning in achieving high-resolution conductivity images. Similarly, Li et al. (2021) [4] conducted a study using a 16-electrode system with ground pork as a phantom for EIT imaging. The researchers aimed to optimize the reconstruction algorithm to improve the accuracy of conductivity images. They explored different algorithms and evaluated their performance in terms of image quality, precision, and computational efficiency.

Despite the valuable insights provided by these studies, several limitations should be considered. First, the use of ground pork as a phantom has inherent differences in electrical properties compared to actual human tissue, which may limit the direct translation of findings to clinical applications. Additionally, the studies often employed simplified models that may not fully capture the complexities of real biological tissues. Moreover, the number and placement of electrodes can impact the spatial resolution and accuracy of the reconstructed images.

In summary, previous studies have utilized ground pork as a phantom for simulating conductivity distribution in biological tissue using EIT. While these investigations have contributed to our understanding of EIT imaging, they have limitations in terms of frequency range exploration, electrode configuration, and the direct applicability of findings to clinical settings. Further research is needed to overcome these limitations and advance the use of EIT for accurate and reliable conductivity imaging in biological tissues [5].

2. METHODS AND IMPLEMENTATION

2.1. Block diagram

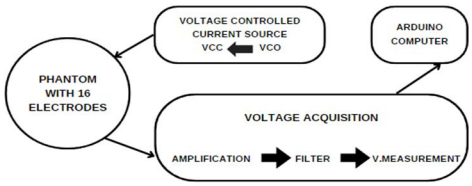

Figure 1. Block diagram of a standard EIT system

A typical schematic of a 16-electrode EIT system with its constituent parts is shown in Figure 1. The array of electrodes is fastened to the basin. For biological tissue simulation, a solution that includes ground pork is placed in the basin to simulate the environment in the body. With the neighboring electrode method, a current source creates a steady sinusoidal alternating current to inject the phantom surface. Through nearby electrodes, the current is applied. Without including the pairings containing both the current electrodes, the voltage is measured successively from all other nearby electrode pairs. The voltmeter and current injector electrodes are switched between the various electrodes using a multiplexer circuit. Voltage is measured with a demodulator and voltmeter. Filters are employed, and the computer is interfaced with using the Analog to Digital Converter (ADC) module which transforms analog signals into digital signals [6].

2.2. Current injection and data processing

An Arduino Mega-2560 is used in this research to detect voltage and control the multiplexer module. The modified Howland-based voltage control current source is made using the Voltage-Controlled Oscillator (VCO) and the Voltage-Current Converter (VCC) with two high-speed Op-Amp AD811. The exact sinusoidal waveform produced by the VCO is common for most applications. In this work, we use a variety of frequencies, between 10.0 kHz to 100.0 kHz, and the generated current ranges from 0 to 100 mA to investigate the voltage distribution in biological tissue simulation.

The Voltage-Controlled Oscillator (VCO) circuit functions as a signal generator to generate an alternating voltage in the system. The alternating voltage can be produced by any commercially available function generator or by using a voltage-controlled oscillator (VCO) circuit [6]. In this study, we used Tektronix AFG3252C to create frequencies

The Voltage-to-Current Converter (VCC) and a waveform generator make up a common current source seen in EIT systems. Having a high output impedance is necessary for the VCC in an EIT system since it needs to be stable and very precise. Thus, it is crucial to consider how this component is designed. In most cases, the sinusoidal waveform produced by the waveform generating portion, whether in digital or analog form, is the waveform that is

employed in EIT systems. The following are the key characteristics of a typical waveform generator: an accurate output waveform, a low output impedance, a broad bandwidth, and a constant amplitude over the frequency range. A high output impedance, linearity in converting voltage to current, the precision of output waveform, support for a wide variety of loads, and correct operation in a wide range of frequencies are other key characteristics of an outstanding Voltage-to-Current Converter (VCC) component [6].

2.3. Filter

To have an exact waveform without any jitter, noise, and distortion, and also to create low output impedance for the next stage a Butterworth band-pass filter has been designed and put between the VCO and VCC parts. There are three filters that the signal must pass: 50.0 Hz notch filter, low pass filter, and high pass filter to get rid of the noise. When the multiplexer receives the boundary potentials, it measures the voltage and sends the information immediately to Arduino, where it is transformed into Excel data for image reconstruction [5].

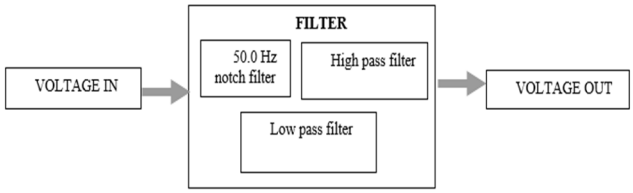

Figure 2. Block diagram of Band-pass filter

2.4. Multiplexer module

In EIT, a boundary potential is measured after a specific current injection technique injects a sinusoidal current signal with a constant amplitude to the tested item's boundary. Consequently, switching the surface electrodes is the main task, which calls for a programmed electrode-switching system. The practical phantom with a module made up of four analog multiplexers the data-gathering apparatus. The electrode switching module is created by shorting all of the comparable pins on four 16:1 MUXs and connecting the common point to the relevant electrodes. The system must measure the voltage potential at all electrodes while also applying a specific current to a selection of those electrodes. Many measurements must be made in such a case, and a high-speed switching mechanism is required [3].

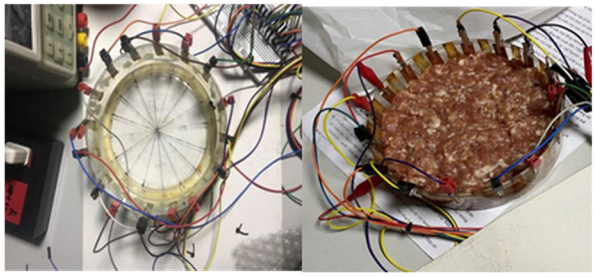

Figure 3. Illustration of the phantom (left) and the phantom filled with ground pork to simulate biological tissue (right).

2.5. Phantom

As seen in Fig. 3, the practical phantom is a shallow basin (150.0 mm in diameter) with sixteen stain steel electrodes equally spaced throughout the inside wall. Electrodes are composed of a rectangular sheet of high-quality stain steel that is 1.0 mm thick. The EIT electrodes are connected to the system via conventional ECG cables and steel crocodile clips. 500 grams of ground pork is filled inside the tank, the meat composition includes a mixture of lean and fat that can simulate the environment inside the human body, shown in **Figure 3.**

The phantom used in the studies was created using ground pork as a medium to simulate biological tissue. Ground pork was carefully shaped and arranged to resemble the internal milieu of the human body, providing a close approximation of the electrical conductivity variations found in living organisms. This pork-based phantom allowed for controlled experimental investigations in Electrical Impedance Tomography (EIT) imaging. However, it's important to note that while ground pork serves as a convenient substitute, there are inherent differences in electrical properties compared to real human tissue. Nevertheless, the use of ground pork as a phantom provided a practical and accessible approach for studying conductivity distribution in biological tissue using EIT.

3. RESULTS

The resistivity distribution is reconstructed using the EIDORS toolkit. Electrical Impedance Tomography and Diffuse Optical Tomography Reconstruction Software (EIDORS) are used for EIT reconstruction and modeling for medical and industrial applications. This is the platform with many reproducible algorithms and is run on Matlab.

To test the conductivity for image reconstruction, we do 2 experiments with non-conductive and conductive objects. The non-conductor is an acrylic cylinder, with a diameter of 30 millimeters and a height of 80 millimeters. For conductive items, a copper block 50 millimeters high and 40 millimeters in diameter is used, reproducing images at 3 frequencies: 10 kHz, 50 kHz, and 100 kHz.

In the experiment with the non-conductive acrylic cylinder, the goal is to obtain an image reconstruction that confirms the absence of electrical conductivity within the object. Since the acrylic material does not conduct electricity, the resulting image should show a uniform distribution of low conductivity values across the cylinder. This serves as a reference point for comparison with the conductive object.

In the experiment with the conductive copper block, the objective is to observe and analyze the variations in electrical conductivity within the object at different frequencies. By capturing impedance data and reconstructing images at 10 kHz, 50 kHz, and 100 kHz, the EIT system can provide valuable insights into the conductivity distribution within the copper block.

At lower frequencies, such as 10 kHz, the electrical currents penetrate deeper into the conductive medium, allowing the imaging system to capture conductivity variations in the interior of the block. As the frequency increases to 50 kHz and 100 kHz, the sensitivity of the system too shallow conductivity changes improves, enabling the visualization of finer details and surface features. The reconstructed images at each frequency can reveal variations in electrical conductivity within the copper block, highlighting higher or lower conductivity regions. These images provide valuable information about the object's internal structure, material composition, and potential anomalies.

3.1. Non-conductive objects

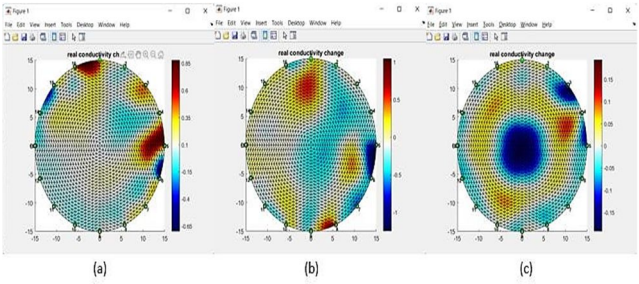

Figure 4. Reconstructed image by EIDORS using 1 non-conductive object placed center of a phantom; (a) 10.0kHz, (b) 50.0 kHz, (c) 100.0kHz

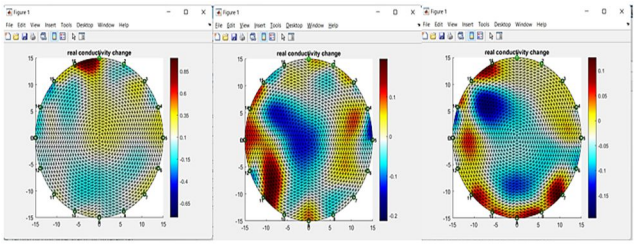

Figure 5. Images reconstructed with two non – conductive objects near the 10th and 14th electrodes; from left to right: 10.0 kHz, 50 kHz, and 100.0 kHz.

3.2. Conductive objects

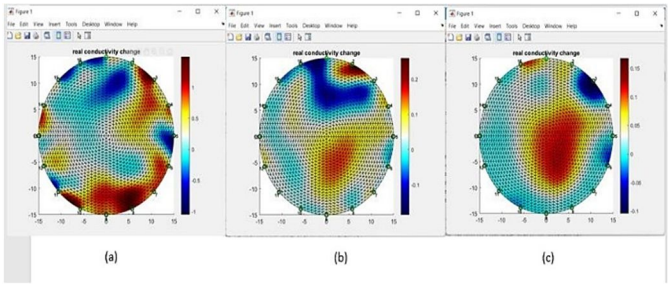

Figure 6. Images reconstructed with a conductive object near the center of the basin; (a) 10.0 kHz, (b) 50 kHz, (c)100.0 kHz.

In the first experiment, we put a non-conductive item in the center of the ground pork meat tank (**Figure 4**). In the second phantom, two non-conductive objects were put near the 10th and 14th electrodes (**Figure 5**). Experiments are conducted for measuring the voltage and reconstructing the cross-sectional image at 10.0 kHz, 50.0 kHz, and 100.0 kHz. The blue area represents the location of the objects. **Figure 6** illustrates the cross-sectional image reconstruction during measure at 3 different frequencies which are 10.0 kHz (left), 50 kHz (center), and 100.0 kHz (right) with a conductive item near the middle of the phantom.

4. DISCUSSION

The simulation experiments conducted at different frequencies using ground pork as a biological tissue surrogate have revealed that 100kHz is the most suitable frequency for conducting EIT studies in biological tissue imaging. This is because the highest-quality reconstruction images were obtained at 100kHz, indicating improved spatial resolution and image quality. The ground pork environment effectively replicated the electrical conductivity properties of biological tissues, suggesting that EIT is a viable option for medical imaging.

Using ground pork as a surrogate tissue can be a cost-effective and readily available alternative to using live human or animal subjects, which can be logistically challenging and unethical. These findings have implications in medical imaging, as EIT can potentially be used to diagnose and monitor various medical conditions.

One of the main challenges of the current EIT is the low spatial resolution. Research is focused on developing advanced image reconstruction algorithms to improve image resolution and quality. Further research is required to optimize the EIT technique and establish standardized protocols for clinical and industrial use. Nevertheless, this study highlights the potential of EIT in the field of medical imaging, particularly for monitoring and diagnosing lung function, blood flow, and breast imaging.

5. CONCLUSION

The studies are carried out in ground pork to imitate the bodily environment with various frequencies to create a low-cost electrical impedance tomography device. Replicating biological tissue in a lab setting can be a challenging task. One approach is to simulate the internal environment of the human body, such as temperature, pH, and ionic strength, to create a tissue-like medium for cell growth and differentiation. In this regard, ground pork has been suggested as a potential material for simulating biological tissue due to its similarities in water content, protein composition, and texture to actual tissue. Ground pork has been shown to provide a suitable environment for the growth of various cell types, including stem cells and cancer cells. Additionally, it has been used to simulate different tissues, such as muscle and adipose tissue. However, there are some limitations to using ground pork as a tissue mimic, including the presence of unwanted substances like antibiotics or hormones that may interfere with cell growth, and the inability to replicate the complex structures and functions of actual biological tissue.

The cross-sectional reconstructed resistivity distribution picture may be created by employing a 16-electrode self-developed prototype and EIDORS software. The outcome supported and validated the viability of self-developed EIT system-based cross-sectional image reconstruction. Among the frequencies used in this EIT system, preliminary studies suggest that 100.0 kHz is a good frequency for future investigations, with the potential to improve spatial resolution and image quality. With this frequency, EIT studies can be applied in many medical and industrial applications, including lung function monitoring, breast imaging, and cerebral blood flow monitoring. However, challenges need to be addressed to improve the accuracy and resolution of EIT images, as well as to develop standardized protocols and techniques for clinical and industrial use. Overall, the EIT system has shown tremendous potential and is an exciting area of research with numerous potential applications. With further research and development, EIT could potentially revolutionize medical imaging and industrial and environmental monitoring.

Conflicts of interest

The authors declare no conflicts of interest.

Acknowledgment

This research is funded by the Office for International Study Programs (OISP), Ho Chi Minh City University of Technology (HCMUT), VNUHCM under grant number **SVOISP-2022-KHUD-106**. We acknowledge the support of time and facilities from HCMUT, VNUHCM for this study.

References

[1] Xie, F., et al. (2018). Electrical impedance tomography system based on FPGA for tissue discrimination. IEEE Transactions on Biomedical Circuits and Systems, 12(1), 115-126.

[2] Zhang, X., et al. (2019). Simulating the conductivity distribution of biological tissue using electrical impedance tomography for educational purposes. Journal of Biomedical Physics & Engineering, 9(1), 99-108.

[3] Liu, J., et al. (2020). Investigation of image reconstruction accuracy in electrical impedance tomography with pork phantom. Journal of Healthcare Engineering, 2020, 1-10.

[4] Li, Z., et al. (2021). Improved conductivity image reconstruction algorithm for electrical impedance tomography based on adaptive finite element method. Biomedical Engineering Online, 20(1), 1-12.

[5] M. Cao Dinh et al., "Development a low-cost electrical impedance tomography system for non-invasively detecting abnormal in breast tissue - Phantom study-", Kalpa Publications in Engineering, vol. 4, pp. 1—8, 2021.

[6] Mohammad Khalighi, Bijan Vosoughi Vahdat, Mohammad Mortazavi, "Practical Design of Low-cost Instrumentation For Industrial Electrical Impedance Tomography (EIT)," 2012.

[7] Tushar Kanti Bera and J. Nagaraju, "A Low-Cost Electrical Impedance Tomography (EIT) Instrumentation for Impedance Imaging of Practical Phantoms: A Laboratory Study," the Third International Conference on Soft Computing for Problem Solving, Advances in Intelligent Systems and Computing 259, pp. 689-701, 2014.

[8] M. Cao Dinh et al., "Development of a low-cost electrical impedance tomography prototype and investigation of changing frequency effect on reconstructed cross-sectional images," 2021. ISBN: 978-604-73-9133-2.

DESIGNING THE GENERAL LAYOUT OF THE DYNAMOMETER USED FOR SMALL POWER ELECTRIC MOTOR

(THIẾT KẾ BỐ TRÍ CHUNG BĂNG THỬ ĐỘNG CƠ ĐIỆN CỠ NHỎ)

Le Do Minh Hoang[1,2,3], Truong Tan Phat[1,2,3], Le Duc Minh[1,2,3], Hong Duc Thong[1,3,*]

[1] Faculty of Transportation Engineering, Ho Chi Minh City University of Technology (HCMUT), 268 Ly Thuong Kiet Street, District 10, Ho Chi Minh City, Vietnam
[2] Office for International Study Programs, Ho Chi Minh City University of Technology (HCMUT), 268 Ly Thuong Kiet Street, District 10, Ho Chi Minh City, Vietnam
[3] Vietnam National University Ho Chi Minh City, Linh Trung Ward, Thu Duc City, Ho Chi Minh City, Vietnam
[*] Corresponding author: hongducthong@hcmut.edu.vn

Abstract

This research paper describes the design of a dynamometer to measure the power of an electric motor with a capacity of less than 1 kW. Through research, the 48V-600W BLDC motors and the Valeo 14V-90A automobile generator were selected as the basis for the design. In designing a general layout, the design is evaluated to ensure it does not overlap or collide with other details and clusters and works properly according to the dynamometer's principle. Additionally, critical dimensions are calculated for the purpose of ensuring the dynamometer is both compact and strong. The results of this research will create the development possibilities for small-power electric motors dynamometer designs to be used for common electric two-wheelers in Vietnam.

Keywords: *brushless motor, dynamometer, electric motor, general layout design*

1. INTRODUCTION

Electric motors can be found everywhere in the world today. In Vietnam today, more and more people are purchasing electric motorcycles to replace traditional motorcycles due to the benefits of lower fuel prices, lower maintenance costs, and so on. Furthermore, Vietnamese corporations such as Vinfast, Datbike, and others are involved in the production of electric motorcycles with reasonable prices and numerous incentives. As a result, checking and evaluating the technical-economic features of electric motorcycles is critical, but at the moment, assessing the performance of electric bikes in Vietnam has been uninteresting. and testing equipment is not yet widely available, and the cost of these devices is frequently prohibitively high.

The research, production, and refinement of details in the powertrain, as well as the electric motor of its own, require supporting equipment as well as testing equipment to evaluate study results, but this evaluation test equipment is now nearly nonexistent in our nation. Therefore, this study is aimed at contributing to the solution to this problem by building a general layout drawing.

Figure 1. The ZXDCM1208 in-wheel motor

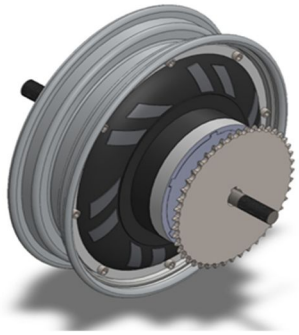

Figure 2. Sprocket installed on in-wheel motor

2. METHODS AND IMPLEMENTATION

2.1. Specification of brushless DC motor and alternator

Brushless DC motor

In this research, we used the brushless DC in-wheel motor ZXDCM1208 as the test sample.

The mechanical and electrical parameters are presented in Table 1.

Table 1. Specification of ZXDCM1208 BLDC motor

Power supply voltage	Nominal power at 48V	Hall sensor	Max. speed
48V	600W	Yes	700 RPM

Alternator

The Valeo SG9S116 alternator used for small truck SYM T880 has been used. This alternator was produced by France manufacturer Valeo. Its parameters have been introduced in Table 2.

Figure 3. The Valeo SG9S116 alternator

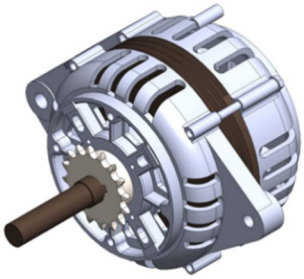

Figure 4. Installing the sprocket on alternator

2.2. Design and calculation

2.2.1. Speed ratio distribution

As the BLDC motor's operating speed range is n_{motor} = 100 ÷ 700 (rpm), and the alternator's operating speed range to work stability is $n_{alternator}$ = 1000 ÷ 8000 (rpm), the difference in working speed range between two components is too great, we must distribute the speed ratio appropriate for the BLDC motor and alternator to function properly.

In addition, we decide to use the roller chain drive because of its advantages such as simple, withstanding high load, easy to distribute transmission ratio, slip-free… However, the transmission ratio $u_{rollerchain}$ is limited at 6; therefore, we need 3 stages transmission to achieve the desired transmission ratio.

Due to the reason above, we assume the BLDC motor operates at two working speed ranges:

+ Low-speed range: 100 – 270 RPM using speed ratio 1:30.
+ High-speed range: 270 – 700 RPM using speed ratio 1:12.

2.2.2. Power transmission system

In this system, we preliminarily choose the 35B roller chain type, 35B chain sprocket because this type made from steel C45 and have lots of module that available on the market. The specifications are shown in Tables 2, 3 below. The sprocket's teeth number in Table 4 is chosen to satisfy the speed ratio as mentioned in Tables 2, 3 above.

Table 2. Specification of Valeo SG9S116

Rated power	1.2 kW
Rated current/voltage	90A/14V
Cut in speed	1000 RPM
Output at 3000 RPM	72 V
Output at 8000 RPM	85 V
Rotation direction	Clock-wise

Table 3. 35B roller chain

Type of roller chain, chain sprocket	Pitch (p_c) (mm)	Material
35B	9.525	Carbon steel (S45C)

Table 4. 35B Chain sprocket dimension

Teeth	*Outside Diameter D_o*	*Pitch diameter D_p*	*Inner diameter*			*Hub diameter BD*	*Sprocket thickness BL*	*Mass*
			Origin	*d_{min}*	*d_{max}*			
15	51	45.81	9.5	10.5	20	35	20	0.16
16	54	48.82	9.5	10.5	20	37	20	0.19

40	127	121.4	12.5	13.5	42	63	25	0.85
45	142	136.55	16	17	42	63	25	1.00
60	187	182	16	17	42	63	25	1.30

Center distance between sprockets

We concentrate on calculating the highest transmission ratio ¼ because if this ratio meets all of the verification criteria, the other transmission stage will be verified as well. The number of tooth on sprocket are used in this transmission ratio are 60 and 15.

The center distance a is preliminarily chosen by the formular below [3],

$$a = (30 \div 50)p_c \quad (1)$$

The number of pitches is preliminarily calculated by the formular [3],

$$X = \frac{2a}{p_c} + \frac{Z_1 + Z_2}{2} + \left(\frac{Z_2 - Z_1}{2\pi}\right)^2 \times \frac{p_c}{a} \quad (2)$$

With Z_1 is number of tooth of driving sprocket, Z_2 is number of tooth of driven sprocket.

Then we calculate the chain length [3]:

$$L = p_c X \quad (3)$$

Finally calculating the accurate center distance [3]

$$a = 0.25p_c E \quad (4)$$

$$where: E = \left[\mathrm{F} + \sqrt{(F)^2 - 8\left(\frac{\mathrm{z}_2 - \mathrm{z}_1}{2\pi}\right)^2}\right]$$

$$F = \mathrm{X} - \frac{\mathrm{z}_1 + \mathrm{z}_2}{2}$$

It is noticeable that the center distance should be reduce by (0.002÷0.004)a because of the chain sag.

Contact number of sprocket's tooth

Contact angle on driving sprocket [2]:

$$\beta_1 = 2\arccos\frac{D_{P2} - D_{P1}}{2a} \quad (5)$$

Contact angle on driven sprocket [2]:

$$\beta_2 = 2\pi - \beta_1 \quad (6)$$

Contact teethes of sprocket [2]:

$$Z_{ci} = Z_i \times \frac{\beta_i}{360} \quad (7)$$

Where, Z_i – number of sprocket's tooth, β_i – contact angle of sprocket.

Average velocity of the chain drive

$$v = \frac{\pi dn}{60000} = \frac{n_i Z_i p_c}{60000} \quad (8)$$

Where, n_i – rev per minute of sprocket (rpm).

Force applied on chain drive

Tension on the tight side (F_1) [3]:

$$F_1 \approx F_t \quad (9)$$

Where, $F_t = \frac{1000P}{v}$ (with $P = P_{elec.motor} = 0.6kW$) *[3]*.

Tension due to centrifugal force (F_v) [3]:

$$F_v = q_m v^2 \quad (10)$$

Where, q_m – mass of 1meter chain on 1 kg, $q_m = 0.41kg/m$ [3].

Initial tension/Weight of slack (F_o) [3]:

$$F_0 = K_f a q_m g \quad (11)$$

Where, a – length of the slack side = center distance (mm); K_f – Chain sag correction factor, K_f= 1 as the transmitting direction is vertical; g – Gravitational acceleration (m/s^2).

Shaft load

$$F_r = F_t K_m \quad (12)$$

Where, K_m – Chain weight ratio, K_m = 1.05 as the centerline of the chain is vertical [3].

Verify by the safety factor condition

$$\mathrm{s} = \frac{Q}{F_1 + F_v + F_0} > [\mathrm{s}] \quad (13)$$

where, Q - Ultimate tensile force (N), Q=9.1 kN; *[s]* - safety factor, s = 11.67 *[3]*.

Verify the power that can be transmitted

The required power of transmission line [7].

$$h_{pr} < [P] \quad (14)$$

$$h_{pr} = h_p \frac{a_1}{a_2} \quad (15)$$

Where, h_p – the power that is transmitted or input (kW), $h_p = P_{elec.motor} = 0.6kW$; a_1 - service factor [7]; a_2 - multi-strand factor [7], the allowable transmitting power [P] is 16.47 kW.

Verify the wear resistance of chain pitch

$$p_c \geq 600\sqrt[3]{\frac{P_1 K}{z_1 n_1 [p_o] \mathrm{K_x}}} \quad (16)\ [3]$$

Where: $[p_o]$ - the allowable pressure on the chain, calculated from the formula below [3]

$$[p_o] = \frac{[\mathrm{P}] \times 6 \times 10^7}{A z_{01} n_{01} p_c} \quad (17)$$

Where, A – area of one - strand chain: $A = d_0 b_0 \approx 0.28 p_c^2 = 17.16\ (mm^2)$; Z_{01} – number of teeth in experiment: $Z_{01} = 25$; n_{01} – Rotational speed of chain sprocket in experiment [3]. K_x – Strand factor X, $K_x = 1$ because using one strand.

K – the operation correction factor [3]

$$K = K_r K_a K_o K_{dc} K_b K_w \quad (18)$$

Where,

K_r – dynamic load correction factor, K_a – chain length correction factor, K_o – Orientation correction factor, K_{dc} – Tension correction factor, K_b – Lubrication correction factor, K_w – Operation shift correction factor.

Verify the number of impacts per second

$$\mathrm{i} = \frac{z_1 n_1}{15X} \leq [i] \quad (20)$$

Follow reference [8], we have $[i] = 95$ corresponding to the chain pitch $p_c = 9.525\ mm$ [3]

2.2.3. Shaft

For the shaft I, we use 1 sprocket with $Z_2 = 15$ teeth and 1 sprocket with $Z_3 = 60$ teeth. And shaft II uses 1 sprocket with $Z_4 = 15$ teeth and 1 sprocket with $Z_5 = 40$ teeth. SKF SY17 TF bearing is initially used for calculating with the specification in Table 5.

Select material and define allowable stress

Select shaft material is C45 steel, with low interference fit [3]:

- Maximum allowable bending stress: $[\sigma] = 80$MPa. Ultimate stress: $\sigma_b = 785$MPa. Yield stress: $\sigma_{ch} = 540$MPa
- Maximum allowable torsional stress: $[\tau] = 0.5[\sigma] = 0.5 \times 80 = 40\ (\mathrm{MPa})$

Tangent force acting on the chain [3]

$$\mathrm{F_t} = \frac{1000 \times \mathrm{P}}{v} \quad (21)$$

Calculating tangent force base on the low motor speed range since at low speed range as the motor produces maximum torque, which means it can create maximum tangent force. If the maximum tangent forces satisfy, the lower force will also satisfy.

Table 5. Dimensions of SKF SY17 TF [9]

Bore diameter	17 mm
Shoulder diameter of inner ring	≈ 24.2 mm
Base width	32 mm
Top width	18 mm
Width of inner ring	27.4 mm
Distance from locking device side face to thread center	4 mm
Height of spherical seat center	30.2 mm
Foot height	14 mm
Overall height	57 mm
Overall length	127 mm

The average velocity of chain at low speed range [3]

Roller chain velocity on shaft I:

$$v_1 = \frac{n_I Z_2 p_c}{60000} \quad (22)$$

Roller chain velocity on shaft II

$$v_2 = \frac{n_I Z_3 p_c}{60000} \quad (23)$$

Roller chain velocity on alternator shaft

$$v_3 = \frac{n_{II} Z_5 P_c}{60000} \quad (24)$$

Where, $n_I = 810$ RPM; $n_{II} = 3240$ RPM.

After having the peripheral forces, calculating all the forces of roller chain applied on the shafts [8]:

Force applied on shaft I

$$F_{r_{11}} = F_{t_1} \times K_m \quad (25)$$

Force applied on shaft I and II

$$F_{r_{12}} = F_{r_{21}} = F_{t_2} \times K_m \quad (26)$$

Force applied on shaft II

$$\mathrm{F_{r_{22}}} = \mathrm{F_{t_3}} \times \mathrm{K_m} \quad (27)$$

Where: K_m – the sprocket chain weight factor, (K_m = 1.15 when the roller chain is in horizontal) and equals 1 when the roller chain is arranged vertical [8]. F_{t1} – the tangent force between motor and shaft I. F_{t2} - the tangent force between shaft I and II. F_{t3} – the tangent force between shaft II and alternator.

Preliminary estimate diameter of shaft [3]

We have torque on shaft at low speed range is:

$$T = 9.55 \times 10^6 \frac{P}{n} \quad (28)$$

Where, n – revolution per minute on each shaft; P – power transmitted on each shaft.

Selecting preliminarily diameter of each shaft by formula:

$$d = \sqrt[3]{\frac{5T}{[\tau]}} \quad (29)$$

The distance between components on shaft is chosen preliminarily. The reaction forces on shafts I and II of a mechanical system were determined by utilizing the equilibrium equation on the xOz and yOz planes [3].

Equilibrium equation on xOz plane:

$$\begin{cases} \sum F_x = 0 \\ \sum M_{Ay} = 0 \end{cases} \quad (30)$$

Equilibrium equation on yOz plane:

$$\begin{cases} \sum F_y = 0 \\ \sum M_{Ax} = 0 \end{cases} \quad (31)$$

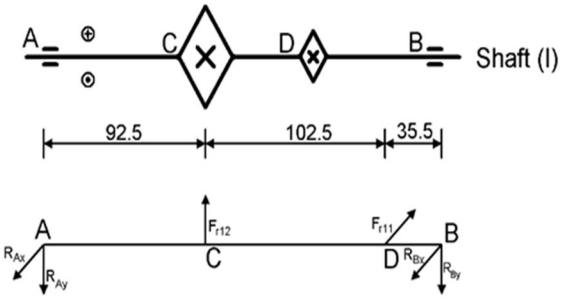

Figure 5. Analyzed forces act on shaft I

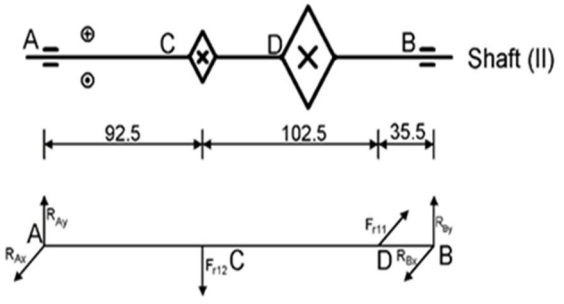

Figure 6. Analyzed forces act on shaft II

Total moment at cross-section of shaft:

After having the internal force diagrams provided, we could determine the most critical and dangerous point cross-section point on shaft. The components of the total moment at each point are calculated as follows:

$$M_i = \sqrt{M_x^2 + M_y^2 + 0.75T^2} \quad (32)$$

Where, M_i – total moment at considered cross-section; M_x, M_y – bending moment around x and y axis; T – torque acts on shaft.

Shaft diameter

The critical section is determined by calculating total moment then determining the shaft diameter for both shafts by formular [3]

$$d = \sqrt[3]{\frac{M}{0.1[\sigma]}} < d_{preliminary} \quad (33)$$

Where: M – total moment at the most critical cross-section on shaft; [σ] – maximum allowable bending stress.

Verify fatigue strength of shaft based on safety factor

The newly designed shaft structure ensures fatigue strength if the safety factor at dangerous sections satisfies the following conditions:

$$s = \frac{s_\sigma s_\tau}{\sqrt{s_\sigma^2 + s_\tau^2}} \geq [s] \quad (34)$$

Where: [s] – The allowable factor of safety is in the range of 1.5÷2.5; when [s] = 2.5÷3 we do not need to test the shaft according to the stiffness [3]. s_σ, s_τ – Factor of safety for bending and torsion stresses only.

The value s_σ and s_τ are determined according to the following formula [3]:

$$s_\sigma = \frac{\sigma_{-1}}{\frac{K\sigma_a}{\varepsilon_\sigma \beta} + \psi_\sigma \sigma_m}; \; s_\tau = \frac{\tau_r}{\frac{K_\tau \tau_a}{\varepsilon_\tau \beta} + \psi_\tau \tau_n} \quad (35)$$

Where: σ_{-1}, τ_r – Fatigue limit of the material is determined by: $\sigma_{-1} = (0.4 \div 0.5)\sigma_b$; $\tau_r = (0.22 \div 0.25)\sigma_b$ [3]

σ_{-1} = 383 (MPa), τ_0 = 226 (MPa) are selected (the shaft rotates in one direction, so r is 0).

ψ_σ, ψ_τ – Coefficients affecting the average stress to fatigue strength depend on the mechanical properties of the material. ε_σ, ε_τ – Dimensional coefficients; β – Surface increase factor depending on the surface processing method. K_σ, K_τ – Coefficient of influence of stress concentration on fatigue strength; σ_a, σ_m, τ_a, τ_m – Amplitude and average value of stress.

Due to the rotation of shaft, the bending stress changes according to the period of symmetry [3]:

$$\sigma_a = \sigma_{m_{ax}} = \frac{M \times 10^3}{W};\ \sigma_m = 0 \quad (36)$$

Torsional stress changes with dynamic circuit period when the shaft rotates in one direction [3]:

$$\tau_a = \tau_m = \frac{\tau_{max}}{2} = \frac{T \times 10^3}{2W_0} \quad (37)$$

Where: M – total moment at the most critical cross-section on shaft. T – torque at the most critical cross-section on shaft.

W – the section modulus under bending,

$$W = \frac{\pi d^3}{32} - \frac{bt(d-t)^2}{d}\ (\text{Nmm}). \quad (38)$$

W_0 – section modulus under torsion,

$$W_0 = \frac{\pi d^3}{16} - \frac{bt(d-t)^2}{d}\ (Nmm). \quad (39)$$

Where, b – key width (mm); h – key height (mm); t – key groove depth on shaft (mm)

Once the diameter was estimated, the key size is selected following *the Vietnam Standard 2261-77*.

Verification based on static strength (overload)

Checking static strength according to equivalent stress when overload [3]:

$$\sigma_{eq} = \sqrt{{\sigma_i}^2 + 3{\tau_i}^2} \le [\sigma]_{eq} = 0.8\sigma_{ch} \quad (40)$$

Where: σ_i – bending stress; τ_i – torsional stress

Checking keyseat based on impact stress

$$\sigma_d = \frac{F}{t_2 l_1} \le [\sigma_b] \quad (41)$$

Where: l_1 – length of key, $l_1 = l - b$ (mm); t_2 – Keyway depth on hub (mm). F – Peripheral force (N).

$$F = \frac{2T \cdot 10^3}{d} \quad (42)$$

$[\sigma_b]$: Maximum allowable stamping stress (MPa), $[\sigma_b] = 150$ (MPa) with key made of C45 steel [3],[8].

Checking keyseat based on shear stress

The shaft's shear stress values were calculated using the formula [3]:

$$\tau_c = \frac{F}{bl_1} \le [\tau_c] \quad (43)$$

Where: $[\tau_c]$ – Maximum allowable shear stress (MPa), F – Peripheral force (N).

2.2.4. Bearing

In this paper, the SKF SY 17 TF ball bearing pillow is chosen resulting from the detailed calculation of radial load and static equivalent force. This bearing has a capacity of 4.75kN which satisfies the requirements for both shaft I and II.

Table 6. SKF SY 17 TF ball bearing pillow calculation data [9]

Basic dynamic load rating C	9.56 kN
Basic static load rating C_0	4.75 kN
Fatigue load limit P_u	0.2 kN
Limiting speed	9500 r/min

The radial load applied on bearing [3]:

$$F_r = \sqrt{R_y^2 + R_x^2} \quad (44)$$

Where: R_x , R_y is the reaction force on shaft at position installing the bearing.

Calculating static equivalent force [3]:

$$Q = Q_r = (XVFr_B + YF_a)K_\sigma K_\tau \quad (45)$$

Where: $X = 1$ and $Y = 0$ since there is no axle force applied on the shaft. K_τ is factor considering the influence of temperature (t°C) on bearing life, V is factor considering the rotation, $V = 1$ if the inner diameter rotates. Fr_B is the radial load applied on bearing at position A and B.

Calculating the working life by millions of revolution [3]:

$$L = \frac{60 \times L_h \times n_I}{1000000} \quad (46)$$

Where:

L_h is working life; n_I is revolutions per minute of shaft I

Calculating static load capacity:

$$C_I = Q\sqrt[m]{L} < C_O \quad (47)$$

Where: Q is dynamic equivalent load; m is ball bearing; L is millions of revolution; C_O is basic static load rating

Calculating the actual working life of bearing [3]:

$$L = \left(\frac{C_0}{Q}\right)^m \quad (48)$$

$$L_h = \frac{1000000L}{60n_I} \quad (49)$$

Where: C_0 – basic static load rating; Q – dynamic equivalent load; m – index number, m=3 for ball bearing.

3. RESULT AND DISCUSSION

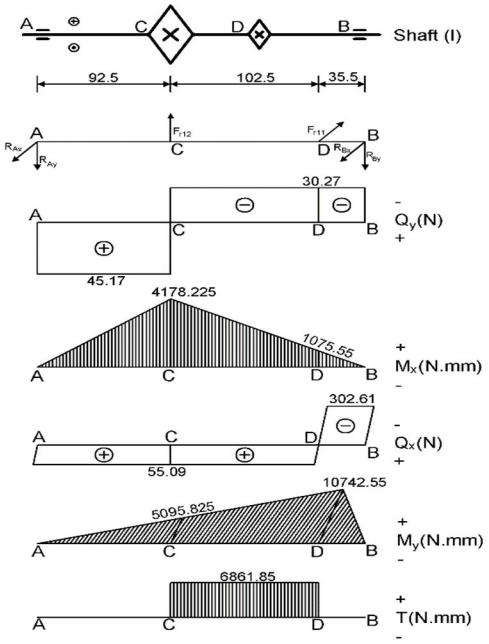

Figure 7. Internal loading diagram of shaft I

After designing and calculating in the sequence as described above, we get the following results:

Industrial 35B chain and sprocket are perfectly suitable for use in the system. The center distance of speed ratio 1:4 is 300mm

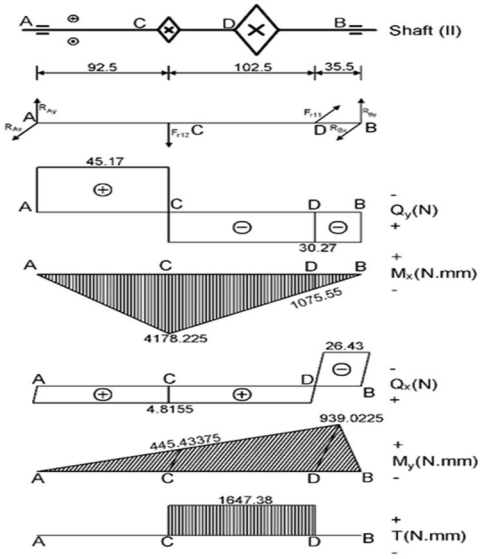

Figure 8. Internal loading diagram of shaft II

Internal loading diagram on shaft shown in Figures 7 and 8. The cross-section D of shaft I is critical. Therefore, a diameter of 17mm is used for both shaft. Key is used with the size of $b = 5mm$; $h = 5mm$; $t_1 = 3mm$, $t_2 = 2.3mm$ and key length $l = 12mm$.

Overall layout diagram

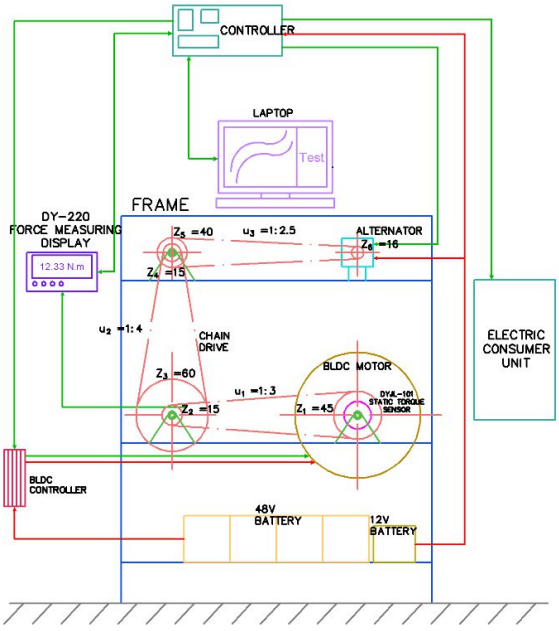

Figure 9. Equivalent general diagram of the dynamometer

4. CONCLUSION

Based on the results of this research, the design of the dynamometer's frame layout is compact and stable, the speed ratio of the BLDC motor and alternator is well distributed, and all components have been verified for strength, durability, and stability. For future development, the dynamometer can be manufactured, and research can be conducted on methods to calibrate the dynamometer for improved operation stability and accuracy. Additionally, a measuring process can be created for the dynamometer. Consequently, it can be concluded that this research demonstrates the potential for a successful dynamometer design.

Acknowledgement

This research is funded by Office for International Study Programs (OISP), Ho Chi Minh City University of Technology (HCMUT), VNUHCM under grant number **SVOISP-2022-KTGT-100**. We acknowledge the support of time and facilities from HCMUT, VNUHCM for this study

References

[1] Martyr, Anthony, and M A Plint, Engine Testing: The Design, Building, Modification Anduse of Powertrain Test Facilities. Oxford, Elsevier/Butterworth-Heinemann, 2012

[2] Inventor 2019, Autodesk Knowledge Network, Calculating Roller Chain Length. Accessed 21 Feb. 2023

[3] Nguyễn Hữu Lộc, Cơ sở thiết kế máy, Nhà xuất bản Đại học Quốc gia Thành phố Hồ Chí Minh, 2010

[4] Atkins, Richard, An Introduction to Engine Testing and Development. Sae International, 2009

[5] Krishnan, Ramu, Permanent Magnet Synchronous and Brushless DC Motor Drives. CRC Press, 19 Dec. 2017

[6] Kim, Sang-Hoon, Electric Motor Control : DC, AC and BLDC Motors. Cambridge, Massachusetts, Elsevier, 2017

[7] Schmid, Steven R, et al., Fundamentals of Machine Elements. CRC Press, 4 Nov. 2013

[8] Trịnh Chất, Lê Văn Uyển, Tính toán hệ dẫn động cơ khí tập 1 và 2, Nhà xuất bản Giáo dục Việt Nam, 2009

[9] SKF, AB, "SY 17 TF". Accessed 17 Mar. 2023

DESIGNING A REAL-TIME VIBRATION MONITORING SYSTEM FOR CVT PUSH-BELT TESTBENCH

(THIẾT KẾ HỆ THỐNG GIÁM SÁT THỜI GIAN THỰC RUNG ĐỘNG DÂY ĐAI HỘP SỐ CVT)

Pham Gia Khanh[1,2], Le Dinh Tuan[1,2]

[1] Faculty of Transportation Engineering, Ho Chi Minh City University of Technology (HCMUT), 268 Ly Thuong Kiet Street, District 10, Ho Chi Minh City, Vietnam
[2] Vietnam National University Ho Chi Minh City, Linh Trung Ward, Thu Duc City, Ho Chi Minh City, Vietnam
[*] Corresponding author: tuan-ledinh@hcmut.edu.vn

Abstract

The topic of this project was chosen because the most outstanding advantage of the continuously variable transmission (CVT) compared to other types of gearbox is fuel economy, thereby reducing fuel consumption, reducing emissions to the environment. In the current situation of shortage of clean energy sources, protecting the environment and saving resources towards sustainable development is also an issue worthy of attention and consideration by engineers in particular and society in general. However, in order to achieve the maximum efficiency of the CVT transmission, we must consider the vibration in the push-belt at different operating statuses to give out the assessment and conclusion for manufacturing or research purposes. This project demonstrates the overall layout design for CVT push-belt vibration data acquisition program, how to use LabView FPGA, and the execution of the system using simulated signals at real-time operating condition with fully functional ability.

Keywords: *CVT, CVT test-bench, GUI, vibration, belt box, LabView FPGA, 3-point belt measurement*

1. PRELIMINARY OF CVT'S PUSH-BELT VIBRATION

Currently, the car market is developed, new car models are increasing, so besides the model and features of the car, the car's gearbox is also an important issue. Many leading car manufacturing companies are interested and directed to this topic.

There are 3 main factors that affect the optimal level and performance of CVT called NVH (Noise-Vibration-Harshness). Therefore, vibrations in the push-belt will affect the efficiency and performance of the CVT transmission. Based on vibrations in the frequency domain, we can analyze belt efficiency, characteristics and operation, diagnose faults or failures between belt components. The results obtained can be useful in selecting the operating conditions of the CVT transmission, ensuring its maximum efficiency. It is also possible to analyze the reasons for the vibration of the moving belt and the amplitude-frequency characteristics.

When a guitar string is plucked, one observes that the string vibrates according to the patterns shown in the Figure 1. When the string is pulled to one side by the finger, the displacement of the string moves off as a travelling wave in both directions. After having reached the bridge at either end of the string, the waves are reflected back. These waves travel back and forth along the string but the resultant motion is a standing wave due to the addition of the left and right travelling components. Each of these vibration patterns is called a mode. For each of these modes, there will be locations on the string with maximum displacement (displacement antinodes) and locations which do not move at all (displacement nodes).

For a guitar string fixed at both ends, these modes have wavelengths related to the length of the string, L, where: $\lambda = 2L, L, 2L/3, L/2, 2L/5,\ldots$ for each of the successive modes shown in the animation below. If n is the order of the mode, the corresponding wavelength is then given by: $2L/n$. Using the wavelength-frequency relationship, $v = f\lambda$, it can be seen that for each of these wavelengths, there is a corresponding frequency $f = v/2L, v/L, 3v/2L, 2v/L, 5v/2L,\ldots$ Here v represents the speed of transverse mechanical waves on the string. These frequencies are also called natural frequencies of vibration of the string. When a string is excited by plucking, the resulting vibration can be thought of as a combination of several modes of vibration. Technically, we consider CVT's push-belt vibration is the same as the vibration of a string together with multiple vibration modes.

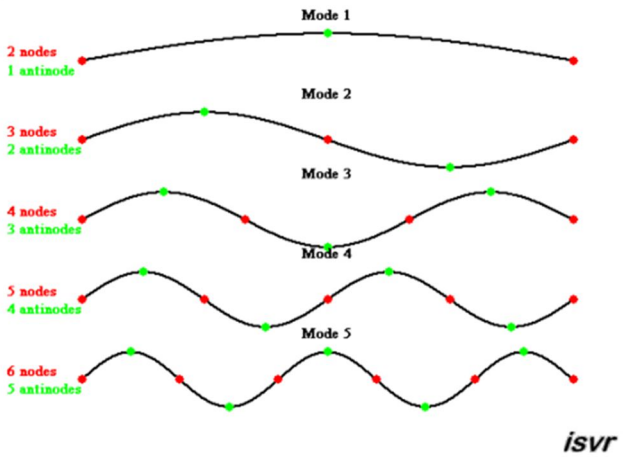

Figure 1. String mode vibration

2. MEASURING POINT CALCULATION AND MOUNTING FIXTURE ASSEMBLY DESIGN

2.1. Measuring point calculation

Calculation of measuring positions:

Given that :

•Push-belt length = 155 mm

•Driving pulley radius = 77,7 mm

•Driven pulley radius = 76,9 mm

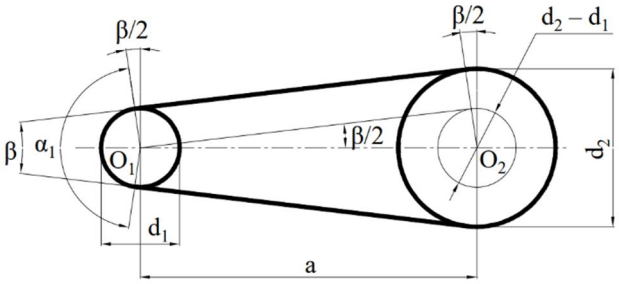

Figure 2. Parameters of belt drive

The contact angle of small pulley (degree) can be calculated by using the formula [6]:

$$\alpha_1 = 180 - 57 \times \frac{d_2 - d_2}{a} = 180 - 57 \times \frac{2\times77,7 - 2\times76,9}{155} = 179,4\ (degree)$$

$$\frac{\beta}{2} = \frac{180 - \alpha_1}{2} = \frac{180 - 179,4}{2} = 0,3\ (degree)$$

The measuring length: $155 + \left(sin\frac{\beta}{2} \times R_1\right) + \left(sin\frac{\beta}{2} \times R_2\right) = 155 + (\sin 0,3 \times 77,7) + (\sin 0,3 \times 76,9) = 155,72\ (mm)$

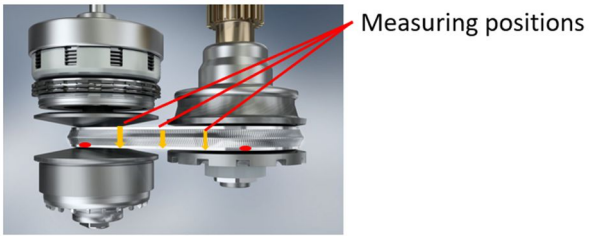

Figure 3. CVT push-belt's measuring positions

The three measuring positions after calculating

Position 1 : 0,25×155,72=38,93mm

Position 2 : 0,5 ×155,72=77,86 mm

Position 3 : 0,75 ×155,72= 116,79 mm

By measuring the vibration at multiple points along the length of the string or belt, it is possible to obtain a more complete picture of its vibration characteristics (mode 1, mode 2, mode 3) and identify any potential issues or irregularities that may need to be addressed. Due to the shortage of measurement equipment, I only focus on 3 modes of vibration, which are mode 1,2,3. Hence, to determine which mode the push-belt vibrates, we only need 3 sensors measuring at 3 points specified by the rule of thumb when it come to vibration measuring on the belt or string surface. These points are specified by reality experience as well as has been applied by many vibration research on the string surface. Furthermore, if we place these sensors on the different positions from the ordered position mentioned above, they may measure the harmonic frequencies which are the nodes in mode 3. As a result, we should use the rule of order suggested and proved by the vibration experts.

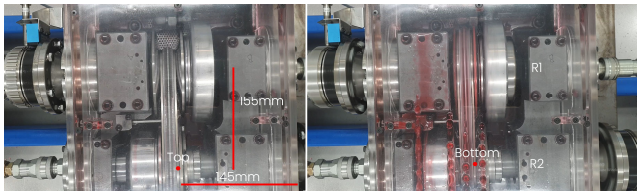

Figure 4. CVT Belt box technical dimensions

- Horizontal distance (perpendicular to the belt) from TOP – BOTTOM when changing gear ratio from 0.5 to 2.2: 13.05mm
- Driving pulley diameter = 77.7mm
- Driven pulley diameter = 76.9 mm
- Width of measuring position = 8mm
- Vertical distance from MICA plate to secondary pulley edge : 50mm

2.2. Design mounting fixture assembly

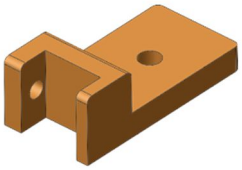

Figure 5. Drawing of sensor's clamp

The sensor's clamp is able to adjust the sensor horizontally (13,05mm) and vertically as well as firmly fix the sensor using hexagonal bolt and torsion rings.

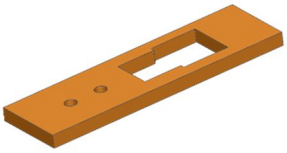

Figure 6. Drawing of oil stoppage

The working condition of CVT Testbench always surrounded by transmission oil pouring into the belt-box to shift the transmission ratio. Hence, the contacting positions between the bet-box and the upper experiment environment must be prevented from oil leakage, which also ensures the hygiene during conducting the experiment.

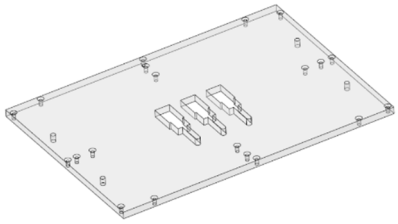

Figure 7. Design mica plate

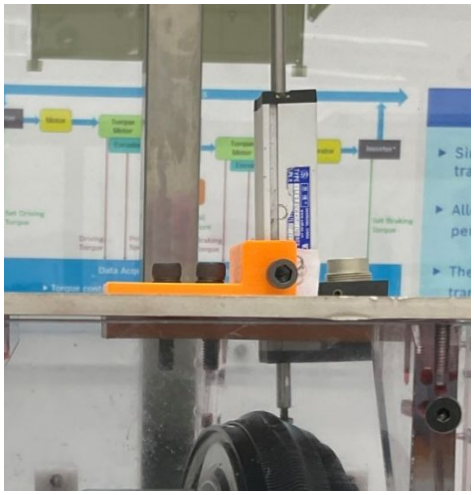

Figure 8. Actual mounting position

Technically, the tip of the linear potentiometer will be placed on top of the loop-set surface, which has the finest surface to guaranteed the precision of the vibration signal.

3. DESIGNING HIGH FREQUENCY DATA ACQUISITION PROGRAM

There was a previous version of GUI which is used to operate the CVT Testbench and had a fixed scanning period of 25 ms, so the maximum sampling frequency is only 50 Hz. In order to meet the requirements of the project, we must design a whole new program which is capable of settings the sampling frequency up to 10kHz and being adjustable .

Some industrial control and monitoring applications are based on single-point I/O data. The data used in these processes represents the current value of a physical I/O channel. The processes are not concerned with tracking the time history of the data, comparing the current value to any of the previous values, or measuring the change rate of a value. Often they do not require loop rates faster than 500 Hz so the previous GUI version can simplify these types of applications by using CompactRIO Scan Mode. But in this project the simulation process has been conducted before and the result has proved that the vibration from the belt could vary form 500 Hz to 1000 Hz which set the requirement for the data acquisition program to have a higher sampling ability, in this case LabView FPGA will do.

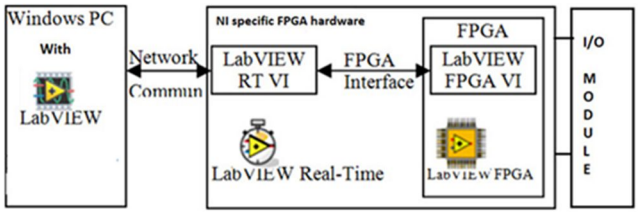

Figure 9. LabView FPGA streaming data from I/O module at high sampling frequency

According to the reference [7], if the data acquisition program needs to stream large amounts of data between the FPGA and real-time processor, or if it requires a small buffer for command- or message-based communication, consider using DMA FIFOs for data transfer. DMA does not involve the host processor when reading data off the FPGA; therefore, it is the fastest method for transferring large amounts of data between the FPGA target and the host. Hence, this is the reason why I chose DMA streaming for my system.

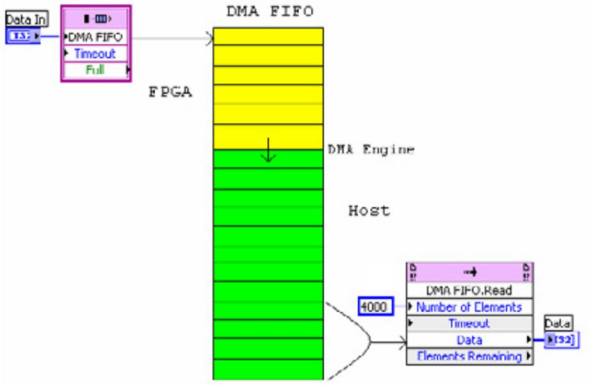

Figure 10. DMA uses FPGA memory to store data and then transfer it at a high speed to host processor memory with very little processor involvement.

The following list highlights the benefits of using DMA communication to transfer data between an FPGA target and a host computer: frees the host processor to perform other calculations during data transfer, reduces the use of front panel controls and indicators, which helps save FPGA resources, especially when transferring arrays of data, Automatically synchronizes data transfers between the host and the FPGA target.

Most CompactRIO systems have three DMA channels. In Hybrid Mode, CompactRIO systems have only one DMA channel. To pack multiple data streams or I/O channels into one DMA FIFO, we used the interleaving technique, and unpack using decimation on the host.

When passing multiple analog input channels into one DMA FIFO, the channels are stored in an arrangement similar to that shown in **Table 1**. This table assumes that four analog input channels are being interleaved into one DMA FIFO. The unpacking algorithm on the host VI is expecting the elements to arrive in this specific order. If the FIFO overflows and elements are lost, then the unpacking algorithm on the host VI fails to assign data points to their correct analog input channels. Therefore, it is extremely important to ensure lossless data transfer when reading from multiple analog input channels.

Table 1. When writing multiple channels to one DMA FIFO, the host VI expects the elements to arrive in a specific order.

Array Index	Element
0	AI 0
1	AI 1
2	AI 2
3	AI 3
4	AI 0
5	AI 1
6	AI 2

The NI-9375 module will simultaneously collect the data from 3 channel and put it in a buffer, then the FPGA VI will send it to the Host VI respectively.

4. DESIGNING GRAPHIC USER INTERFACE (GUI)

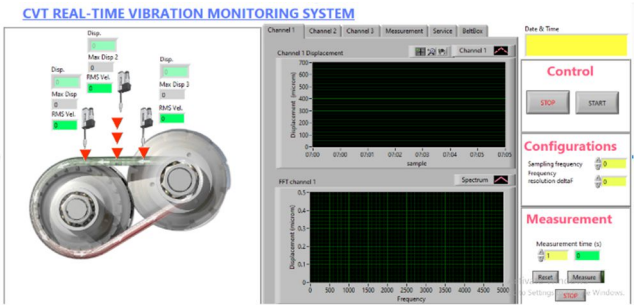

Figure 11. Control tab

The graphic user interface satisfied the prerequisite demands. For instances, it has the ability of showing real-time vibration signal, calculate and display the FFT spectrum, sampling frequency and FFT spectrum resolution adjustment. Lastly, the raw data export to excel file function and measurement and recording function have also been added.

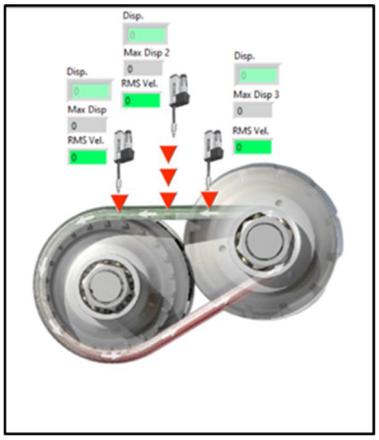

Figure 12. Real-time parameters display

In this area, there are three parameters displayed for the user to assess the operating conditions according to the vibration standard. For the purposes of this part of ISO 10816 [5] , the following quantities are used: displacement of vibration, expressed in μm; vibration velocity, expressed in mm/s.

The result of measuring the vibration quantities by measuring equipment is called the vibration magnitude at the specified position and measurement direction.

In general, based on experience, when evaluating wide-band vibration for camcorders it is important to consider the value of the effective vibration velocity, because vibrational energy can be related. However, other quantities such as displacement or acceleration and peak values instead of root mean square. values may be more appropriate. Then, another criterion is needed, which does not need a simple relationship with the criterion based on the root mean square values. In this program, I will use the peak value of the displacement to display on the screen.

Over the years, effective vibration velocity measurement has been widely accepted for response characterization of very successful and continuing machines. For different waveforms that combine several discrete harmonics with magnitude and phase components, and that do not contain significant random vibration or shock components, then a Fourier analysis can be used to relate combine different fundamental quantities (e.g. displacement, velocity, acceleration, peak, root mean square value, mean, etc.) This issue is not the subject of this Appendix. However, some of the useful equations are summarized below:

From the vibration velocity measured against the recorded time, the root mean square value of the velocity can be calculated as follows:

$$v_{rms} = \sqrt{\frac{1}{T}\int_0^T v^2(t).dt}$$

Acceleration, velocity and/or magnitude of displacement (a_j, v_j, s_j; j = 1, 2, …, n) can be determined for different frequencies (f_1, f_2, …, f_n) from spectrum analysis was obtained.

$$v_{rms} = \pi.10^{-3}\sqrt{\frac{1}{2}\left[(s_1.f_1)^2 + (s_2.f_2)^2 + ... + (s_n.f_n)^2\right]} =$$

$$= \sqrt{v_1^2 + v_2^2 + ... + v_n^2} = \frac{10^3}{2\pi}\sqrt{\left(\frac{a_1}{f_1}\right)^2 + \left(\frac{a_2}{f_2}\right)^2 + ... + \left(\frac{a_n}{f_n}\right)^2}$$

According to ISO 2041 [5] , the frequency f is also known as the period frequency f.

In the case of vibrations containing only two significant frequency components that produce the root mean square value vibration span: v_{min}, v_{max} and v_{rms} can be approximated by the expression:

$$v_{rms} = \sqrt{\frac{1}{2}\left(v_{max}^2 + v_{min}^2\right)}$$

In general, mainly because there is no common standard for evaluating the vibration of the CVT transmission belt, we refer to a number of other vibration evaluation standards and perform the calculation of the parameters for the user to base on that to evaluate according to the standards they apply.

We used a Waveform generator SIGLENT's SDG2000X to simulate a square wave and a sine wave to check whether the programmed system operate correctly or not according to the theoretical basis of digital signal processing. The sampling process should satisfy the Nyquist theorem and FFT resolution adjustment as follows:
Nyquist theorem:

$$sampling\ frequency \geq 2f_{max}$$

If the sampling frequency is lower than the frequency, the reconstructed signal will be distorted. In order to prove the program work in accordance with this theorem, we generated a square waveform from the generator and set the sampling frequency at two different frequencies, the first frequency is lower than the Nyquist frequency and the other is the same as the Nyquist frequency to see the result.

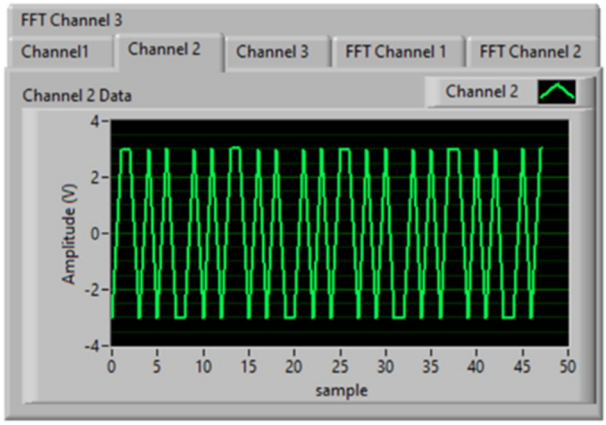

Figure 13. Distorted/Aliasing square wave

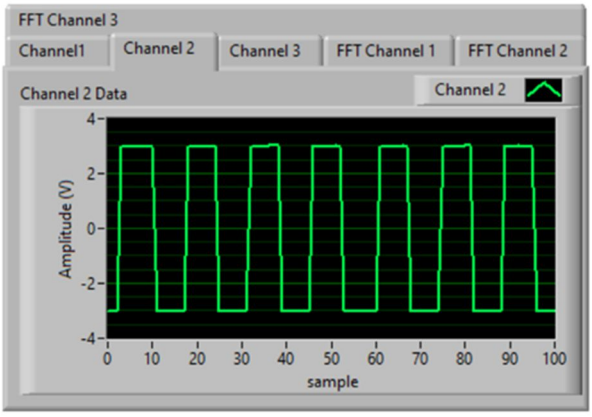

Figure 14. Undistorted square wave

FFT resolution adjustment:

$$\Delta F = \frac{sampling\ frequency}{number\ of\ sample}$$

Frequency resolution is used to tune to FFT spectrum to gain the desired and correct amplitude of the input signal.

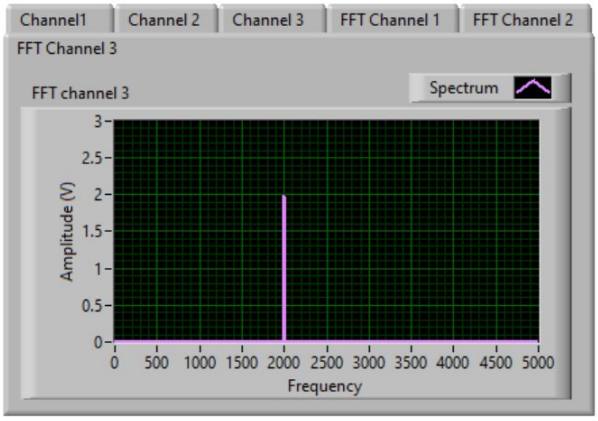

Figure 15. High resolution FFT spectrum

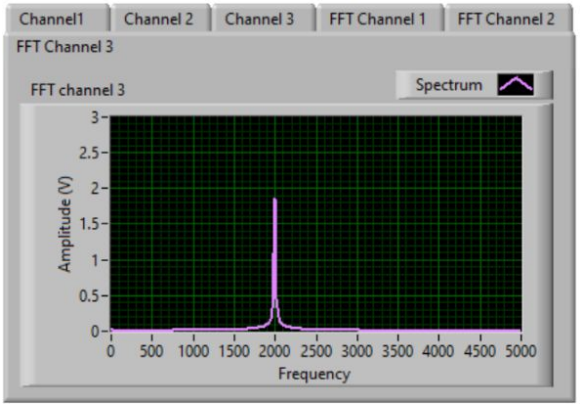

Figure 16. Low resolution FFT spectrum

5. CONCLUSION

Firm fixture is adjustable to specified requirements. The well-calibrated linear potentiometer and high accuracy together with the standard data acquisition (NI DAQ) permits high performance vibration measurement system for the push-belt. the calculation of the measurement point ensures that the belt vibration is under control without missing any modes. The high frequency signal acquisition program works properly and is compatible with the old system program. The GUI is easy to use and the parameters can be changed according to the vibration theory. The raw exporting function works well, threshold warning works properly, automatically generated excel file whenever the values reach emergency value.

Acknowledgement

This research is funded by the Office for International Study Programs (OISP), Ho Chi Minh City University of Technology (HCMUT), VNUHCM under grant number **SVOISP-2022-KTGT-103**. We acknowledge the support of time and facilities from HCMUT, VNUHCM for this study.

References

[1] EN| Bosch Pushbelt – Efficiency on the Road. [Film]. BOSCH, 2013.

[2] EN| Bosch Continuously Variable Transmission. [Film]. BOSCH, 2013.

[3] Nguyễn Thùy Linh (2022). Design mechanical components for continuously variable transmission test bench

[4] Lê Quỳnh Như (2022). Design an SCADA system for test bench examining push belt used in continuously variable transmission

[5] Rung cơ học - đánh giá rung động của máy bằng cách đo trên các bộ phận không quay TCVN 9229-1 : 201

[6] Nguyễn Hữu Lộc (2020). Thiết kế máy và Chi tiết máy

[7] FullCrioDevGuide (2021)

THE IMPACT OF CORPORATE SOCIAL RESPONSIBILITY ON FIRM RISK: THE IMPORTANCE OF INSTITUTIONAL OWNERSHIP

(TÁC ĐỘNG CỦA TRÁCH NHIỆM XÃ HỘI ĐẾN RỦI RO DOANH NGHIỆP: TẦM QUAN TRỌNG CỦA SỞ HỮU TỔ CHỨC)

Tran Van Son[1,2,3], Nguyen Thuy Khanh Linh[1,2,3], Huynh To Quan[1,2,3], Pham Hieu Hanh[1,2,3], Nguyen Ngoc Van Anh[1,2,3], Dang Quoc Bao[1,2,3], Pham Tien Minh[1,3,*]

[1] School of Industrial Management, Ho Chi Minh City University of Technology (HCMUT), 268 Ly Thuong Kiet Street, District 10, Ho Chi Minh City, Vietnam
[2] Office for International Study Programs, Ho Chi Minh City University of Technology (HCMUT), 268 Ly Thuong Kiet Street, District 10, Ho Chi Minh City, Vietnam
[3] Vietnam National University Ho Chi Minh City, Linh Trung Ward, Thu Duc City, Ho Chi Minh City, Vietnam
[*] Corresponding author: ptminh@hcmut.edu.vn

Abstract

Corporate social responsibility is a growing trend in the corporate world, with businesses increasingly recognizing the importance of responsible and sustainable practices for long-term success. The aim of this paper is to investigate the relationship between corporate social responsibility disclosure (CSRD) and firm risk for listed companies in the VN100 group of Vietnam from 2014 to 2020. The study also examines the role of institutional ownership in this relationship. The research employs various regression models, including ordinary least squares (OLS), fixed-effects model (FEM), and random-effects model (REM). Moreover, to ensure the reliability of the results, the Hausman test and the model's defect tests are also used. The tests reveal the presence of first-order autocorrelation and heteroskedasticity, so the general least squares (GLS) method is used to rectify the model's defects. The research results suggest that CSRD contributes to reducing firm risk, with both environmental and social CSRD having a negative impact on firm risk. However, social CSRD has a more significant impact than environmental CSRD. Besides, the study finds no moderating effect of institutional ownership on the relationship between CSRD and firm risk. Overall, the research findings provide a valuable perspective for managers and policymakers on the role of CSRD and institutional ownership in mitigating firm risk.

Keywords: *corporate social responsibility, firm risk, institutional ownership*

Tóm tắt

Trách nhiệm xã hội của doanh nghiệp là một xu hướng đang phát triển trong thế giới doanh nghiệp, các doanh nghiệp ngày càng nhận ra tầm quan trọng của các hoạt động có trách nhiệm và bền vững để đạt được thành công lâu dài. Bài viết này điều tra về tác động của mức độ công bố trách nhiệm xã hội doanh nghiệp (CSRD) lên rủi ro doanh nghiệp đối với các công ty niêm yết tại Việt Nam thuộc nhóm VN100 trong giai đoạn từ năm 2014 đến năm 2020. Nghiên cứu cũng xem xét vai trò của sở hữu tổ chức trong mối quan hệ này. Nghiên cứu sử dụng các mô hình hồi quy khác nhau, bao gồm mô hình bình phương nhỏ nhất (OLS), mô hình ảnh hưởng cố định (FEM) và mô hình ảnh hưởng ngẫu nhiên (REM). Ngoài ra, để đảm bảo độ tin cậy của kết quả, kiểm định Hausman và các kiểm định kiểm tra khuyết tật mô hình cũng được sử dụng. Các kiểm định cho thấy có hiện tượng tự tương quan bậc một và phương sai sai số thay đổi, nên phương pháp bình phương nhỏ nhất tổng quát (GLS) được sử dụng để khắc phục các khuyết tật của mô hình. Kết quả nghiên cứu cho thấy CSRD góp phần làm giảm rủi ro doanh nghiệp, với cả CSRD về

môi trường và CSRD về xã hội đều có tác động nghịch đến rủi ro doanh nghiệp. Tuy nhiên, CSRD về xã hội có tác động mang ý nghĩa cao hơn so với CSRD về môi trường. Bên cạnh đó, nghiên cứu không tìm thấy tác động điều tiết nào của sở hữu tổ chức đối với mối quan hệ giữa CSRD và rủi ro doanh nghiệp. Nhìn chung, các kết quả nghiên cứu cung cấp một góc nhìn có giá trị cho các nhà quản lý và hoạch định chính sách về vai trò của CSRD và quyền sở hữu tổ chức trong việc giảm thiểu rủi ro doanh nghiệp.

Từ khóa: *trách nhiệm xã hội, rủi ro doanh nghiệp, sỡ hữu tổ chức*

Acknowledgement: This research is funded by Office for International Study Programs (OISP), Ho Chi Minh City University of Technology (HCMUT), VNUHCM under grant number **SVOISP-2022-QLCN-136**. We acknowledge the support of time and facilities from HCMUT, VNUHCM for this study.

SUSTAINABLE TOURISM DEVELOPMENT BASED ON THE SOCIAL EXCHANGE THEORY AND BOTTOM-UP SPILLOVER THEORY: A CASE STUDY IN HO CHI MINH CITY

(PHÁT TRIỂN DU LỊCH BỀN VỮNG DỰA TRÊN LÝ THUYẾT SOCIAL EXCHANGEVÀ LÝ THUYẾT BOTTOM-UP SPILLOVER: NGHIÊN CỨU TÌNH HUỐNG TẠI THÀNH PHỐ HỒ CHÍ MINH)

Thai Minh Nhat[1,2,3], Lai Bao Ngoc[1,2,3], Nguyen Trinh Hoang Oanh[1,2,3], Pham Quoc Trung[1,2,*]

[1] School of Industrial Management, Ho Chi Minh City University of Technology (HCMUT), 268 Ly Thuong Kiet Street, District10, Ho Chi Minh City, Vietnam

[2] Office for International Study Programs, Ho Chi Minh City University of Technology (HCMUT), 268 Ly Thuong Kiet Street,District 10, Ho Chi Minh City, Vietnam

[3] Vietnam National University Ho Chi Minh City, Linh Trung Ward, Thu Duc City, Ho Chi Minh City, Vietnam

[*] Corresponding author: pqtrung@hmcut.edu.vn

Abstract

Most research on residents' support for tourism has been done around the world. In this study, the island economy of Thieng Lieng, which is located in Can Gio, is examined in terms of community support towards sustainable tourism development using two typical theories for tourism study namely the social exchange theory and bottom-up spillover theory. In addition, many previous researches proposed that the material life and non-material life domains of the locals have fulfilled; they will contribute to the sustainability of tourism development. In our study, we confirmed the positive relationship between these theories and sustainable tourism development. Also, the study's drawbacks and real-world implications are examined.

Keywords: *sustainable tourism development; social exchange theory (SET); bottom-up spillover theory; material life domain; non-material life domain; quality of life (QoL); community attachment; economic impacts, environmental impacts, sociocultural impacts*

Tóm tắt

Hầu hết các nghiên cứu về sự ủng hộ của người dân đối với du lịch đã được thực hiện trên khắp thế giới. Trong nghiên cứu này, kinh tế đảo Thiềng Liềng, thuộc Cần Giờ, được xem xét dưới góc độ hỗ trợ cộng đồng hướng tới phát triển du lịch bền vững bằng cách sử dụng hai lý thuyết tiêu biểu cho nghiên cứu du lịch là lý thuyết social exchange theory và lý thuyết bottom-up spillover. Ngoài ra, nhiều nghiên cứu trước đây cho rằng các lĩnh vực đời sống vật chất và phi vật chất của người dân địa phương đã đáp ứng được thì sẽ góp phần tạo nên sự bền vững cho phát triển du lịch. Trong nghiên cứu của chúng tôi, chúng tôi khẳng định mối quan hệ tích cực giữa các lý thuyết này và phát triển du lịch bền vững. Ngoài ra, những hạn chế của nghiên cứu và ý nghĩa trong thế giới thực cũng được xem xét.

Từ khóa: *phát triển du lịch bền vững; lý thuyết social exchange theory (SET); lý thuyết bottom-up spillover; miền đời sống vật chất; miền đời sống phi vật chất; chất lượng cuộc sống (QoL); gắn bó cộng đồng; tác động kinh tế, tác động môi trường, tác động văn hóa xã hội*

Acknowledgement: This research is funded by the Office for International Study Programs (OISP), Ho Chi Minh City University of Technology (HCMUT), VNUHCM under grant number **SVOISP-2023-QLCN-50**. We acknowledge the support of time and facilities from HCMUT, VNUHCM for this study.

DETECTION OF ROAD SURFACE DAMAGE FROM DRONE IMAGES

(NHẬN DIỆN HƯ HỎNG BỀ MẶT ĐƯỜNG GIAO THÔNG TỪ ẢNH CHỤP BỞI DRONE)

Nguyen Dang Khoa[1, 3, 4], Nguyen Thi Khanh Ly[1, 3, 4], Nguyen Vu Nhat Minh[1, 3, 4], Nguyen Thanh Toan[1, 3, 4], Quach Bao Khang[2, 3, 4], Hoang Duc Trung[2, 3, 4], Assoc. Prof. Dr. Ngo Khanh Hieu[*]

[1] Faculty of Transportation Engineering, Ho Chi Minh City University of Technology (HCMUT), 268 Ly Thuong Kiet Street, District 10, Ho Chi Minh City, Vietnam
[2] Faculty of Civil Engineering, Ho Chi Minh City University of Technology (HCMUT), 268 Ly Thuong Kiet Street, District 10, Ho Chi Minh City, Vietnam
[3] Office for International Study Programs, Ho Chi Minh City University of Technology (HCMUT), 268 Ly Thuong Kiet Street, District 10, Ho Chi Minh City, Vietnam
[4] Vietnam National University Ho Chi Minh City, Linh Trung Ward, Thu Duc City, Ho Chi Minh City, Vietnam
[*] Corresponding author: ngokhanhhieu@hcmut.edu.vn

Abstract

The quality verification of existing road works is typically done through site inspections and the review of project data. But these methods are often time-consuming and limited in their ability to detect road surface damage. To address this issue, we propose using drones to capture images of road surface damage, which can be digitized to create an intuitive 3D model for damage inspection. Our project aims to reduce costs and time spent on data collection while creating a sustainable data warehouse. Though the use of smart drone technology is still a new concept in Vietnam, its increasing convenience is evident. In the end, this project can be a useful resource for future research, specifically in the development of an autonomous drone-based imaging system for detecting potholes in rural roads, contributing to the growing field of drone technology and its potential to revolutionize road maintenance.

Keywords: *drones, pothole detection, road surface damage, road maintenance, autonomous systems, 3D modeling*

Tóm tắt

Thẩm tra công trình đường bộ đang khai thác phụ thuộc chủ yếu vào công tác kiểm tra hiện trường, rà soát các hồ sơ hoàn công, và các dữ liệu của dự án. Nhưng các phương pháp này thường tốn thời gian và xuất hiện hạn chế trong khả năng phát hiện hư hỏng bề mặt đường. Để giải quyết vấn đề này, chúng tôi đề xuất sử dụng drone để chụp ảnh các vết tích hư hại trên bề mặt đường, sau đó số hóa để tạo ra mô hình 3D trực quan hỗ trợ công tác kiểm tra hư hỏng. Dự án của chúng tôi nhằm giảm chi phí và thời gian thu thập dữ liệu và đồng thời tạo ra một kho dữ liệu bền vững. Mặc dù sử dụng công nghệ drone thông minh vẫn là một khái niệm mới tại Việt Nam, nhưng sự tiện lợi mà drone mang lại ngày càng được thể hiện rõ ràng và thực tế. Chúng tôi tin rằng dự án này có thể trở thành một tài nguyên hữu ích cho nghiên cứu trong tương lai, đặc biệt là trong việc phát triển hệ thống nhận diện tự động dựa trên drone để phát hiện hố sâu trên đường nông thôn, góp phần vào lĩnh vực công nghệ drone đang ngày càng phát triển và tiềm năng của nó để cách mạng hóa, hiện đại hóa quy trình bảo trì đường bộ.

Từ khóa: *drones, phát hiện hố sâu, hư hỏng bề mặt đường, bảo trì đường bộ, hệ thống tự động, mô hình 3D*

Acknowledgement: This research is funded by the Office for International Study Programs (OISP), Ho Chi Minh City University of Technology (HCMUT), VNUHCM under grant number **SVOISP-2022-KTGT-99**. We acknowledge the support of time and facilities from HCMUT, VNUHCM for this study.

COUNCIL 4
Faculty of Electrical and Electronics Engineering
Faculty of Computer Science and Engineering
Faculty of Civil Engineering

ANALYSIS OF PILES LOCATION FOR STABILIZING SLOPE BY FINITE ELEMENT METHOD

(PHÂN TÍCH VỊ TRÍ TỐI ƯU CỦA CỌC DÙNG CHO VIỆC ỔN ĐỊNH MÁI BẰNG PHƯƠNG PHÁP PHẦN TỬ HỮU HẠN)

Tran Nhat Linh[1,2,3], Nguyen Minh Quan[1,2,3], Huynh Trong Tri[1,2,3], Nguyen Trung Kien[1,3,*]

[1] Faculty of Civil Engineering, Ho Chi Minh City University of Technology (HCMUT), 268 Ly Thuong Kiet Street, District 10, Ho Chi Minh City, Vietnam
[2] Office for International Study Programs, Ho Chi Minh City University of Technology (HCMUT), 268 Ly Thuong Kiet Street, District 10, Ho Chi Minh City, Vietnam
[3] Vietnam National University Ho Chi Minh City, Linh Trung Ward, Thu Duc City, Ho Chi Minh City, Vietnam
[*] Corresponding author: nguyentrungkien@hcmut.edu.vn

Abstract

Slope stability is a critical aspect in geotechnical engineering, ensuring the structural integrity and preventing loss of human lives. There are several approaches to improve the stabilization of slopes, such as retaining wall, soil nailing, slope grading, etc. in which piles installation is one of the most effective methods. The crucial point of this remedy lies in the positioning of the pile rows. Previous work, using different analysis approaches, has shown some inconsistencies in the optimum position of pile rows to stabilize the slopes. Some studies suggested the pile row should be in the middle, while others recommended the positions near the top of the slopes. Accordingly, this paper focuses on determining the optimum locations of a single row of piles to achieve highest factor of safety in the slope analysis, using finite element method (FEM) implemented in Plaxis commercial software. The FEM results are initially verified with published documents. The verified model is subsequently used to examine the factor of safety in different cases of pile location, considering a variation in soil and pile properties, such as friction angle, cohesion, slope angle and pile spacing. The tabulated and graphical results provide useful tools for engineers in locating the optimum position of a single pile row, given the geotechnical site conditions.

Keywords: *slope stability, pile location, finite element method, factor of safety*

1. INTRODUCTION

In geotechnical engineering, slope stability is a critical aspect that requires careful evaluation and appropriate mitigation measures. The stability of natural or man-made slopes is often compromised by factors such as geological conditions, ground movement, or human-induced activities. To ensure the safety and longevity of infrastructure projects and the surrounding environment, it is imperative to implement effective stabilization techniques. One commonly employed method for slope stabilization is the use of piles. Piles are deep foundation elements that transfer the loads from structures or embankments to more competent soil layers or bedrock. By integrating piles into the slope, the load-bearing capacity and overall stability of the slope can be enhanced. The determination of optimal pile locations plays a crucial role in ensuring the effectiveness of slope stabilization measures. However, identifying the most suitable positions for piles is a complex task due to the nonlinear behavior of soils and the intricate interaction between the piles and the surrounding soil. To address this challenge, the finite element method (FEM) has gained considerable popularity in geotechnical engineering for the analysis of slope stability. The FEM is a numerical technique that can simulate the behavior of complex systems, taking into account various factors such as soil properties, structural elements, and boundary conditions. By utilizing the FEM, engineers can assess the performance of different pile configurations and optimize the positioning of piles to achieve the desired level of slope stability. This scientific paper aims to present a comprehensive analysis of pile location for stabilizing slopes using the finite element method. The research investigates the influence of pile spacing, depth, and inclination on slope stability under different loading conditions. The study also explores the significance of soil properties and geotechnical parameters in determining the optimal pile arrangement. By evaluating the results obtained from the numerical simulations, this research contributes to the understanding of the behavior of piles in slope stabilization. The findings will aid geotechnical engineers and researchers in making informed decisions regarding the design and implementation

of effective and efficient slope stabilization strategies. The results of this study will be systematized with tables and charts, providing the construction and geotechnical community with a useful tool in determining the optimal location of a single row of piles, based on geological conditions. From there, new knowledge about the method of using piles to stabilize the slope and reduce risks during construction. We hope that our research will help experts in this field come up with more efficient and cost-effective solutions for the construction of pitched roofs in the future. Overall, this study emphasizes the importance of utilizing advanced numerical techniques such as the finite element method to analyze and optimize the positioning of piles for slope stabilization. By integrating geotechnical expertise and computational simulations, engineers can enhance the reliability and safety of slope stabilization projects, ultimately contributing to the sustainable development of infrastructure and the preservation of the natural environment.

2. METHODOLOGY AND IMPLEMENTATION

2.1. Method of Calculation: Finite Element Method – PLAXIS 2D software

The Finite Element Method (FEM) is such an approximation method that subdivides a complex space or domain into several small, countable, and finite number of pieces (thus the name finite elements) whose behaviors can be described with comparatively simple equations.

Plaxis 2D is a typical choice for FEM software in the geotechnical field. The model will be made, meshed and calculated by nodes.

Plaxis 2D software is generally simpler to use compared to its 3D counterpart. The user interface and modeling techniques are often more intuitive, making it easier for engineers and geotechnical professionals to quickly analyze and calculate slope stability.

Since 2D Plaxis software focuses on analyzing slopes in two dimensions, it typically requires less computational time and resources compared to 3D Plaxis software. This can be particularly beneficial when dealing with large-scale projects or when performing numerous slope stability analyses.

That is the reason why our study chooses to use PLAXIS 2D.

2.2. Problem Definition

In the study conducted by Won et al. and Cai and Ugai [1], a slope with a height of 10 meters and a 1:1.5 horizontal units was examined (**see Figure 1**). To simplify the problem, two symmetric extreme boundaries were employed, resulting in a configuration with a row of piles and a plane of symmetry. The study utilized steel tube piles with an outer diameter (D) of 0.8 meters. These piles were treated as linear elastic solid materials and were installed at the midpoint of the slope. The distance along the slope (L_x) between the piles was fixed at 7.5 meters, while the center-to-center spacing (s) ranged from 2D to 8D. The piles were assumed to be embedded and anchored into either the bedrock or a stable layer, assuming an infinite pile length.

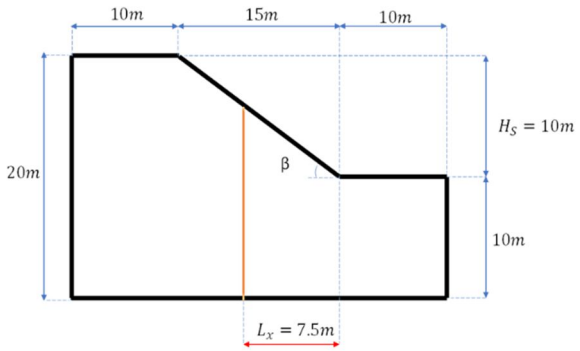

Figure 1. Problem definition

In this model, the pile head is free. The constitutive model and material properties adopted in the numerical analysis are shown in Table 1 below:

Table 1. The constitutive model and material properties adopted in the numerical analysis

Materials	Constitutive model	Material properties
Soil	Mohr – Coulomb model	$\gamma = 20\ kN/m^3$ $c = 10kPa$ $\varphi = 20°$ $E = 200\ MPa$ $\vartheta = 0.25$
Pile	Elastic model	$E = 60\ MPa$ $\vartheta = 0.2$

The goal is to find the best place to put piles on a slope, using the slope models developed by Won et al. and Cai and Ugai [1]. To achieve this, we will adjust some parameters such as the Distance from the end of slope to the piles (Lx), Cohesion (c), Friction angle (φ), Angle of slope (β), Space between pile rows (Lspacing - with D=0.8m). The properties of the pile, including elastic modulus (E), Poison's ratio (v), and diameter (0.8m), will remain constant during the analysis. The purpose of these adjustments is to increase the slope's stability and get the highest Factor of Safety (FoS).

Table 2. The Parameters which need changing to get the efficiency

Parameter	Parameter properties							
L_x	0	3.75	7.5	11.25	15			
Cohesion (c)	10	30	50					
Friction angle (φ)	10	20	30					
Angle of slope (β)	33	45	60					
Lspacing (with D=0.8m)	0.8	1.6	2.4	3.2	4	4.8	6.4	∞

2.3. Numerical Modelling Procedures

2.3.1. Material Properties

In PLAXIS 2D, material properties play a significant role in accurately representing the behavior of the soil and other materials within a geotechnical analysis. These properties define the mechanical and physical characteristics of the materials and are crucial for obtaining realistic and reliable results. In this study, various characteristics of the soil were taken in account in the models which are detailed in Table 1.

2.3.2. Boundary Conditions

The boundary conditions in PLAXIS 2D refer to the constraints and external influences imposed on the model to simulate the real-world behavior of the analyzed system. These conditions are essential for accurately representing the interactions between the soil and structures within the geotechnical analysis. The boundary condition restricts the displacement and rotation of nodes along specific boundaries. In this study, the fixed boundary conditions are represented in Figure 1.

2.3.3. Optimum Mesh Size

The outcomes of the numerical analyses depend significantly on the mesh and model size. Therefore, efforts were made to optimize these parameters. The most suitable values for the mesh size and domain size were determined by employing a trial-and-error approach. Interestingly, the results remained largely unchanged when reducing the mesh size or enlarging the model size. All cases were subjected to analysis, and a subset of the results is provided in this presentation.

Therefore, the mesh model can be made according to the Figure 2.

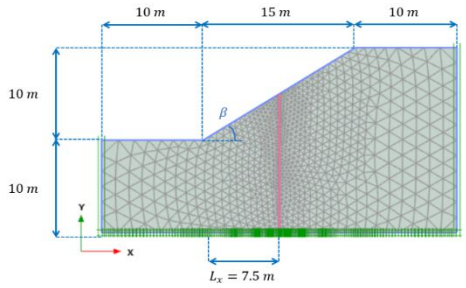

Figure 2. Numerical Model

3. RESULTS AND DISCUSSION

3.1. Verification with previous results

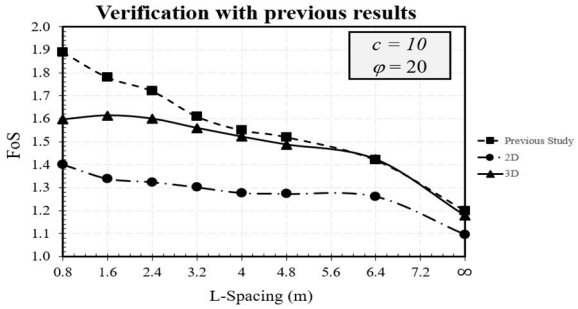

Figure 2. Verification with the published study [2]

Utilizing a soil model with a cohesion c of 10kPa and a friction angle φ of 20, we conducted a comparative analysis of the Factor of Safety (FoS) along the L-Spacing between pile rows using data from the work conducted by W.B. Wei and Y.M. Cheng [2], 2D (PLAXIS 2D), and 3D (PLAXIS 3D) models. The obtained line graph shows a good agreement with the published data, in both shape and magnitude. Consequently, we inferred that the PLAXIS 2D software could yield comparable results to the software used in the previous study and selected it for use in our project.

3.2. The effect of Lx on the slope stability

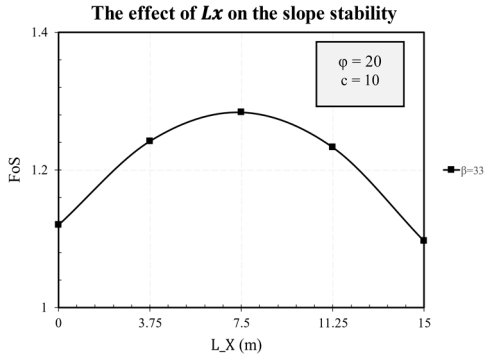

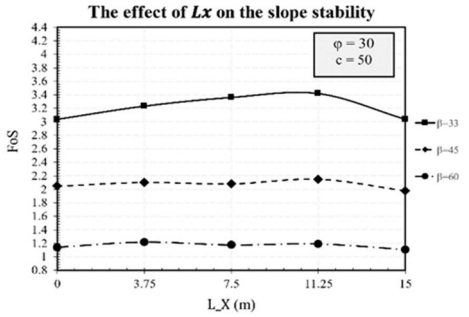

Figure 4. The effect of Lx on the slope stability

Figure 4 shows the variation of FoS depending on the L_x, for three cases of slope angles of 33, 45, and 60 degrees.

Utilizing a soil model with a cohesive coefficient c of 10 and a friction angle φ of 20, our results indicated that for the model with a slope angle of 33 degrees, the FoS reached its maximum value when L_x was 7.5m.

Employing a soil model with a cohesive coefficient c of 50 and a friction angle φ of 30, all models exhibited maximum FoS values when the distance from the end of the slope to the piles (L_x) was 11.25m. Additionally, our results indicated that the model with a slope angle of 33 degrees had the highest FoS, followed by the 45-degree model in second place and the 60-degree model in last place.

3.3. The effect of Lspacing on the slope stability

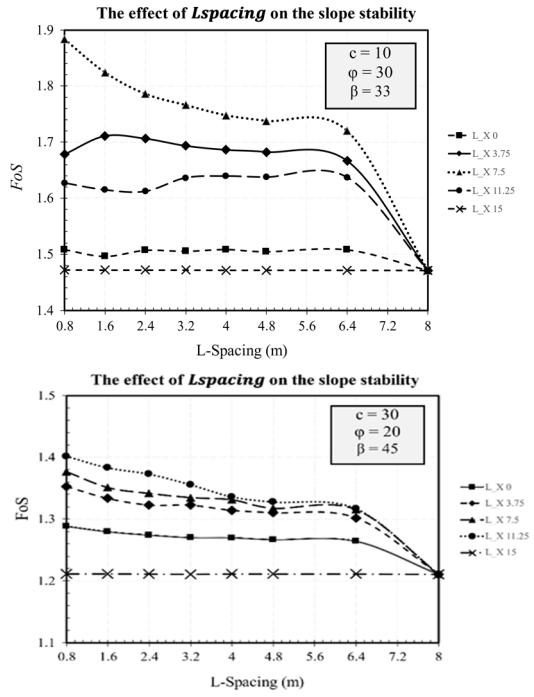

Figure 5. The effect of Lspacing on the slope stability

To assess the impact of L-Spacing between pile rows on slope stability, a graphical comparison was conducted, as shown in Figure 5. The FoS was compared across L-Spacing values of 0.8m, 1.6m, 2.4m, 3.2m, 4m, 4.8m, 6.4m and infinity for five different Distances from the end of the slope to the piles (L_x 0, L_x 3.75, L_x 7.5, L_x 11.25, and L_x 15).

For a soil model with a cohesive coefficient c of 10, a friction angle φ of 30 and a slope angle β of 33, the line generated by L_x 7.5m exhibited the highest FoS. The graph indicates that soil stability gradually decreases with increasing L-Spacing for pile rows at L_x 7.5m, L_x 3.75m and L_x 11.25m. However, pile rows at Lx 0 and Lx 15m appear to remain constant across the range of L-Spacing values.

For a soil model with a cohesive coefficient c of 30, a friction angle φ of 20 and a slope angle β of 45, the line generated by L_x 11.25m exhibited the highest FoS. Soil stability also decreases with increasing L-Spacing, albeit at a slower rate for pile rows at L_x 0, L_x 3.75m, L_x 7.5m and L_x 11.25m. However, pile rows at Lx 15m maintain a constant FoS across the range of L-Spacing values.

3.4. The effect of c on the slope stability

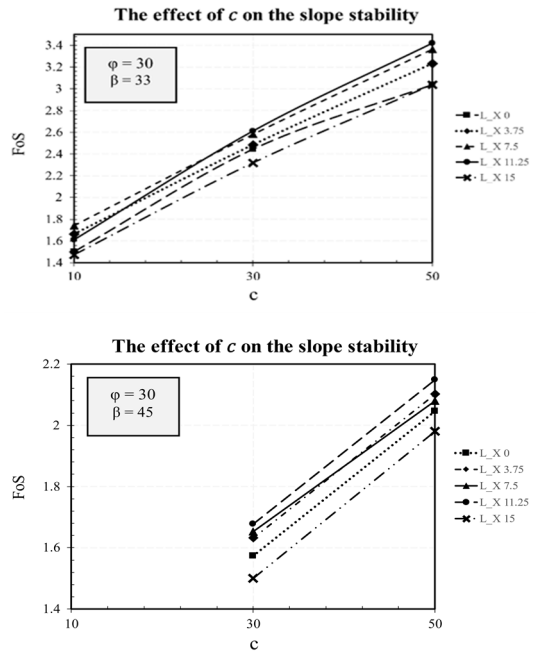

Figure 6. The effect of c on the slope stability

Figure 6 shows the effect of cohesion c on the FoS. The FoS was compared for cohesive coefficient values of 10, 30 and 50 across five different distances from the end of the slope to the piles (L_x 0, L_x 3.75m, L_x 7.5m, L_x 11.25m and L_x 15m).

For a soil model with a friction angle φ of 30 and a slope angle β of 45, soil with a cohesive coefficient of 10 failed. The FoS appears to increase with increasing cohesive coefficient c for

the remaining soil models. Pile rows at L_x 11.25m exhibited the highest FoS.

For soil with a friction angle φ of 30 and a slope angle β of 33, soil stability increases with increasing cohesive coefficient c. Pile rows at L_x 11.25m exhibit low stability at cohesive coefficients c of 10 and 30 but increase rapidly to achieve the highest stability at cohesive coefficients c of 30 to 50. Pile rows at L_x 7.5m exhibit contrasting stability with those at L_x 11.25m, achieving the highest stability at cohesive coefficients c of 10 to 30 and the second highest at cohesive coefficients c of 30 to 50.

3.5. The effect of φ on the slope stability

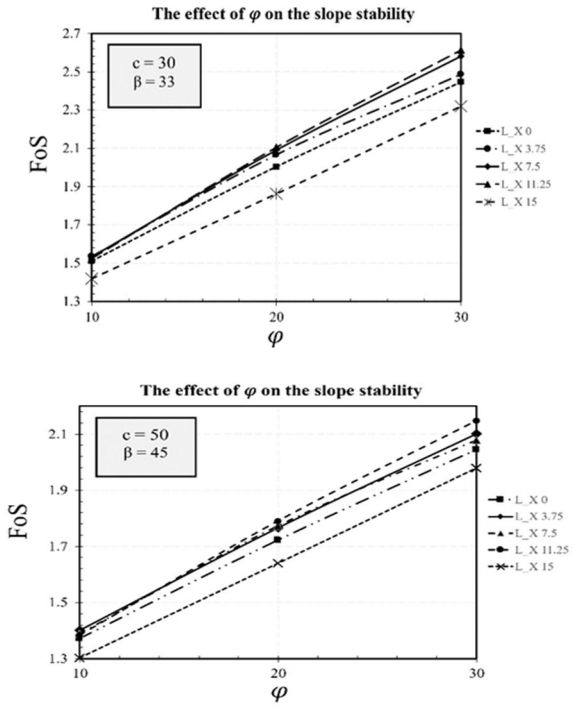

Figure 7. The effect of φ on the slope stability

In order to thoroughly investigate the impact of friction angle φ on the stability of slopes, a detailed comparison was conducted, as shown in Figure 7. This comparison examined the FoS at various friction angles, specifically at 10, 20, and 30 degrees. Additionally, the comparison took into account the distance from the end of the slope to the piles (Lx), with measurements taken at 0, 3.75, 7.5, 11.75, and 15 meters.

In a soil model with a cohesive coefficient c of 30 and a slope angle β of 33 degrees, the Factors of Safety increase with increasing Friction angles. Notably, the line corresponding to L_x = 11.25m exhibits the highest value of FoS.

In a soil model with a coefficient c of 50 and a slope angle β of 45 degrees, the Factors of Safety increase with increasing Friction angles. Furthermore, the line corresponding to L_x = 11.25m exhibits the highest value of FoS.

In general, the soil's quality, as measured by its Factor of Safety, increases with increasing Friction angles. Additionally, the pile rows at L_x = 11.25m exhibit the highest Factor of Safety and provide the greatest stability.

3.6. The effect of β on the slope stability

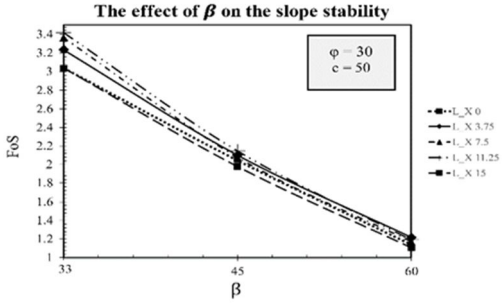

Figure 8. The effect of β on the slope stability

Figure 8 illustrates the effect of the Slope angle β on slope stability. This effect is evaluated by comparing the Factor of Safety at different Slope angles β (33, 45, and 60 degrees) and at various distances (L_x) from the end of the slope to the piles (0, 3.75, 7.5, 11.75, and 15 meters).

In a soil model with a cohesive coefficient c of 50 and a friction angle φ of 30 degrees, the Factor of Safety decreases with increasing Slope angles β. The line corresponding to L_x = 11.25m exhibits the highest value of FoS. In summary, the soil's stability decreases as the Slope angle β increases, and the pile rows at Lx = 11.25m provide the greatest stability.

4. CONCLUSION

This study presented a solution for the analysis of pile placement for slope stabilization. A numerical technique is built by employing the finite element method in the PLAXIS 2D application to give useful insights into the aspects that impact the performance and stability of a certain row of piles. As a result, the safety factors of a single row of piles grow as the cohesive coefficients and friction angle increase. However, this safety factor achieves a maximum near the top of the slope where the Lx has a specific value at 11.25. Furthermore, the decrease in the safety factor of the piles row's stability is shown in this study to demonstrate the major effects of the slope angle and the L-spacing of the piles row.

The study's findings can be used by geotechnical and civil engineers to design and perform the response of piles and surrounding soil interactions by taking into account aspects such as soil parameters, slope geometry, external loads, safety factors, slope angle, and distances between pipes in a single row in order to minimize risks associated with slope instability while providing robust and cost-effective stabilization measures.

This assists the engineer in designing the best pile row on a slope. Continued research and advancements in computational methodologies will enhance our capacity to forecast and minimize slope risks, resulting in safer and more sustainable geotechnical solutions.

Acknowledgement

This research is funded by the Office for International Study Programs (OISP), Ho Chi Minh City University of Technology (HCMUT), VNUHCM under grant number **SVOISP-2022-KTXD-135**. We acknowledge the support of time and facilities from HCMUT, VNUHCM for this study.

References

[1] Cai F, Ugai K. “Numerical analysis of the stability of a slope reinforced with piles”. Soils Found 2000; 40(1): 73–84.
[2] W.B. Wei, Y.M. Cheng. “Strength reduction analysis for slope reinforced with one row of piles”. Computers and Geotechnic, vol. 36, pp. 1176-1185, 2009.
[3] Ho, I-hsuan, "Optimization of Pile Reinforced Slopes Using Finite Element Analyses" (2009). Graduate Theses and Dissertations.11130.
[4] Won J, You K, Jeong S, Kim S. “Coupled effects in stability analysis of pile-slope systems”. Computers and Geotech 2005; 32(4): 304–315.
[5] Ren-Ping Li. “Stability Analysis of Cutting Slope Reinforced with Anti-Slide Piles by FEM”. GeoHunan International Conference 2009.
[6] Koushik P, Shantanu S, Manojit S, Mahesh S. “Stability analysis and design of slope reinforcement techniques for a Himalayan landslide”. Recent Advances in Rock Engineering (RARE 2016).

HAND GESTURE RECOGNITION FOR GAME-BASED HAND REHABILITATION

(NHẬN DIỆN CỬ CHỈ TAY CHO VIỆC CHƠI TRÒ CHƠI HỖ TRỢ PHỤC HỒI CHỨC NĂNG TAY)

Ho Tri Khang[1,3,4,*], Tran Tien Phat[1,3,4], Vo Ngoc Sang[1,3,4] , Nguyen Ngoc Thanh Xuan[1,3,4], Le Gia Phat[1,2,4]

[1] Faculty of Computer Science and Engineering, Ho Chi Minh City University of Technology (HCMUT), 268 Ly Thuong Kiet Street, District 10, Ho Chi Minh City, Vietnam
[2] School of Industrial Management, Ho Chi Minh City University of Technology (HCMUT), 268 Ly Thuong Kiet Street, District 10, Ho Chi Minh City, Vietnam
[3] Office for International Study Programs, Ho Chi Minh City University of Technology (HCMUT), 268 Ly Thuong Kiet Street, District 10, Ho Chi Minh City, Vietnam
[4] Vietnam National University Ho Chi Minh City, Linh Trung Ward, Thu Duc City, Ho Chi Minh City, Vietnam
[*] Corresponding author: khang.ho.0@hcmut.edu.vn

Abstract

Hand rehabilitation is an influential aspect of post-injury recovery for many patients. During the hand rehabilitation process, the patients are required to practice repetitive movements to regain the loss of hand functions. Traditional rehabilitation methods can be tedious and unengaging, leading to poor adherence to treatment plans. Video games have emerged as a potential tool to make rehabilitation more engaging and effective. Moreover, the rapid growth of Artificial Intelligence and Machine Learning recently has led to the idea of applying hand gesture recognition in game-based hand rehabilitation. By playing interactive games, the patients will feel more enjoyable and motivated, thus encouraging the process of recovery. In this work, we propose a real-time skeleton-based hand gesture recognition for game-based rehabilitation. The proposed system aims to support and encourage patients in practicing hand rehabilitation exercises via interesting rehabilitation games. Our system makes use of a Leap Motion controller to extract 3D hand skeletons from the user's hand. A pose-based recognizer will identify the key hand poses from hand skeletal data to recognize the hand gesture. For the system to effectively support the hand rehabilitation process, a set of suitable hand gestures selected from common wrist and finger rehabilitation exercises will be adopted. When a gesture is recognized, the corresponding action will be sent to the game environment to control the game. We also propose three simple, interactive video games designed specifically for hand rehabilitation. Playing these games involves repetitively performing hand rehabilitation exercises, which can help to speed up the recovery process. Our system provides an engaging and interactive way for patients to perform their rehabilitation exercises while also enjoying the benefits of playing video games.

Keywords: *hand rehabilitation, hand gesture recognition, Machine Learning, interactive video games*

1. INTRODUCTION

According to the World Stroke Organization (WSO) [1] and the Global Burden of Disease (GBD) Study 2019 [2], stroke is the second-leading cause of death globally, accounting for 11.6% of total deaths. It is also the third-leading cause of death and disability combined, accounting for 5.7% of total DALYs (Disability-Adjusted Life Years). Stroke survivors often experience hand and upper extremity impairment, which significantly impedes their ability to carry out daily, work, and leisure activities. Therefore, post-stroke hand rehabilitation is essential to restore the strength, mobility, and coordination of the patient's hands.

Post-stroke rehabilitation, however, is a challenging process, since it can be difficult, intensive, and lengthy, depending on the severity of the stroke and which parts of the brain were damaged. Therefore, the success of the recovery process depends on how well patients can commit to the treatment plan. Traditionally, stroke patients follow a rehabilitation method that involves repetitive hand exercises under the guidance of a hand therapist. However, this approach can be tedious and unengaging due to its repetitive nature, leading to the poor adherence of patients to the treatment plan. Therefore, it is crucial to develop an efficient and interesting rehabilitation method that can engage patients and motivate them to follow the treatment plan.

In recent years, there is a growing interest in developing game-based approaches for hand rehabilitation [3], [4]. By adopting modern technologies such as Virtual Reality [5], [6], Augmented Reality [7] and advanced sensors for hand motion

tracking such as Kinect [8], and Leap Motion [9], game-based approaches are useful for creating an interactive environment where patients can enjoy the games while still participating in the hand function recovery process. This is done by performing repetitive hand movements while playing the games. Therefore, game-based rehabilitation is more enjoyable and interactive, enhancing patient engagement and participation in the treatment plan.

In this work, we propose a real-time, skeleton-based hand gesture recognition system for game-based hand rehabilitation. Our system uses a Leap Motion Controller to capture hand movement and extract hand skeletal data. We also developed a gaming application consisting of 3 simple interactive games designed specifically for hand rehabilitation. Interacting with these games involves repetitively performing hand gestures, which simulates the common exercises used in hand rehabilitation. Therefore, patients can enjoy the games while still participating in the recovery process. Compared to previous work on hand gesture recognition in hand rehabilitation, our approach is simpler, faster and is more practical by adopting the set of hand gestures from common hand therapy exercises. We also conducted a user survey with 10 individuals to evaluate the effectiveness of the system on real users. The result shows that the proposed system is enjoyable and can be a potential solution to hand rehabilitation.

2. METHODS AND IMPLEMENTATION

2.1. Overview

We propose a real-time, skeleton-based approach that recognizes hand gestures based on the idea of key pose identification. The workflow of the system is summarized in Figure 1. Generally, the system workflow contains three main stages:

- **Skeleton extraction**: In this stage, the Leap Motion Controller extracts hand skeletal information from the user's hand and sends the data to the next stage to recognize hand gestures.
- **Hand pose identification**: Important features are extracted from hand skeletal data and a trained Support Vector Machine (SVM) will identify hand poses.
- **Gesture recognition from key poses**: The system reads the sequence of identified hand poses and checks if the sequence matches with any valid key pose sequences to construct hand gestures. If there is a hand gesture found, the system will output the result and the corresponding action will be sent to the game environment.

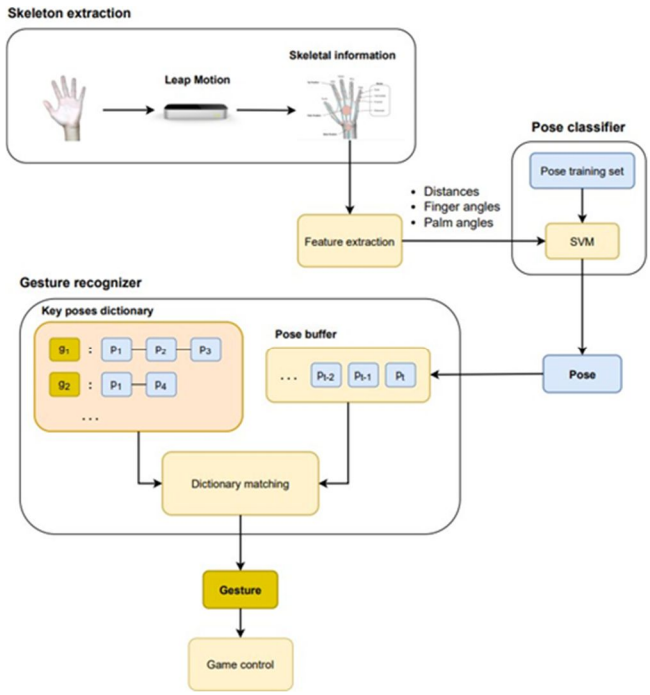

Figure 1. Overview of the proposed system. Our system extracts features from Leap Motion data and recognizes the gesture based on key pose identification

We adopted 9 hand gestures, all of which were selected from common hand, wrist and finger rehabilitation exercises [10], [11] that help patients to recover their hand mobility, strength and flexibility. All of the gestures can be performed by one hand, either the left hand or the right hand. The list of gestures and their equivalent hand exercises are shown in Table 1.

Table 1. List of hand gestures and their corresponding hand exercises

Gesture	Exercises
Move left/right	Wrist ulnar/radial deviation
Move up/down	Wrist extension/flexion
Rotate left/right	Wrist supination/pronation
Close fist	Close fist
Stop	Spreading and closing fingers
Thumb in	Thumb stretch

2.2. Datasets collection

We collected two datasets, a pose dataset to train and evaluate the hand pose classification model, and a gesture dataset to evaluate the proposed hand gesture recognition approach.

Leap motion data: The hand skeletal data extracted by the Leap Motion Controller consists of 3D coordinates of 27 distinct hand joints and hand elements from the user's hand. Each 3D coordinate is a tuple of three values x, y, and z representing the position of an object in the Leap Motion's coordinate system. The Leap Motion's coordinate system sees objects above it in units of real-world millimetres. The origin is located at the top, centre of the hardware. The x-axis and the z-axis lie on the horizontal plane and the x-axis runs parallel to the long edge of the device. The y-axis is a vertical axis perpendicular to the horizontal plane, representing the height from the object to the origin of the device. The skeletal model and the Leap Motion's coordinate system are shown in Figure 2.

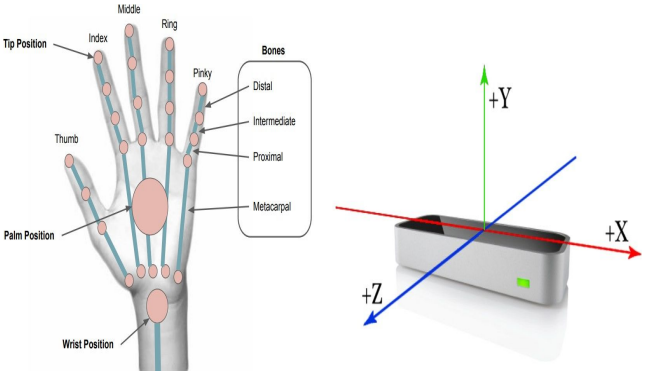

Figure 2. The Leap Motion's skeletal model (left) and the Leap Motion's coordinate system (Right)

Pose dataset: The pose dataset consists of 12 distinct hand poses that are identified by the system (Figure 3). These poses are the main components that are necessary to construct hand gestures. The dataset was collected by six subjects, four men and two women. For a robust evaluation, the training set was collected from four subjects while the test set was collected from the other two. Each sample contains the hand skeletal information captured by the Leap Motion Controller in each frame. The samples are collected by both left and right hands, and from different angles and positions relative to the device. In total, there are 4396 training samples and 1928 test samples.

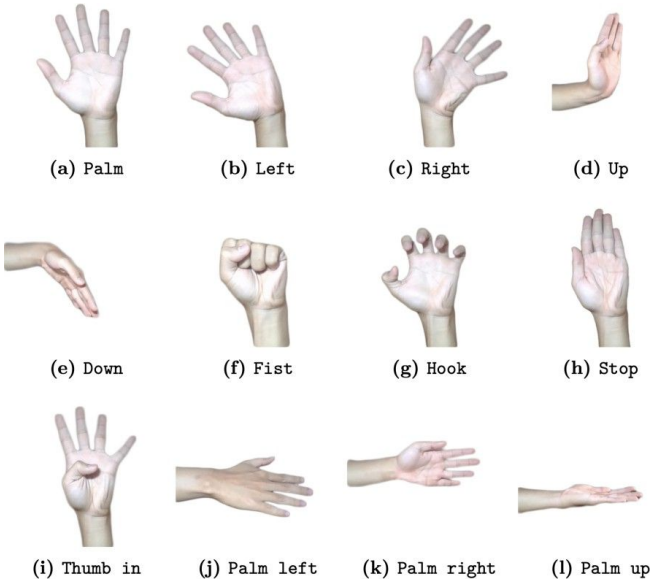

Figure 3. The visual representation of the 12 selected key poses

Gesture dataset: The gesture dataset was generated by 5 subjects, each generating 7 to 10 samples per gesture, using both their left and right hands. Each sample represents one gesture and consists of the sequence of hand-skeletal data recorded for each frame during that gesture. In total, there are 443 samples of 9 hand gestures that are recognized by the system (Table 1).

2.3. Hand pose classification

Feature extraction: From the skeletal data captured by the Leap Motion Controller, we perform feature extraction to extract important features that will be used for pose identification. We first extract 13 local features, including the Euclidean distances between the palm center and the five fingertips, the distances between adjacent fingertips and the angles between adjacent fingers. Such local features not only extract useful hand information but also act as a normalizer that helps remove the noise effects of varying hand positions and angles relative to the Leap Motion's sensors.

Let P denote the point representing the palm centre within the Leap Motion's coordinate system. The five fingertips, denoted as F_i where i in [1, 5], correspond to the thumb, index finger, middle finger, ring finger, and pinky finger, respectively. The distance-based features can be calculated as follows:

$$D_i = \big||F_i - P|\big|, i \in [1,5]$$

$$D_{F_i} = \big||F_{i+1} - F_i|\big|, i \in [1,4]$$

where D_i represents the Euclidean distances between the

palm centre and the five fingertips, and D_{F_i} represents the distances between every pair of adjacent fingertips.
The angles between adjacent fingers will be

$$\alpha_i = \arccos\left(\frac{(F_i - P)\cdot(F_{i+1} - P)}{||F_i - P||\cdot||F_{i+1} - F_i||}\right), i \in [1,4]$$

where α_i represents the angles (in radians) between every pair of adjacent fingers.

Next we extracted three global features, including the yaw, pitch, and roll angles of the hand. These features represent the global movement of the user's hand relative to the Leap Motion Controller. After feature extraction, the final feature vector V consists of 16 distinct features:

$$V = (D_1 \dots D_5, D_{F_i} \dots D_{F_4}, \alpha_1 \dots \alpha_4, yaw, pitch, roll)$$

This feature vector is standardized and fed to the pose classifier for hand pose classification.

Pose classification:

In this stage, the feature vector is classified as one of the hand poses that were introduced in Figure 3. Several machine learning algorithms were tested. We found that Support Vector Machine (SVM) with radial basis function (rbf) kernel demonstrated the highest accuracy of **96.84%** on our pose dataset (see Section 3 for more detail). Therefore, we chose SVM with the rbf kernel as the pose classifier of the system.

2.4. Gesture recognition from key poses

In our setting a gesture g is represented as a sequence of key poses $g = (p_1, p_2, \dots, p_{g_n})$, where p_i belongs to a finite set of key poses p. Most of the gestures are composed of 2 to 3 key poses and can have different combinations of key poses. We built a key pose dictionary that contains all the mappings from gestures to key pose sequences. Each record in the dictionary is a pair of key-value (k, v) where k is a hand gesture and v is the list containing all possible key pose sequences that can be used to build up that gesture. To ensure the generalization of our approach, 6 subjects were asked to perform each gesture in several ways. We then captured the sequences of poses and manually inserted all possible key pose sequences into the key pose dictionary. The final key pose dictionary is shown in Table 2.

Table 2. Key pose dictionary for gesture recognition. Each gesture can be defined by a finite sequence of key poses

Gesture	ID	Key Pose Sequences
Move left	g0	(p0, p1), (p7, p1)
Move right	g1	(p0, p2), (p7, p2)
Move up	g2	(p0, p3), (p7, p3)
Move down	g3	(p0, p4), (p7, p4)
Rotate left	g4	(p0, p10, p11), (p7, p10, p11)
Rotate right	g5	(p0, p9, p11), (p7, p9, p11)
Close fist	g6	(p0, p5), (p0, p6, p5), (p0, p8, p6, p5)
Stop	g7	(p0, p7, p0)
Thumb in	g8	(p0, p8, p0), (p7, p8, p7)

When a hand pose pt is identified by the pose classifier at time t, it will be inserted into a pose buffer β. The gesture recognizer will then read the sequence of all identified poses $s = (p_{t-n}, \dots, p_{t-1}, p_t)$ from the buffer and search from the key pose dictionary to see if there is any key pose sequence $x = (p_1, \dots, p_{g_n})$ contained in s. If the match is found, the gesture g composed of the sequence x will be recognized. The buffer will then be cleared and ready to store the next hand pose. If no match is found, nothing will be recognized. The buffer will continuously store newly identified hand poses until a match is found. More details of the gesture recognition process are described in Algorithm 1.

Figure 4. Shapes and Colors

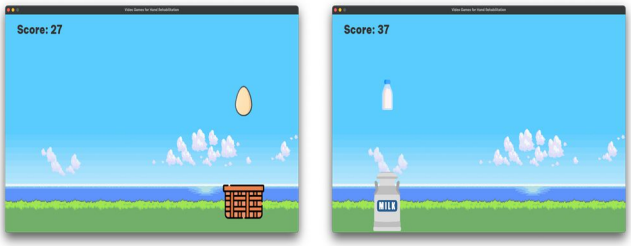

Figure 5. Eggs and Milk

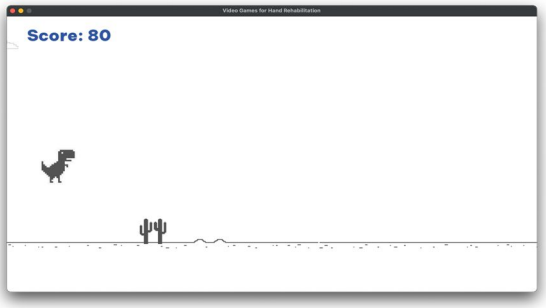

Figure 6. Dino Run

2.5. Interactive games for hand rehabilitation

We developed 3 interactive games for hand rehabilitation: Shapes and Colors, Eggs and Milk and Dino Run, as shown in Figure 4, Figure 5 and Figure 6, respectively. These three games were developed using Python 3.9.0 and PyGame 2.3.0. In the first game, Shapes and Colors, the player needs to select the correct shape and colour according to the question prompted on the screen. In the second game, Eggs and Milk, the player needs to move the container to catch the falling object from the top of the screen. Finally, the Dino Run game requires controlling the dinosaur to avoid as many obstacles as possible. In all of the three games, the player has to perform hand gestures to interact with the application. Therefore, the application helps improve hand mobility and flexibility and guarantees a positive effect on hand rehabilitation.

3. RESULTS AND DISCUSSION

3.1. Hand gesture recognition

We performed some experiments to evaluate the performance of the system on our pose and gesture datasets. All experiments were conducted on an ASUS laptop equipped with an Intel Core i5-8250U 1.6GHz CPU and 12GB RAM.

Table 3. Evaluation results on the pose test set of five classification models. * : The precision, recall and F1 score is the weighted average from all classes.

Model	Accuracy (%)	Precision *	Recall*	F1 score*
SVM	**96.84**	0.9698	0.9684	**0.9684**
MLP	**96.47**	0.9686	0.9673	**0.9675**
Random Forest	91.34	0.9300	0.9134	0.9145
Logistic Regression	82.21	0.8336	0.8221	0.8211
k-NN	92.21	0.9323	0.9222	0.9225

To find out the best pose classifiers, we trained 5 different machine learning models, including Support Vector Machine (SVM), Multilayer Perceptron (MLP), Random Forest, Logistic Regression and *k*-Nearest Neighbors (*k*-NN) on our pose training set. During the training process, we used k-fold cross-validation with k = 10 and applied Grid Search [12] to find the best hyperparameter settings for each model. After that, we evaluated the performance of these models on the pose test set. From the result (Table 3), we found that SVM has the highest test set accuracy (96.84%), so we chose SVM as the pose classifier of the system.

The precision, recall and F1 score on each hand pose class using SVM are depicted in Table 4. Our pose classifier achieves outstanding results on all of the classes (all larger than 0.9). Some of the classes have maximum precision (Right), recall (Stop) and F1 score (Thumb_in).

Table 4. The precision, recall and F1 score on each hand pose class using the SVM model

Pose	Precision	Recall	F1 score
Palm	**0.9130**	0.9492	**0.9307**
Left	0.9218	0.9593	0.9492
Right	**1.0000**	0.9722	0.9859
Up	0.9939	0.9760	0.9849
Down	0.9803	**0.8922**	0.9342
Fist	**1.0000**	0.9897	0.9948
Hook	0.9867	0.9867	0.9867
Stop	0.9321	**1.0000**	0.9649
Thumb_in	**1.0000**	**1.0000**	**1.0000**
Palm_left	**0.9044**	**1.0000**	0.9498
Palm_right	0.9916	**1.0000**	0.9958
Palm_up	**1.0000**	**0.9060**	0.9507

We also studied the effect of different feature extraction settings on hand pose classification using SVM and MLP (Table 5). We found that Distances (distance-based features) and Palm angles (Yaw, pitch, and roll angles) are the two most important groups of features, omitting one of which can lead to a significant drop in classification accuracy.

Table 5. Performance of pose classifier on different feature extraction settings

Feature extraction setting	Accuracy	
	SVM (rbf)	MLP (100,)
Distances + Palm angles + Finger angles	96.84	96.47
Distances + Finger angles	66.8	69.5
Palm angles + Finger angles	75.99	79.72
Distances + Palm angles	96.68	95.38
Raw skeleton data	85.32	84.96

After finding the best hand pose classifier, we evaluated our pose-based gesture recognition approach on the gesture dataset. The precision, recall and F1 score on each gesture class are shown in Table 6. We achieved an accuracy of 94.46% on the gesture dataset and obtained impressive results for many gesture classes. However, there are still many false positive cases in which the system recognizes non-existent hand gestures or misclassifies a gesture as another one.

Table 6. Precision, recall and F1 scores on the gesture dataset

Gesture	Precision	Recall	F1 score
Move left	1.0000	0.9792	0.9895
Move right	0.9245	0.9800	0.9514
Move up	0.8909	0.9800	0.9333
Move down	0.7539	1.0000	0.8596
Rotate left	1.0000	0.9750	0.9873
Rotate right	1.0000	**0.8684**	0.9296
Close fist	0.9259	1.0000	0.9615
Stop	**0.8444**	1.0000	0.9157
Thumb in	0.9250	0.9250	0.9250
Weighted average	0.9159	0.9702	0.9393

3.2. Time performance

We also evaluated the time performance of the system by calculating the average elapsed time per frame of the system. The result is shown in Table 7. Our system relies on the hand skeleton tracking process from Leap Motion, which operates consistently at 16.67ms (60FPS) in our experiments. Meanwhile, the execution time per frame for hand gesture recognition (1.2 ms) is significantly lower than the time required for skeleton extraction (16.67 ms). Therefore, the system's overall execution time remains within 16.67 ms (60 FPS), meaning that the system can achieve real-time performance.

Table 7. Execution time and frame per second of our system.

Skeleton Extraction by LMC		Hand Gesture Recognition		Overall	
Time	FPS	Time	FPS	Time	FPS
16.67	60	1.2	833	16.67	60

3.3. User Study

We conducted a user study with 10 individuals to study the effectiveness of our system on real users. The study was conducted in both a residential area and a private home. There are two main stages in our study, a pre-survey study and a post-survey study.

In the pre-survey stage, we collected background information of the 10 participants, including their age, sex and general experiences to hand rehabilitation. The pre-survey results are shown in Table 8. From the results, it can be seen that the majority of participants are elderly (70% of them are over 60 years old). Two of them have experienced hand therapy before and three of them have played hand-interactive games before.

Table 8. Demographic characteristics of the study population

Variable		n
Age (years)	15-30	1
	30-45	1
	45-60	1
	> 60	7
Gender	Male	5
	Female	5
Have experienced physical therapy?	Yes	2
	No	8
Have played hand-interactive games?	Yes	3
	No	7
Gaming frequency per week?	0	6
	1-5	2
	5-10	1
	> 10	1

In the post-survey stage, we collected their feedback after they had tried our solution. The pose-survey result is shown in Figure 7. Overall, all participants expressed favourable feedback, finding the solution compact, enjoyable, and easy

to use. Aesthetic design is crucial in motivating individuals to use the game regularly, and all participants found our application aesthetically pleasing. And most importantly, all the participants found our application is meaningful and necessary for hand rehabilitation.

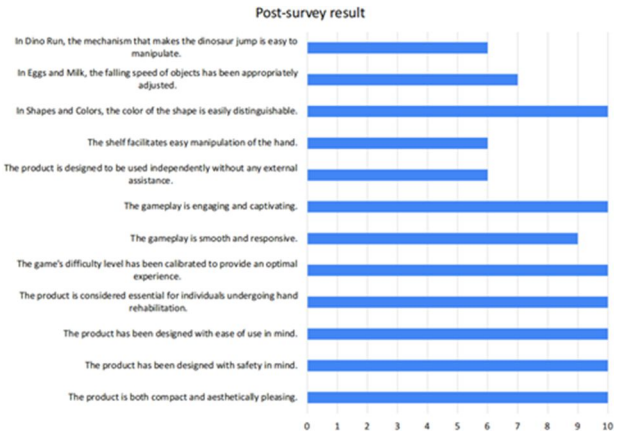

Figure 7. Post-survey result

4. CONCLUSION

In this work, we have implemented a real-time, skeleton-based hand gesture recognition system for hand rehabilitation and achieved remarkable results on our two self-generated datasets (96.84% on the pose dataset and 94.46% on the gesture dataset). We also developed a gaming application for hand rehabilitation and conducted a user study to collect feedback from real users. Most of the users agree that our system is interesting and is a potential solution for hand rehabilitation.

However, there is still some room for improvement in our work. Firstly, our self-generated datasets are small and our user study is still limited to only 10 individuals, which means the system might not be generalized enough to new data, and the collected feedback from the users may still be biased. Secondly, the pose-based gesture recognition approach can face some robustness issues when there are some errors in hand pose classification, and the design using hand poses may not be a good choice for more complex hand gestures which require exact hand movement from the user. These limitations will be addressed in our future work.

Acknowledgement

This research is funded by the Office for International Study Programs (OISP), Ho Chi Minh City University of Technology (HCMUT), VNUHCM under grant number **OSTS - 2023 - KH&KTMT - 01**. We acknowledge the support of time and facilities from HCMUT, VNUHCM for this study.

References

[1] V. L. Feigin, M. Brainin, B. Norrving, S. Martins, R. L. Sacco, W. Hacke, M. Fisher, J. Pandian, and P. Lindsay, "World Stroke Organization (WSO): Global Stroke Fact Sheet 2022," International Journal of Stroke, vol. 17, no. 1, pp. 18–29, 2022.

[2] GBD 2019 Stroke Collaborators, "Global, regional, and national burden of stroke and its risk factors, 1990-2019: a systematic analysis for the Global Burden of Disease Study 2019," Lancet Neurol, vol. 20, no. 10, pp. 795–820, 2021.

[3] I. Ayed, A. Ghazel, A. Jaume-i Capo, G. Moy ´ a Alcover, J. Varona, and ` P. Martinez Bueso, "Vision-Based Serious Games and Virtual Reality Systems for Motor Rehabilitation: A Review Geared Toward a Research Methodology," International Journal of Medical Informatics, vol. 131, 2019.

[4] J. Byra and K. Czernicki, "The Effectiveness of Virtual Reality Rehabilitation in Patients with Knee and Hip Osteoarthritis," Journal of Clinical Medicine, vol. 9, no. 8, 2020.

[5] R. M. Al-Whaibi, M. S. Al-Jadid, H. R. ElSerougy, and W. M. Badawy, "Effectiveness of virtual reality-based rehabilitation versus conventional therapy on upper limb motor function of chronic stroke patients: a systematic review and meta-analysis of randomized controlled trials," Physiother Theory Pract, vol. 38, no. 13, pp. 2402–2416, 2021.

[6] K. E. Laver, B. Lange, S. George, J. E. Deutsch, G. Saposnik, and M. Crotty, "Virtual reality for stroke rehabilitation," Cochrane Database Syst Rev, vol. 11, no. 11, p. CD008349, 2017.

[7] E. R. Ram´ırez, R. Petrie, K. Chan, and N. Signal, "A Tangible Interface and Augmented Reality Game for Facilting Sit-to-Stand Exercises for Stroke Rehabilitation," in Proceedings of the 8th International Conference on the 18. Association for Computing Machinery, 2018. [Online]. Available: https://doi.org/10.1145/3277593.3277635

[8] Y. Bouteraa, I. B. Abdallah, and A. M. Elmogy, "Training of Hand Rehabilitation Using Low Cost Exoskeleton and Vision-Based Game Interface," Journal of Intelligent & Robotic Systems, vol. 96, no. 1, pp. 31–47, 2019.

[9] W. Li, C. Hsieh, L. Lin, and W. Chu, "Hand gesture recognition for post-stroke rehabilitation using leap motion," in Proceedings of the 2017 IEEE International Conference on Applied System Innovation, T.-H. Meen, A.

Lam, and S. Prior, Eds. Institute of Electrical and Electronics Engineers Inc., 2017, pp. 386–388.

[10] H. H. Publishing, "5 exercises to improve hand mobility," https://www.health.harvard.edu/pain/5-exercises-to-improve-h and-mobility, accessed: 2023-05-05.

[11] N. inform, "Exercises for wrist, hand and finger problems," https: //www.nhsinform.scot/illnesses-and-conditions/muscle- bone-and joints/exercises/exercises-for-wrist-hand-and-finger-problems, accessed: 2023-05-15.

[12] Scikit-learn contributors, "Scikit-learn - Tuning the hyperparameters of an estimator," https://scikit-learn.org/stable/modules/grid search, accessed: 2023-05-11

BACHKHOA ECO-FRIENDLY GUIDE - AN AIOT DEVICE FOR RAISING AWARENESS ABOUT TRASH CLASSIFICATION AT SOURCE

(BACHKHOA ECO-FRIENDLY GUIDE - THIẾT BỊ AIOT NÂNG CAO NHẬN THỨC VỀ PHÂN LOẠI RÁC TẠI NGUỒN)

Vo Ngoc Sang[1,3,4,*], Pham Hoang Anh[1,3,4*], Ho Tri Khang[1,3,4], Tran Tien Phat[1,3,4], Nguyen Ngoc Thanh Xuan[1,3,4], Le Gia Phat[1,2,4], Nguyen Lam Tam Nhu[1,2,4]

[1] Faculty of Computer Science and Engineering, Ho Chi Minh City University of Technology (HCMUT), 268 Ly Thuong Kiet Street, District 10, Ho Chi Minh City, Vietnam
[2] School of Industrial Management, Ho Chi Minh City University of Technology (HCMUT), 268 Ly Thuong Kiet Street, District 10, Ho Chi Minh City, Vietnam
[3] Office for International Study Programs, Ho Chi Minh City University of Technology (HCMUT), 268 Ly Thuong Kiet Street, District 10, Ho Chi Minh City, Vietnam
[4] Vietnam National University Ho Chi Minh City, Linh Trung Ward, Thu Duc City, Ho Chi Minh City, Vietnam
[*] Corresponding author: sang.vo27042001@hcmut.edu.vn

Abstract

For the sake of protecting the environment and promoting sustainable growth, waste segregation is an urgent and vital issue. However, in Vietnam, there is still a relatively low level of awareness and action when it comes to waste separation at source. This is a critical area in which every individual, especially students, plays a significant role in changing society's waste disposal practices. According to Science and Technology Magazine No. 70 (April 2022), up to 57% of students struggle with incorrect or incomplete waste categorization [1]. To raise public awareness and address this issue, our research team proposes an IoT device incorporating AI technology - Computer Vision. The device utilizes a camera to take photos of trash, which are then classified into categories using a Convolutional Neural Network. Then, a display screen provides information about the waste and guides users on how to dispose of it properly. This tool can be used in student spaces, such as dormitories, schools, and cafeterias, to promote waste separation at source and raise environmental awareness among students. Our team believes that implementing this solution will reduce improperly disposed waste and establish a successful circular economy.

Keywords: *artificial intelligence, computer vision, internet of things, human awareness, waste segregation*

1. INTRODUCTION

In the modern era, the utilization of science and technology, including artificial intelligence (AI), has become indispensable across various aspects of life. Deep learning, a subfield of artificial intelligence (AI), has witnessed remarkable advancements and emerged as a powerful tool in multiple applications. Its ability to automatically learn and extract complex patterns from large datasets has led to breakthroughs in many domains, including computer vision, natural language processing, and speech recognition. Promoting sustainable practices and mitigating the environmental impact of improper waste management requires individuals worldwide to be aware of waste sorting at source. Vietnam, however, still lacks awareness and action in this area. In [1], a survey of 1513 students at the Vietnam Maritime University was conducted. The survey results show that 95.85% of the students have an understanding of the harmful effects of single-use plastic, but only 57% of the students could identify groups of waste sorting. The student's concern and understanding of the meaning of plastic codes/labels are still limited. Based on the survey results, most students are aware of the harms of plastic waste, but this awareness is still insufficient. Therefore, it is extremely necessary to implement propaganda, dissemination, and education to raise students' awareness about waste sorting, reduction, reuse, recycling, and treatment. In that scenario, the integration of cutting-edge technologies holds significant promise in promoting sustainable practices. This study introduces a revolutionary product called BEG (Bachkhoa Eco-friendly Guide) that utilizes computer vision and machine learning to educate people about environmental issues and improve waste management. This study makes several significant contributions. Firstly, the BKTrashImage

dataset is introduced, which contains 6205 images belonging to five different categories, including Paper Cup, Aluminum Can, Milkbox, PET Bottle, and Foam Box. Secondly, the study develops BEGNet, an efficient trash image classification model. Thirdly, an architecture for IoT devices is proposed to effectively implement and deploy the trash bin system. Finally, experiments are conducted to demonstrate the effectiveness of the proposed model compared to state-of-the-art approaches for trash classification on both Trashnet and BKTrashImage datasets.

2. METHODS AND IMPLEMENTATION

2.1. Data collection

In order to address the problem of students' awareness of classifying garbage at source, we generate a dataset that has classes focusing on the trash that is frequently disposed of by students.

In the phase of data collection, we combine the data set Trashnet [2], with other images collected both on the Internet and manually. The combined dataset, named BKTrashImage, has six classes, which are: Paper Cup, Aluminum Can, Milk Box, PET Bottle and Foam Box, including 6205 images in total.

The Trashnet dataset was collected by mobile devices, containing 2527 images with six classes: glass, paper, cardboard, plastic, metal, and trash. The object of images was placed on a white background and using sunlight and/or room lighting. The statistic of images for each class was presented in Table 1 while Figure 1 shows several samples in each class of this dataset.

Table 1. The statistic of the Trashnet dataset

No	Classes	Number of images
1	Glass	501
2	Paper	594
3	Cardboard	403
4	Plastic	482
5	Metal	401
6	Trash	137

We try to make the dataset as balanced as possible, Table 2 shows the distribution of our dataset BKTrashImage. To have more insight into how BKTrashImage looks, Figure 2 shows some samples of each class of the dataset.

Figure 1. Samples of Trashnet dataset

Table 2. The statistics of the BKTrashImage dataset

No	Classes	Number of images
1	Paper Cup	1556
2	Aluminum Can	1531
3	Milk Box	1625
4	PET Bottle	1499
5	Foam Box	1395

Figure 2. Samples of BKTrashImage dataset

2.2. Process-deciding and image-classifying components

In this section, we would like to introduce the implementation of our Computer Vision technique to detect if trash is in front of the camera to begin processing the image, and the deep-learning solution for the image-classifying purpose.

To avoid feeding the image constantly to the Image Classifying module, we implement a Process-Deciding module to decide when to process the captured image in the next steps. In detail, to detect if there is a person putting trash on the screen, we use the K-nearest neighbours (KNN)-based Background/Foreground Segmentation Algorithm [3] - a method used for detecting moving objects in videos, which has been completely implemented in the library OpenCV[4], a library of programming functions mainly for real-time computer vision.

This KNN-based Background/Foreground Segmentation Algorithm uses the squared distance to compute the distance between the pixels and the sample to decide whether a pixel is close to that sample or not. Considering 2 pixels as 2 vectors in the 3-dimension space (3 channels of colour for red, green and blue), we could calculate the squared distance of that 2 pixels as in Equation 1:

$$distance = \sqrt{(p_{1,red} - p_{2,red})^2 + (p_{1,green} - p_{2,green})^2 + (p_{1,blue} - p_{2,blue})^2} \quad (1)$$

With $p_{i,c}$ is a value of the pixel number i, at the colour channel c.

The KNN-based Background/Foreground Segmentation Algorithm will return a binary image called a mask. Upon receiving this mask, we calculate the ratio between the number of pixels of the foreground and that of the whole image, then check if this ratio exceeds a given threshold, which is empirically set.

The calculation of the ratio mentioned above is

$$ratio = \frac{number\ of\ foreground\ pixels}{number\ of\ image\ pixels} \quad (2)$$

Figure 3. The changes of the mask when a moving object is in front of the camera. The moving object is considered the foreground (white pixels), and the remaining area is the background (black pixels).

Figure 3 shows how the mask changes if there are moving objects in front of the camera. In this circumstance, the student's hand holding a piece of garbage is considered a moving object. Figure 4 shows the flowchart of how the 2 components, Process-Deciding and Image-Classifying, work together.

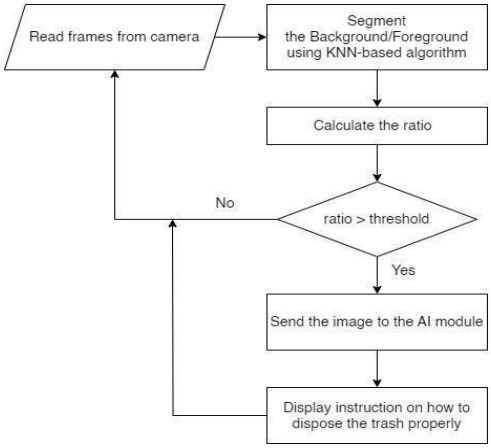

Figure 4. The flowchart of how the 2 components, Process-Deciding and Image-Classifying, work together. Ifthe Process-Deciding module recognizes a moving object in front of the camera, the Image-Classifying module will process the image.

Radosavovic et al. [5] proposed RegNetX and RegNetY, which present the network design space for reducing the computation and the number of epochs. The design space concept has an important property that is more interpretable. For the purpose of classifying images, a robust framework utilizing Deep Neural Networks for trash classification namely BACHKHOA Eco-friendly Guide Network (BEGNet) is introduced, which uses the RegNetY120, whose weight was pre-trained with the dataset ImageNet, followed by a Global Average Pooling layer and a Sigmoid activation function.

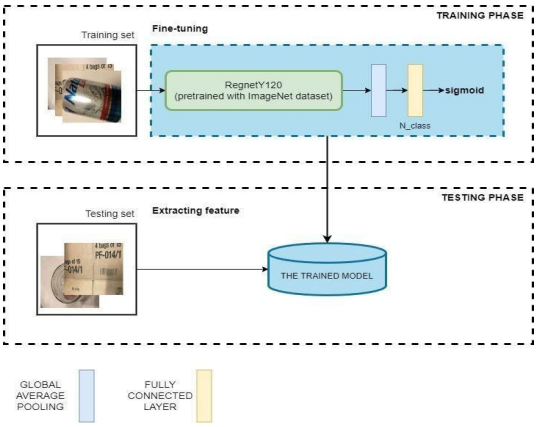

Figure 5. The approach of BEG. The backbone RegNetY120, whose weight was pre-trained with the dataset ImageNet, is followed by a Global Average Pooling layer and a Sigmoid activation function.

2.3. Proposed architecture of the device

In this section, we propose an IoT architecture for our solution. The overall system consists of three interconnected components: smart trash bins with built-in our classification models, a database, and a mobile application. This system operates through the Internet, enabling real-time communication between the components.

The trash bin system comprises three primary modules: Jetson Nano, Jetson Nano IMX219 8MP camera module, and a display screen.

The workflow of our product follows a series of key steps. Firstly, when the camera sensor detects the presence of trash, it activates the system. Subsequently, the camera is engaged to capture an image of the trash, temporarily storing it in the Jetson Nano's storage. Next, the Jetson Nano employs our BEGNet model to analyze the captured image. Once the classification result is obtained, the system promptly determines the type of that trash and displays guidance to dispose of it properly on the screen.

Each bin is also equipped with a sensor that measures the volume of trash inside. Whenever a trash bin reaches its capacity, a signal is immediately transmitted to a real-time database. This information is then seamlessly transferred to the mobile application, ensuring users receive instant updates.To better visualize the system, refer to Figure 6, which presents the diagram of the entire architecture.

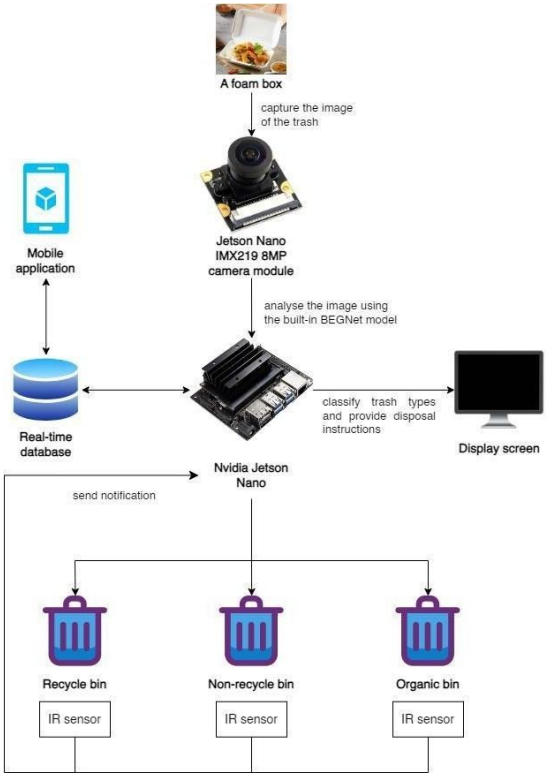

Figure 6. The workflow of BEG

The trash bin system comprises three primary modules: Jetson Nano, Jetson Nano IMX219 8MP camera module, and a display screen.

The workflow of our product follows a series of key steps. Firstly, when the camera sensor detects the presence of trash, it activates the system. Subsequently, the camera is engaged to capture an image of the trash, temporarily storing it in the Jetson Nano's storage. Next, the Jetson Nano employs our BEGNet model to analyze the captured image. Once the classification result is obtained, the system promptly determines the type of that trash and displays guidance to dispose of it properly on the screen.

Each bin is also equipped with a sensor that measures the volume of trash inside. Whenever a trash bin reaches its capacity, a signal is immediately transmitted to a real-time database. This information is then seamlessly transferred to the mobile application, ensuring users receive instant updates. To better visualize the system, refer to Figure 6, which presents the diagram of the entire architecture.

3. RESULTS AND DISCUSSION

3.1. Experimental setting

In this section, a quantitative evaluation of the proposed image-classifying module and other methods is presented, based on two experimental datasets including Trashnet and BKTrashImage datasets that were introduced in the previous section. For each dataset, we spend 80% for training and the remaining 20% for testing.

About the environment, the experimental methods were implemented in Python 3.10.11 and performed on the Tensorflow framework which is a free software deep learning library for the Python programming language. The operating system is Ubuntu 20.04.5 LTS with a GPU NVIDIA A100-SXM4-40GB and 83.48 GB of RAM.

This study utilizes state-of-the-art methods for trash classification including Densenet121_Aral[6], InceptionResNet_Ruiz[7], MobileNetV2_Lam [8] and DNN-TC_Vo[9], to compare with the proposed approach for trash image classification. For the two other approaches, the Stochastic Gradient Descent (SGD) is used as an optimizing algorithm with a learning rate $\alpha = 0.0001$. In addition, this research uses batch size = 128 with 20 epochs and evaluates the model's performance on the testing set for every epoch during training processing. In the testing phase, this study performs the comparison between the experimental methods based on the testing set for trash image classification.

3.2. Experimental results

The accuracy of the proposed Image-Classifying module compared with the other experimental approaches for the Trashnet dataset was presented. The experimental result in terms of accuracy is shown in Table 3. Empirically evaluated on the Trashnet dataset, our proposed approach outperforms other approaches for the Trashnet dataset. Specifically, our method achieved 94.26%, taking first place, while Densenet121_Aral, Inception-ResNet_Ruiz, DNN-TC_Vo and MobileNetV2_Lam obtained 93.66%, 93.27%, 93.07% and 88.12% in terms of accuracy respectively.

Next, We performed experimental methods on the BKImageTrash dataset, which contains many objects in each class, to demonstrate the effectiveness of our proposed approach. As shown in Table 4, our method achieved the highest accuracy of 97.17% compared to all other experimental methods for the BKImageTrash dataset. The next best-performing models were Inception-ResNet Ruiz (96.45%) and Densenet121 Aral (96.32%). Although MobileNetV2 Lam and DNN-TC Vo achieved high accuracies of 95.73% and 95.79%, respectively, they still fell short by over 1% compared to our proposed model.

Table 3. The accuracy of the experimental methods on the Trashnet dataset

No	Method	Accuracy (%)
1	Densenet121_Aral [6]	93.66
2	Inception-ResNet_Ruiz [7]	93.27
3	MobileNetV2_Lam [8]	88.12
4	DNN-TC_Vo [9]	93.07
5	BEGNet	**94.26**

Table 4. The accuracy of the experimental methods on the BKImageTrash dataset

No	Method	Accuracy (%)
1	Densenet121_Aral[6]	96.32
2	Inception-ResNet_Ruiz[7]	96.45
3	MobileNetV2_Lam [8]	95.73
4	DNN-TC_Vo [9]	95.79
5	BEGNet	**97.17**

3.3. Discussion on the result

To demonstrate the effectiveness of our approach, we compared it with state-of-the-art methods on both the Trashnet and BKTrashImage datasets. The Trashnet dataset is a small dataset in which most images contain a single object, while the BKTrashImage dataset focuses on the trash frequently disposed of by students, but has the same format. We empirically evaluated BEGNet on both datasets and achieved impressive results. For the Trashnet dataset, our approach achieved a 94.26% accuracy rate, outperforming other approaches. For the BKTrashImage dataset, our approach achieved the highest accuracy of 97.17%. These results demonstrate the effectiveness of our proposed approach and its potential for practical applications.

4. CONCLUSION

This paper proposes a deep neural network model called BEGNet for classifying trash. In this study, we made two significant contributions. First, we created the BKTrashImage dataset, which includes 6205 images in six different trash categories. Second, we developed the BEGNet model by modifying the RegNetY120 architecture to improve classification performance. In terms of accuracy, BEGNet outperformed other state-of-the-art methods on both the Trashnet and BKTrashImage datasets. Third, an architecture for IoT devices is also introduced to effectively implement and deploy the trash bin system into practice. The proposed solution can have significant benefits for the environment, society, and the economy. By raising awareness about trash classification at source of students, it can promote behavioural change among them, who play a critical role in changing society's waste disposal practices. In conclusion, the proposed IoT device - BACHKHOA Ecofriendly Giude (BEG), which incorporates AI technology - Computer Vision, has shown promising results in addressing the critical issue of waste segregation and raising environmental awareness among students. Implementing this solution can have significant benefits for the environment, society, and the economy. Further research and development are needed to optimize the proposed approach and scale it up for broader applications. Overall, it is a step in the right direction towards promoting sustainable waste management practices and a greener future.

Acknowledgement

This research is funded by Office for International Study Programs (OISP), Ho Chi Minh City

University of Technology (HCMUT), VNUHCM under grant number **OSTS - 2023 - KH&KTMT - 02**. We acknowledge the support of time and facilities from HCMUT, VNUHCM for this study.

References

[1] D. P. Thi and H. D. T. Thuy, "Survey and assessment of the student's awareness and behaviors about waste sorting and single use plastic consumption habits." [Online]. Available: https://jmst.vimaru.edu.vn/index.php/tckhcnhh/article/view/21

[2] M. Yang and G. Thung, "Classification of trash for recyclability status," CS229 project report, vol. 2016, no. 1, p. 3, 2016.

[3] Z. Zivkovic and F. Van Der Heijden, "Efficient adaptive density estimation per image pixel for the task of background subtraction," Pattern recognition letters, vol. 27, no. 7, pp. 773–780, 2006.

[4] [Online]. Available: https://docs.opencv.org/4.x/db/d88/classcv1 1BackgroundSubtractorKNN.html#details

[5] I. Radosavovic, R. P. Kosaraju, R. Girshick, K. He, and P. Dollar, "Designing network design spaces," in Proceedings of the IEEE/CVF conference on computer vision and pattern recognition, 2020, pp. 10 428– 10 436.

[6] R. A. Aral, S. R. Keskin, M. Kaya, and M. Hacıomeroglu, "Classification of trashnet dataset based on deep learning models," in 2018 IEEE International Conference on Big Data (Big Data). IEEE, 2018, pp. 2058–2062.

[7] V. Ruiz, A. S anchez, J. F. V elez, and B. Raducanu, "Automatic image- based waste classification," in From Bioinspired Systems and Biomedical Applications to Machine Learning: 8th International Work-Conference on the Interplay Between Natural and Artificial Computation, IWINAC 2019, Almer´ıa, Spain, June 3–7, 2019, Proceedings, Part II 8. Springer, 2019, pp. 422–431.

[8] K. N. Lam, N. H. Huynh, N. B. Ngoc, T. T. H. Nhu, N. T. Thao, P. H. Hao, V. V. Kiet, B. X. Huynh, and J. Kalita, "Using artificial intelligence and IoT for constructing a smart trash bin," in Future Data and Security Engineering. Big Data, Security and Privacy, Smart City and Industry 4.0 Applications: 8th International Conference, FDSE 2021, Virtual Event, November 24–26, 2021, Proceedings 8. Springer, 2021, pp. 427–435.

[9] A. H. Vo, M. T. Vo, T. Le et al., "A novel framework for trash classification using deep transfer learning," IEEE Access, vol. 7, pp. 178 631–178 639, 2019.

APPLICATION OF GENETIC ALGORITHM TO OPTIMIZE THE COMPARATOR CIRCUIT WITH RESPECT TO SPEED AND POWER CONSUMPTION

(NGHIÊN CỨU VÀ ỨNG DỤNG THUẬT TOÁN DI TRUYỀN VÀO TỐI ƯU HÓA TỐC ĐỘ VÀ CÔNG SUẤT TIÊU THỤ CỦA MẠCH SO SÁNH)

Nguyen Trong Hoang[1,2,3], Hoang Trang[1,3]

[1] Faculty of Electrical and Electronics Engineering, Ho Chi Minh City University of Technology (HCMUT), 268 Ly Thuong Kiet Street, District 10, Ho Chi Minh City, Vietnam
[2] Office for International Study Programs, Ho Chi Minh City University of Technology (HCMUT), 268 Ly Thuong Kiet Street, District 10, Ho Chi Minh City, Vietnam
[3] Vietnam National University Ho Chi Minh City, Linh Trung Ward, Thu Duc City, Ho Chi Minh City, Vietnam
[*] Coressponding author: hoang.nguyen3702k20@hcmut.edu.vn

Abstract

With the rapid advancement of technology, integrated circuit (IC) design has become more complex and demanding, requiring the use of cutting-edge tools and methodologies to keep pace with the latest developments. Regarding the design of ICs, analog circuits make a significant contribution as the interface between the real and digital world signals. Although analog circuits account for a relatively small portion of the overall circuit, their design process often demands the major amount of design time. Much of the analog design time is from the phase of manual iteration of circuit parameters to meet the predetermined specifications, after a suitable topology has been selected. Since analog circuit sizing is repetitive and time-consuming, and to an extent, a monotonous task, design automation of analog circuits arises as a promising candidate to address the issue. Therefore, efficient optimization techniques are necessary for the automated optimal sizing of CMOS analog ICs. Among optimization algorithms, while genetic algorithm (GA) has been shown to be effective in finding near-optimal solutions, it has not been extensively applied to the field of analog circuit design. Hence, this paper proposes a method to utilize GA in the optimization of a widely used circuit topology, namely the comparator. Comparator is considered the fundamental block in the design of most analog-to-digital converters (ADC). For high-speed ADCs, high-speed and power-efficient comparators are highly desirable. As a result, the idea of applying GA to optimize speed and power consumption of comparators gradually comes up. In short, this paper demonstrates how GA can be applied to the optimization process of the comparator circuit with respect to speed and power consumption, for the sake of effort and time saving.

Keywords: *automation, genetic algorithm, analog-to-digital converter, comparator, speed, power consumption*

1. INTRODUCTION

Comparators are crucial to analog to digital converters (ADCs). They are used to convert from analog to digital domain signals in modern signal processing and communications. In designing high-speed ADCs, high-speed and low-power comparators are of great demand [1]. Dynamic comparators have higher speed and less static power consumption compared to static comparators due to strong positive feedback and dynamic bias provided by a pair of cross-coupled inverters as the latching stage [2]. Therefore, to optimize comparators' performance in terms of speed and power consumption, the dynamic comparator is chosen as a feasible topology.

In the design of the comparator, this paper focuses on two stages of analog circuit design, topology selection and circuit sizing in specific. Both stages must ensure that the resulting circuit meets specifications [3]. Since the first phase completed with the topology of the dynamic comparator, the second phase involves choosing the size of components. Owing to the repetition of manual iteration of circuit parameters, this sizing procedure is considered monotonous and time-consuming [4]. Hence, automation in the process of optimizing the sizes of circuits' components is critical to the ability to design high-performance circuits quickly [5].

To solve the problem of laborious circuit sizing in analog circuit design, effective optimization techniques are essential. Classical optimization techniques such as deterministic methods and statistical methods have been tested, but they prove to be ineffective owing to the applicability to small size optimization problems and uncertainty of convergence towards global optimum solution [5].

Gradient search methods are also inefficient because of its high tendency to get stuck in local minima. On the other hand, genetic algorithm (GA), based on the Darwinian principle of natural selection and concepts of natural genetics, has been found to be an effective solution to large search spaces without being trapped in local minima [4]. In spite of GA's advantages, it has not been extensively applied to the field of circuit design. To the authors' best experience and knowledge, the algorithm are mostly implemented in the design of operational amplifiers as in [4], [5] and has not been utilized for the case of the dynamic comparator. Therefore, this paper proposed a hybrid framework of GA and Spectre simulator that might set the prototype for the optimization problem of propagation delay and power dissipation for the dynamic comparator. With only 300 iterations of GA, the power-delay product (PDP) achieved is 0.2257 fJ, including an average delay of 77.7803 ps and power consumption of 2.9013 µW at 1 GHz clock frequency and 1.2 V supply voltage. These are promising values for assessment parameters, especially for the case of PDP since this work's PDP surpasses its counterparts in the work of [11], [13], [14], [15]. More importantly, thanks to its adaptibility, the combination of GA and Spectre can also be the optimization tool for different circuits, which is likely to revolutionize the work approach of analog circuit engineers.

The remaining part of the paper is organized as follows. Section 2 illustrates the operation of the single-tail dynamic comparator as well as its delay and power analysis. Subsequently, Section 3 demonstrates GA's flow and the proposed new architecture combining GA and Spectre simulator to optimize delay and power of the dynamic comparator. Simulation results and discussion are presented in Section 4, followed by the conclusion of the paper in Section 5.

2. METHODS AND IMPLEMENTATION

2.1. Working principle of the single-tail dynamic comparator

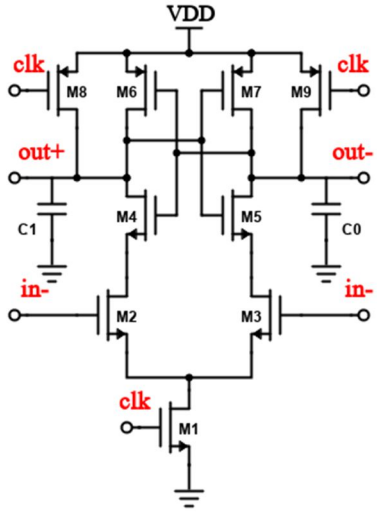

Figure 1. Conventional single-tail dynamic comparator

The operation of the conventional single-tail dynamic comparator depicted in Figure 1 consists of two phases [6]:

- Reset phase: The reset phase starts when clk = 0. The reset transistors M_8 and M_9 are on while the tail transistor M_1 is off. As a result, output nodes out+ and out- are pulled up to V_{DD}, which ensures the initial condition as well as valid logic level for the comparator.

- Comparison phase (decision-making phase): The comparison phase starts when clk = V_{DD}. The reset transistors M_8 and M_9 are off while the tail transistor M_1 is on. The output nodes out+ and out-, previously precharged to V_{DD}, turn M_4 and M_5 on. Also, these two output nodes begin to discharge their voltages, which is still high enough to keep M_4 and M_5 on. The discharging rate of out+ and out- depends on the voltages at two input nodes in+ and in-.

+ When in+ > in-: Out+ discharges at a faster rate compared to out-. This means that the voltage at out+ drops to $V_{DD} - |V_{THP}|$ before out-, making M_7 turn on before M_6. Since (M_4, M_6) and (M_5, M_7) together form back-to-back inverters, the latch regeneration is activated. Hence, out+ and out- are pulled down to GND and pulled up to V_{DD}, respectively.

+ When in+ < in-: The circuit works in the opposite manner with the final result of out+ and out- being pulled up to $\mathbf{V_{DD}}$ and pulled down to GND, respectively.

2.2. Delay analysis

Propagation delay is one of the key features of a comparator. It consists of two parts:

- Delay for the capacitors C_0 and C_1 to discharge to the point when M_6 and M_7 turn on:

$$t_0 = \frac{C_i|V_{THP}|}{I_3} \approx \frac{C_i|V_{THP}|}{\frac{I_1}{2}} = 2\frac{C_i|V_{THP}|}{I_1} \quad (1)$$

where C_i is the load capacitor at the output nodes with equal values (i = 0, 1 and $C_0 = C_1$); V_{THP} is the threshold voltage of p-channel MOSFETs M_6, M_7 ; I_1, I_3 are the drain currents through M_1, M_3.

- Delay from the two cross-coupled inverters:

The latch delay is calculated as:

$$t_{latch} = \frac{C_i}{gm_{eq}} \ln\left(\frac{\Delta V_{out}}{\Delta V_0}\right) = \frac{C_i}{gm_{eq}} \ln\left(\frac{V_{DD}/2}{\Delta V_0}\right) \quad (2)$$

where gm_{eq} is the equivalent transconductance of the latch, ΔV_{out} is the output voltage swing , V_{DD} is the supply voltage and ΔV_0 is the output voltage difference.

At time t_0:

$$\Delta V_0 = |V_{THP}|\frac{\Delta I_{in}}{I_1/2} = \frac{2|V_{THP}|\sqrt{\beta_{2,3}I_1}}{I_1}\Delta V_{in}$$
$$= 2|V_{THP}|\sqrt{\frac{\beta_{2,3}}{I_1}}\Delta V_{in} \quad (3)$$

where ΔI_{in} is the current difference at the input end and $\beta_{2,3} \equiv \beta_2, \beta_3$ are the current factors of M_2, M_3, respectively.

Substitute (3) into (2):

$$t_{latch} = \frac{C_i}{gm_{eq}}\ln\left(\frac{V_{DD}/2}{2|V_{THP}|\sqrt{\beta_{2,3}/I_1}\Delta V_{in}}\right)$$
$$= \frac{C_i}{gm_{eq}}\ln\left(\frac{V_{DD}}{4|V_{THP}|\Delta V_{in}}\sqrt{\frac{I_1}{\beta_{2,3}}}\right) \quad (4)$$

- Total delay is the sum of its two parts:

$$t_{delay} = t_0 + t_{latch}$$
$$= 2\frac{C_i|V_{THP}|}{I_1} + \frac{C_i}{gm_{eq}}\ln\left(\frac{V_{DD}}{4|V_{THP}|\Delta V_{in}}\sqrt{\frac{I_1}{\beta_{2,3}}}\right) \quad (5)$$

Simlation results illustrate that t_0 dominates t_{latch} [1], t_{delay} follows the change in t_0. In other words, when I_1 decreases, t_0 increases and t_{delay} hence increases, and vice versa.

Figure 2 demonstrates the transient simulation of the conventional dynamic comparator in one clock period, consisting of both the comparison and the reset phase.

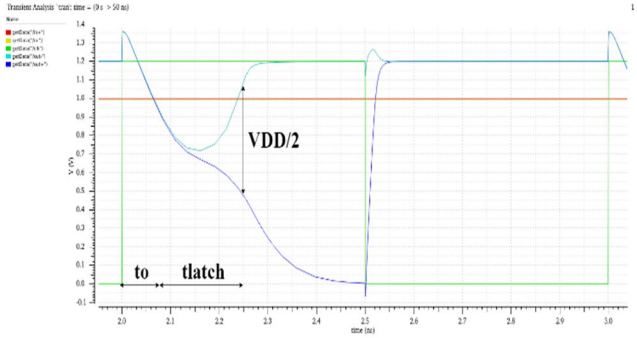

Figure 2. Transient simulation of the conventional dynamic comparator

2.3. Power analysis

For one period of comparison, the average power of the supply voltage is calculated as:

$$Power_{avg} = \frac{1}{T}\int_0^T V_{DD}I_{supply}dt = f_{clk}V_{DD}\int_0^T I_{supply}dt \quad (6)$$

where f_{clk} is the frequency of the comparator's clock, V_{DD} is the supply voltage, I_{supply} is the current drawn from the supply voltage.

Figure 3 shows the transient simulation of the current I_{supply} in one period. To calculate the power dissipation of the dynamic comparator, we integrate I_{supply} with respect to time in one period and multiply with f_{clk} and V_{DD} as in equation (6) to obtain the result.

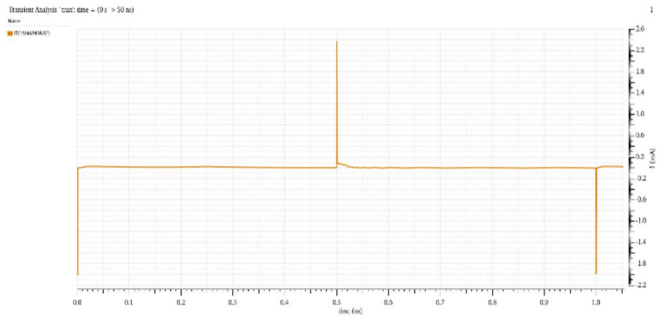

Figure 3. Transient simulation of the current I_{supply}

3. OPTIMIZATION BY GENETIC ALGORITHM

3.1. Genetic algorithm (GA)

Genetic algorithm (GA) is one of the evolutionary computation methods widely used in optimization problems. GA's basis is the principle of natural selection, in which suitable individuals in a specific environment survive and reproduce while others are eliminated [9]. With the idea of "survival to the fittest", better solutions are generated thanks to successive evolution of generations.

The implementation of GA is described in the flowchart of Figure 4:

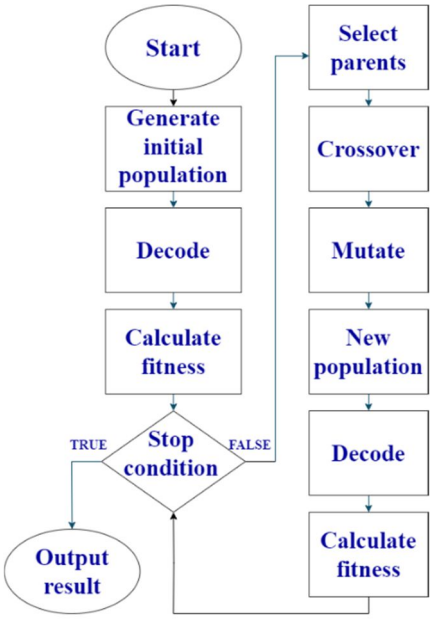

Figure 4. Genetic algorithm's flowchart

The algorithm starts by initializing a population of a fixed size with randomly created solutions. These solutions, usually encoded in bitstring of a fixed length, are modeled as

chromosomes. The chromosomes consist of genes, represented by one bit or a group of bits. Every generation, the bitstrings of chromosomes are decoded for fitness calculation to find the best individual in the current population. After this step, the stop condition, including the number of iterations or the comparison with the target, is considered. If this condition is not met, the algorithm continues with the selection process.

According to the fitness value, a subgroup of chromosomes - the parents - is selected to create the new population of offspring in the process of crossover and mutation. During crossover, the bitstrings of two randomly selected parents from the set of chosen parents are separated into parts at the same location and swapped together to create two children chromosomes for the next generation. In order for the solutions to avoid being stuck at local optima, the next step involves the mutation process, which can be as simple as inverting one bit in the bitstring or more complicated as complete gene modifications [9]. The crossover and mutation step is implemented with certain probabilities r_{cross} and r_{mut} inside the range [0;1]. Since a new population has already been created, the algorithm continues with decoding and fitness calculation. When the fitness results of the children population are available, the best chromosome can be found. Afterwards, the terminating condition is re-evaluated. GA stops only when this condition is true. The output result of GA is the decoded solution of the chromosome with the best fitness value.

3.2. Proposed hybrid model of GA and Spectre to optimize delay and power of the dynamic comparator

When applying GA to optimization problems, it is necesary to make suitable modifications to the step of fitness calculation for specific problems. For the optimization of analog circuit design, the "Calculate fitness" block in Figure 4 consists of two substeps. The first one is delay and power simulation, which are executed by Spectre simulation platform of Cadence Virtuoso tool in the TSMCN65 process. The remaining step is the evaluation of fitness values according to delay and power data collected in the previous step.

In this research, GA is implemented in Python programming language. The interrelation between Spectre and Python is described as followed. At first, the values for the population of design variables are created by Python and sent to Spectre via an Ocean-based script. This Ocean script is responsible for automated circuit simulations based on received numbers and the results are sent back and further processed by the Python script to evaluate fitness scores of each individual. This repetitive process carries on until the algorithm reaches its stopping point.

Regarding the case of optimizing delay and power of the dynamic comparator, firstly, determining the optimization variables, parameters that mainly contribute to delay and power results, is essential. Since we use the TSMCN65 process for the design, the lengths of all the MOSFETs in the circuit are set to 65 nm. Since ΔV_{in} of the dynamic comparator is fixed at 5 mV, I_1 and C_i are responsible for delay adjustment.

Therefore, we declare two delay-related variables: the width of M_1 (W_1) and the capacitors' values (C_i). Similarly, as the values of V_{DD} and frequency of the clock signal clk is assigned to 1.2 V and 1 GHz, our power-related variables are determined based on the current I_{supply}, which is the sum of four currents flowing through M_6, M_7, M_8, M_9. Due to the symmetry of the circuit, the width of M_6 and M_7, M_8 and M_9 should be equal. Hence, we declare two more variables: width of M_6 and M_7 (W_{67}), width of M_8 and M_9 (W_{89}). The remaining MOSFETs widths are set to 0.2 µm, which is the default width from the process. In order to satisfy the range of the process and assure the functional correctness of the dynamic comparator, simulation results indicate that the bounds for W_1, W_{67}, W_{89}, C_i are [0.12 µm; 2 µm], [0.12 µm; 2 µm], [0.12 µm; 2 µm], [0.1 fF; 0.8 fF].

For subsequent GA initializing steps, the number of bits for each chromosome representation and the number of individuals in a population are defined to be 16 bits and 6 individuals, correspondingly. While crossover has high probability, the probability of mutation is typically low; [10] shows that r_{cross} and r_{mut} are inside the range [0.8; 0.95] and [0.001; 0.05]. Finally, the choice of a suitable fitness function is also critical. With a view to optimizing both delay and power of the dynamic comparator, we choose the figure of merit (FoM) in the form of PDP similar to [11] as the fitness function for GA. In this case, the comparator is considered to perform better with lower value of PDP.

Our optimization problem can be summarized as:

minimize PDP(W_1, W_{67}, W_{89}, C_i)

subject to $L = 65$ nm, $W_2 = W_3 = W_4 = W_5 = 200$ nm

$\Delta V_{in} = 5$ mV, $V_{DD} = 1.2$ V, $f_{clk} = 1$ GHz

$0.12\ \mu m \leq W_1, W_{67}, W_{89} \leq 2\ \mu m$

$0.1\ fF \leq C_i \leq 0.8\ fF$.

4. RESULTS AND DISCUSSIONS

Simulation results indicate that the lowest value for PDP of 0.2257 fJ is achieved for the case of r_{cross} = 0.9 and r_{mut} = 0.015625. With PDP = 0.2257 fJ, delay and power of the conventional dynamic comparator are 77.7802 ps and 2.9013 µW, respectively. PDP fitness values as well as delay and power over 300 iterations of GA are illustrated in Figure 5 and Figure 6.

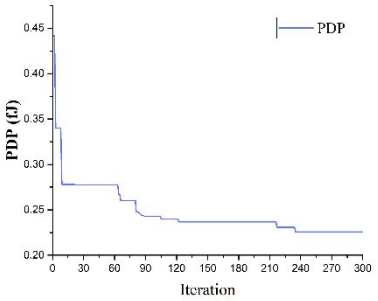

Figure 5. Fitness value of PDP versus 300 iterations

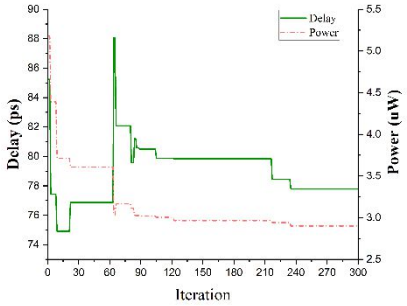

Figure 6. Delay and power versus 300 iterations

In terms of the variables declared for GA, the optimal set $(W_1, W_{67}, W_{89}, C_i)$ = (0.2308 µm, 0.1203 µm, 0.1269 µm, 0.1005 fF) is obtained after 100 iterations of the algorithm.

The post-optimization sizes of all MOSFETs in the circuit are presented in Table 1:

Table 1. Post-optimization transistors' sizes

Device	Size (W/L)
M_1	0.2308 µm/65 nm
M_2, M_3, M_4, M_5	0.2 µm/65 nm
M_6, M_7	0.1203 µm/65 nm
M_8, M_9	0.1269 µm/65 nm
C_0, C_1	0.1005 fF

Table 2 summarizes the performance of the conventional dynamic comparator of this research and other research works:

Table 2. Performance summary of different dynamic comparator designs

Parameters	References					
	[1]	*[11]*	*[13]*	*[14]*	*[15]*	***This work***
CMOS Process (nm)	90	65	65	90	40	65
Supply voltage (V)	1.2	1	1.2	1	1.1	1.2
Clock frequency (GHz)	3.07	20	6	1	6	1
Average delay (ps)	410	14.28	42.7	51.76	54	77.7802
Power dissipation (µW)	0.24	67.8	381	32.62	288	2.9013
PDP (fJ)	0.0984	0.968	16.3	1.67	15.552	0.2257
Energy per conversion (fJ/conv.)	0.07818	3.39	63.5	32.62	48	2.9013

As the conventional dynamic comparator in this work has zero static power consumption, its power consumption at 1 GHz is much lower than that of the circuit of [14]. Since clock frequency is directly proportional to power dissipation as presented in equation (6), the designs of [11], [13] and [15] with higher clock frequency exhibit higher power than our design, which is reasonable. Meanwhile, the power consumption in [1] is still lower despite operating at higher frequency. The parameter energy per conversion, which is equal to the ratio of power over sampling frequency (or clock frequency), is therefore needed to evaluate dynamic comparators' performance with respect to power. From Table 2, it is clear that our research work has the second-lowest energy per conversion value at 2.9013 fJ per conversion.

In addition, compared to [13], [14] and [15], our work has approximately 20% higher average delay. On the contrary, our average delay is less than one-fifth in comparison with the delay of [1]. Because delay and power trade off with each other, PDP is utilized as the FoM in the case of optimizing both parameters. With respect to PDP, our design obtained the second-best value of 0.2257 fJ versus the lowest number of 0.0984 fJ by [1].

5. CONCLUSION

GA can be considered a novel approach of using software algorithm to optimize analog circuit. Instead of trial-and-error process of circuit sizing, the hybrid framework of GA and Spectre solves the problem in a much more effective and time-saving way. This paper successfully applied this framework to optimize the dynamic comparator with the result of 77.4902 ps delay and 2.9629 µW power dissipation. Hence, the algorithm proves to be a promising solution to the optimal circuit's parameters. Since the mentioned architecture of GA and Spectre could also be applied to optimization problems of different circuits, it might bring about the transformation in the way analog circuit engineers work.

Acknowledgement

This research is funded by the Office for International Study Programs (OISP), Ho Chi Minh City University of Technology (HCMUT), VNUHCM under grant number **SVOISP-2022-ĐĐT-127**. We acknowledge the support of time and facilities from HCMUT, VNUHCM for this study.

References

[1] Sahil Jakhara, Vishal Singh Mandloi, Rupam Goswami, Kavindra Kandpal, "A Low Power, High Speed 1.2 V Dynamic Comparator for Analog-to-Digital Converters," in Third International Conference on Computing and Network Communications, 2020.

[2] Yao Wang, Mengmeng Yao, Benqing Guo, et al., "A Low-Power High-Speed Dynamic Comparator with a Transconductance-Enhanced Latching Stage," IEEE Access, 2019.

[3] Miri Weiss Cohen, Michael Aga, Tomer Weinberg, "Genetic Algorithm Software System for Analog Circuit Design," in 25th CIRP Design Conference, 2015.

[4] Kenneth V. Noren, John E. Ross, "Analog Circuit Design Using Genetic Algorithms," in Online Symposium for Electronics Engineers.

[5] S. Mallick, R. Kar, D. Mandal, S. P. Ghoshal, "Optimal sizing of CMOS analog circuits using gravitational search algorithm with particle swarm optimization," 2015.

[6] R.Rameshkuma, S.Bharathiraja, "A COMPARATIVE ANALYSIS OF HIGH SPEED DYNAMIC COMPARATOR IN 180NM AND 90NM USING H-SPICE," International Journal of Innovations in Scientific and Engineering Research (IJISER), 2014.

[7] Samaneh Babayan-Mashhadi, Mojtaba Daliri, Reza Lotfi, "Analysis of Power in Dynamic Comparators," in IEEE, 2013.

[8] Y. Tsividis, K.Suyama and K.vavelidis, "Simple reconciliation MOSFET model valid in all regions," IEE Electronic, 1995.

[9] Yanfeng Jiang, Jiaxin Ju, Xiaobo Zhang, Bing Yang, "Automated Analog Circuit Design Using Genetic Algorithms," Beijing.

[10] Xin-She Yang, Su Fong Chien, Tiew On Ting, in Bio-Inspired Computation and Optimization: An Overview, 2015, p. 11.

[11] Folla JK, Crespo ML, Wembe ET, et al., "A low-offset low-power and high-speed dynamic latch comparator with a preamplifier-enhanced stage," in IET Circuits, Devices & Systems, 2020.

[12] Lourans Samid, Patrick Volz, Yiannos Manoli, "A DYNAMIC ANALYSIS OF A LATCHED CMOS COMPARATOR," in 2004 IEEE International Symposium on Circuits and Systems (ISCAS), Vancouver, BC, Canada, 2004.

[13] Hossein Ghasemian, Razieh Ghasemi, Ebrahim Abiri, Mohammad Reza Salehi, "A Novel High-Speed Low-Power Dynamic Comparator with Complementary Differential Input in 65nm CMOS Technology," Microelectronics Journal, 2019.

[14] Vijay Savani, N. M. Devashrayee, "Analysis and design of low-voltage low-power high-speed double tail current dynamic latch comparator," Analog Integr Circ Sig Process, 2017.

[15] Sen Huang, Lin He, Yu-Kai Chou, and Fujiang Lin, "A 288-μW 6-GHz Hybrid Dynamic Comparator with 54-ps Delay in 40-nm CMOS," in IEEE MTT-S International Wireless Symposium (IWS), Shanghai, China, 2016.

OPTIMIZING THE PSRR PARAMETER OF THE BANDGAP REFERENCE CIRCUIT BY USING THE BAYESIAN OPTIMIZATION ALGORITHM

(ỨNG DỤNG GIẢI THUẬT TỐI ƯU BAYESIAN NHẰM TỐI ƯU THÔNG SỐ PSRR CỦA MẠCH BANDGAP REFERENCE)

Nguyen Quoc Thang[1,2,3,*], Hoang Trang[1,3,*]

[1] Faculty of Electrical and Electronics Engineering, Ho Chi Minh City University of Technology (HCMUT), 268 Ly Thuong Kiet Street, District 10, Ho Chi Minh City, Vietnam
[2] Office for International Study Programs, Ho Chi Minh City University of Technology (HCMUT), 268 Ly Thuong Kiet Street, District 10, Ho Chi Minh City, Vietnam
[3] Vietnam National University Ho Chi Minh City, Linh Trung Ward, Thu Duc City, Ho Chi Minh City, Vietnam
[*] Corresponding author: thang.nguyenvt123@hcmut.edu.vn, hoangtrang@hcmut.edu.vn

Abstract

Bandgap Reference (BGR) Circuit is extensively utilized as a voltage reference generator in several analog integrated circuits. The supply-ripple independence of the reference voltage, represented by the power supply rejection of the ratio (PSRR) parameter, plays a vital role in the performance of the whole circuit. Therefore, improving the PSRR value of the BGR circuit has garnered significant attention. In this work, the design of a 65nm-CMOS low-voltage BGR Circuit, and how to improve its PSRR parameters, are presented. To increase the PSRR value, there is a modification in the structure of the op-amp employed in the proposed BGR circuit, compared to the conventional BGR core. The small signal model and how to determine the differential gain of the proposed op-amp are explained in the paper. Besides, to reduce the time consumption of the device sizing process, the optimum PSRR value is obtained by implementing the Bayesian optimization algorithm to choose the suitable geometrical size of each MOSFET. In addition, the procedure of using Ocean language to make the interaction between the optimization algorithm and the computer-aided design (CAD) tool, and to run the simulation automatically, is also introduced in this paper. After all, the simulation result shows that the value of output voltage at typical PVT conditions is $V_{REF,typ} = 800.6mV$, with a temperature coefficient of 9.0ppm/°C and PSRR value of 102.4dB at 1kHz. In conclusion, the modification in the op-amp's architect, the application of the Bayesian Optimization algorithm to optimize the PSRR value, and how to use Ocean language in analog IC design flow are the main contributions of this work.

Keywords: *Analog circuit sizing, Bandgap reference circuit, Bayesian optimization, PSRR*

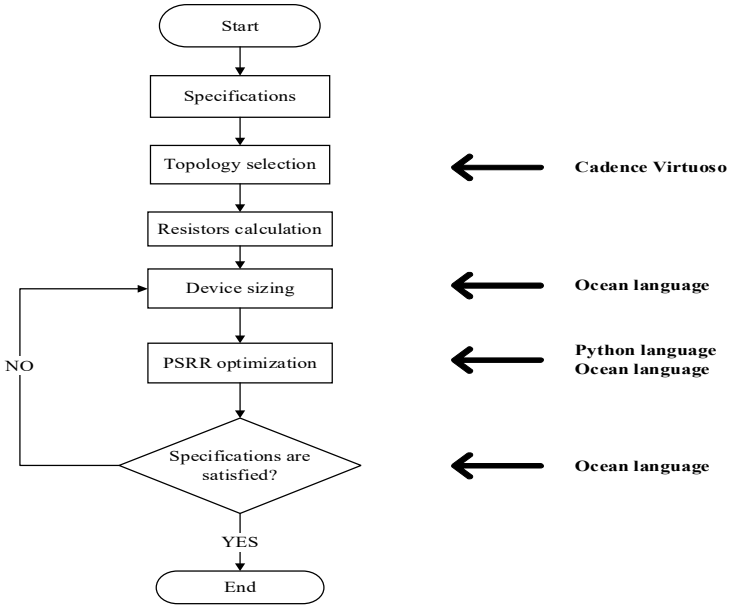

Figure 1. Design process overview

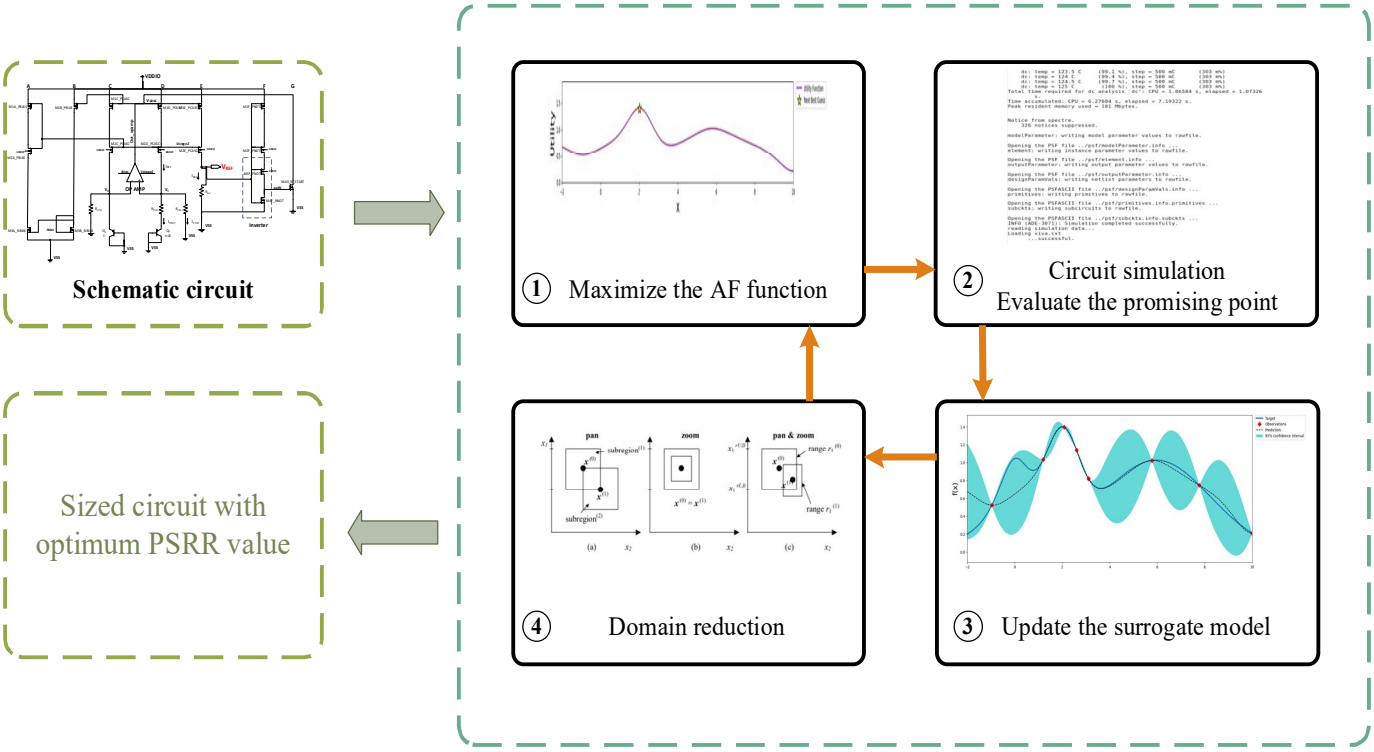

Figure 2. PSRR optimization process overview

Tóm tắt

Mạch Bandgap Reference (BGR) là một mạch được sử dụng rất phổ biến để tạo ra điện áp tham chiếu trong các vi mạch tương tự. Sự độc lập của điện áp tham chiếu vào nhiễu tại điện áp nguồn, đặc trưng bởi thông số PSRR, có vai trò quan trọng đối với hiệu suất của toàn mạch. Do đó, việc cải thiện PSRR của mạch BGR rất được quan tâm nghiên cứu. Trong nghiên cứu này, tác giả trình bày một mạch BGR được thiết kế trên nền công nghệ 65nm. Nhằm cải thiện giá trị của thông số PSRR, cấu trúc của op-amp được đề xuất sử dụng trong mạch BGR này có một số sửa đổi so với cấu trúc mạch BGR truyền thống. Bên cạnh đó, nhằm giảm thời gian thực hiện quá trình thiết kế mạch, việc tối ưu hoá thông số PSRR được thực hiện bằng cách áp dụng thuật toán tối ưu Bayesian nhằm lựa chọn thông số hình học cho các MOSFET. Ngoài ra, quy trình sử dụng ngôn ngữ Ocean nhằm tương tác giữa thuật toán tối ưu và phần mềm thiết kế, và thực hiện mô phỏng một cách tự động, cũng được giới thiệu trong bài báo. Kết quả mô phỏng cho thấy, tại điều kiện thông thường, điện áp ngõ ra của mạch BGR là $V_{REF,typ} = 0.8006\,V$, với hệ số nhiệt độ bằng 9.0ppm/°C và giá trị PSRR là 102.4dB tại 1kHz. Tóm lại, ba đóng góp chính của bài báo là đề xuất một cấu trúc op-amp khác, ứng dụng thuật toán Bayesian vào bài toán tối ưu hoá thông số PSRR, và áp dụng ngôn ngữ Ocean trong quy trình thiết kế vi mạch tương tự.

Từ khoá: *Điều chỉnh kích thước trong thiết kế vi mạch tương tự, Mạch Bandgap reference, Tối ưu Bayesian, Thông số PSRR*

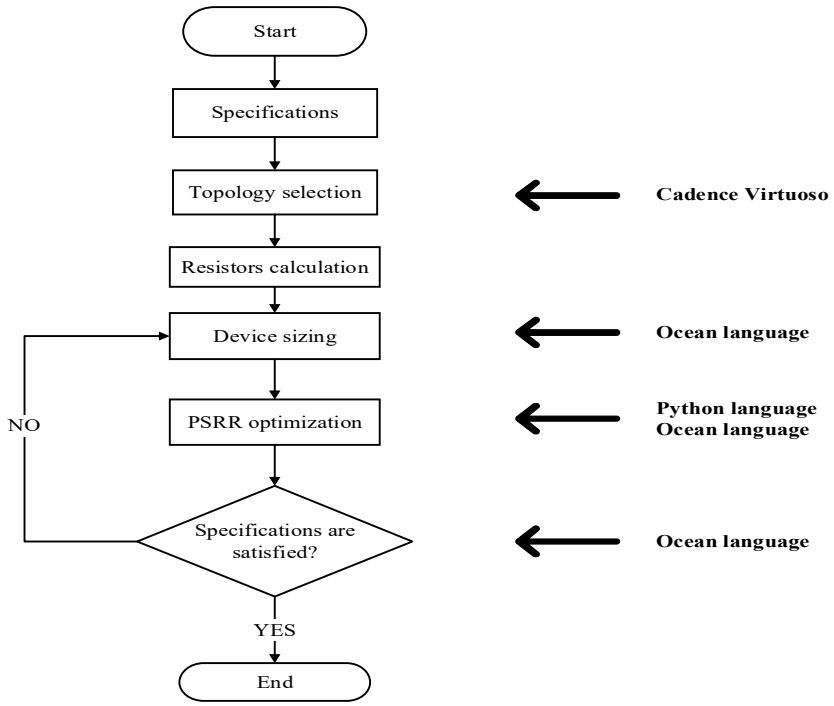

Hình 1. Tổng quan quá trình thiết kế

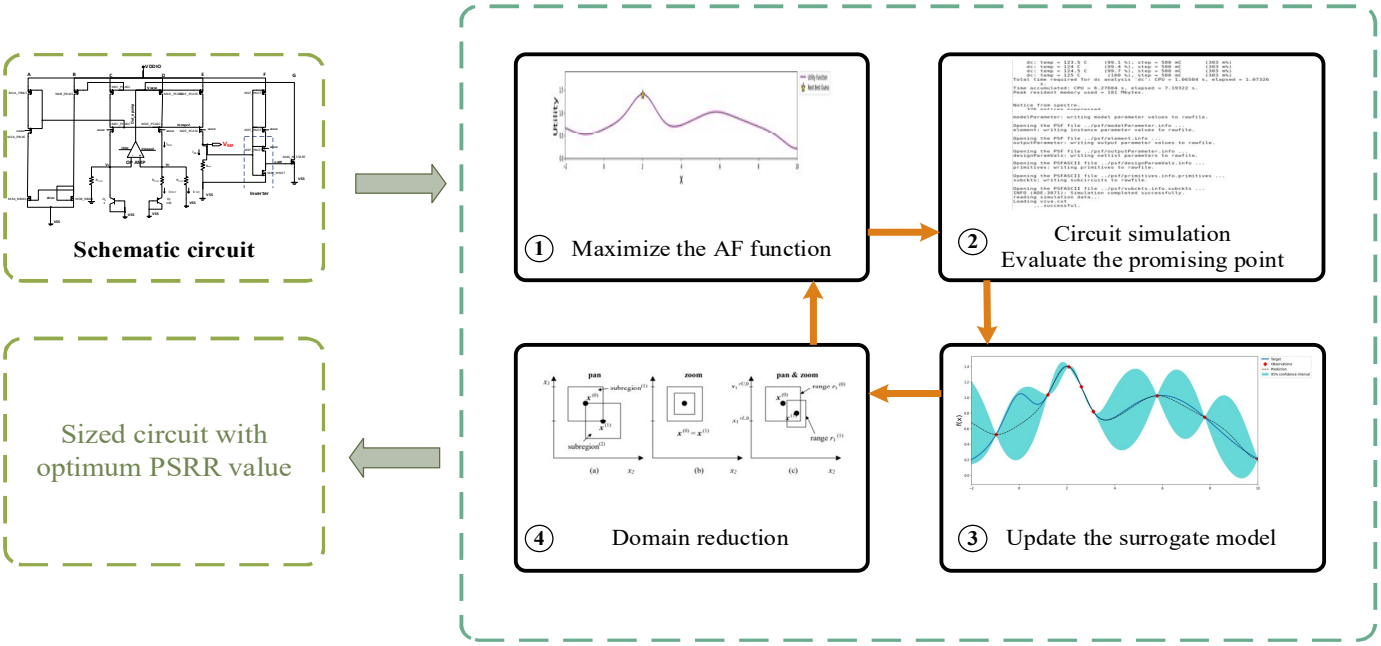

Hình 2. Tổng quan quy trình tối ưu hoá thông số PSRR

Acknowledgement: This research is funded by the Office for International Study Programs (OISP), Ho Chi Minh City University of Technology (HCMUT), VNUHCM under grant number **SVOISP-2022-ĐĐT-128**. We acknowledge the support of time and facilities from HCMUT, VNUHCM for this study.

FINITE ELEMENT INVESTIGATION AND PREDICTION OF THE BEARING CAPACITY OF CIRCULAR FOOTINGS RESTING ON SLOPING ROCKS

(KHẢO SÁT VÀ PHÂN TÍCH KHẢ NĂNG CHỊU TẢI CỦA MÓNG TRÒN TRÊN MÁI DỐC ĐÁ ÁP DỤNG PHƯƠNG PHÁP PHẦN TỬ HỮU HẠN)

Do Vo Kim Khue[1,2,3], Nguyen Hoang Phuc[1,2,3], Ho Ngoc Hao[1,2,3], Nguyen Tri Dung[1,2,3], Lai Van Qui[1,3,*]

[1] Faculty of Civil Engineering, Ho Chi Minh City University of Technology (HCMUT), 268 Ly Thuong Kiet Street, District 10, Ho Chi Minh City, Vietnam
[2] Office for International Study Programs, Ho Chi Minh City University of Technology (HCMUT), 268 Ly Thuong Kiet Street, District 10, Ho Chi Minh City, Vietnam
[3] Vietnam National University Ho Chi Minh City, Linh Trung Ward, Thu Duc City, Ho Chi Minh City, Vietnam
[*] Corresponding author: lvqui@hcmut.edu.vn

Abstract

The soil and slope strengths aspects are crucial in determining the bearing capacity of a circular footing on a rock slope, emphasizing the importance of rigorous study and design considerations. Previous research has typically concentrated on simple circular footing scenarios, either on the sloping ground using Mohr-Coulomb principles or on a horizontal soil plane using the Hoek-Brown model. This research illustrates the parametric study to investigate the bearing capacity of circular footing on the rock slope using the commercial finite element software, Plaxis 3D. The Hoek-Brown criteria are applied to describe the behavior of the rock slope, in which the geological strength index (GSI) and experimental constant of intact rock (m_i) are all considered. Moreover, the geometry parameters, including slope angle β and the setback ratio b/R, are studied to investigate the effect of slope on the bearing capacity of the circular footing on the slope. The results of this study are verified and compared with prior studies in case the setback ratio is large enough to eliminate the effect of the slope. The results also indicate that the bearing capacity of the circular footing changes concerning various parameters; all data are shown in graphs. This study provides the impact of different parameters on the bearing capacity of circular footings on Hoek-Brown slopes, which can assist in optimizing the design of foundations in geotechnical engineering.

Keywords: *circular footing, Hoek-Brown, Plaxis 3D*

Tóm tắt

Các khía cạnh cường độ của đất và độ dốc rất quan trọng trong việc xác định khả năng chịu lực của móng tròn trên dốc đá, nhấn mạnh tầm quan trọng của việc nghiên cứu và cân nhắc thiết kế nghiêm ngặt. Những nghiên cứu trước đây thường tập trung vào các bối cảnh móng tròn đơn giản, trên mặt đất dốc sử dụng nguyên tắc Mohr-Coulomb hoặc trên mặt phẳng đất nằm ngang sử dụng mô hình Hoek-Brown. Nghiên cứu này tập trung nghiên cứu tham số để khảo sát khả năng chịu lực của móng tròn trên mái dốc bằng phần mềm phần tử hữu hạn, Plaxis 3D. Tiêu chí Hoek-Brown được áp dụng để mô tả ứng xử của mái dốc đá, trong đó chỉ số về độ cứng của đất (GSI) và các thông số về tính toàn vẹn của đá (mi) đều được xem xét. Ngoài ra, các thông số hình học gồm góc dốc β và khoảng lùi b/R được nghiên cứu để khảo sát ảnh hưởng của độ dốc đến khả năng chịu lực của móng tròn trên mái dốc. Kết quả của nghiên cứu này được kiểm chứng và so sánh với các nghiên cứu trước trong trường hợp hệ số lùi đủ lớn để loại bỏ ảnh hưởng của độ dốc. Kết quả cũng chỉ ra rằng khả năng chịu lực của móng tròn thay đổi theo các thông số khác nhau; tất cả dữ liệu được hiển thị trong biểu đồ. Nghiên cứu này cung cấp tác động của các thông số khác nhau đến khả năng chịu lực của móng tròn trên mái dốc Hoek-Brown, và có thể giúp tối ưu hóa thiết kế nền móng trong địa kỹ thuật.

Từ khóa: *Móng tròn, Hoek-Brown, Plaxis 3D*

Acknowledgement: This research is funded by the Office for International Study Programs (OISP), Ho Chi Minh City University of Technology (HCMUT), VNUHCM under grant number **SVOISP-2022-KTXD - 135**. We acknowledge the support of time and facilities from HCMUT, VNUHCM for this study.

SPECIFICATION FOR THE INTERMEDIATE BRACING SYSTEM DESIGN OF STEEL I GIRDER SIMPLE SPAN BRIDGES

(NGHIÊN CỨU ĐỀ XUẤT QUY TRÌNH THIẾT KẾ HỆ GIẰNG TRUNG GIAN TRONG CẦU THÉP DẦM GIẢN ĐƠN)

Pham Thi Khanh Van[1,2,3], Tran Van Huynh[1,3], Tran lam Ha[1,3], Huynh Ngoc Thi[1,3,*]

[1] Faculty of Civil Engineering, Ho Chi Minh City University of Technology (HCMUT), 268 Ly Thuong Kiet Street, District 10, Ho Chi Minh City, Vietnam
[2] Office for International Study Programs, Ho Chi Minh City University of Technology (HCMUT), 268 Ly Thuong Kiet Street, District 10, Ho Chi Minh City, Vietnam
[3] Vietnam National University Ho Chi Minh City, Linh Trung Ward, Thu Duc City, Ho Chi Minh City, Vietnam
[*] Corresponding author: huynhngocthi@hcmut.edu.vn

Abstract

Nowadays, composite steel bridges are becoming a development trend in the transportation industry both domestically and overseas because of the outstanding benefits in terms of materials compared to concrete bridges, as well as the simplicity of installation, manufacturing, and fast construction. Steel is notable for its strong resistance to a wide range of stresses. In particular, the intermediate bracing system is critical in resisting overall instability and provides effective bearing capacity for the construction during the construction phase. The design of the intermediate bracing system requires a high level of precision. The exceed or lack of the number of the required intermediate bracing system in the design will both result in unsafety during construction and operation. Currently, neither the American Association of State Highway and Transportation Officials Standards (AASHTO) nor the Vietnamese standard TCVN 11823-2017 provides the specific procedure for this system, resulting in wastage of materials and safety design. This research was carried out to suggest a design process for an intermediate bracing system for a simple span I-beam steel girder bridge.

Keywords: *intermediate bracing systems, composite beam bridge, overall instability*

Tóm tắt

Ngày nay, cầu thép đang trở thành xu hướng phát triển của ngành giao thông vận tải cả trong và ngoài nước vì những ưu điểm nổi bật về mặt vật liệu so với cầu bê tông cũng như sự đơn giản trong lắp ráp, chế tạo và thời gian thi công nhanh. Đặc điểm nổi bật của thép là tính chịu lực cao ứng với mọi loại ứng suất. Trong đó, hệ liên kết ngang là bộ phận cực kỳ quan trọng giúp chống lại sự mất ổn định tổng thể và đảm bảo khả năng chịu lực tốt nhất cho công trình đặc biệt trong giai đoạn thi công. Thiết kế hệ liên kết ngang trong cầu thép đòi hỏi sự chính xác tương đối cao. Nếu hệ liên kết ngang được thiết kế dư (quá lớn), hay thiếu (quá nhỏ) đều sẽ dẫn đến sự mất an toàn trong quá trình thi công và khai thác. Hiện nay, trong tiêu chuẩn xây dựng cầu TCVN 11823-2017 vẫn chưa đưa ra một quy trình cụ thể cho việc thiết kế bộ phận này dẫn đến nhiều hệ giằng ngang được thiết kế khá lớn gây lãng phí về mặt vật liệu cũng như kém an toàn trong giai đoạn khai thác. Phương pháp nghiên cứu của đề tài là vừa tổng hợp các lý thuyết, kết quả nghiên cứu khác và kiểm tra bằng phần mềm mô phỏng để xây dựng quy trình tính toán riêng. Từ đó xây dựng quy trình thiết kế cho hệ giằng trung gian

Từ khóa: *hệ giằng trung gian, cầu dầm liên hợp, mất ổn định tổng thể*

Acknowledgement: This research is funded by the Office for International Study Programs (OISP), Ho Chi Minh City University of Technology (HCMUT), VNUHCM under grant number **SVOISP-2022-KTXD**. We acknowledge the support of time and facilities from HCMUT, VNUHCM for this study.

The 12th OISP Science and Technology Symposium for students

Edited by Authours, Vietnam National University Ho Chi Minh City, BK- OISP

NHÀ XUẤT BẢN ĐẠI HỌC QUỐC GIA THÀNH PHỐ HỒ CHÍ MINH

Trụ sở:

Phòng 501, Nhà Điều hành ĐHQG-HCM, P. Linh Trung, TP Thủ Đức, TP.HCM.

ĐT: 028 62726361

E-mail: vnuhp@vnuhcm.edu.vn

Website: www.vnuhcmpress.edu.vn

Chịu trách nhiệm xuất bản và nội dung

TS ĐỖ VĂN BIÊN

Biên tập

SIN KẾ DUYÊN

Sửa bản in

NHƯ NGỌC

Trình bày bìa

NGÔ THỤC NHƯ

Đối tác liên kết

VĂN PHÒNG ĐÀO TẠO QUỐC TẾ

Xuất bản lần thứ 1. Số lượng in: 100 cuốn, khổ 20 x 29 cm. Số XNĐKXB: 3228-2023/CXBIPH/1-54/ĐHQGTPHCM. QĐXB số: 224/QĐ-NXB cấp ngày 26/9/2023. In tại: Công ty TNHH TM DV Thiết kế in ấn Thiên Ấn. Địa chỉ: 240A Lê Văn Lương, phường Tân Hưng, quận 7, TP.HCM. Nộp lưu chiểu: Năm 2023. ISBN: **978-604-479-185-2.**

VIET NAM NATIONAL UNIVERSITY
HO CHI MINH CITY

BK - OISP

OFFICE FOR INTERNATIONAL STUDY PROGRAMS
268 LY THUONG KIET, WARD 14, DISTRICT 10, HCMC
PHONE NUMBER: [028] 7300 4183

ISBN:978-604-479-185-2
9 786044 791852
NXB ĐHQG-HCM

NOT FOR SALE